

UNIVERSIDADE DE SÃO PAULO
Instituto de Ciências Matemáticas e de Computação

Digital 3D Animation of Powder-Snow Avalanches

Filipe de Carvalho Nascimento

Tese de Doutorado do Programa de Pós-Graduação em Ciências de Computação e Matemática Computacional (PPG-CCMC)

SERVIÇO DE PÓS-GRADUAÇÃO DO ICMC-USP

Data de Depósito:

Assinatura: _____

Filipe de Carvalho Nascimento

Digital 3D Animation of Powder-Snow Avalanches

Thesis submitted to the Instituto de Ciências Matemáticas e de Computação – ICMC-USP – in accordance with the requirements of the Computer and Mathematical Sciences Graduate Program, for the degree of Doctor in Science. *EXAMINATION BOARD PRESENTATION COPY*

Concentration Area: Computer Science and Computational Mathematics

Advisor: Prof. Dr. Afonso Paiva

USP – São Carlos
January 2024

Ficha catalográfica elaborada pela Biblioteca Prof. Achille Bassi
e Seção Técnica de Informática, ICMC/USP,
com os dados inseridos pelo(a) autor(a)

d278d de Carvalho Nascimento, Filipe
Digital 3D Animation of Powder-Snow Avalanches /
Filipe de Carvalho Nascimento; orientador Afonso
Paiva. -- São Carlos, 2024.
187 p.

Tese (Doutorado - Programa de Pós-Graduação em
Ciências de Computação e Matemática Computacional) --
Instituto de Ciências Matemáticas e de Computação,
Universidade de São Paulo, 2024.

1. . I. Paiva, Afonso, orient. II. Título.

Filipe de Carvalho Nascimento

Animação Digital de Avalanches de Neve

Tese apresentada ao Instituto de Ciências Matemáticas e de Computação – ICMC-USP, como parte dos requisitos para obtenção do título de Doutor em Ciências – Ciências de Computação e Matemática Computacional. *EXEMPLAR DE DEFESA*

Área de Concentração: Ciências de Computação e Matemática Computacional

Orientador: Prof. Dr. Afonso Paiva

USP – São Carlos
Janeiro de 2024

RESUMO

NASCIMENTO, F. **Animação Digital de Avalanches de Neve**. 2024. 187 p. Tese (Doutorado em Ciências – Ciências de Computação e Matemática Computacional) – Instituto de Ciências Matemáticas e de Computação, Universidade de São Paulo, São Carlos – SP, 2024.

A animação digital baseada em física de fluidos, como fumaça, água e fogo, fornece alguns dos efeitos visuais mais impressionantes da indústria do entretenimento. Porém, diversos fenômenos ainda precisam ser totalmente compreendidos, e suas formulações ainda são foco de intensa pesquisa em outras áreas, como Física e Engenharia Civil. É o caso das avalanches de neve, cuja modelagem numérica é desafiadora devido à sua dinâmica complexa. A manipulação de tais fenômenos é nova na computação gráfica e existem ainda poucos trabalhos sobre o assunto. Este projeto tem por objetivo trazer estas formulações para o campo da computação gráfica no que diz respeito à animação digital de avalanches de neve.

Palavras-chave: Computação Gráfica, simulação física, animação digital, animação baseada em física, renderização.

ABSTRACT

NASCIMENTO, F. **Digital 3D Animation of Powder-Snow Avalanches**. 2024. 187 p. Tese (Doutorado em Ciências – Ciências de Computação e Matemática Computacional) – Instituto de Ciências Matemáticas e de Computação, Universidade de São Paulo, São Carlos – SP, 2024.

Physically based animation of fluids such as smoke, water, and fire provides some of the most stunning computer graphics in the entertainment industry. However, several phenomena still need to be fully understood, and their formulations are still the focus of intense research in other fields, such as Physics and Civil Engineering. That is the case of snow avalanches, whose numerical modeling is challenging due to their complex dynamics. The manipulation of such phenomena is new to computer graphics, and few works exist. This project aims to bring such formulations to the field of computer graphics regarding the digital animation of powder-snow avalanches.

Keywords: Computer Graphics, physics simulation, Digital Animation, physically based animation, rendering.

LIST OF ABBREVIATIONS AND ACRONYMS

CMT	Continuum Mixture Theory
CMT	Continuum Mixture Theory
DEMs	Digital Elevation Models
DEMs	Digital Elevation Models
DILU	Diagonal-based Incomplete LU
DILU	Diagonal-based Incomplete LU
DSL	Dense-Snow Layer
FAM	Finite Area Method
FCT	Flux Corrected Transport
FCT	Flux-Corrected Transport
FVM	Finite Volume Method
FVMs	Finite Volume Methods
MULES	Multidimensional Universal Limiter for Explicit Solution
PBiCGStab	Preconditioned bi-conjugate gradient
PDEs	Partial-Differential Equations
PISO	Pressure Implicit with Splitting of Operators
PSA	Powder-Snow Avalanche
PSAs	Powder-Snow Avalanches
PSL	Powder-Snow Layer
SH	Savage-Hutter
SIMPLE	Semi-Implicit Method for Pressure-Linked Equations
SPDEs	Surface PDEs
SPH	Smooth Particle Hydrodynamics
TVD	Total Variation Diminishing
VS	Voellmy-Salm

LIST OF SYMBOLS

$\bar{\mathbf{u}}$ — dense snow layer velocity

h — dense snow layer height

ρ — dense snow layer density

ρ_a — air density

ρ_s — powder-snow density

ρ_c — snow cover density

e_b — erosion energy

τ_b — basal friction

μ — dry friction coefficient

\mathbf{g} — gravity acceleration

α_s — powder-snow concentration of volume

α_a — air concentration of volume

D_{AB} — molecular diffusivity

Sc — Schmidt number

ν_t — turbulent eddy viscosity

p_b — basal pressure

p_{rgh} — hydrostatic pressure

ξ — dynamic friction coefficient

CONTENTS

1	ANATOMY OF SNOW AVALANCHES	15
1.1	Gravity Flows	15
1.2	Powder-Snow Avalanches	22
1.3	Remarks	25
2	RESEARCH ON SNOW AVALANCHES	27
2.1	General View	28
2.2	Field Observations and Experimental Data	30
2.3	Dense-Snow Avalanche Models	36
2.3.1	<i>Statistical Models</i>	38
2.3.2	<i>Deterministic Models</i>	39
2.3.3	<i>Sliding Block Models</i>	40
2.3.4	<i>Hydraulic Models</i>	42
2.3.5	<i>Kinetic Models</i>	46
2.3.5.1	<i>Granular Flow Models</i>	49
2.3.6	<i>Slope Treatment</i>	53
2.3.7	<i>Snow Entrainment</i>	54
2.3.8	<i>Other Models</i>	56
2.4	Powder-Snow Avalanche Models	57
2.4.1	<i>Similarity Models</i>	59
2.4.2	<i>Two-Phase Models</i>	63
2.4.3	<i>Single-Phase Mixture Models</i>	66
2.4.4	<i>Entrainment</i>	68
2.5	Numerical Methods	71
2.6	Software Packages	72
2.6.1	<i>Proprietary & Commercial Software</i>	72
2.6.2	<i>Open Source Software</i>	73
2.7	Avalanche-Like Phenomena in Computer Graphics	74
2.8	Remarks	75
3	SIMULATION METHOD	77
3.1	Method Pipeline	77
3.2	Dense-Snow Layer Model	80

3.2.1	<i>Numerical Model</i>	82
3.3	Powder-Snow Layer Model	86
3.3.1	<i>Transition Layer Model</i>	89
3.3.2	<i>Numerical Model</i>	93
3.4	Remarks	99
4	RESULTS	101
4.1	Numerical Setup	101
4.1.1	<i>DSL</i>	102
4.1.2	<i>PSL</i>	103
4.1.3	<i>Transition Layer</i>	107
4.2	Discussions	112
4.3	Rendering	114
4.4	Natural Terrain Examples	118
4.4.1	<i>Wolfsgrube</i>	119
	BIBLIOGRAPHY	121

APPENDIX 155

APPENDIX A	– BACKGROUND CONCEPTS	157
A.1	Eulerian and Lagrangian Descriptions	157
A.2	Continuum Mixture Theory	157
APPENDIX B	– NUMERICAL METHODS	159
B.1	Finite Volume Method	159
B.1.1	<i>The Divergence Theorem</i>	161
B.1.2	<i>Spatial Discretization</i>	163
B.1.3	<i>Time Integration</i>	165
B.1.4	<i>Face Computations</i>	167
B.1.5	<i>Advection Schemes</i>	170
B.1.6	<i>Numerical System</i>	172
B.1.7	<i>Boundary Conditions</i>	173
B.2	Finite Area Method	174
APPENDIX C	– OPENFOAM	177
C.1	Field Representations	178
C.2	Discretizations	179
C.3	Numerical Algorithm	181

ANATOMY OF SNOW AVALANCHES

The general concept of an avalanche consists of a large amount of mass sliding down an incline due to gravity. Once friction and cohesion forces fail to hold the material over the terrain, gravity force becomes prevalent and initiates motion. The surrounding fluid may support sediment transport during motion, increasing velocity, *runout distance*¹, and mass. Many fields of science study such sediment and fluid flows and define classifications for the different avalanches.

This chapter briefly introduces the dynamics of Powder-Snow Avalanches (PSAs), a member of the family of *mixed-type avalanches*, and the different categories of natural mass motion phenomena. The chapter starts by presenting the common classification of snow avalanches, then [section 1.2 on page 22](#) delves into the details of PSAs. The chapter finishes with a remarks [section 1.3 on page 25](#), listing the essential concepts relevant to the rest of the text.

1.1 Gravity Flows

Physical phenomena like snow avalanches belong to the broad family of mass transport phenomena called *gravity flows*. Gravity Flows comprise the various natural phenomena characterized by the sediment transport under the action of gravity. Here, sediment means all the particulate substances, from thin snow powder to huge boulders. Due to its particulate nature, sediment will also be referred to as *granular material* throughout the text.

The *interstitial fluid*² plays a central role in removing friction forces, adding cohesion, causing lubrication, or supporting the motion through turbulence and buoyancy. Shortly, the following properties have a significant effect on the behavior of granular materials:

¹ The runout distance, *avalanche runout*, is the final segment of an avalanche path where the avalanche slows down and stops.

² The interstitial fluid is the fluid that fills the space between sediment grains, such as the mixture of water and dirt in mudflows.

- **Cohesion** creates tangential forces between grains due to humidity or electrostatic forces. For example, the thin liquid films' surface tension between two snow particles is responsible for cohesion in melting snow³. Cohesion is more significant in rest states, as motion may generate larger forces that overcome cohesive forces. In snow avalanches, cohesion delays the initial break-off and keeps large snow chunks from fragmenting.
- **Lubrication** reduces the friction between grains and other bodies due to the presence of another medium called the *lubricant*. In many flows, the motion produces the lubricant. In snow avalanches, the heat generated by the friction between the sliding snow and the terrain maintains a thin layer of liquid water that lubricates the flow. The presence of lubricants may increase runout distances even in low slopes.
- **Fluidization** reduces the internal friction related to grain-to-grain collisions by balancing out the gravity force with the buoyancy force generated by the interstitial fluid. The consequence is the fluid-like behavior of the granular material. In snow avalanches, fluidization generally occurs in steep slopes as the air trapped between snow grains temporarily displaces the snow. Compared to lubrication, which happens on the boundaries of the flow, fluidization happens internally. Similarly, *liquefaction* happens when the downward motion of the granular material displaces the fluid upwards (LOWE, 1976).

In many flows, the interstitial fluid is the same as the ambient fluid, which is the case for the powder cloud in PSAs. Many authors define *Sediment Gravity Flows* when the sediment's gravity-driven motion causes the fluid's motion, and *Fluid Gravity Flows* the inverse – see [Figure 1](#) on next page. [Middleton and Hampton \(1973\)](#) classifies different sediment gravity flows into four categories based on the *sediment support mechanism*:

- **Debris Flows**, also referred to as mudflows, characterize flows with high cohesive strength. The cohesion originates from the nature of the constituent materials, generally water, dirt, and rocks⁴. A mixture of water and fine sediments supports sediment, allowing the motion of large blocks of mass — see [Figure 2a](#).
- **Grain Flows** are cohesionless flows supported by direct grain-to-grain interactions. Due to grain geometries, shearing deformations lead to volume expansion⁵. The interstitial fluid is the same as the ambient fluid, which can also be water. Examples of grain flows are sand avalanches — see [Figure 2b](#).
- **Fluidized Flows** occur under fluidization processes. In the presence of interstitial fluid, the grains disperse, and fluid motion takes into play. The injection of air in the bottom

³ Conversely, the lack of liquid water in colder temperatures makes snow less cohesive.

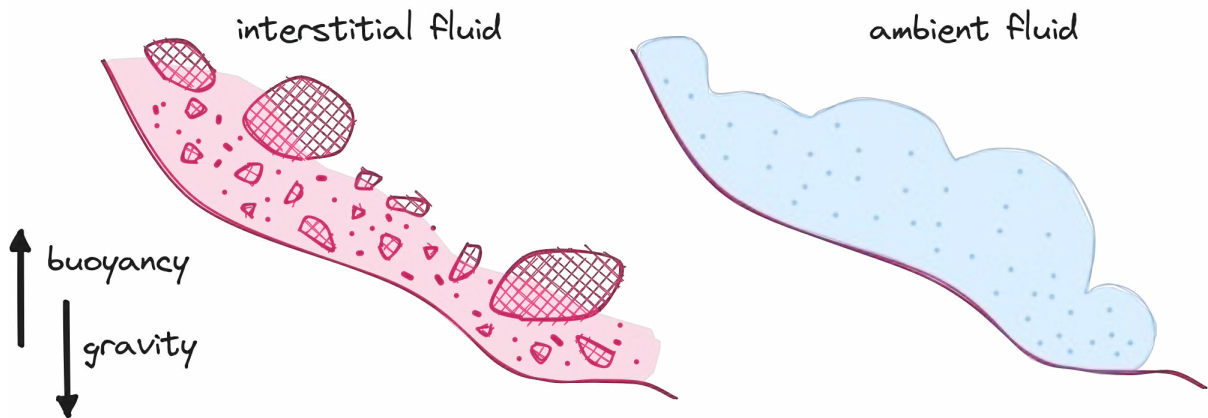
⁴ Debris flows have enough strength to carry much more than dirt and rocks. Due to its enormous mass and fluid behavior, the flow can take debris of large sizes, such as trees and boulders.

⁵ Granular materials are also called *dilatant materials*.

of a sand tank is an example of such a phenomenon. [Lowe \(1979\)](#) considers a separate category called *Liquified Flow*, where support comes from the pore-fluid pressure.

- **Turbidity Currents** are particle-driven flows that generally occur on the ocean floor and are responsible for sediment transport to the deep sea. The density difference between the ambient fluid (water) and the sediment mixture drives the motion. The suspension caused by the turbulence of the fluid supports the motion, which may take even days and cover vast distances of more than 1000 km ([TALLING *et al.*, 2022](#)).

Figure 1 – Sediment Gravity Flows are motions of mass motivated by gravity. As sediment moves, the ambient fluid gets into motion as well. In the presence of an interstitial fluid, effects such as lubrication, cohesion, and buoyancy may come into play, supporting the motion (left). If sediment grains, such as sand underwater or snow powder in the air, disperse enough, the turbulence of the ambient fluid may also support the motion.



Source: Elaborated by the author.

Figure 2 – Sediment flows cover various grain flow properties, such as cohesion. For example, debris flows are highly cohesive, while sand flows are cohesionless. (a) The 1/9 *Debris Flow* event on January 9, 2018, triggered in Santa Barbara County, United States. (b) Tongue-shaped grain-flow lobes on the surface of sand dunes.

(a)



Source: [Hill \(2019\)](#).

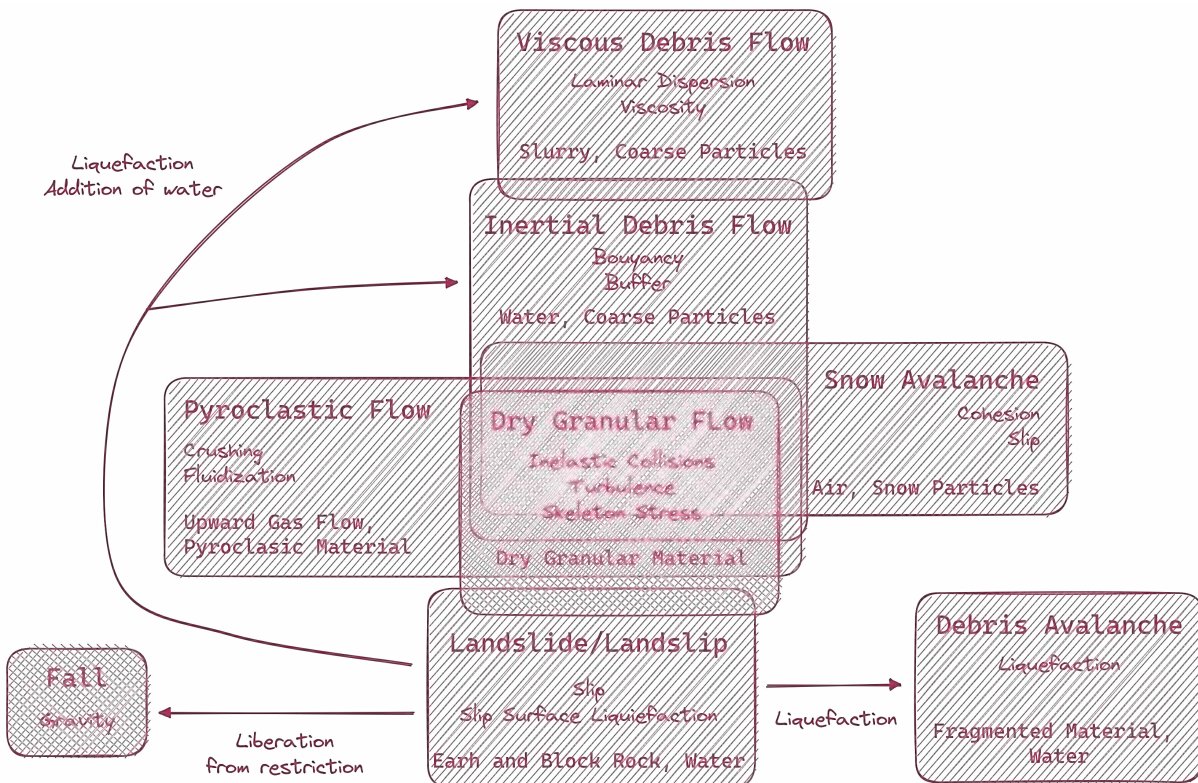
(b)



Source: [Barale \(2015\)](#).

Over the years, the classification above proved insufficient due to the diversity and complexity of gravity flows. Dasgupta (2003) suggests that the flows listed above are too different to be defined under the same category of sediment gravity flows. Moreover, the properties of lubrication, fluidization, and cohesion are not necessarily mutually exclusive, and neither the flow types are. A powder-snow avalanche, for example, contains a mixture of flow types and properties. Therefore, the gravity flows were further classified based on material type, sediment concentrations, velocity, grain size distributions, flow front speeds, shear strength, shear rate, and other criteria (VARNES, 1978; PIERSON; COSTA, 1987).

Figure 3 – Characteristics of different sediment transport/motion types.



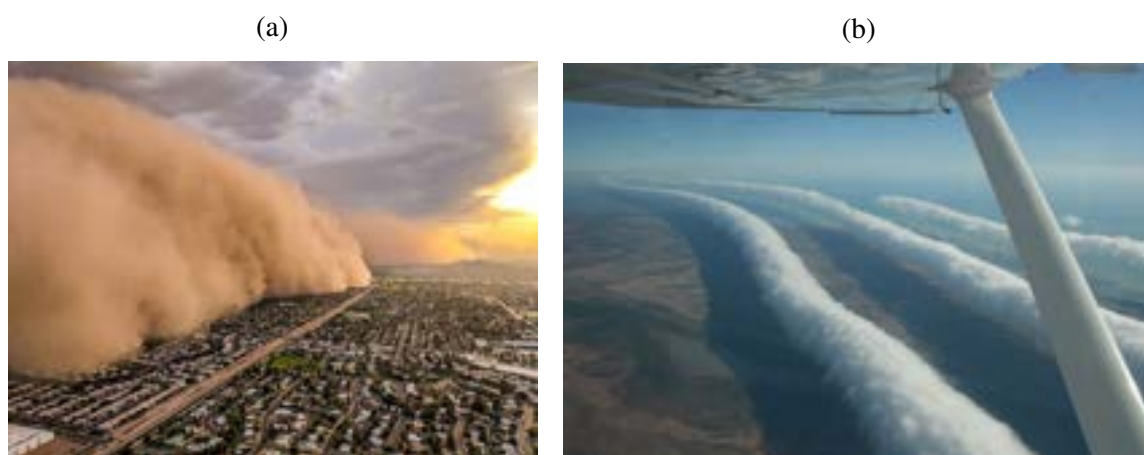
Source: Adapted from Takahashi (2014).

One important example is the classification proposed by Takahashi (2014), represented in Figure 3, focuses on particle concentration and the support mechanism. For example, particles are dispersed in the flowing body for the five upper blocks categories, while the lower three blocks present moving bodies composed mainly of agglomerates of soil and rocks. As the interaction of solid and fluid forces distinguishes debris flows physically, arrows connecting lower blocks and upper blocks on the diagram represent the water concentration. Each block lists the effects particular to each flow type that go beyond the commonly operating stresses and the participating materials.

In parallel, a *Gravity Current* is a term geologists use to characterize flows motivated by density differences between two fluids. Gravity currents, sometimes called *buoyancy currents*, are primarily horizontal flows where a fluid propagates through the ambient fluid with lesser or

greater density, such as sand storms and bores — see [Figure 4](#). Many authors generalize gravity currents to encompass phenomena such as pyroclastic and lava streams initiated by volcanic eruptions, suspension flows, turbidity currents, and other gravity-controlled flows, including debris flows. In this context, an airborne powder-snow avalanche is considered a large-scale turbidity current.

Figure 4 – Examples of gravity currents. (a) A massive *haboob* (sand storm) hits the city of Phoenix in the United States. (b) Bores in the atmosphere making the phenomenon called the 'Morning Glory' over Australia.



Source: [Stewart \(2018\)](#).

Source: [Petroff \(2009\)](#).

In the realm of avalanches, characterized by motions of mass in mountain inclines ranging from landslides to rockfall, [Pudasaini and Hutter \(2007\)](#) distinguishes three large groups:

- **Flow Avalanches** are *dense gravity-driven flows* where the role of solid particles dominates, and the interstitial fluid is minor or negligible. Its particles vary with sizes ranging from sizes of clay to boulders. Such flows are present in certain types of snow avalanches, and many debris flows, having similarities with *dense granular flows*. For example, in certain dense pyroclastic flows, the solid volume fraction can be of the order of 70%.
- **Powder Avalanches** consist of light powdery grains with low or no cohesion. These avalanches are much less dense than flow avalanches and can be called *turbulent-type flows* of airborne particles. Powder avalanches are characterized by their large volume and the rapid wind that accompanies the flow. For instance, the powder avalanche formed in a PSA can move at high velocities as impressive $100 \text{ m} \cdot \text{s}^{-1}$ and form clouds of 100 m in height ([SIMPSON, 1999](#)).
- **Mixed-type Avalanches** are flow avalanches overlaid by a powder avalanche. This category of avalanches presents multiple layers in which a distinct physical behavior characterizes the layer's dominant dynamical processes. Generally, the process starts with a flow avalanche that produces enough motion and powder mass to generate a powder avalanche. The dense layer feeds the powder layer as the chunks of material break into smaller pieces

and eventually into particles. The turbulent motion of the ambient fluid ejects the particles and forms the upper layer powder avalanche. Examples of mixed-type avalanches appear in turbidity currents, pyroclastic volcanic eruptions, dust clouds in the desert, and **powder-snow avalanches**.

Due to their diverse natures, flow avalanches differ significantly from powder avalanches⁶. For example, flow avalanches have significant basal friction and are bound to the terrain following small-scale features, while powder avalanches follow just the large-scale topography. [Table 1](#) lists the fundamental differences encountered in both flows. In particular, notice the contrast in the scales for density and velocity values.

Table 1 – Table extracted from [Pudasaini and Hutter \(2007\)](#), showing the differences between the two type of avalanches. The values in the table are typical values measured in such flows.

	Flow Avalanches	Powder Avalanches
Flow type	Laminar	Turbulent
Velocities $[m \cdot s^{-1}]$	$\sim 5 - 30$	$\sim 40 - 100$
Density $[kg \cdot m^{-3}]$	$\sim 100 - 400$	~ 5
Flow height $[m]$	$\sim 1 - 10$	~ 100

Environmental factors, such as temperature and humidity, affect the physical state of snow, creating different behaviors of snow avalanches. Therefore, snow avalanches receive further classifications that distinguish their diverse characteristics. The WSL Institute for Snow and Avalanche Research SLF ([SLF, 2022](#)) lists the following categories for snow avalanche types:

- The snow cover on the surface of a mountain is the accumulation of several snowfalls that occur over time. Throughout the days, the precipitations might bring snow in different conditions, such as particle sizes, temperature, and humidity. The stacking of different snowfalls makes the snow cover a stratified layer consisting of sub-layers of variable strength. The weight of the upper layers and the slope of the terrain impose mechanical forces that can lead to the failure of weak layers. When a weak layer of significant area lies underneath meters of snow collapses, a fracture quickly propagates throughout the snow cover. The fracture causes the sudden detachment of the whole body of snow that enters motion. The heavy snow slides freely on top of the weak layer underneath, producing the so-called **Slab Avalanches**⁷ – see [Figure 5a](#) and [Figure 5b](#).
- **Loose Snow Avalanches**, also called *sluffs* or *point releases*, generally occur during quick temperature increases. The release of loose snow starts from a single point, and the

⁶ Some authors refer to PSAs as powder avalanches, which can be confusing when dealing with different classifications. Here, PSAs are mixed-type avalanches.

⁷ Slab avalanches are responsible for 90% of the deaths that occur in snow avalanches because of the fast acceleration and large area they have. Skiers and mountaineers usually find themselves suddenly inside the avalanche perimeter at the time of release.

avalanche entrains snow as it fans downhill. Loose snow avalanches can reach large sizes due to wet snow entrainment – see [Figure 5c](#) and [Figure 5d](#).

- In **Gliding Avalanches**, the entire snowpack is released, but they occur only in smooth substrata, such as flattened grass. As water penetrates the deeper layer, the friction with the ground decreases, and the avalanche is triggered.
- **Wet Snow Avalanches** generally happen in the event of rain. The main characteristic of wet snow avalanches is the presence of liquid water that wakens the snowpack.
- **Powder-Snow Avalanches** generally originate from slab avalanches. Their definition is the same as mixed-type avalanches mentioned earlier and are detailed in the next section.

Figure 5 – Slab avalanches originate from the failure of the weak layer in the snow cover. (a) The fracture line, also called the *crown line*, becomes evident after the release of a slab avalanche. (b) For persistent snow covers, the height of the slab can reach many meters. (c) Dry-loose snow avalanches start from a single point and entrain only the soft snow near the surface of the snow cover. (d) However, wet-loose snow avalanches entrain heavier snow, becoming more destructive.

(a)



Source: [Vidic \(2022\)](#).

(b)



Source: [McGill \(2023\)](#).

(c)



Source: [Avalanche.org \(2023\)](#).

(d)



Source: [Avalanche.org \(2023\)](#).

1.2 Powder-Snow Avalanches

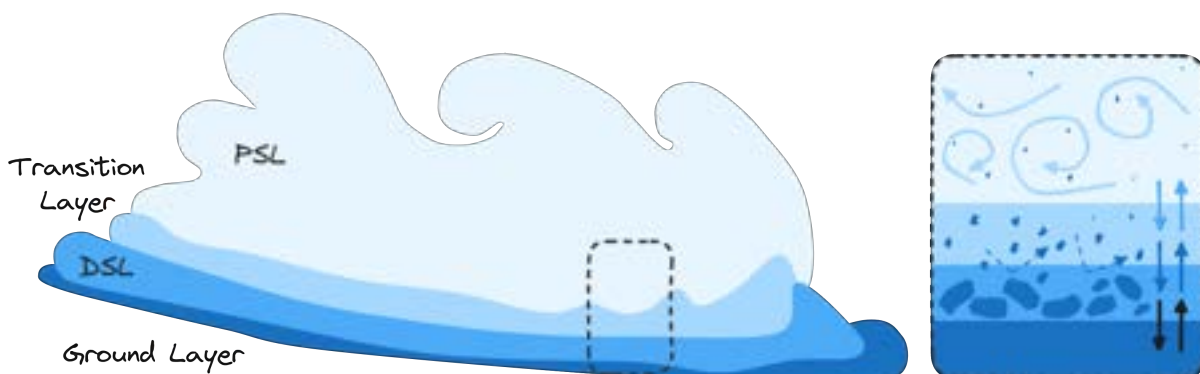
In literature, the Powder-Snow Avalanche (PSA) usually consists of two principal layers: the Dense-Snow Layer (DSL) and the Powder-Snow Layer (PSL), representing the flow avalanche and the powder avalanche, respectively. In addition, two extra layers are used to explain the changes in mass observed in the DSL and PSL. The first layer, referred to here as the *ground layer*, consists of the static snow cover encountered in the terrain. The second layer, referred to as the *transition layer* (also called the *saltation layer*), appears above the DSL and below the PSL and is responsible for the exchange of mass and momentum between the two layers. Table 2 lists the four mentioned layers and their main characteristics.

Table 2 – Layers of a powder-snow avalanche.

Layer	Description	Flow Type
PSL	Suspension layer (fully turbulent)	Turbulent particle laden flow
Transition	Two-phase viscous wall layer	Turbulent two-phase flow
DSL	Flow avalanche layer	Laminar flow
Ground	Stagnant snow layer	Snow at rest

During a PSA, the DSL may gain mass from the ground layer by snow entrainment and lose mass from snow deposition processes. However, there are also exchanges between the DSL and the PSL. As collisions fracture large chunks of snow, the surface of the DSL becomes fluidized. The increasing wind causes particles to leave the dense layer surface in ballistic motion, creating a transition region. Some particles make their way up to the PSL, called the *suspension layer*, where collisions are less frequent and get into strong aerodynamic turbulence. Figure 6 depicts the anatomy of the avalanche described above.

Figure 6 – Powder-snow avalanches can be dissected into four main layers of different flow types. The DSL is composed of big snow packs that break into smaller pieces as the flow develops. Particles at the fluidized surface of the dense flow layer are stirred up, forming a transition layer. Small particles may be suspended by turbulent air and form the PSL, which is self-accelerated by gravity and turbulence. The DSL exchanges mass with the static snow cover that forms the ground layer by entrainment and deposition processes.



Source: Elaborated by the author.

The sequential events of a PSA happen along three distinct phases that roughly split the avalanche path into three parts: the *start zone*, the *track*, and the *runout zone*. The **start zone** is where the primary block of snow detaches from the mountain surface and starts to slide down the incline (see the slab avalanche description in the previous section on [page 20](#)). The **track** is the following section of the path where the flow develops as the avalanche accelerates and increases in size by entraining snow from the ground. The amount of entrained snow will influence how fast and long the flow will advance. In the final portion, the **runout**, the avalanche starts to slow down until it stops and the snow is deposited. Avalanches will stop depending on many factors, such as terrain topography and the decrease in entrainment.

The entrainment of snow plays a central role in the evolution of an avalanche flow, particularly in a PSA. The entrainment processes⁸ feed the cloud and dictate the size of the powder cloud. [Issler \(2014\)](#) describes four mechanisms of entrainment in snow avalanches:

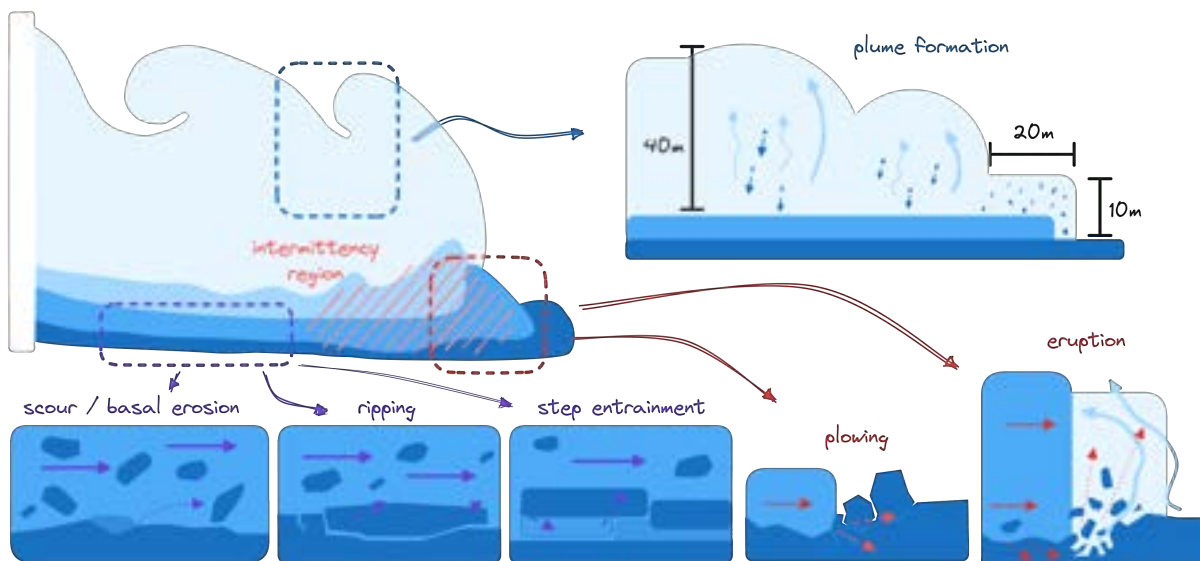
- **Plowing**, or *ploughing*, in the front of the flow occurs as the dense core incurs into the snow cover. The frontal impact pushes the snow cover forward. The amount of entrained snow (displaced snow cover) depends on the depth of the snow cover, its strength, and the speed of the avalanche.
- Depending on the strength of the snow cover, particularly in the presence of dry snow that has low cohesion, the compression force of the arriving avalanche, right in the front of the flow, creates a high pore pressure that forces the interstitial air out. The drag caused by the airflow pushes the snow upwards as an **eruption**, creating the characteristic frontline of PSAs. The process happens quickly, $0.1 \sim 2 \text{ s}$, with significant entrainment rates up to $350 \text{ kg} \cdot \text{m}^{-2} \cdot \text{s}^{-1}$ ([SOVILLA; BURLANDO; BARTELT, 2006](#))⁹.
- Between the bed and the dense core, there is a continuous **scour** of the ground layer due to the friction of the passing flow. As erodible snow loses cohesion and strength, the chunks of snow break into smaller pieces. The loose portions get trapped by the avalanche flow. [Sovilla, Burlando and Bartelt \(2006\)](#) relates this process to *basal erosion*, which happens away from the front and at low entrainment rates of $10 \text{ kg} \cdot \text{m}^{-2} \cdot \text{s}^{-1}$.
- The **ripping** of bed slabs occurs when the friction exceeds the shear strength of the snow cover. The sudden failure of the snow cover projects an entire slab portion into the avalanche core. [Sovilla, Burlando and Bartelt \(2006\)](#) describes a similar process called *step entrainment*, characterized by the failure of a resistant top layer of the snow cover. When the *crust* breaks, the flow suddenly entrains the weak layer underneath, producing entrainment rates as large as in eruption.

⁸ The physical processes in entrainment processes still pose many open questions to scientists. Many challenges in field measurements limit the comprehension of entrainment mechanisms. The entrained mass results directly from the *erosion* process of the snow cover. The next chapter discusses some of these challenges.

⁹ Sovilla and other authors also use *plowing* to encompass the *eruption* mechanism.

The plowing and eruption mechanisms described above are responsible for the plume formation in PSAs. The blow-out that occurs in the *leading edge* of the avalanche creates the conditions for plume formation. Bartelt *et al.* (2013) observed that after an initial plume quickly achieves 10 m of height, the growth pauses and resumes as the plume is no longer at the front (20 ~ 50 m behind). The air intake at the leading edge, which is velocity-dependent, expands the volume of the cloud. As the ejected heavy particles fall, the entrained air is displaced upwards, suspending the ice dust up to 100 m. This process creates vertical movement of the plumes, but not horizontal. This vertical movement of the plumes agrees that the plumes travel many times slower than the leading edge¹⁰. Figure 7 shows the several entrainment processes mentioned earlier.

Figure 7 – The various entrainment processes present in a PSA. Away from the front, the continuous friction forces in the ground surface cause *scour*, *basal erosion*, *ripping*, and *step entrainment*. In the leading edge, snow can be *plowed* frontwards but can also be violently ejected into the air by *eruption*. Plumes are born from the eruption and grow as heavy particles settle down and displace air upwards. The *intermittency region* includes surges of rapid flows and produces the oscillatory behavior of the PSA front.



Source: Elaborated by the author.

For decades, observations indicated an oscillatory behavior occurring in the front of a PSA. The plume formation mentioned above is the direct consequence of this dynamics¹¹. Such oscillations manifest as short-time streaks in radar data signatures, representing surges of velocities faster than the avalanche front. These flow structures happen in the *intermittency region* depicted in Figure 7 and quickly decelerate once they arrive at the leading edge of the avalanche. The dynamics of this *intermittent flow regime* are still poorly known (SOVILLA; MCELWAIN; KHLER, 2018).

¹⁰ Bartelt *et al.* (2013) also observed plumes traveling at $4 \text{ m} \cdot \text{s}^{-1}$ while leading edges were traveling up to $50 \text{ m} \cdot \text{s}^{-1}$.

¹¹ Bartelt *et al.* (2013) observed plumes being created at approximately 0.4 Hz (plumes per second).

1.3 Remarks

- PSAs are primarily born from slab avalanches. In a fully developed PSA, many flow regimes come into play, which makes the mathematical modeling of PSAs particularly challenging. The typical approach is to divide the PSA into two layers, the DSL and the PSL, that communicate with each other through an intermediate layer, the *transition layer*.
- The DSL flow presents high densities of up to $400 \text{ kg} \cdot \text{m}^{-3}$ and depths of up to 10 m . The entrainment happens by *scour* and *basal erosion* at slow rates of $10 \text{ kg} \cdot \text{m}^{-2} \cdot \text{s}^{-1}$ but may entrain more significant amounts quickly by *ripping* and *step entrainment*.
- The PSL flow presents low densities of around $5 \text{ kg} \cdot \text{m}^{-3}$ but can reach heights of up to 100 m . Entrainment occurs primarily by the *eruption* process at the leading edge of the avalanche at incredible rates of up to $350 \text{ kg} \cdot \text{m}^{-2} \cdot \text{s}^{-1}$.
- From the many entrainment processes, the eruption is the primary source of mass for the PSL. Therefore, the dynamics at the front of a PSA need special attention when modeling PSAs.
- Plumes do not travel downhill at the same speed as the front of the avalanche. The velocity of the plumes can be as low as $4 \text{ m} \cdot \text{s}^{-1}$, with the leading edge traveling at $50 \text{ m} \cdot \text{s}^{-1}$.
- The front of a PSA presents an oscillatory behavior caused by the *intermittent region* just behind. This oscillation directly influences the formation of the plumes, which pulse from the front (e.g., 0.4 plumes per second).

RESEARCH ON SNOW AVALANCHES

Modeling and simulating avalanche phenomena have been the goal of many researchers for decades. Research has focused mainly on avalanche prediction, hazard control, mitigation measures, and dynamics. This chapter explores the chronological advances in snow avalanche science, focusing on avalanche dynamics.

The chapter starts with an overview of the history of snow avalanche research throughout the last century in [section 2.1](#). A complete taxonomy covering the entire period would be too extensive and beyond the purpose of this text. Consequently, the section follows the history of the leading families of models and their ramifications.

Although practical research — read observation and experimentation — goes beyond the focus of this text, measurement data plays a crucial role in numerical model validation. Field observations and laboratory experiments form the basis for physical and mathematical models. Therefore [section 2.2](#) on [page 30](#) briefly covers the history of field and laboratory research on the different types of snow avalanches.

The following sections delve into the history of physical and mathematical models of the two main types of snow avalanches, dense-snow and powder-snow avalanches, roughly covering the last 150 years of avalanche research. [section 2.3](#) on [page 36](#) explores the history of dense-snow avalanche models, and [section 2.4](#) on [page 57](#) treats the mixed-type models that simulate the different avalanche flow layers simultaneously, characteristic of powder-snow avalanches.

Lastly, [section 2.6](#) on [page 72](#) lists commercial and open-source software packages for snow avalanche simulation. [section 2.7](#) on [page 74](#) presents avalanche-related methods employed in Computer Graphics, which is the final goal of this project. The chapters close with relevant remarks to the subsequent chapters in [section 2.8](#) on [page 75](#).

2.1 General View

Since civilization spread into mountainous regions, avalanches soon became a permanent threat to human life. In the mid-20th century, mountain communities experienced considerable growth, raising the interest and urgency in avalanche research since then.

Although the first physical models appeared in the 1950s, much of their inspiration and assumptions came decades earlier. [Figure 8](#) draws a general timeline of the scientific study of snow avalanches over the last century. The timeline depicts crucial branches of research and ideas that led to the most recent methods described in the following sections.

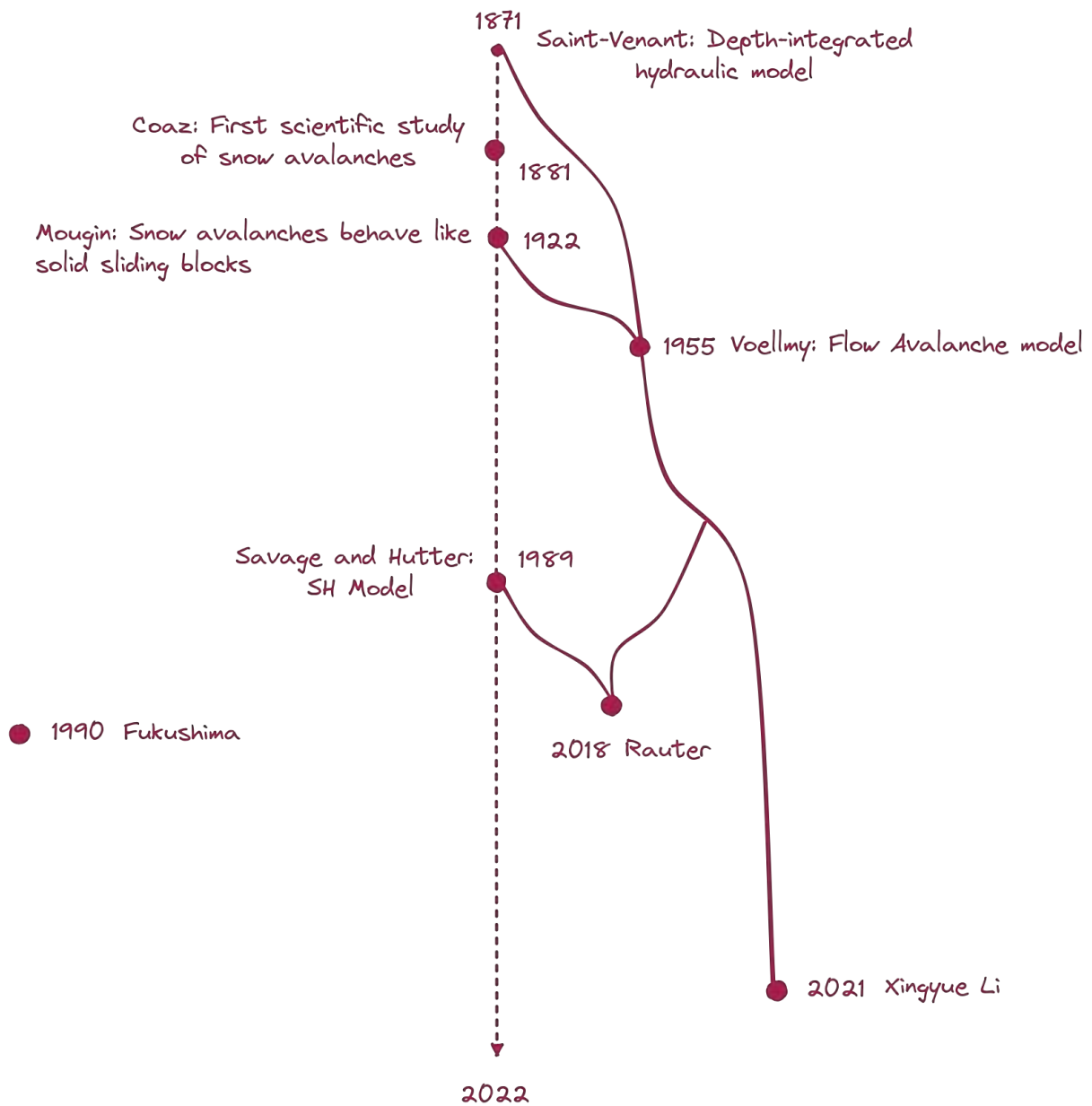
The first scientific study of snow avalanches dates back to 1881, pioneered by the Swiss scientist (forester) Johann Coaz ([COAZ, 1881](#)). However, only a half-century later, [Seligman, Seligman and Douglas \(1936\)](#) called attention to the complex nature of the phenomenon, attempting to list the multitude of physical and environmental factors that produce an avalanche. Earlier in the 20th century, [Mougin \(1922\)](#) calculated avalanche velocity and run-out distance by treating avalanches as sliding blocks, a solution that originated many avalanche models in use today.

Inspired by Mougin, [Voellmy \(1955\)](#) made the first significant attempt to formulate the dynamics of dense-snow avalanches by bringing basal friction relations to the depth-integrated hydraulic model, introduced by Barré de Saint-Venant ([VENANT, 1871](#)). Since then, Voellmy's basal friction model has been used as the starting point for most subsequent models ([LACHAPELLE, 1977](#); [ANCEY, 2016](#)). In particular, the Voellmy-Salm (VS) model, created in the 1960s, spanned decades of influence and received many extensions and applications — being officially used by governments on avalanche hazard calculation programs ([SALM, 2004](#)). In parallel, the Russian model, referred to as the MSU model ([GRIGORIAN; OSTROUMOV, 2020](#)), also occupied an important position of influence for decades, dictating not only Eastern models but also having a significant impact on Western research.

The dense-snow avalanche research achieved its pivot point when granular flow models surged in the 1980s with the Savage-Hutter (SH) model ([SAVAGE; HUTTER, 1989](#)). The SH model brought features from VS and MSU models along with a continuum mechanics perspective, allowing the simulation of a wide range of physical processes such as entrainment, avalanche body deformation, and complex terrain flows. The SH model received great approval and is one of today's leading models for dense-snow avalanche simulations ([RAUTER *et al.*, 2018](#)). In recent years, the advance in computing resources allowed new numerical methods to offer particle-based models the capacity to handle internal flow processes and large-scale deformations on real-world terrains ([GAUME *et al.*, 2018](#); [LI *et al.*, 2021](#)).

Models for the powder-snow cloud may follow different origins and approaches, such as the gravity currents and plume theory ([ELLISON; TURNER, 1959](#); [BARTELT *et al.*, 2013](#)) — see [Figure 8](#). Attempts to model the family of gravity current phenomena are contemporary to

Figure 8 – Snow avalanche research timeline. Mathematical studies on snow avalanche dynamics started approximately 150 years ago and spawned many physical models. In 1922, Mougin treated the avalanche as a single-sliding block. Over the years, the sliding block model integrated laws from 1871's Saint-Venant hydraulic equations and friction, thanks to Voellmy in 1955. Voellmy's sliding-block / hydraulic model received many extensions, and its friction models are still used today. In the 1980s, the continuum mechanics approach surged in avalanche modeling, and the analogy with granular flows produced one of the most prominent dense-snow avalanche models, the SH model. Since then, the models can handle avalanches with deformable body and flowing in complex terrains. Recently, particle-based models gained space due to computational power. Powder-snow avalanche research took a different path toward multi-phase models, concentrating on the mixture of air and ice caused by turbulence.



Source: Elaborated by the author.

dense avalanche studies (KARMAN, 1940; BENJAMIN, 1968). Like dense avalanche models, scientists also favored the depth-averaged models (from shallow-water theory) of powder-snow

avalanches over the years. [Plapp and Mitchell \(1960\)](#) firstly modeled turbidity currents (siblings of powder–snow avalanches) with depth-averaged equations. Decades later, [Parker, Fukushima and Pantin \(1986\)](#) included equation terms for mass entrainment and turbulence. The improved model was then used to simulate powder-snow avalanches by [Fukushima and Parker \(1990\)](#). Recently, [Ivanova et al. \(2021\)](#) developed a shear shallow water model with turbulence applied to powder-snow avalanche simulations.

Before delving into a detailed research timeline, it is worth listing some reviews ([MELLOR, 1968](#); [MELLOR, 1978](#); [HOPFINGER, 1983](#); [HARBITZ, 1998](#); [HARBITZ; ISSLER; KEYLOCK, 1998](#); [ECKART MCELWAINE JIM, 2012](#); [ANCEY, 2016](#)) and books ([BOZHINSKIY; LOSEV; BARTELT, 1998](#); [PUDASAINI; HUTTER, 2007](#); [LOUCHET, 2021](#)) published over the years in the general topic of snow avalanches. Likewise, a review of Russian¹ research history on snow avalanches is covered in ([EGLIT; YAKUBENKO; ZAYKO, 2020](#)).

2.2 Field Observations and Experimental Data

Field observations and laboratory experiments are the primary sources of evidence for understanding avalanche dynamics and allow researchers to design numerical models. Measurements on real large-scale PSAs² offer essential data for validating numerical models. Furthermore, [Nishimura, Barpi and Issler \(2021\)](#) calls attention to what they call the *underrated potential of field observations* by commenting “[...] the study of snow avalanches have been made in well over a dozen countries for nearly a century, with pioneering works dating back as far as 150 years [...] despite substantial progress — many fundamental questions of primary practical significance still lack a well–founded and comprehensive answer”.

The knowledge about the various physical processes of snow avalanches extracted from field data over the decades is carefully discussed by [Issler et al. \(2020\)](#). Reports on field observations, such as [Issler \(2020\)](#) and [Furdada et al. \(2020\)](#), provide consistent conclusions about the destructive force of snow avalanches and offer valuable estimates for mass, speed, and run-out distances. For instance, data from several real avalanches helped [Sovilla, Burlando and Bartelt \(2006\)](#) to model the complex impact of entrainment processes on run-out distances, and [Gauer \(2014\)](#) to validate models dealing with front velocity.

Test sites play an essential role in the empirical study of snow avalanches. A test site is a mountain area containing avalanche paths where scientists install measurement instruments; as the famous Lautaret Pass test site in the French alps, actively in use since 1972 ([THIBERT et al., 2015](#)). Over the past decades, scientists have used various equipment and methods to collect data from snow avalanches on test sites ([ECKART MCELWAINE JIM, 2012](#)). [Bardolini et al.](#)

¹ For many decades, the work of researchers from the Soviet Union and Russia was not accessible to the Occident due to translation issues and other reasons.

² A large data base of more than 4000 avalanche data is provided online in the website <<http://www.data-avalanche.org/>> ([Trésorier, Marc, 2021](#)).

(2005) offers an extensive discussion and analysis of measurement techniques applied in several test sites over Europe. Measurement techniques include photogrammetry (DREIER *et al.*, 2016), radars (VRIEND *et al.*, 2013), and pylons equipped with instrumental devices containing several types of sensors (SOVILLA; SCHAEER; RAMMER, 2008); see Figure 9. Chart 1 lists typical measurement techniques of relevant physical properties to snow avalanche models used in field observations.

Chart 1 – A list of physical quantities required by snow avalanche models and their respective measurement techniques / instrumental apparatus.

Property	Measurement	Source
Density	capacitance sensors	(DENT <i>et al.</i> , 1998)
Volume	videogrammetry and photogrammetry	(DREIER <i>et al.</i> , 2016)
Velocity	array radar systems	(VRIEND <i>et al.</i> , 2013)
Internal velocities	optical sensors	(DENT <i>et al.</i> , 1998)
Shear and normal stresses	shear plates	(DENT <i>et al.</i> , 1998)
Mass entrainment and deposition	radars	(SOVILLA, 2004)

Vallet *et al.* (2004) used videogrammetry to measure a large powder–snow avalanche triggered at the Swiss Vallée de la Sionne test site. The avalanche velocity achieved an impressive speed of $55 \text{ m} \cdot \text{s}^{-1}$, with a cloud volume of more than $6 \times 10^6 \text{ m}^3$ and 20 m of cloud height; see Table 3. Such volume measurements supported earlier plume theories (ELLISON; TURNER, 1959) — described in section 2.4. Additionally, Turnbull and McElwaine (2007) provided data supporting plume theories, showing that the front velocity is independent of slope angle due to air entrainment. Bartelt *et al.* (2013) showed that plumes decelerate quickly, obtaining measurements of $4 \sim 16 \text{ m} \cdot \text{s}^{-1}$ — with almost stationary plumes at the tail — against front velocities of $50 \text{ m} \cdot \text{s}^{-1}$. Plumes are created at a frequency of approximately 0.4 Hz, quickly reaching 10 m of height and slowly growing up to 40 m, due to buoyancy flux, 20 ~ 50 m behind the front; see Figure 10 on page 33.

Table 3 – A list of real scale snow avalanche measurements.

Front Speed [$\text{m} \cdot \text{s}^{-1}$]	Height [m]	Source
55	20	(VALLET <i>et al.</i> , 2004)
50	40	(BARTELT <i>et al.</i> , 2013)

Data collected at the Vallée de la Sionne and Monte Pizzac test sites showed avalanches growing 12 times due to snow entrainment and show that avalanches with the same speed run different distances due to entrainment mechanisms (SOVILLA; BURLANDO; BARTELT, 2006). Estimates of entrainment and deposition depth can be found in Sovilla *et al.* (2010). Sovilla (2004) extensively discusses various field measurement techniques to model mass entrainment and deposition processes with the following observations:

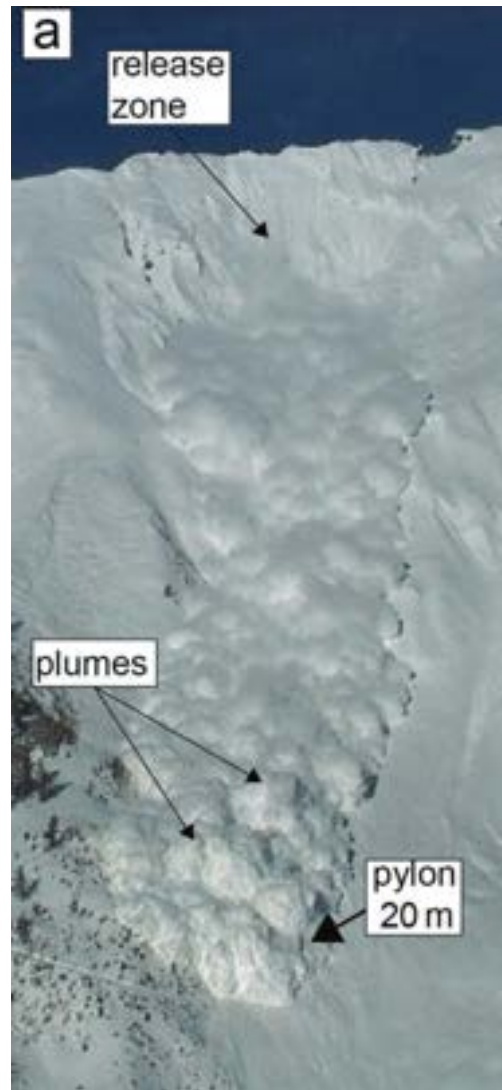
Figure 9 – Instrumental pylons are placed in test site avalanche paths to collect data from avalanche flow.

(b) A similar pylon being hit by a large-scale avalanche in the Vallée de la Sionne test site.

(a) A 20 m pylon equipped with sensors able to measure flow depth, impact pressure, cloud density and many other quantities.



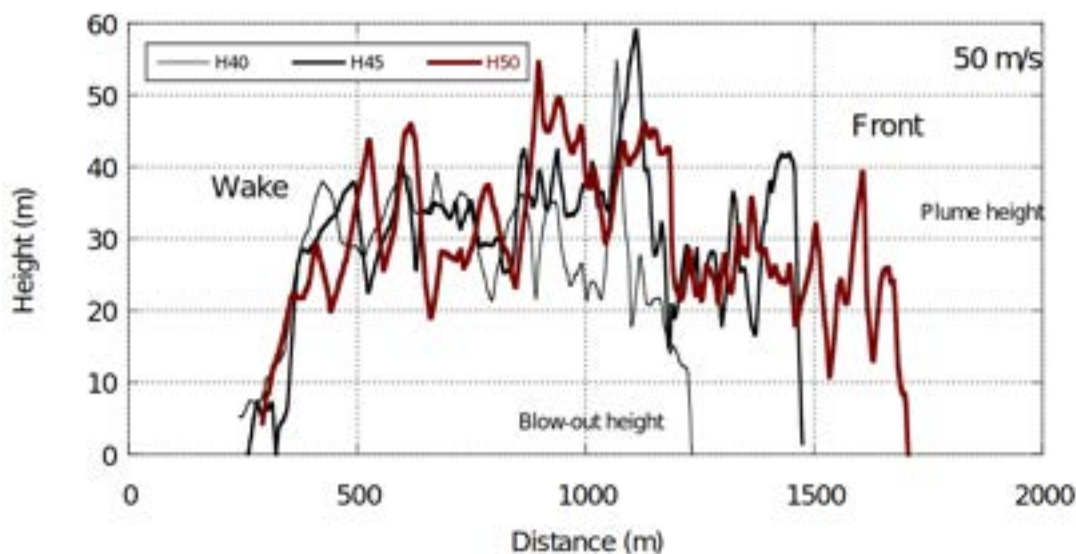
Source: [Sovilla, Schaer and Rammer \(2008\)](#).



Source: [Bartelt et al. \(2016\)](#).

- On average, avalanches grow their mass by a factor of 4.6;
- The topography of the terrain has little influence on entrainment. Entrainment is also independent of avalanche size;
- On average, avalanches entrain 67% of the release snow depth (fresh snow on the ground at the moment of the release);
- The characteristics of snow directly influence entrainment. For example, high cohesion due to wet snow limits entrainment, while low cohesion leads to higher entrainment.
- High bed friction increases snow deposition and difficult entrainment due to deceleration;

Figure 10 – Cross-section of plume heights and positions of an avalanche after 40 s, 45 s, and 50 s. The avalanche moves at $50 \text{ m} \cdot \text{s}^{-1}$ and plumes rise 40 m above the mountain surface.



Source: Bartelt *et al.* (2013).

- During ploughing (frontal entrainment), the entrainment rate of low-density and cohesionless snow is up to $350 \text{ kg} \cdot \text{m}^{-2} \cdot \text{s}^{-1}$ and snow cover shear strength $< 1 \text{ kPa}$;
- During basal erosion (internal entrainment), ice crust and high-strength snow are entrained at a rate of $10 \text{ kg} \cdot \text{m}^{-2} \cdot \text{s}^{-1}$, and snow cover shear strength $> 25 \text{ kPa}$.

Sovilla, McElwaine and Louge (2015) presented an anatomy model of the powder–snow avalanche based on field and experimental data by discussing the various profiles of density and speed throughout the avalanche body. Later, Sovilla, McElwaine and Khler (2018) refined their earlier anatomy model by considering an *intermittency frontal region* — a highly active $\approx 10 \text{ m}$ near front region presenting high densities of $20 \text{ kg} \cdot \text{m}^{-3}$ and velocities 60% larger than front speed. Based on radar data analysis, Köhler, McElwaine and Sovilla (2018) could distinguish seven simultaneous flow regimes in a powder–snow avalanche. The authors concluded that numerical models should handle at least 5 of those regimes. Refer to Gauer *et al.* (2008) for a previous discussion on flow regimes within powder–snow avalanches.

Despite the invaluable data collected from field observations on test sites, real-scale avalanche experiments are expensive, dangerous, unpredictable, and dependent on weather conditions. Hence laboratory experiments play a critical role in avalanche research. Controlled flow and reduced-scale experiments consist of similar flow mechanisms to real-scale avalanches. Issler (2003) examines 60 years of experimental studies over snow avalanches, discussing the similarity issues inherent to the reduced scale utilized in the laboratory.

Dimensionless numbers — refer to table 42.1 in Eckart McElwaine Jim (2012) — can be used to quantify the similarity between small and real-scale flows. Some examples of dimension-

less numbers used in laboratory experiments in avalanche research are:

- **Density ratio** $\Delta\rho$ — the density difference between the two fluids (ex. air and snow):

$$\Delta\rho = \frac{\rho_1 - \rho_0}{\rho_0}$$

where ρ_0 is the density of the ambient fluid (air) and ρ_1 is the density of the fluid in suspension (snow);

- **Reynolds number** Re — the ratio of inertial forces to viscous forces:

$$Re = \frac{u_f h \rho_1}{\mu}$$

where u_f is the front velocity, μ is the dynamic viscosity of the ambient fluid, and h is the front head height;

- **Richardson number** Ri — the ratio of potential energy to kinetic energy at the interface between fluids:

$$Ri = \frac{g' h \cos \theta}{u_f^2}$$

where $g' = g\Delta\rho$, and θ is the slope angle;

- **Densimetric Froude number** Fr — the ratio of the viscous diffusion time to the convective time scale:

$$Fr = \frac{u_f^2}{g' h}$$

Small-scale experiments can be validated by other similarity criteria as well. [Faillettaz et al. \(2002\)](#) analyzed data from more than 5000 avalanches and confirmed that slab-avalanche size distributions are scale-invariant, similar to other geophysical phenomena such as earthquakes and landslides. For powder–snow avalanches, similarity is usually borrowed from small-scale turbidity current (small $\Delta\rho$) tests performed in water tanks, although small-scale non-Boussinesq (higher $\Delta\rho$) experiments can be found in [Ancy \(2004\)](#), [Turnbull and McElwaine \(2008\)](#), [Dellino et al. \(2019\)](#), and [Dai and Huang \(2021\)](#).

In the case of laboratory experiments of powder–snow avalanches — emulated by small-scale turbidity currents — diverse materials are often used in place of actual snow. Examples of materials range from dry or fluidized granular materials ([ROCHE et al., 2011](#)), mixture solutions of water ([BEGHIN; OLAGNE, 1991](#)) (see [Figure 11a](#)), and other sorts of materials such as glass ([GREVE; HUTTER, 1993](#)) and quartz ([KELLER, 1995](#)). [Linden and Simpson \(1986\)](#) used bubbling water to emulate ambient air turbulence and showed that the a gravity current can be destroyed by the background turbulence. Later, [Hermann and Hutter \(1991\)](#), utilized polystyrene powder and water to emulate turbulent suspension flows and achieved similarity

by the Froude number; see [Figure 11b](#). Results showing $Fr \approx 1$ explain why gravity currents speed is independent of flow angle ([SHIN; DALZIEL; LINDEN, 2004](#)). In parallel, [Turnbull and McElwaine \(2007\)](#) analyzed front position and volume data from test site avalanches and found values for the Froude number of 2.2 ± 0.18 .

Figure 11 – Different mixtures can be utilized in laboratory experiments to emulate powder–snow suspensions.

(a) Dyed salt solution.



Source: [Beghin and Olagne \(1991\)](#).

(b) Polystyrene powder.



Source: [Hermann and Hutter \(1991\)](#).

Outdoor experiments allow the use of actual snow material under natural ambient temperatures ([STEINKOGLER *et al.*, 2015](#)). Ski jump hills have also been used to simulate intermediate-scale avalanches, see ([MCELWAIN; NISHIMURA, 2001](#)) and ([TSUNEMATSU; MAENO; NISHIMURA, 2020](#)), where ping-pong balls serve as the granular material particles; see [Figure 12](#).

Figure 12 – Outdoor experiment of granular flow utilizing 300000 ping-pong balls at the Miyanomori ski jump hill in Hokkaido, Japan.



Source: [Tsunematsu, Maeno and Nishimura \(2020\)](#).

Internal velocities, density profiles, and stress quantities are particularly valuable to understanding the internal processes of snow avalanches. For example, an increase of internal velocity was detected by [Nishimura *et al.* \(1993\)](#) seconds after the passage of the front due to the arrival of the dense flow. [Naaim and Martinez \(1995\)](#) measured vertical profiles of particle concentration in the powder-clouds discharged in laboratory. However, due to the violent nature of such phenomena, measuring these properties is very difficult. Snow frozen at the sensors can damp signals, and physical vibrations during avalanche flow can introduce noise into measurement data and create many other issues ([KERN *et al.*, 2009](#)). Only a few measurements were partially successful, such as in [Dent *et al.* \(1998\)](#).

Small-scale experiments, such as [Savage and Sayed \(1984\)](#) and [Tiefenbacher and Kern \(2004\)](#), allow the investigation of the internal flow in avalanche-like phenomena. However, the study of mass entrainment — decisive to the dynamics of powder–snow avalanche internal processes — is a complicated problem to solve in small-scale experiments. To the author’s knowledge, no significant advances in mass entrainment experiments for powder–snow avalanches have been achieved — even in laboratories.

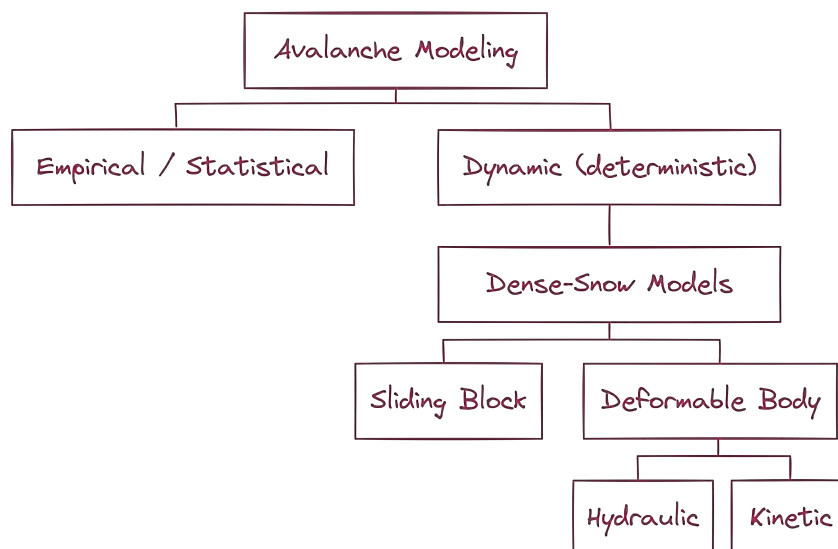
Despite the difficulty of performing measurements, research on entrainment and deposition in dense-snow avalanches has seen advances in field observations and laboratory experiments ([BARBOLINI *et al.*, 2005](#); [FARIN](#); [MANGENEY](#); [ROCHE, 2014](#); [EDWARDS *et al.*, 2021](#)). Entrainment by bed erosion directly influences avalanche motion by restricting or enhancing its mass and velocity ([BARBOLINI *et al.*, 2005](#)). Entrainment has been associated with greater runout distances ([STEINKOGLER](#); [SOVILLA](#); [LEHNING, 2014](#)). Observations indicate that entrainment (basal erosion) occurs mainly in the front, while deposition happens in the tail ([Sovilla; Bartelt, 2002](#)). [Gauer and Issler \(2004\)](#) discusses the different mechanisms of erosion in snow avalanches. [Issler *et al.* \(2008\)](#) observed the dominance of such mechanisms for different types of flow regimes of wet and dry snow avalanches. [Issler and Jóhannesson \(2011\)](#) and [Issler \(2014\)](#) offer a theoretical discussion about such mechanisms on various types of flows, including field observations and mathematical models presenting peaks of influx rates of up to $1000 \text{ kg} \cdot \text{m}^{-2} \cdot \text{s}^{-1}$. [Issler *et al.* \(2020\)](#) suggests that the eroded mass is only entrained into the avalanche.

2.3 Dense-Snow Avalanche Models

Despite the different physical properties of snow, dense snow avalanches have many similarities with other avalanches, such as debris flows and mudslides. Many mathematical models of such avalanche types share similar origins. Compared to the powder–snow avalanches, dense-snow avalanche research appears to be more extensive and explored.

[Figure 13](#) arranges popular models of dense-snow avalanche models roughly based on the SAME (Snow Avalanche Modeling and Warning in Europe) model survey ([HARBITZ; ISSLER;](#)

Figure 13 – General organization of dense-snow avalanche models.



Source: Adapted from [Harbitz, Issler and Keylock \(1998\)](#).

[KEYLOCK, 1998](#)). This text focus only on a subset of models to avoid overextending the scope of this section, concentrating on the deterministic type between the two main divisions, statistical and deterministic, as statistical models offer little detail about the internal flow dynamics of such avalanches. This section explores the dense-snow avalanche models in the same order of the following division:

- *Empirical / Statistical models* — described in [subsection 2.3.1](#) on [page 38](#) — apply statistical inference methods on historical data of field observations and laboratory experiments to predict general quantities of the avalanche such as runout distances and avalanche size;
- *Deterministic models* — described in [subsection 2.3.2](#) on [page 39](#) — encompass all the following. Such models use mathematical equations to describe motion at different scales;
- *Sliding Block models* — described in [subsection 2.3.3](#) on [page 40](#) — represent the avalanche body as a single rigid (non-deformable) block that slides down over an inclined plane;
- *Hydraulic models* — described in [subsection 2.3.4](#) on [page 42](#) — borrow laws and relations from hydrodynamics to better reproduce the mechanical behavior of snow in sliding block models;
- *Kinetic models* — described in [subsection 2.3.5](#) on [page 46](#) — use balance equations from continuum mechanics to full describe the avalanche;
- *Granular Flow models* — described on [page 49](#) — like kinetic models, stand from the continuum point of view but bring relations from the laws of motion of granular materials.

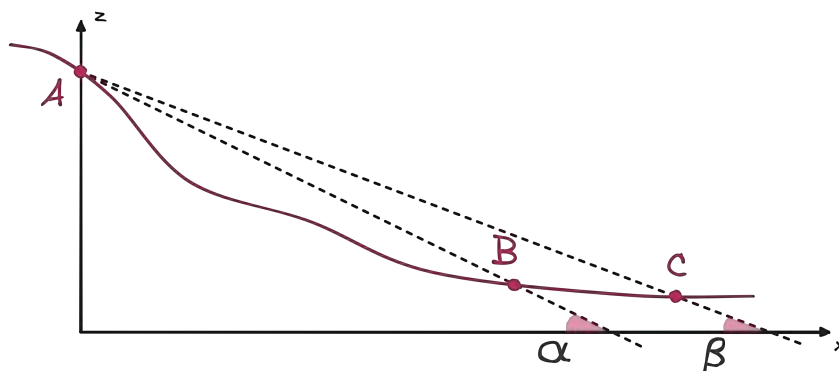
Such models consider internal friction processes and other complex internal phenomena of snow avalanches, such as entrainment and deposition.

Before continuing, it is worth noticing that the above division of models is neither definitive nor inflexible since there are models that share origins and aspects of different groups simultaneously. For example, some methods combine statistical and deterministic models, while some granular flow and kinetic models borrow terms from hydraulic models. In other words, such a division of models is not necessarily a set of disjoint groups of methods, concepts, or assumptions.

2.3.1 Statistical Models

As mentioned in [section 2.2](#), field observations and historical data provide essential resources for understanding physical phenomena. Such data is the primary input of statistical models. *Statistical models* use historical information to predict the size of new avalanches by establishing correlations between the run-out distances and the underlying topographic parameters, such as the avalanche initiation point, stopping point, and slope angles representing the avalanche track path ([MCCLUNG; LIED, 1987](#)). Based on such parameters, the $\alpha - \beta$ model by [Lied and Bakkehøi \(1980\)](#) uses regression methods to estimate the run distance of an avalanche over a given terrain topography; see [Figure 14](#) on [page 38](#). Other examples of statistical models are the run-out ratio model by [McClung, Mears and Schaerer \(1989\)](#), and the space-time (ST) model by [McClung \(2000\)](#). Refer to [Sinickas \(2013\)](#) and [Schweizer, Bartelt and van Herwijnen \(2021\)](#) for further references and details about statistical models.

Figure 14 – Parameters used by the $\alpha - \beta$ model. The model uses the (A) starting zone location, the (B) deceleration zone location, the (C) run-out zone location, and the *average inclination angle* β . Along with regression constants γ and λ , the *stopping angle* α can be determined as $\alpha = \gamma\beta + \lambda$.



Source: Elaborated by the author.

Statistical methods have been extensively used in avalanche zoning or even in combination with deterministic methods for estimating the run-out distance of long-return period

avalanches (ANCEY; GERVASONI; MEUNIER, 2004). However, such methods present several shortcomings related to issues of input data quality and the wrong assumption that avalanches' dynamic behavior is governed by topographic features (MEUNIER; ANCEY, 2004). Such limitations require the use of deterministic approaches.

2.3.2 Deterministic Models

Under the *deterministic* approach, physical and mathematical equations describe the avalanche motion. Different methods deal with different scales of representation of mass; see Figure 15 on page 40. These scales range from individual snow particles (Figure 15c) to a single sliding block representing the entire avalanche body (Figure 15a), with intermediate representations that split the avalanche body into moving columns of variable height (Figure 15b). Larger scale representations lead to simpler models and crude estimations, while more miniature scale representations offer precise flows at the cost of complicated models and computational effort.

The mathematical equations used by deterministic models may use different coordinate spaces to describe the physical quantities and the motion of avalanches. Figure 16 on page 41 depicts the two standard coordinate systems used by avalanche models: the local and global coordinate systems. In global coordinates, the axes of the basis are aligned to the Cartesian basis and do not depend on the geometry of the domain; see Figure 16a. In local coordinates, axes vary along the geometry, and usually, the basis vectors are the bed's normal and tangential directions; see Figure 16b. Vector quantities such as the velocity and acceleration forces, in particular, are sensitive to coordinate systems and must be appropriately defined. For example, in a position in the bed surface with slope angle θ , the gravitational force \mathbf{g} translates to the following projections in a local coordinate system: the tangential component along the slope, $\mathbf{g} \sin \theta$ ³, and the component $\mathbf{g} \cos \theta$ along the slope normal; see Figure 16c.

All avalanche model equations in this section use the same local coordinates system — except for kinetic models, which use the global coordinate system. In the one-dimensional case, the horizontal direction x' ⁴ in the local coordinate system is tangential to the slope. Therefore, spatial derivatives along the horizontal⁵ direction are defined by $\partial/\partial x'$. The dynamic variables can be functions of the time t and the position along the slope x' . For instance, the height $h'(x', t)$ of the avalanche body, measured in meters, is the height along the slope's normal direction. The velocity vector $u(x', t)$ points to the motion direction (parallel to x'). For curved slopes, the angle of the slope $\theta(x')$ is a function of the position; see Figure 17 on page 42.

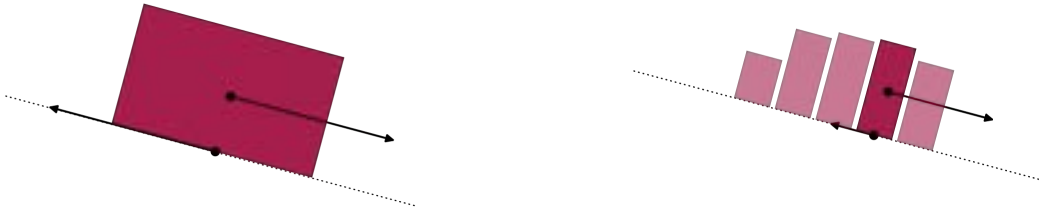
³ The projected gravitational force is common in models of flows over inclined terrains — once such models usually use local coordinates along the slope.

⁴ The prime superscript, \star' , refers to local coordinates. However, for the sake of generality, the prime may be omitted throughout the text.

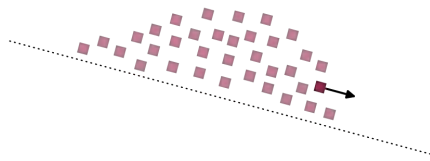
⁵ Although the term *horizontal* refers to the aligned direction of left and right, as in the Cartesian coordinate system, in the context of inclined flows, the term also refers to the principal flow direction.

Figure 15 – Deterministic models describe the avalanche — body in different scales of representation. Model accuracy depends on the level of representation, with more refined representations leading to higher precision on flow dynamics.

- (a) A single solid block represents the avalanche body. Equations describe the movement of the center of mass, and velocity is assumed uniform throughout the block — friction forces with the inclined surface decelerate the slide.
- (b) Separate columns of mass represent the avalanche body. Each column block has its center of mass and friction with the bottom surface. The height of columns varies as mass is transported between columns.



- (c) Small individual blocks, called particles, describe finite volumes of the avalanche. The particles have individual properties, such as velocity and mass, and collide with each other. The collisions produce friction forces, and particles' collective movement shapes the flow.



Source: Elaborated by the author.

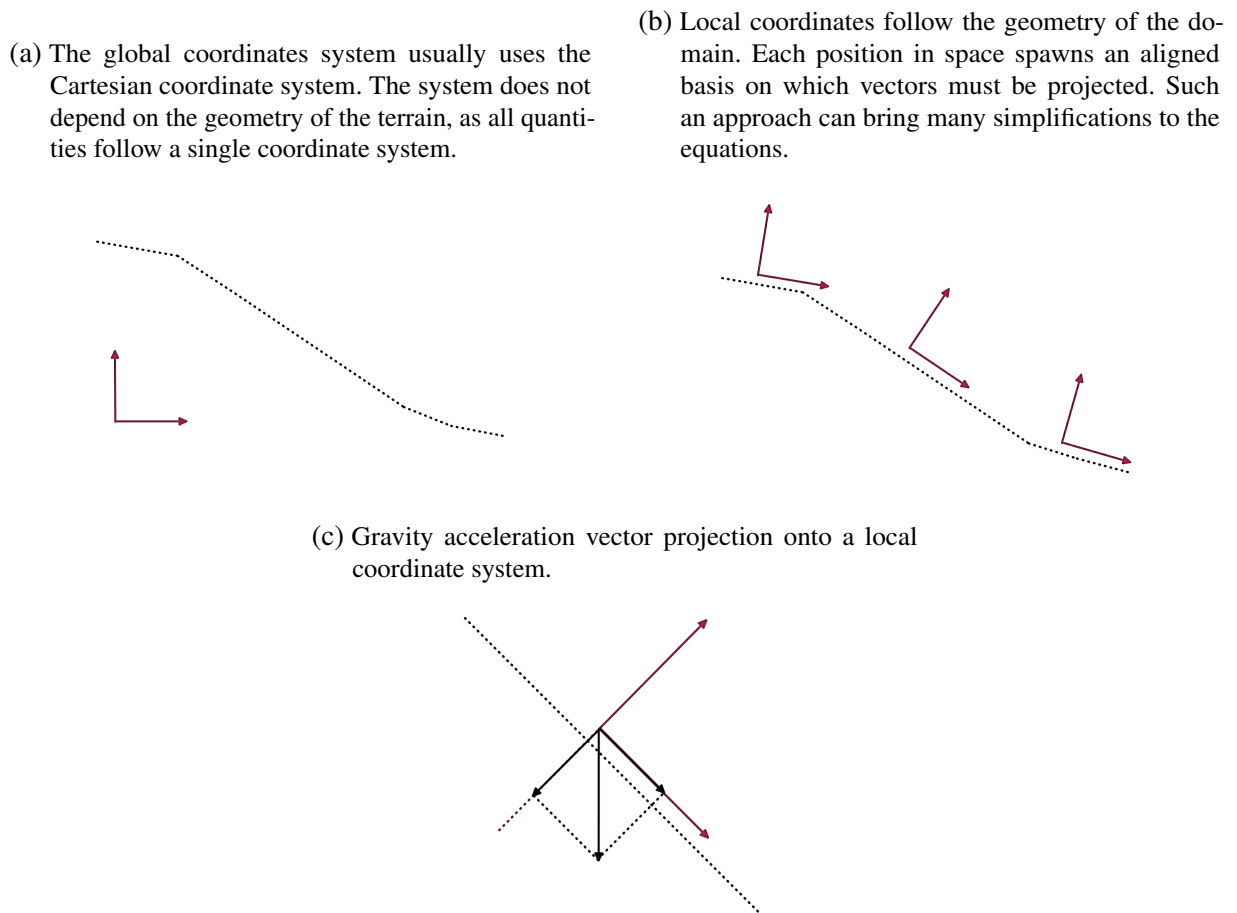
2.3.3 Sliding Block Models

The simplest and earliest approach is the so-called *sliding block model*, introduced by [Mougin \(1922\)](#), and describes the avalanche as a single rigid (non-deformable) body that slides over an inclined plane representing the mountain terrain (see [Figure 15a](#) on [page 40](#)). In 1924, such early approaches were used to compute the velocity of avalanches during the Olympic Games at Chamonix ([LAGOTALA, 1927](#)). Sliding block models make the calculations relative to the center of mass of the sliding block and use specific friction forces to emulate the avalanche mechanical behavior. Typically, only one-dimensional schemes are considered and motion is described as:

$$\frac{du}{dt} = g \sin \theta - F, \quad (2.1)$$

where $u(x,t)$ is the velocity, θ is the mean slope of the inclined plane, g is the gravitational acceleration, and $F(x,t)$ is the frictional force. The mechanical behavior of the avalanche due to its interaction with the mountain soil relies on the frictional force term F , responsible for

Figure 16 – Models can use different coordinate systems to describe flow quantities. In the case of local coordinate systems, vector quantities must be projected onto the local basis system to guarantee consistency in equations.



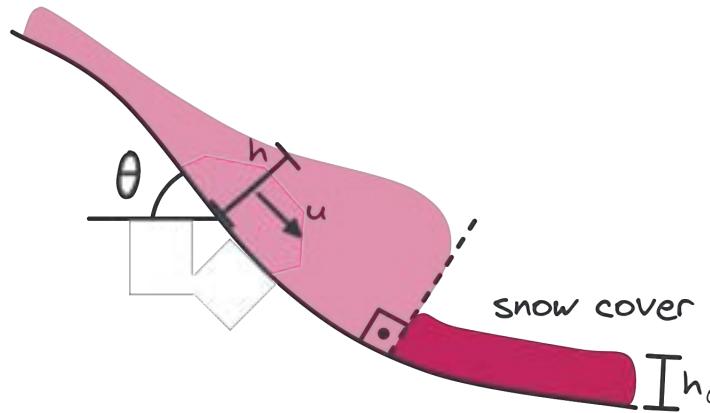
Source: Elaborated by the author.

the deceleration of the flow. The most significant development in the friction term came with Voellmy (1955)'s friction model — called *Voellmy fluid* by Hungr (1995). Voellmy's model combines a dynamic friction component τ_h with a Coulomb-like dry friction (POPOVA; POPOV, 2015) component τ_d :

$$F_v = \tau_b = \tau_h + \tau_d, \quad \tau_h = g \frac{u^2}{\xi h}, \quad \tau_d = \mu g \cos \theta, \quad (2.2)$$

where ξ is the coefficient of dynamic friction related to the terrain roughness, μ is the friction coefficient related to the snow fluidity, and $h(x, t)$ is the mean flow depth of the avalanche. The letter b in τ_b stands for bed, as Voellmy's model F_v represents the bed shear stress. The term τ_h , named by Voellmy as *turbulent friction* and sometimes referred to as *shear resistance* (BARTELT; SALM; GRUBER, 1999) or *hydraulic friction* (EGLIT; YAKUBENKO; ZAYKO, 2020), is based on the Chézy resistance formula for turbulent water flow in open channels and refers to the viscous resistance — see page 170 in Kay (2017). The Voellmy's friction model is used by many generations of models today, such as debris flow models (PIRULLI; SORBINO,

Figure 17 – Common variables present in avalanche models. The height h and velocity u are functions of position x and time t . The bed slope θ varies only with position. Some models also consider the entrainable snow cover, which has depth h_0 .



Source: Adapted from Eglit, Yakubenko and Zayko (2020).

2008; HUSSIN *et al.*, 2012; SCHRAML *et al.*, 2015; ABRAHAM *et al.*, 2022).

Sliding block models overcome many statistical model shortcomings but still offer few details about the flow dynamics. These models inherently consider the body of the avalanche as non-deformable. In order to account for more complex phenomena such as mass entrainment, straining, and other physical properties of an avalanche flow, avalanche models need to dive further into smaller-scale representations.

2.3.4 Hydraulic Models

The contributions of Voellmy⁶ go beyond the frictional model. His analogies to hydrodynamics also brought attention to the so-called depth-integrated flow model, which has become the most prominent model for dense-snow avalanches since then (LACHAPELLE, 1977; ANCEY, 2016). The depth-integrated flow model, also called shallow water equations (SWE), is based on the works of Barré de Saint-Venant on hydraulic modeling (VENANT, 1871). Depth-integration simplifies fluid mechanics equations by neglecting vertical velocities, assuming that the flow height h is much smaller than the flow length l . The horizontal velocity at any given point is averaged over the whole depth of the flow, yielding $\bar{u}(x, t)$. In terms of scales of representation of the avalanche body, the depth-integrated flow is an intermediate scale that sees the fluid body as columns of mass that vary in height; see Figure 15b on page 40. The one-dimensional Saint-Venant's equations (SWE) are:

$$\frac{\partial h}{\partial t} + \frac{\partial}{\partial x}(\bar{u}h) = 0, \quad (2.3)$$

$$\frac{\partial h\bar{u}}{\partial t} + \frac{\partial (h\bar{u}^2)}{\partial x} = -\frac{\partial}{\partial x}\left(\frac{1}{2}gh^2\right), \quad (2.4)$$

⁶ The works of Voellmy can be found in volume 73 of the series *Schweizerische Bauzeitung* at <<https://www.e-periodica.ch/digbib/volumes?UID=sbz-002>> (ETH, Zürich, 2022), by Wanger (2018).

where again x is the slope coordinate axis and g is the gravitational acceleration.

Notice that the hydrostatic pressure gradient dictates the flow on the right-hand side of Equation 2.4 but does not consider any friction forces. Models based on the SWE are called *hydraulic models* and can be referred to by some authors as Saint-Venant models — models using Voellmy’s friction may receive this name as well. Although Voellmy popularized the depth-integration approach by using depth-averaged velocities and suggesting the use of the hydraulic model, his model lacks Equation 2.3, the continuity equation. Therefore, Voellmy assumes depth and depth-averaged velocity to be the same at all points of the avalanche, which essentially makes his model a sliding block model.

Many works extended Voellmy’s model throughout the years in order to complete his equations. Particularly, the set of works made by Salm — Salm (1966), Salm (1967), Salm (1972) — are considered the most significant extensions and form the Voellmy-Salm (VS) model, with Salm and Gubler (1985) and Salm, Burkard and Gubler (1990) being referred to as the Voellmy-Salm-Gubler (VSG) model. A comparison between the VS and VSG variations can be found in Gubler (1989). The extensions incorporated by the VS model handle non-uniform flows and internal friction under the assumption that snow behaves like ideal elastoplastic cohesionless materials (like dry sand) (HEIMGARTNER, 1977), with different values for the friction coefficients of F_v . Following the *earth-pressure* definition of Rankine (1857), the VS model also adapted the hydrostatic pressure to depend on the internal friction angle ϕ replacing the momentum Equation 2.4 by

$$\frac{\partial u}{\partial t} + u \frac{\partial u}{\partial x} = g \sin \theta - F_v - \frac{\partial}{\partial x} (\lambda_{\pm} g \cos \theta \frac{h^2}{2}), \quad (2.5)$$

where the term $\lambda_{\pm} = \tan^2(45^\circ \pm \phi/2)$ is the active/passive⁷ pressure coefficient with internal friction angle ϕ and the operation \pm depends on the value of $\partial u/\partial x$ (+ for $\partial u/\partial x > 0$, and – otherwise) (SALM, 2004). The WSL Institute of Snow and Avalanche Research SLF (SLF) (SLF, 2022) has used the VS model since earlier 1990s (SALM, 1993). Table 4 and Table 5 list the values for the coefficients of dynamic friction ξ and dry friction μ suggested by the institute (GUBLER, 2005). Software packages cited in section 2.6 use the VS model. Examples of methods based on the VS model are Sovilla and Bartelt (2002) and Christen, Kowalski and Bartelt (2010).

Table 4 – Typical values in the VS model of the dynamic friction ξ for different dense-snow avalanche conditions suggested by the SLF (GUBLER, 2005).

Dynamic friction (ξ)	Condition
> 1000	very cold dry snow, very low bed roughness
500 ~ 600	large bed roughness, channelled flow
400	avalanche flowing through a forest

⁷ According to Salm, internal friction (plugged into the pressure term in the VS model) arises as the snow gets under a tensile (active) or compressive (passive) longitudinal strain.

Table 5 – Typical values in the VS model of the dry friction μ for different dense-snow avalanche conditions suggested by the SLF (GUBLER, 2005).

Dry friction (μ)	Condition
0.155	extreme avalanches with large volumes, flow depth of 1 ~ 2 m
0.25 ~ 0.3	smaller avalanches with volumes $< 10^4 m^3$
0.3	wet snow avalanches of any size

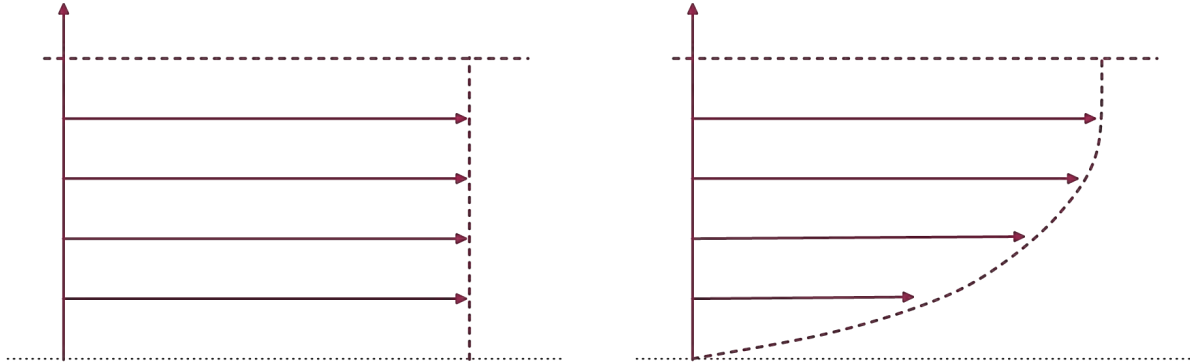
Despite its success, the VS model has received many criticisms. Critics of the VS model point out several shortcomings and limitations regarding the accuracy of its predictions on runout distances and deposition heights (MCCLUNG; MEARS, 1995). Indeed, the VS model is considered by many as a sliding block model since its original formulation does not include the continuity equation (BARTELT; BUSER; PLATZER, 2006; PUDASAINI; HUTTER, 2007). Perla, Cheng and McClung (1980) derived the PCM model, which uses a calibrated mass-to-drag ratio M/D coefficient applied to the velocity squared, replacing the dynamic friction coefficient ξ - so only the dry friction coefficient μ must be estimated. An early extension of the PCM, the PLK model by Perla, Lied and Kristensen (1984), uses particles to handle snow entrainment and deposition. The PCM model offers better runout distances in complex terrains than the VS model (LIED *et al.*, 1995; JAMIESON; MARGRETH; JONES, 2008). Bartelt, Salm and Gruber (1999) solved some shortcomings of the VS model by combining characteristics from the Norwegian NIS model, by Norem, Irgens and Schieldrop (1989), and modifications to Voellmy's friction from Russian models — described on page 45.

The critical characteristic of the NIS model that puts it one step forward from sliding block models is that it considers the avalanche body as completely fluidized. The VS model, for example, alternates between three flow regimes: sliding⁸, partly fluidized, and fully fluidized. Salm and Gubler (1985) adapted these flow regimes from the studies of Haff (1983) on treating the movement of granular materials from a continuum point of view. The flow regime determines the velocity profile along the depth; see Figure 18 on page 45. Non-steady and non-constant velocity profiles result from internal stresses in the avalanche body, which the previous models do not adequately handle. Allowing such velocity profiles — as in the NIS model — leads to more precise simulation results.

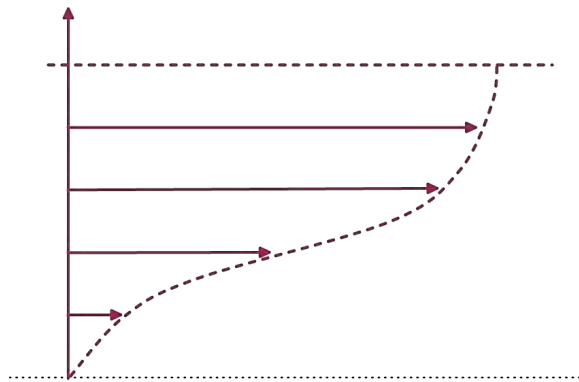
⁸ The sliding regime, when velocity is constant across the depth, is also called *plug flow* (LIGNEAU; SOVILLA; GAUME, 2022).

Figure 18 – Velocity profile on different flow regimes.

- (a) In the sliding regime, velocity ($1 \sim 5 \text{ m/s}$) is constant across the depth and is usually characterized by high cohesive snow.
- (b) As velocity increases, snow is disintegrated into clods and a partial layer becomes fluidized. The shear stress depends linearly on flow velocity.



- (c) At higher speeds, snow clods mobility allow changes in flow depth and deformations. The shear stress now depends on the square of the flow velocity.



Source: Adapted from [Salm and Gubler \(1985\)](#).

In parallel to western models, Russian models also have a long history. The first sliding block models in the Soviet Union appeared in the early 1930s following the same [Equation 2.1](#) on [page 40](#) ([BOZHINSKIY; LOSEV; BARTELT, 1998](#)). Similar to the VS model, the works of Grigorian and Eglit — [Grigorian, Eglit and Iakimov \(1967\)](#), [Bakhvalov and Églit \(1973\)](#), [Grigorian and Ostroumov \(1977\)](#), [Eglit \(1998b\)](#) — constitute the Moscow State University (MSU) hydraulic model. The one-dimensional MSU momentum equation is quite similar to VS model's [Equation 2.5](#) on [page 43](#):

$$\frac{\partial u}{\partial t} + u \frac{\partial u}{\partial x} = g \sin \theta - F_v - \frac{1}{2h} \frac{\partial}{\partial x} (h^2 g \cos \theta), \quad (2.6)$$

where F_v uses a modified dry friction τ'_d . The full MSU model includes the continuity [Equation 2.3](#) on [page 42](#) and a set of hydraulic equations to handle snow entrainment in the leading edge. Entrainment equations are treated in the [subsection 2.3.7](#) on [page 54](#).

From [Equation 2.6](#), two main differences to the VS model stand out. Firstly, the MSU model discards the active/passive pressure coefficient by setting $\lambda_{\pm} = 1$. The second relies on the

term F_v . Grigorian stated there should exist an upper limit to friction, arguing that friction cannot rise indefinitely with an increase in normal stress (GRIGORYAN, 1979). Therefore, the MSU model limits the dry friction $\tau_d = \mu g \cos \theta$ by the shear stress $\tau_\gamma = \mu p$ with a yield condition $\tau_{\gamma*}$ representing the minimal shear strength of the snow in the avalanche:

$$\tau'_d = \begin{cases} \tau_d, & h \leq h_* \\ \frac{\tau_{\gamma*}}{h}, & h > h_* \end{cases}, \quad h_* = \frac{\tau_{\gamma*}}{\mu \rho g \cos \theta}. \quad (2.7)$$

In other words, the dry friction reaches a maximum value as avalanche depth h rises. In practice, larger avalanches will travel longer distances in simulations, for which Voellmy's friction model fails to produce satisfactory results (BARTELT; SALM; GRUBER, 1999). A post-mortem paper by Grigorian was recently published with the state-of-the-art version of the MSU model, discussing updates in the friction coefficients and the handling of entrainment (GRIGORIAN; OSTROUMOV, 2020). The MSU model found its way to the west due to its snow entrainment equations with Sovilla (2004). An extensive literature in English of Russian models can be found in Bozhinskiy, Losev and Bartelt (1998) and a modern review in Eglit, Yakubenko and Zayko (2020).

Hydraulic models have been present in avalanche-like phenomena research for many decades now. Due to its simplicity and convenient analogy to hydrodynamics, hydraulic models could quickly gain space in avalanche research during the 1970s. However, the complexities of the mechanical behavior of snow during avalanche motion and the intricate relations of internal friction forces demanded new research paths and new types of models.

2.3.5 Kinetic Models

The fluid-like motion of dense-snow avalanches makes using fluid mechanics equations attractive. However, formulating a full fluid mechanics model still encounters several challenges and limitations. Most difficulties come from the inherent complexity of the dynamics of snow:

- Snow particles change in size with time and position, spanning a wide range of sizes (0.001 ~ 1 m) (BARTELT; MCADELL, 2009);
- Phenomena like erodible basal surface pose ill-known boundary conditions;
- Surge front and free surface instabilities lead to flows with abrupt changes over time;
- Dense snow flows are non-Newtonian viscoplastic flows (DENT; LANG, 1982);
- Variations in snow microstructure due to thermodynamic transformations make snow rheometry very difficult, consequently impeding the identification of constitutive relations.

Therefore, the usual fluid mechanics approach is to treat the snow material as a whole at the macroscopic scale — but far from a single piece as in sliding block models. The snow

avalanche body is usually represented by a set of particles or fine numerical grids that represent small volumes of snow, as in Figure 15c on page 40. In such treatment, the bulk rheological⁹ properties of snow are used instead of directly dealing with real snow particles individually at the microscopic scale. Such formulations from continuum mechanics, called *kinetic models*, combine the rheological conditions with mass, momentum, and energy balance equations (PUDASAINI; HUTTER, 2007). For instance, an example of a local momentum balance equation for a bulk material is:

$$\rho \frac{d\mathbf{u}}{dt} = \rho \mathbf{g} - \nabla p + \nabla \cdot \Sigma, \quad (2.8)$$

where ρ is the bulk density, \mathbf{u} is the bulk velocity, \mathbf{g} is the gravity acceleration, p is the pressure, and Σ a second-order tensor called the bulk extra stress tensor¹⁰. In particular, the stress tensor determines the relation between stress and the different physical states or acting forces that characterize the behavior of different materials. In terms of stress-generating mechanisms during snow avalanches, Hutter (1996) gives some examples:

- The rolling of snow particles over each other, known as the *dry Coulomb rubbing friction*, that causes plastic behavior;
- The continuous and instantaneous collision of snow particles, without rubbing, transports momentum and causes viscous behavior;

where the influence of each varies on the type of the avalanche and may occur simultaneously along with other mechanisms. In dense snow avalanches for example, the dry Coulomb rubbing friction is more present. Such stress response mechanisms are represented by the material's *constitutive relations*, defined by the so-called *constitutive equations*, or *rheological models* in the present context, which describe the tensor Σ ¹¹ components σ_{ij} in Equation 2.8 on page 47 (GONZALEZ; STUART, 2008).

The study of the relationship between stress and deformation rates traces back to the beginning of the 19th century (YU, 2002). Since then, scientists have been measuring constitutive relations for many types of materials and physical phenomena, such as debris flows (MAJOR; PIERSON, 1992) and mudflows (HUANG; AODE, 2009). Different properties of a material can also lead to different stress-strain responses, as demonstrated by Arenson, Springman and Segio (2007) for different types of frozen soil; see Figure 19a on page 48. The behavior of materials can also change depending on their stress state. For example, a material with elastic behavior can transit to plastic behavior when suffering too much of a certain type of stress. Such

⁹ E.C. Bingham and M. Reiner defined the term *rheology* in 1929 to refer to "the science devoted to the study of the deformation and flow of matter" (BINGHAM, 1944).

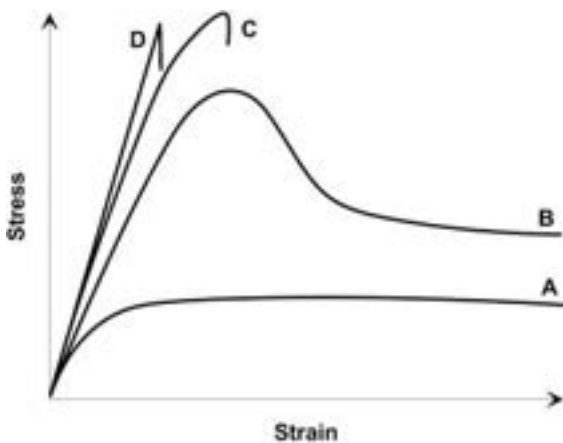
¹⁰ The pressure p and extra tensor Σ are decomposed parts of the so-called *Cauchy stress tensor* $S = -pI + \Sigma$, where Σ is the *deviatoric stress tensor* and $-pI$ is the *spherical stress tensor* (GONZALEZ; STUART, 2008).

¹¹ The equations system does not has enough equations to solve all the 9 variables introduced by Σ . The constitutive equations complete the system and are usually referred to as *closure model*.

transitions are represented by the so-called *yield surfaces*, which define the different regions in principal stress space that represent the different material behaviors. The principal stress space is a three-dimensional space formed by the three principal stresses ($\sigma_1, \sigma_2, \sigma_3$), *eigenvalues* of Σ , on which yield surfaces determine for which stress conditions, *yield conditions* or *yield stress criteria*, the material will undergo plastic deformation. Figure 19b on page 48 shows an example of a yield surface, the Mohr–Coulomb yield failure criterion that spans a six-side pyramidal surface, for which the material undergoes plastic deformation when stresses reach any of the sides/edges (see (LABUZ JOSEPH F.AND ZANG, 2012)).

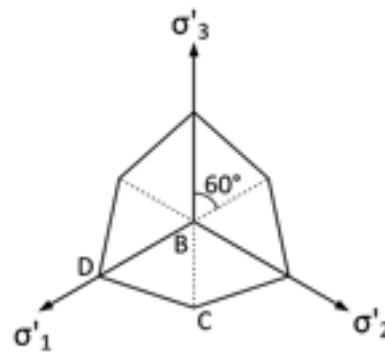
Figure 19 – Constitutive relations describe stress responses to acting forces and material deformations, such as strain. Yield surfaces define stress states of materials and yield criteria characterize material behavior.

(a) The stress-strain responses for ice and frozen soil. The four curves, A, B, C, and D, represent the ductile, dilatant, brittle, and brittle failure behaviors, respectively.



Source: Arenson, Colgan and Marshall (2015).

(b) A cross-section of the Mohr–Coulomb yield surface for an isotropic material. The surface is pyramidal with an irregular hexagonal base defined in the principal stress space ($\sigma_1, \sigma_2, \sigma_3$). The edges represent the cross-section of the surface on the π -plane — perpendicular to line $\sigma_1 = \sigma_2 = \sigma_3$.



Source: Labuz Joseph F.and Zang (2012).

Examples of common constitutive equations and yield surfaces found in the literature are the Coulomb-like friction laws (IVERSON; DENLINGER, 2001), the Drucker-Prager elastoplastic model (DRUCKER; PRAGER, 1952), the Mohr-Coulomb-Cap criterion for snowpack failure (REIWEGER; GAUME; SCHWEIZER, 2015), and the nonlinear viscous law $\mu(I)$ -rheology (GRAY; EDWARDS, 2014). The Voellmy's friction law described earlier is an example of constitutive equation used by kinetic models. Ligneau, Sovilla and Gaume (2022) discusses the role of friction in dense snow avalanches, and Voellmy's friction coefficients are explored in Ancey and Meunier (2004), Naaim *et al.* (2013), Sanz-Ramos *et al.* (2020).

Laboratory experiments and measurements from field observations of rheological properties help design constitutive relations of materials. However, the measurement of constitutive relations is more complicated or sometimes impossible for more complex materials like snow (ANCEY; MEUNIER, 2004). In such cases, the models borrow characteristics from other physical phenomena, such as granular and viscoplastic flows (TAI; HUTTER; GRAY, 2001; ANCEY,

2001; NICOT, 2004). Examples of rheological models used in snow applications are the Burgers model for viscoelastic materials (MELLOR, 1974), models for elastoplastic materials (SINGH *et al.*, 2022; GAUME *et al.*, 2019), models based on the micro-structural configuration of snow (St. Lawrence; LANG, 1981; MAHAJAN; BROWN, 1993), and models considering the compressibility of snow (MISHRA; MAHAJAN, 2004). Refer to Salm (1982) for more details on the earlier approaches of constitutive models for snow.

2.3.5.1 Granular Flow Models

One of the most successful approaches used by kinetic models of dense-snow avalanches is the treatment of snow as a granular material. Although the first experiments with the motion of granular materials started in 1954 with the pioneering work of Bagnold (1954), theoretical models started to appear only decades later (HAFF, 1983). Refer to Savage (1984) for a review of early models of granular flows. Complete reviews on granular flow models can be found in Campbell (1990), Hutter and Rajagopal (1994). Such models take the behavior of the granular material from a continuum point of view, which allows the use of continuum mechanics equations. Haff (1983) uses the following assumptions regarding the material grains and their analogy to fluid molecules in the continuum treatment:

- Individual grain motion follows the laws of classical mechanics;
- Different from molecules that may undergo completely elastic collisions, grain-grain collisions always involve a loss of kinetic energy (the amount of energy lost in such granular systems is significantly different from fluids);
- Although different grains have different sizes, minor differences between grain sizes do not affect the motion significantly. Therefore, such granular systems assume all particles are roughly the same size;
- Similar to the same size assumption, all grains are assumed to be roughly the same shape (spheres). Otherwise, grain-grain collisions must account for grain rotation due to torque caused by friction;
- Grains are orders of magnitude bigger than molecules, so the number density of particles in a granular flow is much smaller than the number density of molecules in a correspondent fluid. Combined with the inelastic nature of grain-grain collisions, the continuum hypothesis might not hold in some instances¹². Thus, the model must be applied only to granular flow situations where the continuum hypothesis is valid;

¹² The continuum hypothesis considers that properties, such as velocity, density, and energy, vary continuously, even over small volumes, due to the small molecular scale. In comparison, the large-scale size of grains will lead to abrupt changes in such properties for the same small volumes.

- The *binary collision hypothesis* can be assumed for such granular systems, meaning that only pairwise collisions are essential for the dynamical evolution of motion;
- Unlike molecular interactions, grain-grain interactions are assumed not to have any attraction force.

The last assumption above considers only cohesionless granular materials. Aside from dry snow avalanches, dense-snow avalanches present strong, cohesive interactions. However, cohesionless models for snow avalanches are widespread due to the difficulties inherent to cohesion modeling. Examples of models using cohesion can be found in [Bartelt *et al.* \(2015\)](#) and [Valero *et al.* \(2018\)](#).

The Savage–Hutter (SH) model is the first, perhaps the most famous, granular flow model for dense-snow avalanches under the continuum mechanical approach. Introduced in 1989 by S. B. Savage and K. Hutter ([SAVAGE; HUTTER, 1989](#)), the SH model considers some additional simplifying assumptions to the list above:

- The flow is density preserving, meaning that volume expansions and compactions do not happen during motion. Volume changes happen in the initiation and stop phases. [Hutter and Koch \(1991\)](#) reported measurements of up to 20% volume changes in sand-avalanche flows;
- The inclination slope angle θ is constant - this limitation was soon overcome by [Savage and Hutter \(1991\)](#), allowing mildly curved topographies;
- The avalanche body is shallow in that the height is orders of magnitude smaller than the longitudinal extensions of the body (similar to Saint-Venant's);
- The velocity is depth-averaged through the avalanche depth (also similar to the depth-integrated flow model);
- The friction is Coulomb-like dry friction with a bed friction angle δ ;
- The Mohr-Coulomb yield criterion defines the constitutive behavior with internal angle of friction $\phi \geq \delta$.

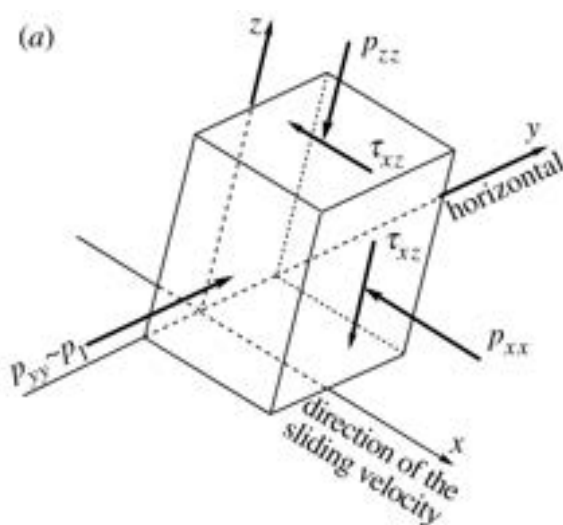
According to [Hutter, Savage and Nohguchi \(1989\)](#), which results and physical model helped construct the SH model; the avalanche surface is assumed to be stress-free. The shearing takes place in a thin layer close to the bed, where the basal shear stress causes the sliding of the upper mass — here, the velocity profile is similar to the fluidized flow regimes in [Figure 18b](#) and [Figure 18c](#) on [page 45](#). This way, the material behavior only needs to be known at the bottom.

[Figure 20](#) on [page 51](#) describes the set of stresses acting in a finite volume element of the avalanche close to the bed surface and their relations. The volume suffers pressure forces from

all sides and develops shear tensions internally and externally. The normal stresses represent pressure forces due to the overburden weight of the snow above and along the path. The shear stresses come from the shear traction exerted on the sliding surfaces. Considering the local coordinate system — where x points in the slope direction, z points in the bed surface's normal direction, and y in the traverse direction — the SH model assumes that traverse shearing is negligible¹³, so only shearing at the xz plane is considered ; see Figure 20a. Therefore the important stresses are the normal stresses, p_{zz} and p_{xx} , and the shear stresses τ_{xz} .

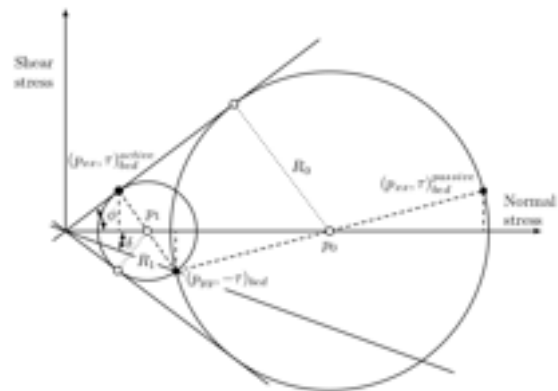
Figure 20 – These figures show the normal and shear stresses acting in the thin basal layer of the avalanche, as assumed by the SH model. The Mohr–circle diagram relates the stress states with the acting stresses through the bed friction angle and the internal angle of friction.

(a) A volume element located at the base of the avalanche is depicted in local coordinates — x in the velocity direction and z perpendicular to the bed. The principal stresses lie in the xy plane, as traverse shearing is small and omitted. p_{yy} and p_{xx} are normal stresses and work as pressure forces due to the snow weight, and τ_{xz} are the shear stresses due to shear traction caused by sliding.



Source: Hutter, Wang and Pudasaini (2005).

(b) The figure shows a representation of the active/passive stress states. The dashed Mohr circle is the active state, while the other is the passive state. The internal friction angle ϕ bounds both circles, and the bed friction angle δ determines the transition points $(p_{zz}, \pm\tau_{xz})$ between states and, therefore, all other points.



Source: Christian Kröner (2014).

The two friction angles, δ and ϕ , listed above define the constitutive behavior by prescribing the passive and active stress states λ_{\pm} . In the shear-normal stress space (p, τ) , the internal friction angle ϕ bounds the possible values of shear and normal stresses by lines $\tau = \pm p \tan \phi$. The Mohr-Coulomb yield criterion defines the principal stress points for which the material transits between the active λ_{+} and the passive λ_{-} states. The transition points are points $(p_{zz}, \pm\tau_{xz})$ and lie in lines $\tau = \pm p \tan \delta$, as shown in Figure 20b on page 51. In the figure, the two circles, called *Mohr circles*, represent the two active/passive states. The Mohr circle is a visual tool that shows the stress states of material in the (p, τ) space; the principal stresses are two diametrically opposed points on the circle — maximum normal stresses are reached when rotating the circle,

¹³ Such assumption implies that p_{yy} is a principal stress.

so both points lie in the p -axis, and maximum shear appears on the vertical poles (notice that points $(p_{xx}, \pm\tau_{xy})$ could be obtained by rotating the circles 180°). The SH model assumes p_{yy} equal to one of the four points depicted in the figure. Lastly, the basal normal stresses are related by earth-pressure coefficient λ_{\pm} as $p_{xx} = \lambda_{\pm}p_{zz}$ and $p_{yy} = \lambda_{\pm}p_{zz}$.

In sum, the SH model considers an incompressible, cohesionless granular material for a dense-snow avalanche sliding down an inclined slope with small curvatures. The shallowness assumptions allow the use of depth integration along with Rankine's earth-pressure (similar to the VS model) controlled by the Mohr-Coulomb yield criterion, which classifies the SH model as a hydraulic model. The one-dimensional equations for conservation of mass and momentum with local coordinates from [Savage and Hutter \(1991\)](#) are:

$$\frac{\partial h}{\partial t} + \frac{\partial}{\partial x}(\bar{u}h) = 0, \quad (2.9)$$

$$\frac{\partial h\bar{u}}{\partial t} + \frac{\partial (h\bar{u}^2)}{\partial x} = hS - \frac{\partial}{\partial x}\left(\frac{1}{2}\beta h^2\right), \quad (2.10)$$

where the terms $S(x, t)$ and $\beta(\phi, \delta)$ include the stress relations mentioned above and are described in detail in [section 3.2](#) in [Chapter 3](#). The term S relates to the gravitational acceleration taking into account the curvature of the terrain and momentum correction due to the drag caused by centrifugal forces. While the term λ_{\pm} in [Equation 2.5](#) on [page 43](#) depends only on the internal friction angle ϕ , the term β is defined in terms of the friction angles ϕ and δ . The SH model is the first to define the earth pressure by both ϕ and δ for a granular material in an avalanche model ([Christian Kröner, 2014](#)). According to experimental data, [Hutter, Wang and Pudasaini \(2005\)](#) suggests the range of values for ϕ and δ are

$$30^\circ < \phi < 40^\circ, \quad 13^\circ < \delta < 22^\circ.$$

Like other models, the SH model received improvements and extensions over the years. The extension to curvilinear coordinates was expanded and tested by [Hutter and Koch \(1991\)](#) and [Greve and Hutter \(1993\)](#), which added small changes to the friction terms of the equations. [Greve, Koch and Hutter \(1994\)](#) and [Koch, Greve and Hutter \(1994\)](#) successfully extended the SH model to the three-dimensional case, later extended to curved terrains by [Gray, Wieland and Hutter \(1999\)](#), [Wieland, Gray and Hutter \(1999\)](#), [Pudasaini and Hutter \(2003\)](#). [Hungar \(1995\)](#) proposed an alternative strain-dependent (rate-dependent) constitutive law for the earth-pressure coefficient used in the SH model. See [Fei et al. \(2015\)](#) for a comparison between the SH and Hungar models. [Hwang and Hutter \(1995\)](#) incorporated the energy balance equation by bringing the elasticity of particles during collisions and allowing variable bulk density. Also considering inelastic collisions, [Takahashi and Tsujimoto \(1998\)](#) included snow flocculation and temperature to model dry and wet snow avalanches. [Gray, Tai and Noelle \(2003\)](#) simplified the SH model with constitutive relations inspired by the MSU model ([page 45](#)), obtaining a hydraulic model with a source term and constant earth-pressure coefficient. Their simplified version was used

by [Viroulet *et al.* \(2017\)](#) to investigate the take-off of the granular material due to bumps in the bed. [Zahibo *et al.* \(2010\)](#) also used a simplified version of the SH model, but to propose multiple analytical solutions for avalanche motion over different types of inclined channels. Recently, [Li and Zhang \(2019\)](#) used a finite volume scheme to solve the SH model equations over unstructured grids representing arbitrary terrains. Other relevant extensions and analogous models include [Iverson and Denlinger \(2001\)](#), [Denlinger and Iverson \(2004\)](#), [Luca *et al.* \(2009\)](#), [Gray and Edwards \(2014\)](#), [Zhai *et al.* \(2015\)](#), [Rauter *et al.* \(2018\)](#). In addition to snow and ice flows, the SH model has been adapted and used for other types of materials and avalanches, such as debris flows ([IVERSON, 1997](#); [MANGENEY-CASTELNAU *et al.*, 2003](#); [IVERSON; GEORGE, 2014](#); [GEORGE; IVERSON, 2014](#)), pyroclastic flows ([PITMAN *et al.*, 2003](#); [Lê; PITMAN, 2010](#); [DOYLE; HOGG; MADER, 2011](#)), and landslides ([LIU; HE; ONYANG, 2016](#)).

2.3.6 Slope Treatment

The hydraulic models cited earlier and others based on Saint-Venant's equations on [page 42](#) assume small slope terrains due to the averaged velocity condition over the flow depth. However, granular flows such as landslides and dense-snow avalanches often occur on steep slopes. Under global coordinates systems, the inherent presence of vertical velocities over a steep slope makes the pressure calculation not trivial as in the SWE ([NI; CAO; LIU, 2019](#)) — the reason why models, like the SH model, end up using local coordinates or curvilinear coordinates. Nevertheless, global coordinate systems are desired for simulating geophysical flows since the terrain is typically described by Digital Elevation Models (DEMs) defined in Cartesian coordinates systems ([XIA; LIANG, 2018](#)). [Tai and Kuo \(2008\)](#) used a unified coordinate system from [Hui, Li and Li \(1999\)](#) to account for dynamic bed curvatures and general topography. Over the years, many researchers attempted to solve the issue and adapt the SWE to arbitrary terrains with steep slopes and large curvatures ([BOUCHUT *et al.*, 2003](#); [LIANG; MARCHE, 2009](#); [JUEZ; MURILLO; GARCÍA-NAVARRO, 2013](#); [HERGARTEN; ROBL, 2015](#); [YUAN *et al.*, 2018](#); [DONG; LI, 2021](#)). Solutions include using different numerical methods, such as the Smooth Particle Hydrodynamics (SPH) and Finite Volume Method (FVM) ([LEVEQUE, 2002](#)). [Rodriguez-Paz and Bonet \(2005\)](#) adapted the SPH for SWE over arbitrary terrains. [Vacondio, Rogers and Stansby \(2012\)](#) presented a variational formulation for SWE under SPH obtaining high particle resolution in small flow depths. The flexibility of FVM for unstructured grids is the reason for its success in handling arbitrary terrain surfaces. Examples of solutions for the slope treatment with the FVM are [Hubbard \(1999\)](#), [Begnudelli and Sanders \(2006\)](#), [Benkhaldoun and Sead \(2010\)](#), [Song *et al.* \(2010\)](#), [Liu *et al.* \(2013\)](#), [Hou *et al.* \(2013a\)](#), [Hou *et al.* \(2013b\)](#), [Duran, Liang and Marche \(2013\)](#), [Xia and Liang \(2018\)](#), [Zhao *et al.* \(2018\)](#), [Buttinger-Kreuzhuber *et al.* \(2019\)](#). Another approach is the formulation of the equations in terms of surface partial differential equations (SPDEs) ([DECKELNICK; DZIUK; ELLIOTT, 2005](#)). The FVM adaptation to element areas called the Finite Area Method (FAM) ([TUKOVI; JASAK, 2012](#)) uses SPDEs to solve differential equations over geometric surfaces, such as thin

liquid films (CRASTER; MATAR, 2009), and flows over three-dimensional surfaces (RAUTER; TUKOVI, 2018). Recently, Rauter *et al.* (2018) solved the SH model with the FAM to simulate dense-snow avalanches over natural terrains.

2.3.7 Snow Entrainment

The difficulty encountered in experimental studies of bed erosion and entrainment mechanisms led researchers to use heuristic models for snow entrainment (ISSLER; PÉREZ, 2011). The typical approach appeared in the 60s along with the MSU model (page 45), considering front entrainment and gradual entrainment (EGLIT; DEMIDOV, 2005). Refer to Eglit and Demidov (2005), Eglit, Yakubenko and Zayko (2020), Grigorian and Ostroumov (2020) for Russian models of snow entrainment and Hopfinger (1983) for early entrainment models in western research. The MSU model considers entrainment in the front resulting from the impact force of the moving snow colliding with the snow cover at rest. The impact force p_i results from the encounter of the avalanche pressure forces p and the snow cover strength p_* . After the collision, if $p_* < p$, then the snow particles at rest get into motion and join the flow. The interface between the erodible snow and the flow, called *entrainment front*, advances at speed¹⁴:

$$u_e = \sqrt{\frac{p_i}{\rho_0(1 - \rho_0/\rho_1)}}, \quad p_i = p - p_*, \quad (2.11)$$

where ρ_0 is the snow cover density, ρ_1 is the avalanche density, p_* is the compressional strength of the snow cover, and p is the avalanche full pressure; see Figure 21 on page 55. Note that the direction of u_e is not necessarily parallel to the flow velocity u , as it is perpendicular to the entrainment front. The angle of the entrainment front $\alpha(x, t)$ is called the *abrasion angle*. According to Gauer and Issler (2004), erosion and abrasion causes a deceleration of the avalanche due to momentum transfer and hit impact. The deceleration force is given by

$$f_e = \frac{\rho_0}{\rho} \frac{\eta_e u_e u}{h}, \quad (2.12)$$

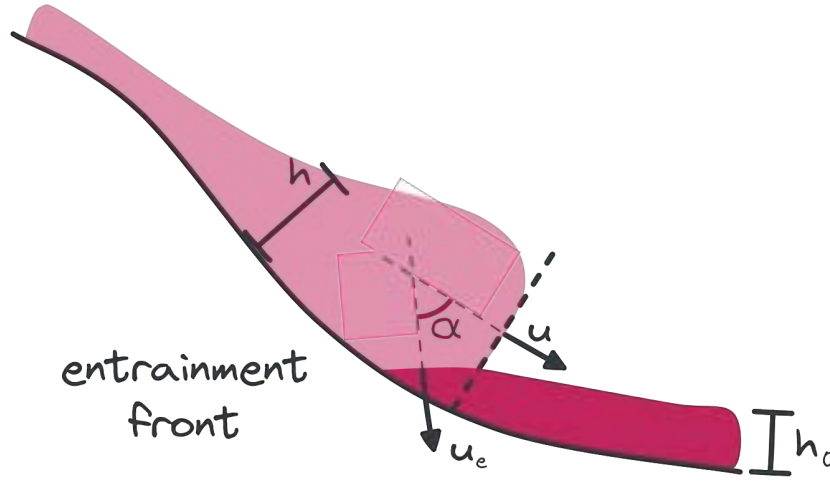
where η_e is the fraction of the eroded snow that is entrained. Gauer and Issler offer typical values for medium-size dry-snow avalanches on a $\theta = 30^\circ$ slope: $h \approx 1 \text{ m}$, $u \approx 30 \text{ m} \cdot \text{s}^{-1}$, $\rho/\rho_0 \approx 1 \sim 2$, and $\eta_e w_e \approx 0.05 \sim 0.10 \text{ m} \cdot \text{s}^{-1}$. Other examples of erosion speed formulas can be found in Issler (2014) — such as a version based on the abrasion angle $u_e = u \tan \alpha$ and another version based in the dry coulomb friction μ coefficient and flow velocity

$$u_e = \frac{2gh(\sin \theta - \mu \cos \theta)}{u}, \quad (2.13)$$

with $u_e \approx 10^{-3} \sim 10^{-2} \text{ m} \cdot \text{s}^{-1}$. Issler keeps the dense-flow depth h constant by considering that mass is skimmed from the top of the flow at the same rate it is eroded from bed.

¹⁴ The details about the definition of the erosion speed u_e can be found in Grigorian and Ostroumov (2020).

Figure 21 – Scheme of the avalanche front entrainment adopted by the MSU model. The entrainment front speed u_e is not necessarily parallel to the avalanche speed, as the entrainment front has an angle α .



Source: Adapted from Grigorian and Ostroumov (2020).

The MSU entrainment equations were incorporated into the SH model extension (BARTELT; SALM; GRUBER, 1999; SARTORIS; BARTELT, 2000) by Betty Sovilla in Sovilla, Burlando and Bartelt (2006), which also borrowed the constitutive equations from the NIS model (page 44). For a small control volume in the interface with cross-sectional area $A = wh$, where $w(x, t)$ is the flow width, the entrained mass m_e and entrainment depth d_e over a time period Δt are:

$$m_e = Au_f \rho_0 \Delta t, \quad d_e = u_f \frac{\rho_0}{\rho} \Delta t. \quad (2.14)$$

The mass balance equation is then defined as:

$$\frac{\partial A}{\partial t} + \frac{\partial Q}{\partial x} = S_e - S_d, \quad S_e = u_e \frac{\rho_0}{\rho} w, \quad S_d = C_d A, \quad (2.15)$$

where $C_d \in [0, 1]$ is the deposition coefficient, and S_e and S_d are the volumetric snow entrainment and deposition rates respectively. The deposition rate is considered zero if velocity is above a critical value and implementations usually consider $C_d = 1$. The term $Q = Au$ is called the *depth-averaged discharge flow*. Sovilla went further and considered multi-layered snow covers, allowing the abrasion angle to vary from layer to layer. The multilayer entrainment approach allows not only frontal plowing but also step entrainment. The collection of works of Betty Sovilla are among the most prominent and relevant studies in mass entrainment and deposition in snow avalanches (SOVILLA, 2004; SOVILLA; BURLANDO; BARTELT, 2006; SOVILLA; MARGRETH; BARTELT, 2007; LI *et al.*, 2022).

A detailed review of erosion rate formulas can be found in Iverson and Ouyang (2015), including formulas for other mass flow phenomena such as debris and pyroclastic flows (PITMAN *et al.*, 2003). Naaim *et al.* (2004) considers a thin layer, representing the entrainment front, upon which a series of forces from both sides operate. The erosion of this thin layer happens in two

stages: first, the cohesion breaks up due to disintegration, and then entrainment occurs by the progressive motion of snow portions. Such an approach finds good agreement with experimental data (NAAIM *et al.*, 2013). Fischer *et al.* (2015) uses the basal shear stress τ_b to compute the entrainment rate as

$$S_e = \frac{\tau_b}{e_b} \| u \|, \quad (2.16)$$

where e_b is a parameter interpreted as specific erosion energy. Recently, Edwards *et al.* (2021) deviated from the heuristic models described above by successfully incorporating the friction coefficient from Baker, Barker and Gray (2016) to simulate erosion and deposition. For simulation validation purposes, erosion S_{er} , deposition S_d and entrainment S_e rates were quantitatively analyzed by Li *et al.* (2022) through the following numerical measurements:

$$S_e = \frac{m_e}{A_{bed}\Delta t}, \quad S_{er} = \frac{m_{er}}{A_{bed}\Delta t}, \quad S_d = \frac{m_d}{A_{bed}\Delta t}, \quad (2.17)$$

where A_{bed} is the initial surface area of the erodible bed and m_{er} , m_e , and m_d are the eroded mass, entrained mass, and deposited mass respectively.

2.3.8 Other Models

The historical review above covered models of dense-snow avalanches considered by many researchers as the most popular in avalanche research. The relation between such models is evident; each model shares at least one aspect, and the centenary sequence of models that starts with sliding blocks in the 1920s, expanding with Voellmy's work, the VS model and its extensions, culminating along with Russian hydraulic models and the granular flow SH model represent only the main trunk of avalanche research. Therefore, this section concludes with a list of models that, although omitted above, are equally relevant.

- **Conceptual Models**

The class of conceptual models found in-between deterministic and statistical models is investigated by Ancy, Meunier and Richard (2003). Such models use statistical and probabilistic analysis to specify coefficient parameters of deterministic models (BARBOLINI *et al.*, 2000; ANCEY; GERVASONI; MEUNIER, 2004; MEUNIER; ANCEY, 2004). The fracture mechanics theory (CORTEN, 1972) is used by Cherepanov and Esparragoza (2008) to stipulate the conditions for a fracture-entrainment regime in order to model step entrainment. The treatment of the snow avalanche as a non-Newtonian fluid was approached by Bovet, Chiaia and Preziosi (2010), Abdelrazek, Kimura and Shmizu (2014).

- **The Random Kinetic Energy Model**

The Random Kinetic Energy model (RKE) (BARTELT; BUSER; PLATZER, 2006) describes the frictional forces acting on an avalanche from the perspective of energy production and dissipation by granular motion (BUSER; BARTELT, 2009). The RKE borrows the

fluctuation-dissipation relationship of kinetic energy dissipation and the random motion of granules (LEMONS, 2003). Such an approach allows the variation of energy density (usually assumed constant) along the avalanche length, allowing more realistic modeling of entrainment and deposition (CHRISTEN; KOWALSKI; BARTELT, 2010). Valero *et al.* (2015) extended the RKE for accounting for temperature effects and thermal entrainment. A review of RKE-based models and a comparison against the classical Voellmy's friction model is provided by Issler, Jenkins and McElwaine (2018). The RKE model has been used in conjunction with the SH model equations in full — with entrainment modeling — three-dimensional simulations of snow avalanches (FISCHER *et al.*, 2015; RAUTER; TUKOVI, 2018; RAUTER; KöHLER, 2020).

2.4 Powder-Snow Avalanche Models

Powder-snow avalanches, or airborne powder avalanches, belong to the large family of physical phenomena of particle-driven currents called gravity currents (SIMPSON, 1999). Gravity currents occur when two fluids of different densities get into motion due to gravity, promoting the intrusion and propagation of one fluid into another (UNGARISH, 2009). Gravity currents comprise a wide range of flows, from viscous magma to turbulent atmospheric currents, from heat flows inside tunnels to enormous sediment movements under the ocean. Some flows, such as katabatic winds, present minimal density ratios, while others may display more significant differences. Powder-snow avalanches are an example of complex gravity currents due to their multi-scale, non-conservative, highly-turbulent nature. Similar gravity currents include turbidity currents on ocean floors and pyroclastic flows on volcano slopes. Refer to Simpson (1999), Huppert (2006), Parsons *et al.* (2007), Ungarish (2009), Meiburg, Radhakrishnan and Nasr-Azadani (2015) for reviews on gravity current research. Particularly for powder–snow avalanches, refer to Ancey (2016).

Despite the fundamental differences between powder–snow avalanches and turbidity currents, experimental research on powder–snow avalanches has used turbidity currents as a fair analogy. Like powder–snow avalanches, turbidity currents are non-conservative, turbulent (high Reynolds number values), and particle-driven flows. Turbidity currents also present mass entrainment by deposition and suspension of particles and entrainment of ambient fluid. Early models start with the pioneering work of Bagnold (1954) on the dispersion of sediments in fluids. Turbidity currents were firstly modeled with depth-averaged equations by Plapp and Mitchell (1960). Bagnold (1962) investigated the conditions which enable a turbidity current to maintain its flow based in terms of turbulent energy. Bagnold referred this process as *auto-suspension*. Later, Pantin (1979) revisited Bagnold's work and showed that erosion and deposition of the bed material can lead to the self-acceleration of the turbidity current, for what Parker (1982) called *ignition*, but neglected entrainment of water. Refer to Wells and Dorrell (2021) for a recent detailed discussion on the relationship of turbulence and entrainment/deposition processes

turbidity currents.

A crucial deviation from turbidity currents models relates to the densities of the fluids involved. Turbidity currents models (MEIBURG; RADHAKRISHNAN; NASR-AZADANI, 2015)(OUILLOON; MEIBURG; SUTHERLAND, 2019) use the Boussinesq approximation (BOUSSINESQ, 1903) since the difference between sediment and water densities is sufficiently small. For powder–snow avalanches, the difference between powder–snow and air densities invalidates the Boussinesq assumption (HOPFINGER, 1983). Non-Boussinesq¹⁵ models for gravity currents can be found in (BIRMAN; MEIBURG, 2006; BARTHOLOMEW; LAIZET, 2019).

Since gravity current flows comprise two or more fluids with different densities, equations use indices to specify properties for each fluid, for example, densities ρ_0 and ρ_1 ; see Figure 22 on page 59. Typically, letters can be used instead to facilitate reading, such as a and s , standing for air and snow respectively, as in ρ_a and ρ_s . Models may use different approaches to deal with multiple fluids by considering:

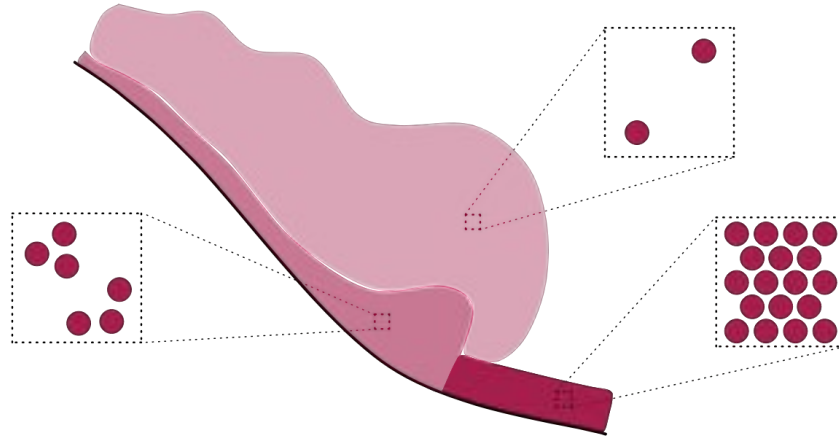
- *two–phase flows* – A set of equations models the different fluid types in the flow – one balance equation for each fluid type, such as air and ice. As mentioned above, the equations use separate variables for density, velocity, and others for each fluid type. Also, such equations usually contain additional terms representing the exchange of mass and energy between fluids;
- *single–phase mixture flows* – Instead of a separate equation for each fluid type, a single set of equations models the mixture of fluids. In such an approach, some variables are combined based on the volume concentration of each fluid. For example, the final value of density becomes an interpolation of the densities of all fluids. The mixture representation reduces the number of equations drastically.

This section separate the powder–snow avalanche models into the following categories:

- *Similarity Models* – described in subsection 2.4.1 on page 59. Also called *conceptual models*, attempt to describe the flow through relations between flow quantities, such as velocity and depth, using dimensional analysis. Therefore, similarity models are more of a tool rather than a category of models since other types of models can use the same relations provided by conceptual models;
- *two–phase flows* – described in subsection 2.4.2 on page 63 and briefly introduced above;
- *single–phase mixture flows* – described in subsection 2.4.3 on page 66 and briefly introduced above.

¹⁵ For non-Boussinesq flows, the inertia created from the density differences is not negligible since the denser fluid carries the most momentum, even with little concentrations per volume.

Figure 22 – Representation of the different densities present in a powder–snow avalanche. Particles of snow differ in density as snow is suspended and mixed with air. The snow cover contains a high density of packed particles that get compressed as the avalanche runs over it or separate into smaller clods and get incorporated into the dense flow. As turbulence and impact forces eject snow into the air, particles get mixed with air and become much less dense. Models deal with the different densities of snow by considering distinct phases or a single–phase mixture with air based on the volume concentration of particles.



Source: Elaborated by the author.

The use of similarity theory in avalanche models refers to the use of non-dimensional numbers and variables to model the flow. The dimensional analysis produces similarity criteria to validate experiments and physical models; see [section 2.2](#) on [page 30](#). Also, the scaling factors allow the use of simpler models and still offer critical insights into the dynamics of such flows with large extensions in space and time ([ECKART MCELWAINE JIM, 2012](#)) — turbidity currents, for example, can cover distances of thousands of kilometers and last for days ([MOSHER *et al.*, 2017](#)). [Rottman and Linden \(2002\)](#) discusses the use of dimensional analysis in gravity current models.

2.4.1 Similarity Models

The first quantitative study — towards a mathematical model — of gravity currents is attributed to von Kármán in 1940 ([KARMAN, 1940](#)); his studies of dense gas cloud propagation suggested that the velocity of the nose u_f is given by

$$\frac{u_f}{\sqrt{g'h}} = \sqrt{\frac{2}{\Delta\rho}} = Fr, \quad (2.18)$$

where h is the front depth, $g' = \Delta\rho g / \rho_1$ is the reduced gravity acceleration (recall the density ratio $\Delta\rho$ from [page 34](#)), and Fr is the Froude number, related to the densimetric Froude number in [page 34](#). Later, [Benjamin \(1968\)](#) revised the formulation, considering the ambient fluid's height H , see [Figure 23](#) on [page 60](#), and obtained the following equation:

$$\frac{u_f}{\sqrt{g'h}} = \sqrt{\frac{\alpha(1-\alpha)(2-\alpha)}{\Delta\rho(1+\alpha)}} = Fr_H, \quad (2.19)$$

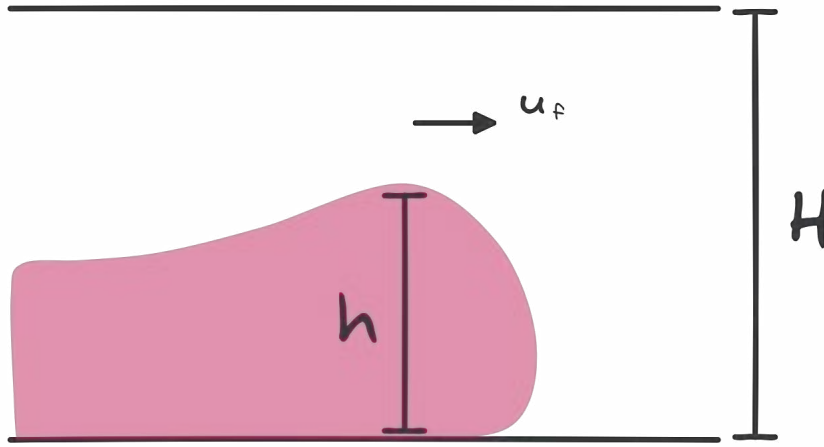
where $\alpha = h/H$ is the fractional height. Note that the Froude number is related to Benjamin's Froude number by $Fr = Fr_H \alpha^{-1/2}$. Benjamin's work is considered the base of the theory of inviscid gravity currents and has been used for gravity currents propagating with a high Reynolds number (HUPPERT, 2006). The formulation of the Froude number as a function of height was later extended to Boussinesq flows by Borden and Meiburg (2013) and non-Boussinesq flows by Konopliv *et al.* (2016) with the relations

$$Fr_H = \sqrt{2\alpha}(1 - \alpha), \text{ and } Fr_H = \sqrt{\frac{2\alpha}{\Delta\rho}}(1 - \alpha), \quad (2.20)$$

respectively. Gröbelbauer, Fanneløp and Britter (1993) proposed a correction of the reduced gravity term for higher density ratios

$$g' = g \frac{\rho_1 - \rho_0}{\rho_1 + \rho_0}. \quad (2.21)$$

Figure 23 – Visual representation of the gravity flow lock–exchange experiment considered by Benjamin: A channel with finite depth H filled with a light density fluid with density ρ_0 . A gravity current of head height h advances with velocity u_f as the heavier fluid of density ρ_1 is released and moves due to the hydrostatic pressure difference.



Source: Elaborated by the author.

The Froude number has also been used to determine cloud formation in powder–snow avalanches. Early studies suggest that suspension occurs due to a combination of kinematic–dynamic shocks and weak intergranular bounds (HOPFINGER, 1983). After achieving a velocity of 10 m/s and the Froude number $Fr > 2$, roll-wave formation occur. The wavelength λ of roll waves is estimated by Brock (1967) as

$$\frac{\sin \theta \lambda}{Fr^2 h} \sim 0.2 - 0.5. \quad (2.22)$$

The mechanisms of formation and dynamics of cloud lobe structures in gravity currents are the center of the study of plume theories (MORTON; TAYLOR; TURNER, 1956; ELLISON;

TURNER, 1959; TURNER, 1973). Tochon-Danguy and Hopfinger (1975), Hopfinger and Tochon-Danguy (1977) extended the theory to powder–snow avalanches. Following the posterior formulation of Britter and Linden (1980), the front velocity is dependent only on the buoyancy flux $g'Q$ and defines the non-dimensional front velocity \tilde{u}_f as

$$\tilde{u}_f = \frac{u_f}{(g'Q)^{\frac{1}{3}}}, \quad (2.23)$$

where $Q = u_f h_e$ is the volume flow rate of supply and h_e is the height of entrained snow cover. The plume theory for an inclined plume defines the mass continuity equation:

$$\frac{d(\bar{u}h)}{dx} = \alpha\bar{u}, \quad (2.24)$$

where $\bar{u}(x, t)$ is the mean velocity in the slope direction x and α is the air-entrainment coefficient. For steady flows, the following relation is obtained through integration

$$h = \alpha\bar{u}(t - t_0), \quad (2.25)$$

where t_0 is the start time with $h(t_0) = 0$. A semi-ellipses represent the plume with volume evolution of

$$V = E\bar{u}^3(t - t_0)^3, \quad E = \frac{\pi\alpha^2}{2}, \quad (2.26)$$

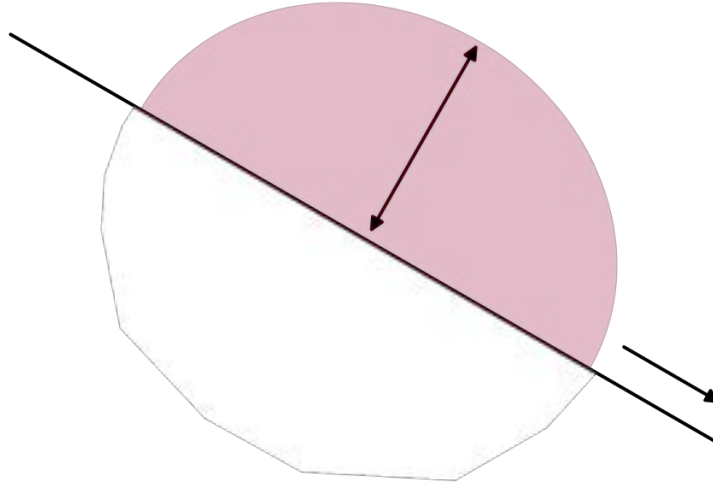
where E is the effective air-entrainment coefficient; see Figure 24 on page 62. Later, Parker, Fukushima and Pantin (1986) generalized the entrainment process from Ellison and Turner (1959) to build a system of depth-averaged equations that takes into account both sediment and water entrainment in turbidity current flows. Stacey and Bowen (1988) considered the vertical structure of the flow by studying the relations between the Richardson number and the settling velocities of suspended particles. Baines (2001) provided an extended model, along with laboratory experiments, considering the mixing process due to entrainment in gravity currents flowing down slopes. Such models consider the powder–snow avalanches similarly to other gravity current flows, particularly turbidity currents. These models can handle the multi-scale nature of gravity flows through dimensional analysis. Despite their success, internal flow properties, such as velocity profiles and turbulent motion, are often omitted or approximated by coefficient terms.

The Kulikovskii–Sveshnikova model (KULIKOVSKII; SVESHNIKOVA, 1977), the KS model, steps forward by considering the flow as a turbulent flow of a material in suspension. The KS model includes a volume change equation and momentum conservation equations considering the kinetic energy generated from turbulence. For a two–dimensional semi-elliptic cross-section powder–snow avalanche, the KS model system of balance equations is:

$$\frac{dA_e}{dt} = \frac{Peu_a}{2}, \quad (2.27)$$

$$\frac{d\tilde{m}}{dt} = \rho_a \dot{A}_e + \dot{m}_e + \dot{m}_d, \quad (2.28)$$

Figure 24 – Similarity models usually model the powder–snow avalanche as a geometrical shape — as the half-ellipse. The equations describe the movement of the ellipses based on the center of mass. The growth due to air entrainment is calculated through the ellipse perimeter..



Source: Elaborated by the author.

$$\frac{d(\tilde{m}u)}{dt} = \tilde{m}g \sin \theta - \rho k 2Lu^2 - \frac{c_x \rho_a H u^2}{2} - \dot{m}_a u, \quad (2.29)$$

$$\frac{d}{dt} \left(\frac{\partial K}{\partial \dot{H}} \right) - \frac{\partial K}{\partial H} = Q + \xi \dot{u}_a. \quad (2.30)$$

Equation 2.27 describes the change of volume due to turbulent mixing of surrounding air; A_e is the area of the semi-elliptic shape representing the cloud volume, P_e is the perimeter, and u_e the velocity of air-entrainment. Equation 2.28 represents the change of mass per unit length, \tilde{m} ; ρ_a is the air density and the right hand side terms are respectively the entrainment of air, snow entrainment, and snow deposition. Equation 2.29 is the change of momentum defined by the gravitational acceleration, the turbulent friction, the air resistance and snow deposition; $\rho = \tilde{m}/A_e$ is the average density of the snow-air mass, c_x is the coefficient of aerodynamic resistance of the cloud, and L_e and H_e are the horizontal and vertical semi-axis of the ellipse; see Figure 24 on page 62. The last equation, Equation 2.30, relates to the internal motion in the cloud; K is the kinetic energy, Q is the generalized force, and ξ is the turbulent diffusion coefficient. Refer to Bozhinskiy, Losev and Bartelt (1998), Ancy (2001), Eglit and Demidov (2005), Eglit, Yakubenko and Zayko (2020) for comparisons and discussions on the KS model.

The KS model received many adaptations and extensions over the years. Beghin (1979), Beghin and Brugnot (1983) simplified the model by discarding entrainment and reduced the system to only one differential equation. Beghin, Hopfinger and Britter (1981) introduced the dependence of the slope angle into the growth rate of the cloud and ignored Equation 2.30 in order to model Boussinesq clouds. Decades later, Ancy (2004) combined the KS model with the simplifications introduced by Beghin, calling the extension the KSB model. Ancy used the KSB model to simulate powder–snow avalanches by adapting the KSB model to non-Boussinesq

clouds and also including an entrainment function dependent to the Richardson number¹⁶ Ri :

$$\frac{dV}{dt} = \alpha_v \sqrt{V} u, \quad \alpha_v = \begin{cases} e^{-1.6 Ri^2} & Ri \leq 1, \\ 0.2/Ri & Ri > 1, \end{cases} \quad (2.31)$$

where α_v relates to the entrainment coefficient. [Turnbull, McElwaine and Ancey \(2007\)](#) further improved the KSB model by including the entrainment of snow in the volume equation to better predict densities with an extra term in

$$\frac{dV}{dt} = \alpha_v \sqrt{V} u + u_f h_e, \quad (2.32)$$

where h_e is the depth of entrained snow cover. In parallel, [Parker, Fukushima and Pantin \(1986\)](#) incorporated the turbulence and entrainment terms into plume theories to model turbidity currents. However, the methods of turbidity currents assume that water and sediment entrainment at the current upstream end (tail) is continuous. This assumption does not hold for powder–snow avalanches ([FUKUSHIMA; PARKER, 1984](#)). The discontinuity was handled by [Fukushima and Parker \(1990\)](#), that added the conservation of kinetic energy of turbulence and entrainment of snow and air, as previously mentioned, to simulate powder–snow avalanches. Their depth-averaged method was based on the important work of [Fukushima \(1986\)](#), which also considers the shape of the avalanche to be a cylinder of half-elliptic section and assumes the avalanche does not show significant transverse spreading. An extension of the model for arbitrary three-dimensional terrains was later proposed by [Fukushima and Hayakawa \(1993\)](#). The method was later applied to model the flow of suspension thermals by [Akiyama and Ura \(1999\)](#), [Fukushima, Hagihara and Sakamoto \(2000\)](#). [Turnbull and Bartelt \(2003\)](#) used Parker’s model to study the exchange of mass due to entrainment and deposition in powder–snow avalanches. [Rastello and Hopfinger \(2004\)](#) included snow entrainment by proposing the rate of particle suspension as a function of the shear stress and particle Reynolds number.

All models so far model the powder–snow avalanche as a finite volume of a homogeneous turbulent suspension of ice particles. The simplified representations in similarity models, including the KSB model and its ramifications, use geometrical shapes — such as the half-ellipse — to describe the avalanche cloud. Also, such models are restricted to steady flows or only certain avalanche regimes (usually the flow regime). However, most real powder–snow avalanches contain dynamic layers of variable density. In particular, the front region and the layer close to the bed surface present much greater densities than the rarefied snow–air cloud.

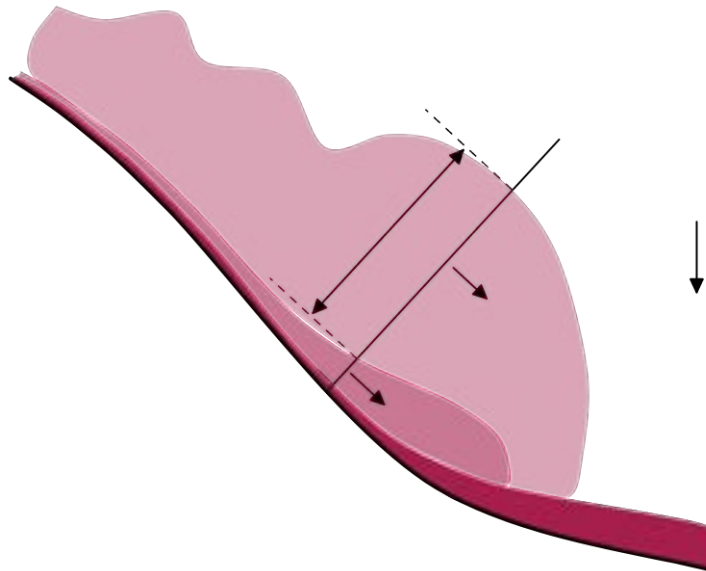
2.4.2 Two-Phase Models

The class of models, called *two-phase*, *two-layer* or *mixed avalanche* models, treats the flows of the powder cloud (PSL) and dense snow (DSL) layers separately and models the

¹⁶ Smaller Richardson number values imply greater instabilities and therefore higher entrainment rate ([ANCEY, 2016](#)).

intricate mechanisms of mass exchange between them — although the term two-phase¹⁷ is usually applied to models that split the PSL into two phases, a phase for air and the other for ice. Figure 25 on page 64 depicts the general scheme of mixed snow avalanches adopted by such models; besides air, labeled by the letter a , the numbers 0, 1, and 2 label the snow cover, the dense core, and the powder cloud layers, respectively. Each layer i has density ρ_i , velocity u_i and height (depth) h_i .

Figure 25 – Representation of a multi-layered scheme of powder-snow avalanches utilized by mixed avalanche models. The snow cover has height h_0 , density ρ_0 , and no velocity. The only term related to air is its density ρ_a . The other layers, 1 and 2, representing the dense snow core and the powder-snow cloud, respectively, have heights h_i , densities ρ_i , and velocities u_i . A different set of equations models each avalanche layer, 1 and 2, and additional terms describe the mass and momentum exchange between both layers and include the role of air and snow cover as entrainment sources.



Source: Adapted from Nazarov (1991).

Early two-layer Russian models (EGLIT, 1983; NAZAROV, 1991), reviewed by Eglit (1998a), Eglit, Yakubenko and Zayko (2020), use five balance equations for the PSL and DSL and a set of variables to control mass exchange between layers. For instance, the respective continuity equations for the PSL and DSL flows are:

$$\frac{\partial h_2}{\partial t} + \frac{\partial h_2 u_2}{\partial x} = V_{2a} + V_{21} - V_s, \quad (2.33)$$

$$\frac{\partial h_1}{\partial t} + \frac{\partial h_1 u_1}{\partial x} = -V_{21} + V_{10} + V_s, \quad (2.34)$$

¹⁷ The term two-phase has a broader meaning in fluid mechanics, such as the characterization of two or more fluids with a defined interface between them. However, some avalanche models consider the mixture of fluids with no separating interface. Refer to (PROSPERETTI; TRYGGVASON, 2007) for a formal definition of multiphase flows. In this text, the terms two-phase and two-layer should clarify the distinction.

where $V_{i \leftarrow j}$ are rates of change in height due to transport of mass from layer j towards layer i ; V_{2a} is the effect of air entrainment in the powder cloud layer, V_{21} and V_{10} are for snow entrainment into the PSL and DSL, and V_s is for snow sedimentation/deposition. The consumption of the snow cover due to entrainment is then given by

$$\frac{\partial h_0}{\partial t} = -V_{10}. \quad (2.35)$$

The terms V_{ij} are defined as

$$V_{2a} = m_a u_2 \rho_{2a}^*, \quad (2.36a)$$

$$V_{21} = m_{12} |u_2 - u_1| \rho_{21}^*, \quad (2.36b)$$

$$V_{10} = m_{01} |u_1| \rho_{10}^*, \quad (2.36c)$$

$$\rho_{ij}^* = \frac{\sqrt{\rho_i \rho_j}}{\rho_i + \rho_j}, \quad (2.36d)$$

where m_a and m_{ij} are empirical coefficients. Equations 2.36a to 2.36c mean that the rate of growth depends on the velocity difference and a combination of densities of the layers. Equations 2.36b and 2.36c work only for $h_1 > 0$ and $h_0 > 0$, respectively. The complete set of equations also include conditions for $h_j = 0$ and $x > x_f$, where x_f is the leading front of the DSL position. The momentum equations for each layer also use terms τ_{ij} to represent friction forces between layers; see Eglit (1998a).

Another approach uses the differential equations of continuum mechanics with the addition of terms of exchange of mass and momentum between phases. Scheiwiller (1986) considers the mixture of two incompressible fluids, air and powder snow cloud, occupying fractions of volume¹⁸ $c(x, t)_i$, so density is given by

$$\rho_i = c_i \hat{\rho}_i, \quad \sum_i c_i = 1, \quad (2.37)$$

where $\hat{\rho}_i$ is the material density of phase i . Scheiwiller starts from the balance equations

$$\frac{\partial \rho_i}{\partial t} + \nabla \cdot (\rho_i \mathbf{u}_i) = 0, \quad (2.38)$$

$$\frac{\partial \rho_i \mathbf{u}_i}{\partial t} + \nabla \cdot (\rho_i \mathbf{u}_i \otimes \mathbf{u}_i) = \nabla \cdot \boldsymbol{\tau}_i + \rho_i f_i + M_i, \quad (2.39)$$

$$\sum_i M_i = 0, \quad (2.40)$$

where M_i is the momentum transferred to phase i , $\boldsymbol{\tau}_i$ is the Cauchy stress tensor of phase i , and f_i is the body force of phase i . Equation 2.40 dictates that no momentum is produced by transfer

¹⁸ The particle volume fraction c_p in a two-phase flow is the ratio between the part of the volume V_p that contains the particles of one phase and the volume V itself, i.e., $c_p = \lim_{V \rightarrow 0} V_p/V$ (ZWINGER; KLUWICK; SAMPL, 2003).

processes and Equation 2.38 implies ρ_i constant. Also, due to incompressibility, pressure p can be separated from the constitutive equations and the stress tensor becomes

$$\tau_i = -c_i p I + t_i, \quad (2.41)$$

where the deviatoric tensor t_i is given by a constitutive relation. Equations 2.38 and 2.39 can be rewritten as

$$\frac{\partial c_i}{\partial t} + \nabla \cdot (c_i \mathbf{u}_i) = 0, \quad (2.42)$$

$$\frac{\partial c_i \mathbf{u}_i}{\partial t} + \nabla \cdot (c_i \mathbf{u}_i \otimes \mathbf{u}_i) = \nabla \cdot \gamma_i + c_i f_i + \frac{M_i}{\hat{\rho}_i}, \quad (2.43)$$

where γ_i accounts for stresses. Scheiwiller also includes eddy viscosity and laminar viscosity into the stress tensor in order to account for turbulence by using the so-called k - ε -model (LAUNDER; SPALDING, 1974). For a complete formulation and details refer to Issler *et al.* (2000). Naaim (1995) compared the model simulation to experimental data. Later, Naaim and Gurer (1998) modified the model to account for turbulence reduction induced by particles using the turbulence model of Chen and Wood (1985). Romanova (2017) used a similar model, which considered two-phase with the k - ε model, using the Herschel-Balkley fluid model (KERN; TIEFENBACHER; MCELWAINE, 2004) to describe the constitutive relations of snow.

Recently, LEPERA (2020) proposed a complete system of equations for a two-phase model of powder-snow avalanches. The model includes thermodynamic balance equations and treats the energy transfer between phases. The equations come from granular flow models and split the stress tensor into a collisional and a frictional part. See Andreotti, Forterre and Pouliquen (2013) for details on the theory used in the model.

2.4.3 Single-Phase Mixture Models

The Continuum Mixture Theory (CMT) (ATKIN; CRAINE, 1976), briefly described in section A.2, models the mixture of fluids by considering the superposition of multiple single continua that represent the mixing fluids (constituents). Particles of all participating fluids (phases) can occupy the volume simultaneously. The occupancy of particles represented by fractions of volume becomes a central concept and determines the mass of constituents present in a particular volume.

The model of Scheiwiller, previously described on page 65, use the exact same concept. The final density given by Equation 2.37 receives the name of mixture density in the CMT context, and the same may apply to any other variable. Therefore, by assuming a mixture velocity, for example, the number of momentum equations can be reduced to one instead of using a separate equation for each constituent. One example of such an approach is the model of Dutykh, Acary-Robert and Bresch (2009), which restricted both phases to share the same velocity \mathbf{u} and defined the mixture density ρ and dynamic viscosity μ as

$$\rho = c\rho_s + (1 - c)\rho_a, \quad \mu = c\rho_s\nu_s + (1 - c)\rho_a\nu_a = \mu_0 + \bar{\nu}\rho, \quad (2.44)$$

where $c = c_s$ is the volumetric concentration of snow particles in the cloud, the coefficients v_i are the kinematic viscosities of air and snow, and μ_0 and \bar{v} are

$$\mu_0 = \frac{v_a \rho_a \rho_s - v_s \rho_s \rho_a}{\rho_s - \rho_a}, \quad \bar{v} = \frac{v_s \rho_s - v_a \rho_a}{\rho_s - \rho_a}. \quad (2.45)$$

Fick's law dictates that the mixing of fluids follows a quasi-compressible constitutive equation

$$\nabla \cdot \mathbf{u} = -\nabla \cdot (\kappa \nabla \log \rho), \quad (2.46)$$

where κ is a coefficient related to the kinematic viscosity. In other words, the equation above accounts for diffusive effects between the constituents (phases) due to density differences. From Equation 2.46, Dutykh, Acary-Robert and Bresch (2011) rewrites the equations into an incompressible system following the approach of Kazhikhov and Smagulov (1977) and using a new variable for velocity

$$\mathbf{v} = \mathbf{u} + \kappa \nabla \log \rho, \quad (2.47)$$

referred as *the fluid volume velocity*, and taking $\kappa = 2\bar{v}$ constant. The new system of equations is

$$\nabla \cdot \mathbf{v} = 0, \quad (2.48)$$

$$\frac{\partial \rho}{\partial t} + \mathbf{v} \cdot \nabla \rho = 2\bar{v} \Delta \rho, \quad (2.49)$$

$$\rho \frac{\partial \mathbf{v}}{\partial t} + \rho (\mathbf{v} \cdot \nabla) \mathbf{v} = -\nabla \pi - 2\bar{v}' \nabla \mathbf{v} \nabla p + 2\bar{v} \nabla \rho \nabla \mathbf{v} + \rho \mathbf{g} + \nabla \cdot (2\mu \mathbb{D}(\mathbf{v})), \quad (2.50)$$

where $\mathbb{D}(\mathbf{v})$ is the strain rate tensor

$$\mathbb{D}(\mathbf{v}) = \frac{1}{2} (\nabla \mathbf{v} + (\nabla \mathbf{v})^T), \quad (2.51)$$

the gravitational acceleration is projected into local coordinates $\mathbf{g} = (g \sin \theta, -g \cos \theta)$, and $\pi(x, t) = p + 4\bar{v}\mu_0 \Delta \log \rho$ is the pressure term. Notice that when $\kappa = 0$, the whole system falls back to the classical Navier-Stokes equations for incompressible fluids in u . A detailed analysis on the numerical methods and the model can be found in Calgato, Creusé and Goudon (2015). An approximation of the mixture model to powder-snow avalanches assuming the Boussinesq regime was presented by Étienne, Saramito and Hopfinger (2004). Recently, Gurjar (2023) proposed a 2D framework extending the work of Bartelt *et al.* (2016) for the DSL and combined with the mixture modeled by Fick's law by Dutykh, Acary-Robert and Bresch (2011) mentioned above.

Some models extend dense-snow avalanche models to support the formation of the powder-snow cloud on top of the dense flow layer by coupling two separate models. For example, Bartelt, Kern and Christen (2000) uses the VS model (see page 43) to simulate the dense core but includes a term for suspension in the mass conservation equation to feed the PSL. A simplification of Parker, Fukushima and Pantin (1986) models the PSL, and the suspension term enters as a mass entrainment term in the equations. In turn, Zwinger, Kluwick and Sampl

(2003) uses a modified version of the SH model (see page 52) — imposing another condition to the normal stress at the bottom — and a modification of the k - ε turbulence model for the powder–snow layer. The momentum balance is similar to Equation 2.39 on page 65, but as in the single mixture model, the particle volume fraction defines the mixture density, and the velocity is the same for both phases:

$$\frac{\partial \rho \mathbf{u}}{\partial t} + \nabla \cdot (\rho \mathbf{u} \otimes \mathbf{u}) = -\nabla \cdot p + \nabla \cdot \bar{\boldsymbol{\tau}} + \nabla \cdot \boldsymbol{\tau}^{Rey} + \rho \mathbf{g}, \quad (2.52)$$

where pressure and stress are split, as mentioned earlier with equation Equation 2.41, p is the static pressure. The stress tensor is also decomposed into mean values of the viscous stress $\bar{\boldsymbol{\tau}}$, and the turbulent Reynolds stresses $\boldsymbol{\tau}^{Rey}$ defined as

$$\tau_{ij}^{Rey} = \mu_{tur} \cdot \left(\frac{\partial u_i}{\partial x_j} + \frac{\partial u_j}{\partial x_i} \right) - \frac{2}{3} \left(\mu_{tur} \frac{\partial u_k}{\partial x_k} + \rho k \right) \delta_{ij}, \quad (2.53)$$

$$\mu_{tur} = C_\mu \rho \frac{k^2}{\varepsilon}, \quad (2.54a)$$

where C_μ is a constant with value 0.09, δ_{ij} is the Kronecker delta function, k is related to the turbulent kinetic energy and ε to its dissipation — both variables also receive balance equations. The transfer of mass and momentum between the DSL and the PSL occurs in a thin region close to the lower bounding surface of the PSL, referred to by Zwinger et al. as the *re-suspension layer* — later named *transition layer* by Sampl and Granig (2009). The model of the transition layer is a set of boundary conditions rather than another flow layer. Such boundary conditions consider the DSL upper surface as a solid wall, and the turbulent particle volume flux at the wall j_{wall} is

$$j_{wall} = -\frac{\tau_{wall}}{\rho} \frac{1}{Sc_{tur}} \frac{\Delta c}{\Delta \mathbf{u}}, \quad (2.55)$$

where τ_{wall} is the local wall shear stress, $\Delta \mathbf{u}$ is the mean velocity difference based on the wall distance and the von Kármán constant, Δc is the volume concentration difference also based on wall distance and density, and Sc_{tur} is the turbulent Schmidt number. A brief introduction and application of the model can be found in Sampl and Zwinger (2004).

2.4.4 Entrainment

Snow entrainment and deposition play a central role in powder–snow avalanches. The roll motion of large structures causes air entrainment, which increases the volume of the cloud. In the front, the transfer of momentum due to air entrainment results in significant drag (ÉTIENNE; SARAMITO; HOPFINGER, 2004) — the cause of turbulence and suspension of snow from lower layers. In turn, snow entrainment from turbulent suspension and snow cover disintegration due to front impact is crucial to momentum transport. Deposition, on the other hand, settles down snow and dissipates energy.

Issler (1998) considers a lower saltation layer, labeled 12 following Nazarov's scheme in Figure 25 on page 64, responsible for the mass exchange in the powder–snow avalanche. The depth of the saltation layer h_{12} is given by

$$h_{12} = \beta_0^2 \frac{u_{12}^2}{2g'} \quad (2.56)$$

where $g' = g \cos \theta$, $\beta_0 = O(0.1)$ is a constant extracted from experimental data, and U is the velocity of the layer. The balance of mass for the saltation layer is governed by the rates of erosion Q_{erod} , sedimentation Q_{sed} , suspension Q_{susp} , and settling Q_{sett} :

$$\frac{\partial(h_{12}\rho_{12})}{\partial t} + \nabla \cdot (h_{12}\rho_{12}u_{12}) = Q_{erod} - Q_{sed} - Q_{susp} + Q_{sett}, \quad (2.57)$$

where $\rho_{12} = 20 \sim 50 \text{ kg/m}^3$ is the density of the saltation layer. Issler describes the mass exchange as a cycle between the suspension and saltation layers represented by particle concentrations from both layers. Such cyclic movement comes from the circling motion caused by turbulent eddies; particles keep getting ejected and settled in the saltation layer — see Figure 26 on page 70. The exchange rate terms in the right hand side are constructed from a series of constants based on the k – ε turbulent model (used in the suspension layer) — see Issler (1998) for details. A similar approach is taken by Bartelt, Kern and Christen (2000), mentioned in the end of the last section, but considering both the saltation and dense–snow layers the same. Updates including temperature changes and energy flux calculations were presented by Bartelt *et al.* (2016) and Bartelt *et al.* (2018).

The experiments on the suspension of currents from localized front blow-out of particles performed by Carroll, Turnbull and Louge (2012) and the works of Louge, Carroll and Turnbull (2011) and Carroll, Louge and Turnbull (2013) form a detailed model for snow avalanche front dynamics. In particular, the mass flow rate of snow emerging from the front is given by

$$\frac{dm}{dt} = \rho_0(\lambda h_0 \cos \theta W)u, \quad (2.58)$$

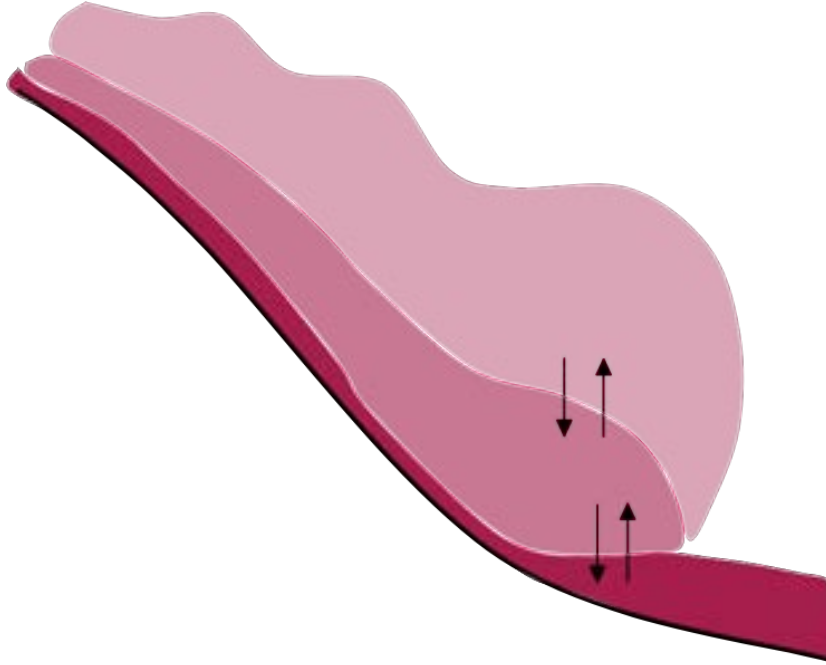
where ρ_0 is the snow cover density, λ is the fraction of the fluidized depth that is scoured, λh_0 is the entrained depth, and W is the width of the frontal region.

Recently, Ivanova *et al.* (2021) proposed a depth-averaged model with turbulence applied to powder–snow avalanches simulations. The model splits the velocity along the depth $u = U + u'$ into mean velocity U and fluctuation velocity u' components. The mass balance for the depth-averaged model due to entrainment is

$$\frac{\partial \hat{h}}{\partial t} + \frac{\partial(\hat{h}U)}{\partial x} = S_e + S_a, \quad (2.59)$$

where \hat{h} is the cloud height with entrainment (the model distinguishes the cloud height without air entrainment h , and with air entrainment \hat{h}), S_e and S_a are the snow and air entrainment source

Figure 26 – Representation of mass exchange between the avalanche layers employed by Issler. The turbulent eddies, represented by the circle arrows, move snow up and down through suspension and settlement through denser regions. The four processes, erosion, deposition, suspension and settling, are represented by the vertical arrows in the figure.



Source: Adapted from Issler (1998).

terms, respectively. The air entrainment, caused by turbulence, is described as

$$S_a = \begin{cases} (\alpha_U U + \alpha_T \sqrt{\langle u'^2 \rangle}) \frac{\hat{\rho}}{\rho}, & \hat{\rho} > 2\rho_a, U > 0 \\ 0, & \text{otherwise,} \end{cases} \quad (2.60)$$

where $\langle u'^2 \rangle = \frac{1}{h} \int_0^h u'^2 dz$ is the variance of velocity fluctuations representing the turbulent kinetic energy, $\alpha_U \in [0, 1]$ is the steady entrainment coefficient, $\alpha_T \in [0, 1]$ is the turbulent entrainment coefficient, and $\hat{\rho}$ is the mean density of the cloud and follows the relationship $\rho h = \hat{\rho} \hat{h}$. The snow entrainment follows an alternative approach by defining an oscillatory injection velocity $U_e(x, t)$ based on a Gaussian pulse of half-length L_0 and amplitude A_0 ,

$$U_e = A_0 \exp \left[-\frac{(x - x_0 - S_0 t)^2}{2 \cdot L_0^2} \right], \quad (2.61)$$

where S_0 is the propagation velocity of the pulse and x_0 is the starting position of core at time $t = 0$. The suggested values for the densities are $\rho = 7 \text{ kg/m}^3$ and $\rho_0 = 10 \text{ kg/m}^3$. The final snow entrainment term is given by

$$S_e = \frac{\rho}{\rho_0} U_e. \quad (2.62)$$

2.5 Numerical Methods

This section describes some of the different numerical approaches used to solve the mathematical models described in this chapter.

The Discrete Element Method

An example of a direct approach is the so-called Discrete Element Method (DEM), known as *molecular dynamics*. The DEM treats the avalanche body as a set of tiny volume elements called particles; recall the scale representation in [Figure 15c](#) on [page 40](#). Simple physical laws, such as Newton's second law of motion and Euler's balance of momentum, model the motion and interactions of particles ([PUDASAINI; HUTTER, 2007](#)). The DEM has been used to compute snow fracture during the start of avalanches ([GAUME *et al.*, 2014](#)), to investigate failure behavior in weak snow ([MULAK; GAUME, 2019](#)), to compute the granular avalanche impact forces ([ALBABA; LAMBERT; FAUG, 2018](#)), to predict the internal friction of granular flows ([FAVIER *et al.*, 2009](#)), to simulate granular debris flows ([ZHOU *et al.*, 2020](#)), and to model the inter-granular bond and collision of snow particles ([KABORE *et al.*, 2021](#)). Although the DEM provides relatively more straightforward models, these models require hundreds of thousands of elements. For large-scale 3D simulation domains, the number of elements can rise to millions of particles. In many cases, such computational effort can become a limitation. Moreover, most applications of the DEM consider only dry granular materials. On the other hand, applications where the interstitial fluid is significant, such as wet-snow avalanches and debris flows become a challenge to DEM, as cohesion plays an essential role.

The Material Point Method

Allied to the advances in computational resources, modern methods such as the Material Point Method (MPM) ([SULSKY; ZHOU; SCHREYER, 1995](#)) are becoming popular among full three-dimensional kinetic models. The hybrid nature of MPM offers an efficient framework for handling deformations through constitutive relations, making the method very attractive for avalanche applications. Recently, [Li *et al.* \(2021\)](#) proposed a three-dimensional and real-scale modeling covering different flow regimes for dense snow avalanches with impressive results. Their model comes along with a recent series of investigations, using the MPM, into snow failure processes and crack propagation ([GAUME *et al.*, 2018](#); [GAUME *et al.*, 2019](#); [TROTTEY *et al.*, 2022](#)), erosion and entrainment mechanisms ([LI *et al.*, 2022](#)), detrainment in natural terrains ([VÉDRINE; LI; GAUME, 2022](#)), and flow regimes ([LI *et al.*, 2020](#))¹⁹. The MPM has also been used to simulate hyperelasticity in granular flows ([HAERI; SKONIECZNY, 2022](#)), and landslides ([ZHAO *et al.*, 2019](#)).

¹⁹ The SLAB ([EPFL, 2022](#)), the EPFL Snow and Avalanche Simulation Laboratory in Switzerland, is worth mentioning, whose researchers are responsible for many recent state-of-the-art publications in avalanche research.

Direct Numerical Simulations

TODO

Large Eddy Simulations

TODO

RANS

TODO

2.6 Software Packages

The crucial importance of snow avalanche models in natural hazards leads to developing software for research or use in hazard mapping by governmental institutions and companies. Over the decades, governments and institutions collaborated on developing such software, as in the case of the Austrian government and the Swiss Federal WSL²⁰ Institute for Snow Avalanche Research (SLF). This section contains a brief list of software packages and libraries, commercial and open source, used for the simulation and study of snow avalanches. A discussion on the limitations and calibration of some packages in the list can be found in [Jamieson, Margreth and Jones \(2008\)](#).

2.6.1 Proprietary & Commercial Software

- **AVAL-1D**: Developed by the SLF, the AVAL-1D ([CHRISTEN; BARTELT; GRUBER, 2002](#)) is a software package consisting of two modules, the FL-1D for dense-snow avalanche simulations and the SL-1D for powder-snow avalanches. AVAL-1D is commonly used by avalanche practitioners to predict runout distances and flow velocities. Based on the VS model, the details of the models can be found in the works presented by [Issler \(1998\)](#), [Bartelt, Salm and Gruber \(1999\)](#), [Issler et al. \(2000\)](#). The package employs the finite difference method to solve equations. [Oller et al. \(2010\)](#) discusses its applications with real avalanche cases and offers several values for the parameters of the VS model. [Figure 27a](#) shows a screenshot of the software. More information is available at [AVAL-1D, WSL \(2022\)](#).
- **SAMOS-AT**: Developed in 1999 and introduced by [Zwinger, Kluwick and Sampl \(2003\)](#), the Snow Avalanche MOdelling and Simulation (SAMOS) tool ([SAMPL; ZWINGER, 2004](#)) was developed for the Austrian Federal Ministry for Agriculture, Forestry, and Environment for avalanche risk assessment. SAMOS is a simulation tool for powder-snow

²⁰ The Swiss Federal Institute for Forest Snow and Landscape Research (WSL) monitors and studies forest, landscape, biodiversity, natural hazards and snow and ice. WSL is a research institute of the Swiss Confederation and part of the ETH Domain ([SLF, 2022](#)).

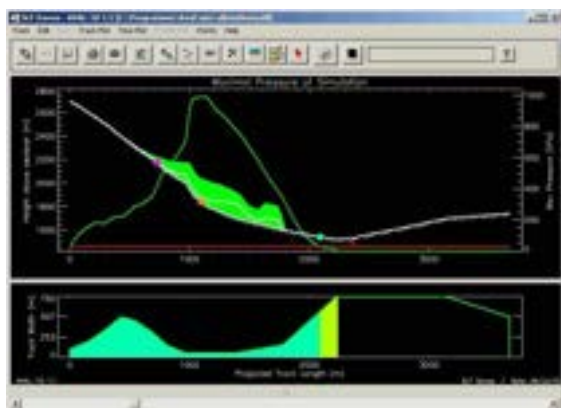
avalanches and uses a two-layer model to simulate the DSL and PSL. SAMOS uses the SH model for dense snow flows and a single mixture phase for the PSL.

In 2007, an improved version of the software, named SAMOS-AT (SAMPL; GRANIG, 2009) (AT stands for Advanced Technology), brought significant modifications to the model. SAMOS-AT solves the DSL with a Lagrangian set of particles representing columns of variable height containing volumes of the dense flow over the bed surface, similarly to the SWE approach. A two-phase model represents the PSL, with separate mass and momentum balances for air and powder snow. A discussion and analysis of the parameters of the software can be found in Fischer (2013), Fischer *et al.* (2015).

- **RAMMS:** Introduced by (CHRISTEN; KOWALSKI; BARTELT, 2010) and developed in SLF, the RApid Mass Movements Simulation (RAMMS) software package offers simulations for three phenomena: avalanches, rockfalls, and debris flows. RAMMS is currently used for hazard mapping in Switzerland and therefore follows the Swizz guidelines. The system combines the VS and the RKE models (subsection 2.3.8 on page 56) and can simulate full three-dimensional dense flows. Figure 50b shows a screenshot of the software. Information about RAMMS is available at RAMMS, WSL (2022).

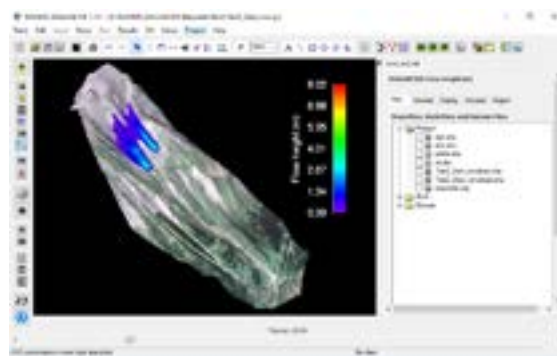
Figure 27 – Examples of graphical user interfaces of commercial software packages for snow avalanche simulation.

- (a) Simulation of a one-dimensional snow avalanche in the AVAL-1D software package.



Source: AVAL-1D, WSL (2022).

- (b) Simulation of a dense-snow avalanche over a three-dimensional terrain in the RAMMS software package.



Source: RAMMS, WSL (2022).

2.6.2 Open Source Software

- **Xcompact3d:** Xcompact3d and its modules is a framework of high-order finite-difference flow solvers dedicated to the study of turbulent flows (BARTHOLOMEW *et al.*, 2020) — in particular, DNS and LES simulations. Introduced by Frantz *et al.* (2021) on the simulation of turbulent gravity currents under the Boussinesq regime, the software has found many applications worldwide by many research groups, such as wake and jet

flows. The software is available at <<https://www.incompact3d.com/about.html>> (LAIZET; LAMBALLAIS, 2022).

- **TRENT2D:** (??) TRENT2D: An accurate numerical approach to the simulation of two-dimensional dense snow avalanches in global coordinate systems
- **TITAN2D:** (PATRA *et al.*, 2005) (SIMAKOV *et al.*, 2019) (PATRA *et al.*, 2020) TITAN2D Parallel adaptive numerical simulation of dry avalanches over natural terrain used to simulate volcanic avalanches based on the SH model by (PITMAN *et al.*, 2003)

2.7 Avalanche-Like Phenomena in Computer Graphics

The numerical methods cited in the previous sections are also present in Computer Graphics research and applications, with various adaptations and optimizations for computational efficiency. For instance, aside from water simulation, the particle-based method SPH found many applications over the years, such as the solution of SWE (SOLENTHALER *et al.*, 2011; CHLDEK; URIKOVI, 2015; XIA; LIANG, 2016), the animation of lava flows in volcano eruptions (ZHANG *et al.*, 2017), viscoplastic materials (PAIVA *et al.*, 2009), granular flows (BELL; YU; MUCHA, 2005; ALDUÁN; OTADUY, 2011), snow avalanches (YNDESTAD, 2011; JONTHAN; DANIEL, 2021), and snow compression (GISSLER *et al.*, 2020).

Eulerian methods based on adaptive grids were used to animate debris flow (WANG *et al.*, 2015) and real-time granular flows for sand animation (ZHU *et al.*, 2019). Other relevant numerical methods are the APIC (JIANG *et al.*, 2015), Power Particles (GOES *et al.*, 2015), and (ZHU *et al.*, 2013) for large-scale domains.

Since the debut of MPM into the graphics community by Stomakhin *et al.* (2013) on the animation of snow for Disney's *Frozen* movie, MPM has rapidly become the state-of-the-art for many types of material simulations. The flexibility of MPM has allowed the simulation of cloth (JIANG; GAST; TERAN, 2017), elastoplastic materials (GAO *et al.*, 2017), *phase-changing* materials (STOMAKHIN *et al.*, 2014), plastic flow for foam (YUE *et al.*, 2015; RAM *et al.*, 2015), *multi-species* materials and fluid mixtures (TAMPUBOLON *et al.*, 2017; GAO *et al.*, 2018), and fracture of materials (WOLPER *et al.*, 2020). In the realm of avalanche-like phenomena, Zhao *et al.* (2019) recently used MPM to animate landslides, and Gaume *et al.* (2018) produced incredible animations of slab avalanches using MPM.

Due to its complexity and high computational demand, alternative approaches solve the turbulent features of flows. In particular, procedural techniques for emulating turbulent motion and generating turbulent patterns became very successful. A few examples are Bridson, Houriham and Nordenstam (2007), Narain *et al.* (2008), Kim *et al.* (2008), Wang *et al.* (2020).

Over the years, people in the entertainment industry have been using graphics tools and usual fluid simulation techniques to emulate snow avalanches (KAPLER, 2003; KIM; FLORES,

2008; [imageworks, 2020](#); [Failes, Ian, 2021](#)). [Tsuda *et al.* \(2010\)](#) is the first to bring physical properties of snow into account by producing a mixed simulation of dense snow flow and powder–snow layers, followed later by [Güçer and ÖZGÜÇ \(2014\)](#), which applies molecular dynamics to the flow. [Cordonnier *et al.* \(2018\)](#) proposed a method for generating visual landscapes covered by snow that considers the effect of avalanches over time using a hydrostatic model. [Tillgren \(2020\)](#) used a procedural scheme based on Voronoi meshes to generate slab fractures on snow avalanches. Recently, [Liu *et al.* \(2021\)](#) presented a Position-based Dynamics (PBD) framework combined with the Bingham viscoplastic model to simulate snow avalanches. To the author’s knowledge, these few references are the only publications directly or indirectly related to the digital animation of snow avalanches.

2.8 Remarks

TODO

- similarity criteria

SIMULATION METHOD

This chapter delves into the details of the overall method. Here, a set of separate numerical methods simulate a mixed-type powder-snow avalanche. In particular, the workflow completely decouples the powder-snow layer from the dense-snow layer. Both layers are treated as separate simulations that communicate with each other numerically.

Refer to [Appendix B](#) on [page 159](#) for a brief introduction to the numerical methods used in this chapter, such as the Finite Volume Method, and [Appendix C](#) on [page 177](#) for a description of the software package OpenFOAM, the framework utilized to implement the models.

The first section gives a complete overview of the method, followed by [section 3.2](#) on [page 80](#) and [section 3.3](#) on [page 86](#), discussing the details of each separate method for the DSL and PSL simulations, respectively. The chapter ends with a list of remarks in [section 3.4](#) on [page 99](#).

3.1 Method Pipeline

As described in [section 1.2](#) on [page 22](#), the powder-snow avalanche consists of four main layers, from bottom to top: a ground layer representing the static snow cover, the DSL, a transition layer, and the PSL. Like [Sampl and Granig \(2009\)](#), this method takes the following assumptions:

Assumption 1. *The layers' physical characteristics are sufficiently different to justify a different set of equations to explain their respective motion.*

Assumption 2. *The transition layer is considered a rough that coincides with the surface of the DSL. The wall moves at the same speed as the DSL.*

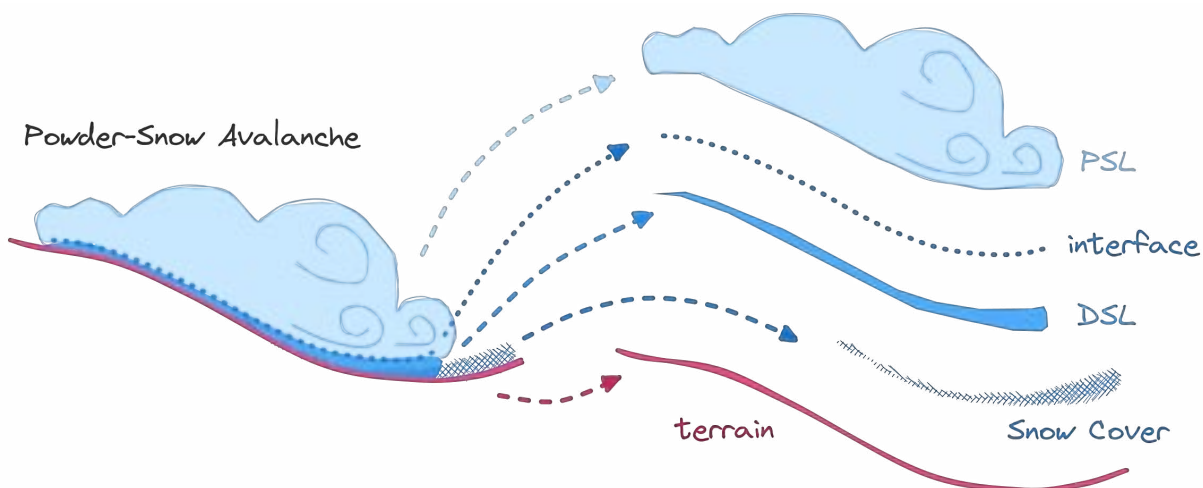
The first assumption is more of a necessity in front of the complexity of the whole phenomenon; it allows the application of more appropriate models for each type of flow. On

the other hand, [Assumption 2](#) enormously simplifies the method by removing the explicit representation of the *transition layer*, which is particularly challenging to model. In practice, the method simulates only the DSL and PSL flows, as boundary conditions for both numerical models could implicitly represent the *transition layer*. However, a third assumption further simplifies the overall setting:

Assumption 3. *Neither the turbulent air nor the deposition processes of the PSL are significant enough to have any effect on the motion or mass of the DSL. Therefore the role of the PSL in the DSL is negligible.*

The direct consequence of [Assumption 3](#) is that the system becomes a one-way coupling system of simulations, meaning that the resulting data of the first simulation serves as input for the second one. Schematically, the main algorithm performs both layer simulations in sequence and *glues* them together by converting the DSL output quantities into boundary conditions for the PSL equations. [Figure 28](#) depicts the final decomposition of the powder-snow avalanche after the abovementioned assumptions.

Figure 28 – The simulation method considers the following decomposition of the powder-snow avalanche. The method simulates only the DSL and the PSL flows. The transition layer is an interface that translates to boundary conditions for the PSL. The snow cover is static and serves as the source of mass for the upper layers.



Source: Elaborated by the author.

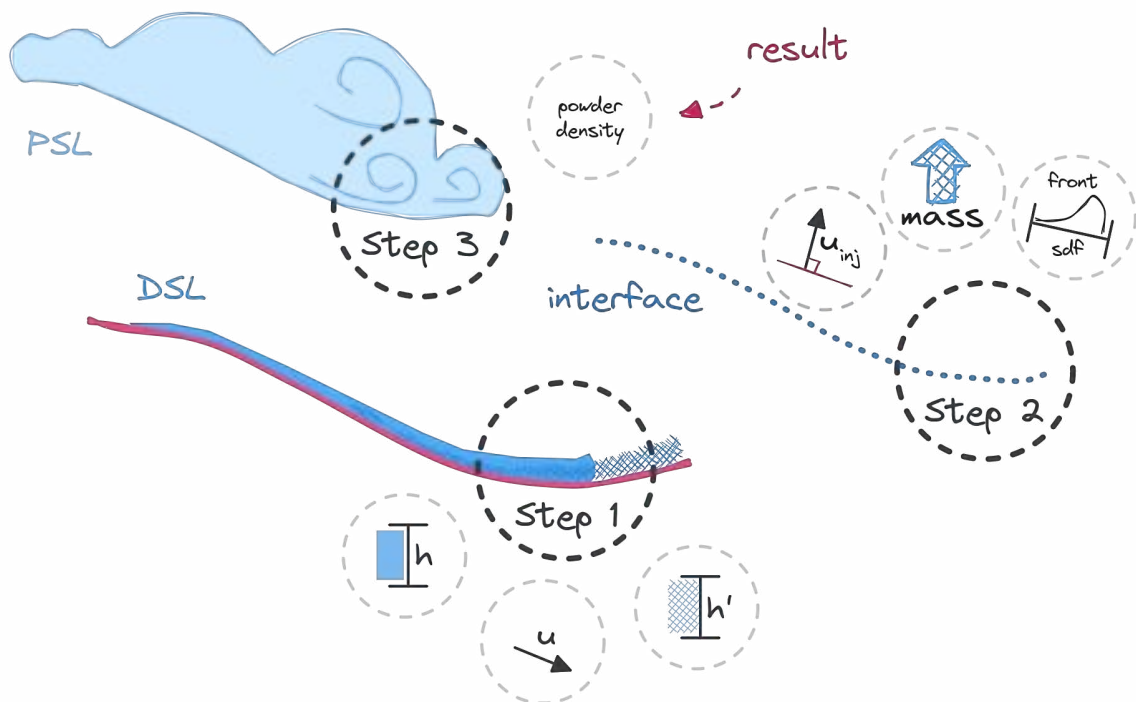
The pipeline consists of three main steps that conduct the numerical information transport from the lower to the upper layers. The middle step converts the output data from the DSL flow simulation into input quantities for the PSL flow simulation. The details will become clear in the next sections. [Figure 29](#) represents the following sequential steps:

- **Step 1:** Since it is a one-way coupling system, the full simulation of the DSL flow can be executed without any dependency. The two essential resulting quantities are the height h

and the velocity \mathbf{u} of the DSL. The velocity vector is parallel to the terrain surface. The final height of the snow cover h' , after its erosion, is also passed forward.

- **Step 2:** The resulting data from the previous step are converted into boundary conditions for the bottom faces of the PSL flow. The output is the amount of injected mass into the powder cloud and the velocity of the injection \mathbf{u}_{inj} . The injection velocity vector is perpendicular to the terrain surface. The computation of the injection quantities requires an extra field representing the distance to the front region of the DSL.
- **Step 3:** The final step simulates the PSL flow. The injection information computed in *step 2* generates mass for the cloud, and the governing equations take care of the motion. The final data is a *density field* representing the occupancy of snow powder in the simulation domain.

Figure 29 – The visual representation of the three steps described in the text. The output data from the DSL flow simulation representing tangential velocity and DSL height is converted into an amount of injected mass with parallel velocity. The injection intensity depends on the distance to the front of the DSL flow. The final result is a volumetric field representing the powder snow cloud.



Source: Elaborated by the author.

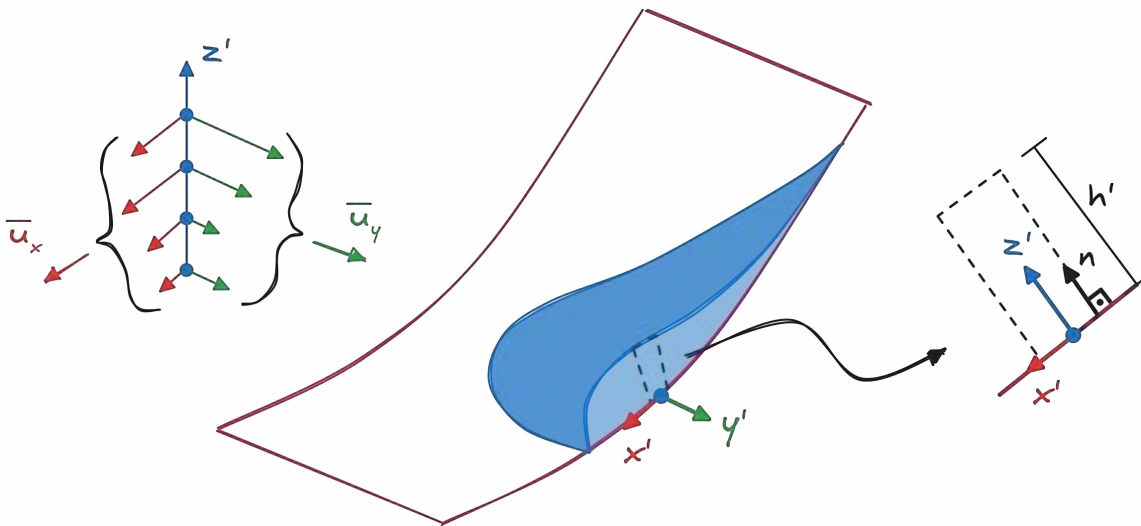
This chapter focuses only on the mathematical models that describe the DSL and the PSL. However, the simulations run over discrete meshes representing the numerical grid for the FVM. The details regarding the generation of the numerical grids from topographical data, the computation of the DSL front distance field, and other computational aspects are discussed in ?? on page ??.

3.2 Dense-Snow Layer Model

This section describes a method for simulating the dense flow avalanche corresponding to the DSL in the powder-snow avalanche. The core assumption is that the DSL behaves as a granular material that undergoes high deformation. The steep slope of the terrain tests the bed friction against the force of gravity. The internal friction also determines the motion of the granular flow by generating heat and resisting deformations.

The method resorts to the successful family of Saint-Venant Equations derived models to reduce the problem to two dimensions, particularly the well-known Savage-Hutter model (SAVAGE; HUTTER, 1991). As introduced in subsection 2.3.5.1 of Chapter 2, the SH extends the SWE by introducing a Coulomb-like dry friction for bed friction and a Mohr-Coulomb yield criterion to handle the internal friction. Additionally, the SH tackles the inherent limitation of the SWE for steep slopes by describing its equations with local curvilinear coordinates (x', y', z') – see Figure 30. In the curvilinear setting, the vector quantity \mathbf{v} is described as $\mathbf{v}' = (v'_x, v'_y)^T$, where the prime superscript $(\star)'$ denotes the curvilinear coordinates¹.

Figure 30 – The SH model describes the equations in the local curvilinear coordinates (x', y', z') . The directions of x' and y' are parallel to the terrain, where x' follows the slope, and the direction of z' points to the normal direction \mathbf{n} . The height h' represents the height of the avalanche in the normal direction. The model takes the averages $\bar{\mathbf{u}}$ of the vertical variation of the velocity \mathbf{u} .



Source: Elaborated by the author.

For a simple ramp, as shown in Figure 30, curved only in the x' direction, Koch, Greve and Hutter (1994) applies the SH equations as the following:

$$\frac{\partial h'}{\partial t} + \nabla' \cdot (h' \bar{\mathbf{u}}') = 0, \quad (3.1)$$

¹ Note that the vectors for the following equations are two-dimensional vectors since the SWE removes one dimension by averaging the values along the vertical direction.

$$\frac{\partial(h'\bar{\mathbf{u}}')}{\partial t} + \nabla' \cdot (h'\bar{\mathbf{u}}' \otimes \bar{\mathbf{u}}') = \frac{\tau'_b}{\rho} + \mathbf{g}'_{xy}h' - \frac{k}{2\rho}\nabla'(h'p_b), \quad (3.2)$$

$$\bar{\mathbf{u}}(\mathbf{x}) = \frac{1}{h'(\mathbf{x})} \int_0^{h'(\mathbf{x})} \mathbf{u}(\mathbf{x} - \mathbf{n}(\mathbf{x})z') dz' \quad [m \cdot s^{-1}], \quad (3.3)$$

where h' is the height of the flow normal to the surface (in the direction of z'), $\bar{\mathbf{u}}' = (\bar{u}_x, \bar{u}_y)^T$ is the average velocity in the z' direction, $\nabla' = (\frac{\partial}{\partial x'}, \frac{\partial}{\partial y'})^T$ is the spatial derivatives in curvilinear coordinates, τ'_b is the basal friction term (based on the Coulomb friction), k is the curvature of the x' curved axis, \mathbf{g}'_{xy} is the tangential components of the gravitational acceleration, and p_b is the basal pressure defined as

$$p_b = \rho h' g'_z + \rho h' k \bar{u}_x'^2 \quad [kg \cdot m^{-1} s^{-2}], \quad (3.4)$$

where the first term represents the gravitational influence and the second term relates to the centrifugal force.

For more complex terrains, the computation of the curvature k is challenging. Alternatively, [Rauter and Tukovi \(2018\)](#) offers an approach based on thin liquid film methods that solves Surface PDEs (SPDEs)² and can handle mildly curved terrains. In contrast to the SH, their method describes the equations in Cartesian coordinates and relates the vertical component of the velocity to the basal pressure. The solution splits the momentum equation into *surface-tangential* and *surface-normal* parts:

$$\frac{\partial h'}{\partial t} + \nabla \cdot (h'\bar{\mathbf{u}}) = 0 \quad [m \cdot s^{-1}], \quad (3.5)$$

$$\frac{\partial(h'\bar{\mathbf{u}})}{\partial t} + \nabla_S \cdot (h'\bar{\mathbf{u}} \otimes \bar{\mathbf{u}}) = -\frac{\tau_b}{\rho} + h'\mathbf{g}_S - \frac{1}{2\rho}\nabla_S(h'p_b) \quad [m^2 \cdot s^{-2}], \quad (3.6)$$

$$\nabla_n \cdot (h'\bar{\mathbf{u}} \otimes \bar{\mathbf{u}}) = h'\mathbf{g}_n - \frac{1}{2\rho}\nabla_n(h'p_b) - \frac{1}{\rho}\mathbf{n}p_b \quad [m^2 \cdot s^{-2}], \quad (3.7)$$

where, for a surface with normal vector \mathbf{n} , the surface-tangential gradient operator ∇_S and the surface-normal gradient operator ∇_n are defined as

$$\begin{aligned} \nabla_n &= (\mathbf{n} \otimes \mathbf{n}) \cdot \nabla, \\ \nabla_S &= (\mathbf{I} - \mathbf{n} \otimes \mathbf{n}) \cdot \nabla. \end{aligned} \quad (3.8)$$

The respective gravitational components, \mathbf{g}_S and \mathbf{g}_n , are defined in the same way. Note that [Equation 3.6](#) and [Equation 3.7](#) are very similar, differenced only by the strictly normal and tangential terms. Essentially, both equations represent a decomposition of [Equation 3.2](#) in a *velocity equation* and a *basal pressure equation*³, respectively. The boundary condition $\bar{\mathbf{u}} \cdot \mathbf{n} = 0$ ensures that the fluid motion is tangential to the surface and helps to solve [Equation 3.7](#). Therefore, the solution for the basal pressure p_b can solve the velocity field $\bar{\mathbf{u}}$.

² See [Deckelnick, Dziuk and Elliott \(2005\)](#).

³ The basal pressure equation relates to [Equation 3.4](#) but does not require the calculation of the curvature the surface curvature k .

In order to account for entrainment processes, [Rauter et al. \(2018\)](#) extends the model above with the entrainment model provided by [Fischer et al. \(2015\)](#). The extension modifies the mass conservation equation [Equation 3.5](#) to include the entrainment rate q_e defined as

$$q_e = \begin{cases} \frac{\tau_b \cdot \bar{\mathbf{u}}}{e_b}, & h'_c > 0, \\ 0, & h'_c = 0 \end{cases} \quad [kg \cdot m^{-2} \cdot s^{-1}], \quad (3.9)$$

where $e_b [m^2 \cdot s^{-2}]$ is the specific erosion energy and h'_c is the height snow cover encountered by the avalanche, defined as

$$h'_c(z) = (H'_c(z_0) + \frac{\partial H'_c}{\partial z}(z - z_0)) \cos \Theta \quad [m], \quad (3.10)$$

where $z[m]$ is the mountain elevation and $\cos \Theta = \mathbf{g} \cdot \mathbf{n}$. The other terms are user parameters, $z_0[m]$ is the elevation reference, $H'_c(z_0)$ is the base value, and $\frac{\partial H'_c}{\partial z}$ is the growth rate. [Equation 3.5](#) then becomes

$$\frac{\partial h'}{\partial t} + \nabla \cdot (h' \bar{\mathbf{u}}) = \frac{q_e}{\rho} \quad [m \cdot s^{-1}], \quad (3.11)$$

and the consumption of the snow cover due to entrainment over time is

$$\frac{\partial H'_c}{\partial t} = -\frac{q_e}{\rho} \quad [m \cdot s^{-1}]. \quad (3.12)$$

Finally, the basal friction τ_b follows the Voellmy friction model, see [subsection 2.3.3](#) of [Chapter 2](#), and is defined as

$$\tau_b = \mu p_b \frac{\bar{\mathbf{u}}}{|\bar{\mathbf{u}}| + u_0} + \frac{\rho g}{\xi} |\bar{\mathbf{u}}| \bar{\mathbf{u}} \quad [kg \cdot m^{-1} \cdot s^{-2}], \quad (3.13)$$

where $\mu[\cdot]$ and $\xi [m \cdot s^{-2}]$ are constant values, and $u_0 [m \cdot s^{-1}]$ is a regularization value to avoid the division by near zero velocities.

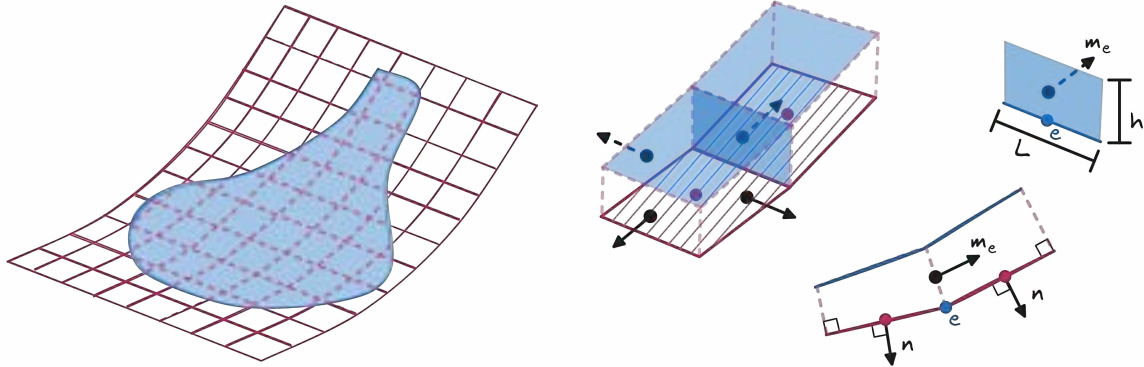
3.2.1 Numerical Model

This section describes the method employed by [Rauter et al. \(2018\)](#) to solve the governing equations described in the previous section. The numerical method, described in [section B.2](#) on [page 174](#), is called the Finite Area Method (FAM) and is a specialization of the FVM for curved surfaces. The FAM discretizes the equations over the decomposition of the surface domain into cells called finite areas, flat polygonal areas bounded by straight edges — left side of [Figure 31](#). Moreover, the FAM is constructed to solve SPDEs by discretizing the differential operators in the tangential and normal directions, fitting [Equation 3.6](#) and [Equation 3.7](#), respectively.

The equations are solved sequentially by an iterative method, represented by [Source code 1](#), that repeats the sequence until convergence is achieved. The sequence is composed of three steps:

1. Use [Equation 3.7](#) to compute a new value for the basal pressure p_b ;

Figure 31 – The FAM solves PDEs on curved surface domains by discretizing the domain into a surface mesh. Each cell The discretization process uses the fluxes passing through the edges of each cell. The flux in an edge is defined by $(h\mathbf{u})_{e_c} \cdot \mathbf{L}_e$, where $\mathbf{L}_e = |\mathbf{L}_e|\mathbf{m}_e$ is the edge length vector pointing outward the cell, and h is the DSL height transported by the velocity \mathbf{u} . Note that \mathbf{m}_e is not necessarily orthogonal to the surface normal \mathbf{n} at the cell center.



Source: Elaborated by the author.

2. Use Equation 3.6 to compute a new value for the velocity field $\bar{\mathbf{u}}$;
3. Use the new velocity $\bar{\mathbf{u}}$ to compute a new value of h' with Equation 3.11.

Source code 1 – DSL Algorithm.

```

1:   u = u_0; pb = pb_0; h = h_0;
2:   for(t = t_0; t < t_final; t += dt) {
3:       while(residual > threshold && ) {
4:           pb = computePb(u, h, pb);
5:           u = computeU(pb, u, h);
6:           h = computeH(u, pb);
7:       }
8:   }

```

The following details consider a finite area cell C , with area C_A and center point C_c . The cell is bounded by a set of edges $e_i \in E$ that may be shared with neighboring cells N_i . The flux of any rank tensor field Ψ through each edge e_i is defined by $(\Psi)_{e_{ci}} * \mathbf{L}_{e_i}$, where \mathbf{L}_{e_i} is the edge length vector pointing outwards the cell, and $*$ is an appropriate product operation. The superscript $(\star)^o$ denotes the current known value of \star in the current time step. The steps of the algorithm above are:

- $p_b \leftarrow \text{computePb}(\bar{\mathbf{u}}^o, h^o, p_b^o)$

The new value of p_b is computed explicitly from Equation 3.7:

$$p_b = -\rho(\nabla_n \cdot (h^o \bar{\mathbf{u}}^o \otimes \bar{\mathbf{u}}^o)) \cdot \mathbf{n} + (\rho h^o \mathbf{g}_n)_{C_c} \cdot \mathbf{n} - \frac{1}{2}(\nabla_n(h^o p_b^o)) \cdot \mathbf{n}$$

where

$$\begin{aligned}\nabla_n \cdot (h^o \bar{\mathbf{u}}^o \otimes \bar{\mathbf{u}}^o) &\approx (\mathbf{n} \otimes \mathbf{n}) \cdot \sum_{e_i \in E} (h^o \bar{\mathbf{u}}^o \otimes \bar{\mathbf{u}}^o)_{e_i} \cdot \mathbf{L}_{e_i}, \\ \nabla_n (h^o p_b^o) &\approx (\mathbf{n} \otimes \mathbf{n}) \cdot \sum_{e_i \in E} (h^o p_b^o)_{e_i} \mathbf{L}_{e_i}.\end{aligned}\quad (3.14)$$

- $\bar{\mathbf{u}} \leftarrow \text{computeU}(\bar{\mathbf{u}}^o, h^o, p_b^o)$

The new value for the velocity field $\bar{\mathbf{u}}$ comes from the solution of the system

$$\mathbf{A}\bar{\mathbf{u}} = \mathbf{b} \quad (3.15)$$

constructed from the discretization of [Equation 3.6](#)

$$\underbrace{\frac{\partial(h^o \bar{\mathbf{u}})}{\partial t}}_1 + \underbrace{\nabla_S \cdot (h^o \bar{\mathbf{u}}^o \otimes \bar{\mathbf{u}})}_2 = \underbrace{-\frac{\tau_b}{\rho}}_3 + \underbrace{h^o \mathbf{g}_S}_4 - \underbrace{\frac{1}{2\rho} \nabla_S (h^o p_b^o)}_5,$$

where each numbered term translates into the system as:

1.

$$\boxed{\frac{\partial(h^o \bar{\mathbf{u}})}{\partial t}}$$

The transient term is discretized by the second-order implicit Euler:

$$\frac{C_A}{2\Delta t} \left(3(h^o \bar{\mathbf{u}}) - 4(h\bar{\mathbf{u}})^{n-1} + (h\bar{\mathbf{u}})^{n-2} \right)_{C_c}, \quad (3.16)$$

where the superscripts $(\star)^{n-1}$ and $(\star)^{n-2}$ denote known values from previous time steps.

2.

$$\boxed{\nabla_S \cdot (h^o \bar{\mathbf{u}}^o \otimes \bar{\mathbf{u}})}$$

The convective term is discretized via the *upwind scheme*⁴:

$$(\mathbf{I} - \mathbf{n} \otimes \mathbf{n}) \cdot \sum_{f_i \in S} \Phi_{e_i} \bar{\mathbf{u}}_{e_i}, \quad (3.17)$$

where

$$\begin{aligned}\Phi_{e_i} &= (h\bar{\mathbf{u}})_{e_i}^o \cdot \mathbf{L}_{e_i}, \\ \bar{\mathbf{u}}_{e_i} &= \begin{cases} (\bar{\mathbf{u}})_{C_c}, & \Phi_{e_i} \geq 0, \\ (\bar{\mathbf{u}})_{N_{ci}}, & \Phi_{e_i} < 0. \end{cases}\end{aligned}\quad (3.18)$$

⁴ See advection schemes in [subsection B.1.5](#) on [page 170](#).

3.

$$\boxed{-\frac{\tau_b}{\rho}}$$

The basal friction term is given by [Equation 3.13](#):

$$\tau_b = \mu p_b^o \frac{\bar{\mathbf{u}}}{|\bar{\mathbf{u}}^o| + u_0} + \frac{\rho g}{\xi} |\bar{\mathbf{u}}^o| \bar{\mathbf{u}},$$

so the term is implicitly solved by the system as

$$C_A \left(\left(\mu p_b \frac{1}{|\bar{\mathbf{u}}| + u_0} + \frac{\rho g}{\xi} |\bar{\mathbf{u}}| \right)^o \bar{\mathbf{u}} \right)_{C_c}. \quad (3.19)$$

4.

$$\boxed{h^o \mathbf{g}_S}$$

The source term is directly translated into the system as

$$(\mathbf{I} - \mathbf{n} \otimes \mathbf{n}) \cdot (h^o \mathbf{g})_{C_A}. \quad (3.20)$$

5.

$$\boxed{\frac{1}{2\rho} \nabla_S (h^o p_b^o)}$$

The last term is also explicitly solved by the system as

$$(\mathbf{I} - \mathbf{n} \otimes \mathbf{n}) \cdot \frac{1}{2\rho} \sum_{e_i \in E} (h^o p_b^o)_{e_i} \mathbf{L}_{e_i}. \quad (3.21)$$

- $h \leftarrow \text{computeH}(\bar{\mathbf{u}}^o, h^o, p_b^o)$

The DSL height is given by the numerical system

$$\mathbf{A}_h[h] = \mathbf{b}_h, \quad (3.22)$$

constructed from the discretization of [Equation 3.11](#):

$$\underbrace{\frac{\partial h}{\partial t}}_1 + \underbrace{\nabla \cdot (h \bar{\mathbf{u}}^o)}_2 = \underbrace{\frac{q_e}{\rho}}_3,$$

where each numbered term translates into the system as:

1.

$$\boxed{\frac{\partial h}{\partial t}}$$

The transient term is discretized by the second-order implicit Euler:

$$\frac{C_A}{2\Delta t} \left(3h - 4h^{n-1} + h^{n-2} \right)_{C_c}. \quad (3.23)$$

2.

$$\boxed{\nabla \cdot (h\bar{\mathbf{u}}^o)}$$

The convective term is discretized via the *upwind scheme*:

$$\sum_{f_i \in S} \Phi_{e_{ci}} h_{e_{ci}}, \quad (3.24)$$

where

$$\begin{aligned} \Phi_{e_{ci}} &= (\bar{\mathbf{u}})_{e_{ci}}^o \cdot \mathbf{L}_{e_i}, \\ h_{e_{ci}} &= \begin{cases} (h)_{C_c}, & \Phi_{e_{ci}} \geq 0, \\ (h)_{N_{ci}}, & \Phi_{e_{ci}} < 0. \end{cases} \end{aligned} \quad (3.25)$$

3.

$$\boxed{\frac{q_e}{\rho}}$$

The right-hand side term accounts for snow entrainment into the DSL and uses [Equation 3.9](#). In the presence of a snow cover, q_e is defined as:

$$q_e = \left(\frac{\tau_b \cdot \bar{\mathbf{u}}}{e_b} \right)^o,$$

and the complete term is explicitly solved as

$$\left(\frac{\tau_b \cdot \bar{\mathbf{u}}}{\rho e_b} \right)^o C_A. \quad (3.26)$$

3.3 Powder-Snow Layer Model

The miscible nature of the turbulent movement of snow and air in the powder-snow layer appeals to mixture models. Therefore, we consider the family of models originated from the Continuum Mixture Theory — see [section A.2](#) on [page 157](#). In particular, our model contemplates the two main mixture constituents, \mathcal{C}_s , and \mathcal{C}_a , representing respectively snow⁵ and air phases⁶. Therefore, the terms in the following equations indexed with the subscript $(\star)_s$ refer to field quantities of snow, and those indexed with the subscript $(\star)_a$ refer to field quantities of air. The model then combines snow and air property quantities to describe the final mixture.

Moreover, allied to the superposition assumption of the CMT, the Volume of Fluid method approach fits naturally in this configuration. This way, the mixture is also characterized by the fraction of volume $\alpha_\gamma \in [0, 1]$ occupied by the constituent \mathcal{C}_γ for any given volume occupied by the mixture. The mixture density ρ , for example, is defined by

$$\rho = \alpha_s \rho_s + \alpha_a \rho_a, \quad \alpha_s + \alpha_a = 1. \quad (3.27)$$

⁵ Recall that the snow phase consists of airborne particles of ice.

⁶ The terms *phase* and *constituent* are interchangeable throughout the text.

The CMT conveniently introduces a mean velocity \mathbf{u} for the mixture, interpreted as the velocity of the center of mass of the constituents. Thus, we can simplify our model using the mean velocity instead of handling \mathbf{u}_s and \mathbf{u}_a explicitly. Additionally assuming incompressibility for both phases, the continuity equation is

$$\nabla \cdot \mathbf{u} = 0, \quad (3.28)$$

imposing ρ_s and ρ_a constant densities. The momentum equation for the mean velocity can be derived directly from the linear momentum balance law:

$$\frac{\partial \rho \mathbf{u}}{\partial t} + \nabla \cdot (\rho \mathbf{u} \otimes \mathbf{u}) = \nabla \cdot \mathbf{S} + \rho \mathbf{g}, \quad (3.29)$$

where \mathbf{S} is the Cauchy stress field and \mathbf{g} the gravitational acceleration. The Cauchy stress field is composed by a *reactive* part \mathbf{S}^r and an *active* part \mathbf{S}^a :

$$\mathbf{S} = \mathbf{S}^r + \mathbf{S}^a. \quad (3.30)$$

For incompressible fluids, the reactive stress field is spherical and its multiplicative term p is interpreted as the pressure:

$$\mathbf{S}^r = -p\mathbf{I}. \quad (3.31)$$

The reactive stress field \mathbf{S}^r would be sufficient to model ideal fluids. However in the case of Newtonian fluids, the Cauchy stress field carries the active term \mathbf{S}^a , defined as⁷

$$\mathbf{S}^a = \mathbf{S} - \frac{1}{3}\text{tr}(\mathbf{S})\mathbf{I}. \quad (3.32)$$

The active term \mathbf{S}^a is related to the shear-rate stresses and is represented by the shear-rate tensor $\boldsymbol{\tau}$, also called *viscous stress tensor* or *deformation-rate tensor*, given as

$$\mathbf{S}^a = \boldsymbol{\tau} = 2\mu\mathbf{D} - \frac{2}{3}\mu\text{tr}(\mathbf{D})\mathbf{I}, \quad (3.33)$$

where $\mathbf{D} = \frac{1}{2}(\nabla \otimes \mathbf{u} + (\nabla \otimes \mathbf{u})^T)$ is the strain-rate tensor and μ is the mixture viscosity⁸

$$\mu = \alpha_s\mu_s + \alpha_a\mu_a. \quad (3.34)$$

The development of the trace operator in Equation 3.33 yields

$$\begin{aligned} \text{tr}(\mathbf{D}) &= \text{tr}\left(\frac{1}{2}(\nabla \otimes \mathbf{u} + (\nabla \otimes \mathbf{u})^T)\right) \\ &= \nabla \cdot \mathbf{u}, \end{aligned} \quad (3.35)$$

⁷ The decomposition of \mathbf{S} splits a matrix \mathbf{S} into a hydrostatic \mathbf{S}^H part and a deviatoric \mathbf{S}^D part, $\mathbf{S} = \mathbf{S}^H + \mathbf{S}^D$. The hydrostatic part is defined as $\mathbf{S}^H = \frac{1}{3}\text{tr}(\mathbf{S})\mathbf{I}$, which is particularly interpreted as the negative pressure $-p\mathbf{I}$. The deviatoric part is simply given by $\mathbf{S}^D = \mathbf{S} - \mathbf{S}^H$.

⁸ If $\mu = 0$ and $\rho = \rho_0$ constant, the system is reduced to the known Euler equations: $\nabla \cdot \mathbf{u} = 0$ and $\rho_0 \frac{\partial \mathbf{v}}{\partial t} + (\nabla \cdot \mathbf{u})\mathbf{u} = -\nabla p + \rho_0 \mathbf{g}$.

therefore the tensor τ can be written as

$$\tau = 2\mu\mathbf{D} - \frac{2}{3}\mu(\nabla \cdot \mathbf{u})\mathbf{I}. \quad (3.36)$$

Note, however, that by the continuity equation [Equation 3.28](#), $\nabla \cdot \mathbf{u} = 0$, the equation above reduces to

$$\tau = 2\mu\mathbf{D}. \quad (3.37)$$

The expansion of [Equation 3.30](#) in [Equation 3.29](#) results into the momentum equation found in the Navier-Stokes equations

$$\frac{\partial \rho \mathbf{u}}{\partial t} + \nabla \cdot (\rho \mathbf{u} \otimes \mathbf{u}) = -\nabla p + \nabla \cdot \tau + \rho \mathbf{g}. \quad (3.38)$$

For numerical purposes, it is also convenient to use a change of variable for the pressure term. The pressure field is modified to account for the hydrostatic pressure p_{rgh} and is defined as:

$$p_{rgh} = p - \rho \mathbf{g} \cdot \mathbf{h}, \quad (3.39)$$

where \mathbf{h} is the position vector read as the height. The substitution of p by p_{rgh} proceeds by applying the gradient on both sides of [Equation 3.39](#):

$$\begin{aligned} \nabla p_{rgh} &= \nabla p - \nabla(\rho(\mathbf{g} \cdot \mathbf{h})) \\ -\nabla p &= -\nabla p_{rgh} - \rho \mathbf{g} \cdot \nabla \otimes \mathbf{h} - \mathbf{h} \cdot \nabla(\rho \mathbf{g}) \\ -\nabla p &= -\nabla p_{rgh} - \rho \mathbf{g} \cdot \mathbf{I}_z - \mathbf{g} \cdot \mathbf{h} \nabla \rho - \rho \mathbf{h} \cdot \nabla \mathbf{g} \\ -\nabla p &= -\nabla p_{rgh} - \rho \mathbf{g} - \mathbf{g} \cdot \mathbf{h} \nabla p \end{aligned} \quad (3.40)$$

where the term $\nabla \otimes \mathbf{h}$ reduces to the tensor \mathbf{I}_z with diagonal $(0, 0, 1)^T$ and null non-diagonal elements. The final linear momentum equation is written as

$$\frac{\partial \rho \mathbf{u}}{\partial t} + \nabla \cdot (\rho \mathbf{u} \otimes \mathbf{u}) = -\nabla p_{rgh} - \mathbf{g} \cdot \mathbf{h} \nabla \rho + \nabla \cdot \tau. \quad (3.41)$$

The remaining equations describe the conservation of mass and use the concentration of volume α_s instead of ρ . Using α in the equation aligns with the Volume of Fluid method and requires only one set of equations since $\alpha_a = 1 - \alpha_s$ ([Equation 3.27](#)). Notice that, in principle, the transport equation for α_s would be

$$\frac{\partial \alpha_s}{\partial t} + \nabla \cdot (\mathbf{u} \alpha_s) = 0, \quad (3.42)$$

which conserves α_s along the motion. However, the turbulent motion in the PSL causes the mixing of both phases and therefore [Equation 3.42](#) gets a source term on the right-hand side. The additional term takes into account the kinetic energy, produced by turbulence, that composes the stress tensor for the field α_s and models the mixing effect of the turbulence:

$$\frac{\partial \alpha_s}{\partial t} + \nabla \cdot (\mathbf{u} \alpha_s) = \nabla \cdot \left(\left(D_{AB} + \frac{V_t}{Sc} \right) \nabla \alpha_s \right). \quad (3.43)$$

The constant Sc is called the Schmidt number and is the ratio of the momentum diffusivity to mass diffusivity⁹. ν_t is the turbulent eddy viscosity, which comes from the transfer of energy due to moving eddies produced by turbulence. The molecular diffusivity, D_{ab} , describes the velocity of diffusion of molecules from the snow phase into the air phase.

3.3.1 Transition Layer Model

The previous section detailed the model equations for linear momentum and mass transport. The set of equations describes the evolution of the powder-snow cloud over time due to gravity. The gravity force causes the acceleration of heavy snow particles in regions where the density difference is high. Besides the gravitational acceleration, mass transport manifests through molecular diffusion between both phases. However, none of the terms in the equations consider the mass exchange between the powder-snow cloud and the sources of snow particles. Moreover, the volume of the cloud also varies due to air drag and air intake, which are also not accounted for by the equations.

As described in previous chapters, the powder-snow layer gains mass from the processes in the interface layer between the DSL and the PSL, called the *transition layer*. This section explores a couple of models for the transition layer and considers the eruption entrainment type, described in section 1.2, as the principal source of mass and momentum injections in the PSL.

Here, boundary conditions in the PSL model system implicitly represent the transition layer. In this sense, a Dirichlet boundary condition for mass and velocity imposes snow injection at the bottom region of the PSL. Since the equations describe the powder-snow mass in terms of concentration of volume $\alpha_s \in [0, 1]$, the transition layer model must define an injected volume concentration α_{inj} driven by an injection velocity \mathbf{u}_{inj} .

Consider a volume V localized at the bottom region of the PSL. During the eruption entrainment process, the total injection flux F_{inj} passing through the bottom surface area A is given by:

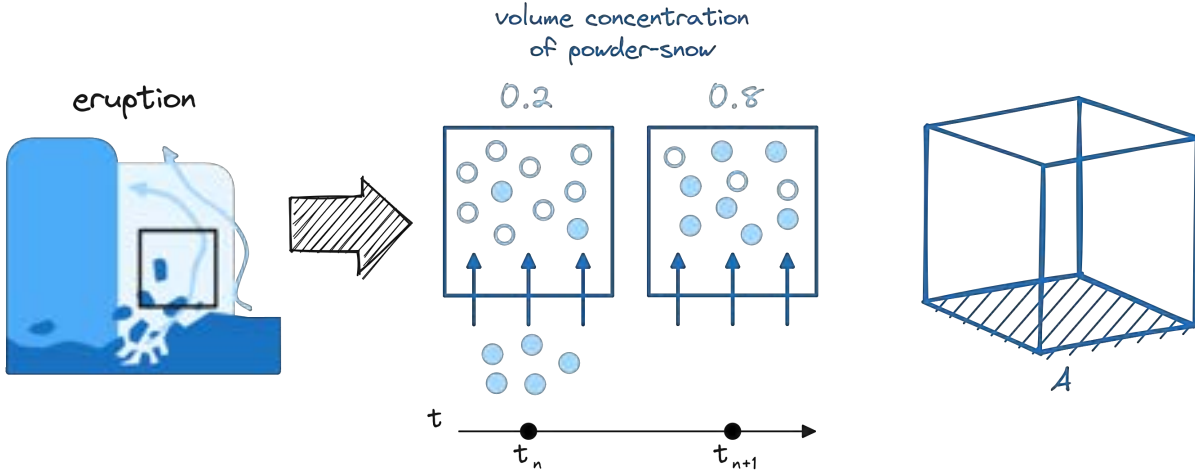
$$F_{inj} = \Phi_{inj} \cdot \mathbf{S}_f = \rho_s \mathbf{u}_{inj} \cdot (\mathbf{A}\mathbf{n}_b) \quad [kg \cdot s^{-1}], \quad (3.44)$$

where $\Phi_{inj} = \rho_s \mathbf{u}_{inj}$ is the mass flux and $\mathbf{S}_f = \mathbf{A}\mathbf{n}_b$ is the surface area vector pointing at the normal boundary vector \mathbf{n}_b outwards the volume. Note that writing the mass in the equation above by terms of concentration of volume inevitably requires the volume V . In the following, the superscript $(\star)^v$ will associate \star to the volume V , such as in the equation of the total powder-snow mass m^v inside the volume V :

$$m^v = \alpha_s^v \rho_s V. \quad (3.45)$$

⁹ Physically, the Schmidt number has a direct relation to the flow strength. The increase in Sc means higher momentum diffusivity leading to an increase in the flow strength.

Figure 32 – The injection of powder snow happens principally through the eruption entrainment process. For a control volume V , represented in the figure by the square/cube, in the bottom region of the PSL, mass flows upwards through the bottom surface area A . The volume concentration of the powder snow inside V increases with the mass inflow.



Source: Elaborated by the author.

Take the injection example in Figure 32, representing an increase of 0.6 in the value of α_s^v over time $\Delta t = t_{n+1} - t_n$. From Equation 3.44, the total amount of injected mass m_{inj}^v in this case is

$$m_{inj}^v = \alpha_{inj}^v \rho_s V = \Delta t F_{inj} = \Delta t (\rho_s \mathbf{u}_{inj}) \cdot (A \mathbf{n}_b), \quad (3.46)$$

which implies

$$\alpha_{inj}^v = \frac{A \Delta t}{V} \mathbf{u}_{inj} \cdot \mathbf{n}_b. \quad (3.47)$$

Over the years, researchers proposed models to compute m_{inj}^v and \mathbf{u}_{inj} . In particular, Carroll, Louge and Turnbull (2013) defines the mass flow rate in the two-dimensional eruption entrainment process as

$$F_{inj} = \rho_{sc} (\lambda h_{sc} \cos \theta W) u_{front}, \quad (3.48)$$

where ρ_{sc} is the snow cover density, h_{sc} is the snow cover depth, $\lambda \in [0, 1]$ is the fraction of the snow cover layer entrained into the PSL, θ is the slope, W is the section width of the front region which the eruption flows through, and u_{front} is the front velocity.

Bartelt *et al.* (2016) breaks down the formation of the powder snow cloud into two processes: *air intake* and *ice-dust blow-out*. Both processes happen simultaneously but at different locations of the avalanche. As particles in the DSL collide with the ground, the *dispersive pressure* causes the DSL to expand, which causes air intake. Then, the downward motion of heavy particles displaces the enclosed air, causing the compression of the DSL. Therefore, the velocity of expansion/compression w_h causes the variation in the DSL height h_{dsl} :

$$\frac{\partial h_{dsl}}{\partial t} + \nabla \cdot (h_{dsl} \mathbf{u}_{dsl}) = w_h \quad [m \cdot s^{-1}], \quad (3.49)$$

where \mathbf{u}_{dsl} is the DSL two-dimensional velocity parallel to the terrain. The variation rate of the DSL height, w_h , is a one-dimensional velocity perpendicular to the terrain and has its own formulation; w_h results from the mechanical energy caused by the shearing in the DSL body, leading to its variation in height. During the blow-out, i.e. the compression of the DSL, the mass flow into the PSL is defined as

$$F_{inj} = \begin{cases} (\rho \mathbf{u}_{inj}) \cdot (\mathbf{A} \mathbf{n}_b), & w_h < 0, \\ 0, & otherwise, \end{cases} \quad (3.50)$$

$$\mathbf{u}_{inj} \cdot \mathbf{n}_b = 2w_h.$$

Recently, [Ivanova et al. \(2021\)](#) proposed a depth-averaged model with turbulence applied to powder–snow avalanches simulations. The model splits the velocity along the depth $u = U + u'$ into mean velocity U and fluctuation velocity u' components. The mass balance for the depth-averaged model due to entrainment is

$$\frac{\partial \hat{h}_{psl}}{\partial t} + \frac{\partial (\hat{h}_{psl} U)}{\partial x} = S_e + S_a, \quad (3.51)$$

where \hat{h}_{psl} is the cloud height with entrainment (the model distinguishes the cloud height without air entrainment h_{psl} , and with air entrainment \hat{h}_{psl}), S_e and S_a are the snow and air entrainment source terms, respectively. The air entrainment, caused by turbulence, is described as

$$S_a = \begin{cases} (\alpha_U U + \alpha_T \sqrt{\langle u'^2 \rangle}) \frac{\hat{\rho}}{\rho}, & \hat{\rho} > 2\rho_a, U > 0 \\ 0, & otherwise, \end{cases} \quad (3.52)$$

where $\langle u'^2 \rangle = \frac{1}{h} \int_0^h u'^2 dz$ is the variance of velocity fluctuations representing the turbulent kinetic energy, $\alpha_U \in [0, 1]$ is the steady entrainment coefficient, $\alpha_T \in [0, 1]$ is the turbulent entrainment coefficient, and $\hat{\rho}$ is the mean density of the cloud and follows the relationship $\rho h = \hat{\rho} \hat{h}$. The snow entrainment follows an alternative approach by defining an oscillatory injection velocity $U_e(x, t)$ based on a Gaussian pulse of half-length L_0 and amplitude A_0 ,

$$U_e = A_0 \exp \left[-\frac{(x - x_0 - S_0 t)^2}{2 \cdot L_0^2} \right], \quad (3.53)$$

where S_0 is the propagation velocity of the pulse and x_0 is the starting position of core at time $t = 0$. The suggested values for the densities are $\rho = 7 \text{ kg/m}^3$ and $\rho_0 = 10 \text{ kg/m}^3$. The final snow entrainment term is given by

$$S_e = \frac{\rho}{\rho_0} U_e. \quad (3.54)$$

The methods described above are only a few examples of a diversity of entrainment models proposed by researchers throughout the years — see [subsection 2.4.4](#) on [page 68](#). The remaining section proposes the method adopted in this project, supported by the concepts presented by the methods listed above.

Injection Velocity (\mathbf{u}_{inj})

The injection velocity is responsible for an increase in the momentum of the PSL by injecting kinetic energy into the system. The entrainment processes at the front eject snow mass upwards into the air and produce the snow cloud. Therefore, the front velocity \mathbf{u}_{front} has a direct influence on such dynamics such that the injection velocity is

$$\mathbf{u}_{inj} = \gamma_{\mathbf{u}} \|\mathbf{u}_{front}\| (-\mathbf{n}_b), \quad (3.55)$$

where scalar $\gamma_{\mathbf{u}}$ is the entrainment factor for the velocity, \mathbf{u}_{front} is the front velocity vector. Note that \mathbf{u}_{inj} has the same direction of $(-\mathbf{n}_b)$ ¹⁰, parallel to the normal of the terrain.

The term $\gamma_{\mathbf{u}}$ accounts for both types of entrainment: powder snow blow-out and air intake. Due to the turbulent nature of the PSL, this factor is generalized as a random perturbation:

$$\gamma_{\mathbf{u}} \approx \gamma_s + \gamma_t, \quad (3.56)$$

where γ_s is a steady factor and γ_t is a perturbation factor caused by turbulence.

As later detailed in [subsection 4.1.3](#), $\gamma_{\mathbf{u}}$ is further reduced into a noise function. Note also that the boundary conditions for the velocity field must include the DSL motion, so the velocity at the boundary is defined as

$$(\mathbf{u})_b = \mathbf{u}_{inj} + \mathbf{u}_{dsl}. \quad (3.57)$$

Concentration of Volume Injection (α_{inj})

As mentioned earlier, the concentration of volume α_{inj} builds from the volume and the total amount of mass entrained at a given time. Analogous to Bartelt's w_h term in [Equation 3.49](#), the variation rate in the DSL's height h_{dsl} can be extracted from the right-hand side of [Equation 3.11](#)

$$\frac{\partial h'}{\partial t} + \nabla \cdot (h' \bar{\mathbf{u}}) = \frac{q_e}{\rho}$$

of the DSL model presented in [section 3.2](#). Let Q_e represent such term, respective to w_h , so

$$Q_e = \frac{q_e}{\rho_{dsl}}. \quad (3.58)$$

The total mass m_e entrained over the period Δt through an area A is given by:

$$m_e = Q_e \rho_{dsl} A \Delta t, \quad (3.59)$$

which is converted for the correspondent volume V as a volume concentration as

$$\alpha_{inj}^v = \frac{m_e}{M^v}, \quad (3.60)$$

where M^v is total mass capacity of the PSL volume V defined as

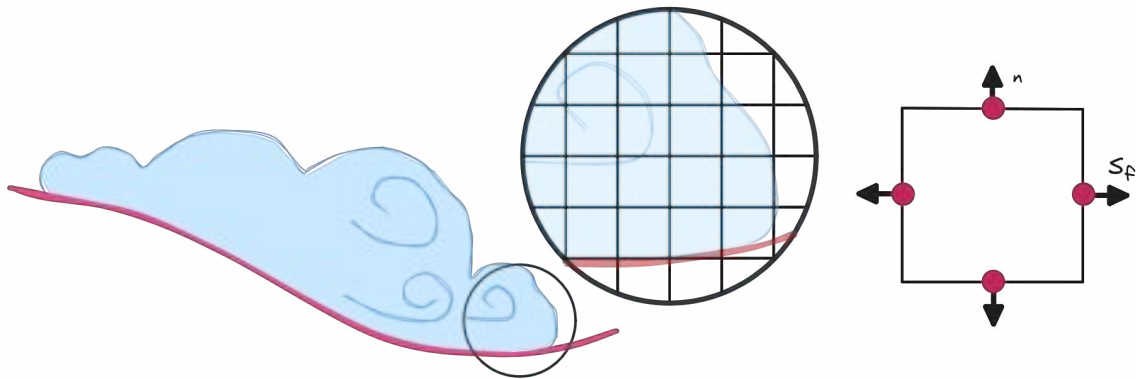
$$M^v = \rho_{psl} V. \quad (3.61)$$

¹⁰ Recall that \mathbf{n}_b points outwards the PSL volume, i.e. downwards into the terrain.

3.3.2 Numerical Model

This section describes the numerical treatment of the core system of the governing equations described in [section 3.3](#). The finite volume method, introduced in the [appendix section B.1](#) on [page 159](#), solves the equations by discretizing them over the decomposition of the physical domain into cells called *finite volumes* — see [Figure 33](#). The FVM integrates the equations for each cell volume and uses the cell boundary fluxes to discretize the volume integrals¹¹. A detailed description of the discretization process is presented in [Appendix B, section B.1](#) on [page 159](#). Therefore, this section only briefly and directly discusses the numerical model used to solve the equations.

Figure 33 – The FVM splits the physical domain into a volumetric mesh where the equations are discretized in each grid cell. The discretization process uses the fluxes passing through the faces of each cell. The flux in a face is defined by $(\phi \mathbf{u})_{f_c} \cdot \mathbf{S}_f$, where \mathbf{S}_f is the face area vector pointing outward the cell, and ϕ is the quantity being transported by the velocity \mathbf{u} .



Source: Elaborated by the author.

Each cell in the grid spans an equation that composes the final system of numerical equations. For a given cell C with center C_c , the flux of a quantity ϕ passing through the cell face f_i is computed in the face center f_{ci} and is represented by $(\phi \cdot \mathbf{u})_{f_{ci}} \cdot \mathbf{S}_{f_i}$, where \mathbf{S}_{f_i} is the face area vector pointing outwards the cell — see [Figure 33](#). The following equations are written in terms of C , where the subscripts $(\star)_{C_c}$ and $(\star)_{f_{ci}}$ represent quantities evaluated at the cell center C_c and the face center f_{ci} , respectively.

The iterative numerical method uses the PIMPLE algorithm, see [section C.3](#) on [page 181](#), which loops through a *prediction-correction* pair of phases that build up the solution for each time step in the simulation. In this case, the PIMPLE algorithm is adapted to include [Equation 3.43](#), the equation for α_s . [Source code 2](#) describes the final algorithm of the PSL model, and the following list details the functions in the code. In the equations, the superscript $(\star)^o$ refers to values from previous time steps or loop iterations.

Source code 2 – PSL Algorithm.

¹¹ See the Divergence theorem in [subsection B.1.1](#) on [page 161](#).

```

1:   u = u_0; p = p_0; rho = rho_0;
2:   for(t = t_0; t < t_final; t += dt) {
3:       // solve alpha equation and update rho
4:       rho = updateMixtureDensity(u);
5:       while(PIMPLE.loop()) {
6:           u_star = predictMomentum(rho, u, p);
7:           while(PIMPLE.correct()) {
8:               p = correct(u_star, p);
9:           }
10:      }
11:  }

```

- `updateMixtureDensity(\mathbf{u}^o, α_s^o)`

The first action in every new time step iteration, right before the PIMPLE loop, is the computation of a new value of ρ . The mixture density ρ , recalling [Equation 3.27](#),

$$\rho = \alpha_s \rho_s + \alpha_a \rho_a,$$

is required by the momentum equation, [Equation 3.41](#), and is computed through α_s , solved by [Equation 3.43](#):

$$\frac{\partial \alpha_s}{\partial t} + \nabla \cdot (\mathbf{u}^o \alpha_s) = \nabla \cdot \left(\left(D_{AB} + \frac{v_t}{Sc} \right) \nabla \alpha_s \right).$$

Here, a sequential operator splitting similar to [Greenshields *et al.* \(2010\)](#) can be used¹². First, just the inviscid portion of the equation is explicitly solved for α_s^I (with the superscript $(\star)^I$ referring to as the inviscid solution), given by

$$\frac{\partial \alpha_s^I}{\partial t} + \underbrace{\nabla \cdot (\mathbf{u}^o \alpha_s^o)}_{\text{advection}} = 0. \quad (3.62)$$

In order to guarantee boundedness in the solution of the advective term marked above, advection is solved explicitly by a *flux-correction transport method*¹³, which provides a bounded value for the fluxes $(\alpha_s^o \mathbf{u}^o)_{fci}$. The resulting α_s^I is assigned to α_s and a second equation containing the diffusion contribution is built:

$$\underbrace{\frac{\partial \alpha_s}{\partial t}}_1 = \nabla \cdot \underbrace{\left(\left(D_{AB} + \frac{v_t}{Sc} \right) \nabla \alpha_s \right)}_2 + \underbrace{\frac{\partial \alpha_s^I}{\partial t}}_3. \quad (3.63)$$

¹² The idea is to split the equation into two equations: the *inviscid equation*, that accounts only for inviscid contributions and the *diffusion correction equation* that includes the diffusion term and the rest.

¹³ See MULES in [Appendix C, section C.2](#)

The equation above is solved by the numerical system

$$\mathbf{A}_\alpha[\alpha_s] = \mathbf{b}_\alpha, \quad (3.64)$$

where each numbered term in Equation 3.63 is translated into the system by the corresponding discretization:

1.

$$\boxed{\frac{\partial \alpha_s}{\partial t}}$$

The transient term is discretized by the first-order implicit Euler:

$$\frac{C_V}{\Delta t} \alpha_s = \frac{C_V}{\Delta t} (\alpha_s^o)_{C_c}, \quad (3.65)$$

where C_V is the volume of the cell. Here and in the following equations, the coefficients multiplying α_s are entries in the matrix \mathbf{A}_α ¹⁴, and coefficients multiplying known values $(\star)^o$ are components of \mathbf{b}_α .

2.

$$\boxed{\nabla \cdot \left(\left(D_{AB} + \frac{v_t}{S_C} \right) \nabla \alpha_s \right)}$$

Considering the coefficients above constant, the laplacian term follows the same procedure detailed in subsection B.1.6 on page 172 in Appendix B:

$$\begin{aligned} \Gamma \Delta \alpha_s &\approx \sum_{f_i \in S} (\nabla_{\mathbf{n}_i} \alpha_s)_{f_{ci}} S_{f_i} \\ &\approx a_C (\alpha_s)_{C_c} + \sum_{f_i \in S} a_{N_i} (\alpha_s)_{N_{ci}} + b_C, \\ a_C &= \Gamma \sum_{f_i \in S} \not\perp_{corr_i} S_{f_i}, \\ a_{N_i} &= -\Gamma \not\perp_{corr_i} S_{f_i}, \\ b_C &= \Gamma \sum_{f_i \in S} (\nabla \alpha_s^o)_{f_{ci}} \cdot (\mathbf{n}_i - \not\perp_{corr_i} \mathbf{d}_i) S_{f_i} \\ \Gamma &= D_{AB} + \frac{v_t}{S_C}, \end{aligned} \quad (3.66)$$

where $\mathbf{d}_i = N_{ci} - C_c$, and $\not\perp_{corr_i}$ is a non-orthogonal correction factor as described in subsection B.1.4 on Appendix B.

3.

$$\boxed{\frac{\partial \alpha_s^I}{\partial t}}$$

The explicit transient term is discretized by the first-order implicit Euler and contributes only to the right-hand side:

$$\frac{C_V}{\Delta t} (\alpha_s^I - \alpha_s^o)_{C_c}. \quad (3.67)$$

¹⁴ Terms related to $(\star)_{C_c}$ correspond to diagonal entries of \mathbf{A}_α , while the remaining correspond to off-diagonal entries.

The resulting value of α_s provides the new value for ρ ¹⁵.

- $\mathbf{u}^* \leftarrow \text{predictMomentum}(\rho, \mathbf{u}^o, p^o)$

In the **momentum prediction** phase, an intermediary velocity field \mathbf{u}^* is computed from the new value of ρ and previous values of velocity and pressure (ρ, \mathbf{u}^o, p^o). This field is the solution of the the numerical system

$$\mathbf{A}\mathbf{u}^* = \mathbf{b}, \quad (3.68)$$

built from the FVM discretization of the momentum equation, Equation 3.41:

$$\underbrace{\frac{\partial \rho^o \mathbf{u}^*}{\partial t}}_1 + \underbrace{\nabla \cdot (\rho^o \mathbf{u}^o \otimes \mathbf{u}^*)}_2 = \underbrace{-\nabla p_{rgh}^o - \mathbf{g} \cdot \mathbf{h} \nabla \rho^o}_3 + \underbrace{\nabla \cdot \boldsymbol{\tau}^*}_4, \quad (3.69)$$

where each term in the equation translates as:

1.

$$\boxed{\frac{\partial \rho^o \mathbf{u}^*}{\partial t}}$$

The transient term is discretized by the first-order implicit Euler:

$$\frac{C_V}{\Delta t} (\rho^o)_{C_c} \mathbf{u}^* = \frac{C_V}{\Delta t} (\rho^o \mathbf{u}^o)_{C_c}. \quad (3.70)$$

2.

$$\boxed{\nabla \cdot (\rho^o \mathbf{u}^o \otimes \mathbf{u}^*)}$$

The convective term follows the usual choice for large eddy simulations, the linear scheme, sacrificing boundedness for accuracy:

$$\sum_{f_i \in S} (w_i \Phi^o)_{f_i} \otimes (\mathbf{u}^*)_{C_c} + \sum_{f_i \in S} (-w_i \Phi^o + \Phi^o)_{f_i} \otimes (\mathbf{u}^*)_{N_{ci}}, \quad (3.71)$$

where $\Phi^o = \rho^o \mathbf{u}^o$ is the mass flux, and w_i is the interpolation weight based on the cell center to face centers distances, $\mathbf{d}_C = f_{ci} - C_c$ and $\mathbf{d}_{Ni} = N_{ci} - f_{ci}$:

$$w_i = \frac{\mathbf{n} \cdot \mathbf{d}_{Ni}}{\mathbf{n} \cdot (\mathbf{d}_C + \mathbf{d}_{Ni})}. \quad (3.72)$$

3.

$$\boxed{-\nabla p_{rgh}^o - \mathbf{g} \cdot \mathbf{h} \nabla \rho^o}$$

The scalar gradient discretization for the source terms produce the following contributions to the right hand side of the system:

$$-\sum_{f_i \in S} (p_{rgh}^o)_{f_i} \mathbf{S}_{f_i} - \mathbf{g} \cdot \mathbf{h} \sum_{f_i \in S} (\rho^o)_{f_i} \mathbf{S}_{f_i}, \quad (3.73)$$

where $\mathbf{h} = C_c$.

¹⁵ Recall $\alpha_a = 1 - \alpha_s$, therefore $\rho = \alpha_s \rho_s + (1 - \alpha_s) \rho_a$.

4.

$$\boxed{\nabla \cdot \boldsymbol{\tau}^*}$$

The expansion of the tensor term is¹⁶:

$$\begin{aligned}\nabla \cdot \boldsymbol{\tau}^* &= \mu \Delta \mathbf{u}^* + \mu \nabla \cdot \mathbf{Dev}^o, \\ \mathbf{Dev}^o &= (\nabla \otimes \mathbf{u}^o)^T - \frac{2}{3} \text{tr}((\nabla \otimes \mathbf{u}^o)^T) \mathbf{I},\end{aligned}\tag{3.74}$$

where the explicit terms are discretized as

$$\begin{aligned}(\nabla \otimes \mathbf{u}^o)_{C_c} &\approx \frac{1}{C_V} \sum_{f_i \in S} (\mathbf{u}^o)_{f_{ci}} \otimes \mathbf{S}_{f_i}, \\ (\nabla \cdot \mathbf{Dev}^o)_{C_c} &\approx \frac{1}{C_V} \sum_{f_i \in S} (\mathbf{Dev}^o)_{f_{ci}} \cdot \mathbf{S}_{f_i}.\end{aligned}\tag{3.75}$$

The laplacian term $\mu \Delta \mathbf{u}^*$ follows the same procedure detailed in [subsection B.1.6](#) on [page 172](#) in [Appendix B](#):

$$\begin{aligned}\mu \Delta \mathbf{u}^* &\approx \sum_{f_i \in S} (\nabla_{\mathbf{n}_i} \otimes \mathbf{u}^*)_{f_{ci}} \mathbf{S}_{f_i} \\ &\approx a_C(\mathbf{u}^*)_{C_c} + \sum_{f_i \in S} a_{N_i}(\mathbf{u}^*)_{N_i} + b_C, \\ a_C &= \mu \sum_{f_i \in S} \not\propto_{corr_i} \mathbf{S}_{f_i}, \\ a_{N_i} &= -\mu \not\propto_{corr_i} \mathbf{S}_{f_i}, \\ b_C &= \mu \sum_{f_i \in S} (\nabla \otimes \mathbf{u}^o)_{f_{ci}} \cdot (\mathbf{n}_i - \not\propto_{corr_i} \mathbf{d}_i) \mathbf{S}_{f_i}.\end{aligned}\tag{3.76}$$

The final form of the discretization in the system becomes:

$$-a_C(\mathbf{u}^*)_{C_c} - \sum_{f_i \in S} a_{N_i}(\mathbf{u}^*)_{N_i} = b_C + (\nabla \cdot \mathbf{Dev}^o)_{C_c}.\tag{3.77}$$

• `correct(u*, p_rgh)`

¹⁶ Recalling the definition of $\boldsymbol{\tau}$ by [Equation 3.33](#), and noting that for any matrix \mathbf{M}

$$\text{tr}\left(\frac{1}{2}(\mathbf{M} + \mathbf{M}^T)\right) = \text{tr}(\mathbf{M}) = \text{tr}(\mathbf{M}^T),$$

the term expands as:

$$\begin{aligned}\nabla \cdot \boldsymbol{\tau} &= \nabla \cdot \left(\underbrace{2\mu \mathbf{D}}_{\text{expand}} - \frac{2}{3} \underbrace{\mu \text{tr}(\mathbf{D}) \mathbf{I}}_{\text{expand}} \right) \\ &= \nabla \cdot \left(\overline{(\mu \nabla \otimes \mathbf{u} + \mu (\nabla \otimes \mathbf{u})^T)} - \frac{2}{3} \overline{\mu \text{tr}((\nabla \otimes \mathbf{u})^T) \mathbf{I}} \right) \\ &= \mu \Delta \mathbf{u} + \mu \nabla \cdot ((\nabla \otimes \mathbf{u})^T) - \frac{2}{3} \text{tr}((\nabla \otimes \mathbf{u})^T) \mathbf{I}\end{aligned}$$

The momentum prediction step provides an estimate for the velocity \mathbf{u}^* by solving the system

$$\mathbf{A}\mathbf{u}^* = \mathbf{b}.$$

However, the system above does not include the continuity equation, $\nabla \cdot \mathbf{u} = 0$, and therefore, \mathbf{u}^* is not a divergence-free field. Also, the system does not compute the coupled pressure field p_{rgh} ; instead, it uses a previous pressure field p_{rgh}^o . A new pressure field p computed from \mathbf{u}^* completes the coupled solution and fixes \mathbf{u}^* .

The pressure equation is constructed by substituting the continuity equation into the divergence of the momentum equation, see [section C.3](#) on [page 181](#). In FVM, the **pressure equation** is defined as

$$\underbrace{\nabla \cdot \frac{1}{A_{diag}} \nabla p_{rgh}}_1 = \underbrace{\nabla \cdot \left(\frac{\mathbf{B}(\mathbf{u}^*)}{A_{diag}} \right)}_2. \quad (3.78)$$

The terms A_{diag} and $\mathbf{B}(\mathbf{u}^*)$ come from the system

$$A_{diag}\mathbf{u}^* = \mathbf{B}(\mathbf{u}^*) - \nabla p_{rgh}, \quad (3.79)$$

where the pressure term is separated from the original system, \mathbf{A}_{diag} contains only the diagonal entries of the resulting system without the pressure term, and $\mathbf{B}(\mathbf{u}^*)$ contains all off-diagonal elements and source terms:

$$\mathbf{B}(\mathbf{u}^*) = -(\mathbf{A} - A_{diag})\mathbf{u}^* + b. \quad (3.80)$$

[Equation 3.78](#) is solved by the system

$$\mathbf{A}_p[p_{rgh}] = \mathbf{b}_p, \quad (3.81)$$

and each numbered term in the equation translates into the system as:

1.

$$\boxed{\nabla \cdot \frac{1}{A_{diag}} \nabla p_{rgh}}$$

The laplacian of the pressure is discretized as in [Equation 3.76](#), resulting in

$$-a_C(p_{rgh})_C - \sum_{f_i \in S} a_{N_i}(p_{rgh})_{N_i} = b_C, \quad (3.82)$$

with appropriate coefficient values.

2.

$$\boxed{\nabla \cdot \left(\frac{\mathbf{B}(\mathbf{u}^*)}{A_{diag}} \right)}$$

The divergence term is explicitly solved, i.e. it becomes a source term discretized as

$$\sum_{f_i \in S} \left(\frac{\mathbf{B}(\mathbf{u}^*)}{A_{diag}} \right)_{f_i} \cdot \mathbf{S}_{f_i}, \quad (3.83)$$

where the terms below come from the momentum equation discretization described earlier:

$$\left(\frac{\mathbf{B}(\mathbf{u}^*)}{A_{diag}}\right)_{C_c} = \frac{1}{A_{diag}} \left(\underbrace{\frac{C_V}{\Delta t} (\rho^o \mathbf{u}^o)_{C_c}}_{\text{Equation 3.70}} + \underbrace{-\mathbf{g} \cdot \mathbf{h} \sum_{f_i \in S} (\rho^o)_{f_{ci}} \mathbf{S}_{f_i}}_{\text{Equation 3.73}} + \underbrace{b_C + (\nabla \cdot \mathbf{Dev}^o)_{C_c}}_{\text{Equation 3.77}} \right). \quad (3.84)$$

With the new value of p_{rgh} , the velocity field \mathbf{u}^* can be corrected with

$$\mathbf{u} \leftarrow \frac{\mathbf{B}(\mathbf{u}^*)}{A_{diag}} - \frac{\nabla p_{rgh}}{A_{diag}}, \quad (3.85)$$

where \mathbf{u} is the new divergence-free velocity field.

3.4 Remarks

- The DSL model consists of Equation 3.11, Equation 3.6, and Equation 3.7, respectively:

$$\frac{\partial h'}{\partial t} + \nabla \cdot (h' \bar{\mathbf{u}}) = \frac{q_e}{\rho},$$

$$\frac{\partial (h' \bar{\mathbf{u}})}{\partial t} + \nabla_S \cdot (h' \bar{\mathbf{u}} \otimes \bar{\mathbf{u}}) = -\frac{\tau_b}{\rho} + h' \mathbf{g}_S - \frac{1}{2\rho} \nabla_S (h' p_b),$$

$$\nabla_n \cdot (h' \bar{\mathbf{u}} \otimes \bar{\mathbf{u}}) = h' \mathbf{g}_n - \frac{1}{2\rho} \nabla_n (h' p_b) - \frac{1}{\rho} \mathbf{n} p_b,$$

where q_e is given by Equation 3.9 and τ_b is given by Equation 3.13.

- The PSL model consists of Equation 3.28, Equation 3.41, and Equation 3.43, respectively:

$$\nabla \cdot \mathbf{u} = 0,$$

$$\frac{\partial \rho \mathbf{u}}{\partial t} + \nabla \cdot (\rho \mathbf{u} \otimes \mathbf{u}) = -\nabla p_{rgh} - \mathbf{g} \cdot \mathbf{h} \nabla \rho + \nabla \cdot \boldsymbol{\tau},$$

$$\frac{\partial \alpha_s}{\partial t} + \nabla \cdot (\mathbf{u} \alpha_s) = \nabla \cdot \left(\left(D_{AB} + \frac{V_t}{SC} \right) \nabla \alpha_s \right),$$

where $\boldsymbol{\tau}$ is given by Equation 3.36.

- The PSL model builds upon the simplification that the mixture fluid of snow and air is incompressible.
- The PSL model is agnostic of the DSL model used, which means that other DSL models serving the same type of information can replace the presented DSL model. The PSL model requires only the DSL height field $h_{dsl}(\mathbf{x})$, surface-tangential field $\mathbf{u}_{dsl}(\mathbf{x})$, and the height variation rate $w_h(\mathbf{x})$ optionally.

Table 6 – Transition Layer models.

Method	\mathbf{u}_{inj}	α_{inj}
1	S	A
2	γw_h	1

- The transition layer becomes a set of Dirichlet boundary conditions for the PSL's bottom boundary, particularly for the PSL velocity field \mathbf{u} and volume concentration of snow field α . [Table 6](#) summarizes the models considered in this chapter.
- An extra oscillatory term applied to the resulting quantities of the transition layer emulates the intermittent behavior caused by turbulence in the front of the avalanche.
- [Table 7](#) and [Table 8](#) list the constants present in the DSL and PSL models.

Table 7 – DSL model parameters.

Parameter	Description	Units
ρ	Snow density	$kg \cdot m^{-3}$
μ	Voellmy's dry friction	$m^2 \cdot kg^{-1}$
ξ	Voellmy's dynamic friction	–
e_b	Erosion energy	–

Table 8 – PSL model parameters.

Parameter	Description
ρ_a	Air density
ρ_s	Powder-snow density
D_{ab}	Molecular diffusivity
ν_t	Turbulent eddy viscosity
S_C	Turbulent Schmidt number

RESULTS

This chapter describes the final pieces to build the system for producing animations of powder-snow avalanches, which includes the creation of the numerical meshes, choosing the values for the parameters of the models, and exporting animation data.

The following section describes all remaining numerical details to complete the simulation workflow. A discussion and analysis of the method is presented in [section 4.2](#) on [page 112](#). Before presenting the final results, [section 4.3](#) on [page 114](#) quickly describes how simulation data is converted into renderable geometry. The chapter finalizes with [section 4.4](#) on [page 118](#), presenting the final results of avalanches simulated on natural terrain surfaces.

4.1 Numerical Setup

As described in the previous chapter, the numerical solutions require discretizing the governing equations over decomposing the physical domain into a set of discrete cells for each simulation. Each cell contains estimates of physical quantities, such as the velocity field U or the concentration of volume A . The transport of such quantities between the cells manifests as fluxes through their boundaries. Each cell spans a discrete version of the governing equation based on its fluxes and cell values, and the set of such equations produces a numerical system. The system produces new values for the physical fields that evolve over simulation time, generating data for each animation frame.

The following subsections detail the process described above for each PSA layer. Each subsection describes the remaining pieces for each simulation: the numerical grid, the *boundary conditions*¹, and the numerical solvers. One extra subsection discusses the implementation of the transition layer.

¹ As mentioned, the fluxes used in the discretizations require a pair of cells. However, cells at the mesh's boundary lack neighbors and need boundary conditions to complete their discretizations. Refer to [subsection B.1.7](#) on how the FVM discretizes such boundary conditions.

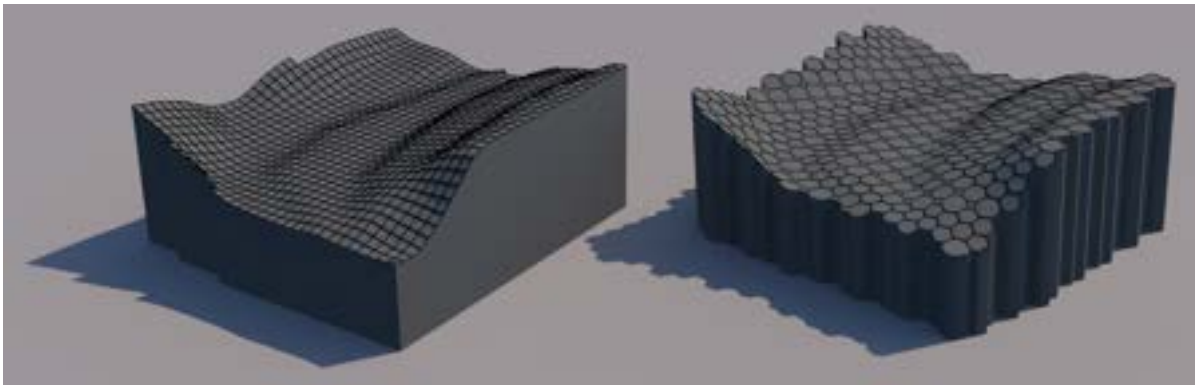
4.1.1 DSL

Numerical Grid

The numerical grid used in the simulation of the DSL is a three-dimensional discrete surface represented by a set of two-dimensional flat² polygonal cells individually bounded by straight edges.

In simulation setups where the terrain is a plane, a set of regular cells poses no difficulties for the numerical solution. However, in natural terrains with high curvatures, other polygonal alternatives, such as triangular meshes, can produce mesh elements that better adapt to the terrain. Particularly, the **pMesh**³ structure provided by OpenFOAM offers a flexible solution. The **pMesh** fills a triangular mesh volume with a polyhedral mesh, composed mainly of hexahedra, providing various benefits for subdivision and adaptiveness. The boundary surface of a **pMesh** may be used as the DSL numerical grid. Figure 34 shows the two types of mesh described above.

Figure 34 – Two examples of meshes tessellating the same patch of terrain. On the left is a regular quadrangular mesh. On the right is a polyhedral mesh that is well adapted for terrains with complex geometries.



Source: Elaborated by the author.

Boundary Conditions

The DSL model consists of Equation 3.11, Equation 3.6, Equation 3.7. The equations contain three unknown variables: the velocity field $\bar{\mathbf{u}}(\mathbf{x})$, the basal pressure field $p_b(\mathbf{x})$, and the DSL height field $h'(\mathbf{x})$. Since the basal pressure is explicitly solved inside the momentum equation, the method needs boundary conditions for only the velocity and the avalanche height fields. As listed in Table 9⁴, a Neumann condition is used in all boundary edges for all fields.

² Note that in practice, the vertices of a cell may not be coplanar.

³ The **pMesh** is a meshing option of the meshing library called *cfMesh*, incorporated in OpenFOAM. See <<https://cfmesh.com/>>.

⁴ Recall the normal gradient $\nabla_{\mathbf{m}}$ along the direction edge bi-normal vector \mathbf{m} . See section B.2 in Appendix B.

Table 9 – DSL Boundary Conditions.

Variable	Boundary	Condition
$\bar{\mathbf{u}}$	All	$\nabla_{\mathbf{m}}\bar{\mathbf{u}} = 0$
h'	All	$\nabla_{\mathbf{m}}h' = 0$

Accuracy

The following tables give information on the solution of the numerical method described in subsection 3.2.1. Table 10 lists the numerical schemes for interpolation used in each discretization term, and Table 11 shows the numerical solvers for each numerical system.

The *upwind* scheme was used to compute all convection terms, while all transient terms were discretized with the *backward* Euler scheme. The gradient terms were directly discretized via the Divergence theorem, where all variables were computed at face centers by linear interpolation. The *boundedness* column in Table 10 indicates if the scheme produces resulting values within the original bounds of their respective fields in the cells.

Table 10 – DSL Numerical Schemes.

Term	Scheme	Boundedness	Accuracy
$\nabla_S \cdot (h^o \bar{\mathbf{u}}^o \otimes \bar{\mathbf{u}})$	Upwind	Bounded	First-Order
$\nabla \cdot (h \bar{\mathbf{u}}^o)$	Upwind	Bounded	First-Order
$\partial \star / \partial t$	Backward Time	-	Second-Order
$\nabla_S (h^o p_b^o)$	Gauss w/ Linear Interpolation	Unbounded	Second-Order

Both numerical systems were solved with Preconditioned bi-conjugate gradient (PBiCGStab)⁵ (VORST, 1992) along with the Diagonal-based Incomplete LU (DILU) preconditioner.

Table 11 – DSL Numerical Solvers.

System	Solver	Preconditioner
$\mathbf{A}\bar{\mathbf{u}} = \mathbf{b}$	PBiCGStab	DILU
$\mathbf{A}_h[h] = \mathbf{b}_h$	PBiCGStab	DILU

4.1.2 PSL

Numerical Grid

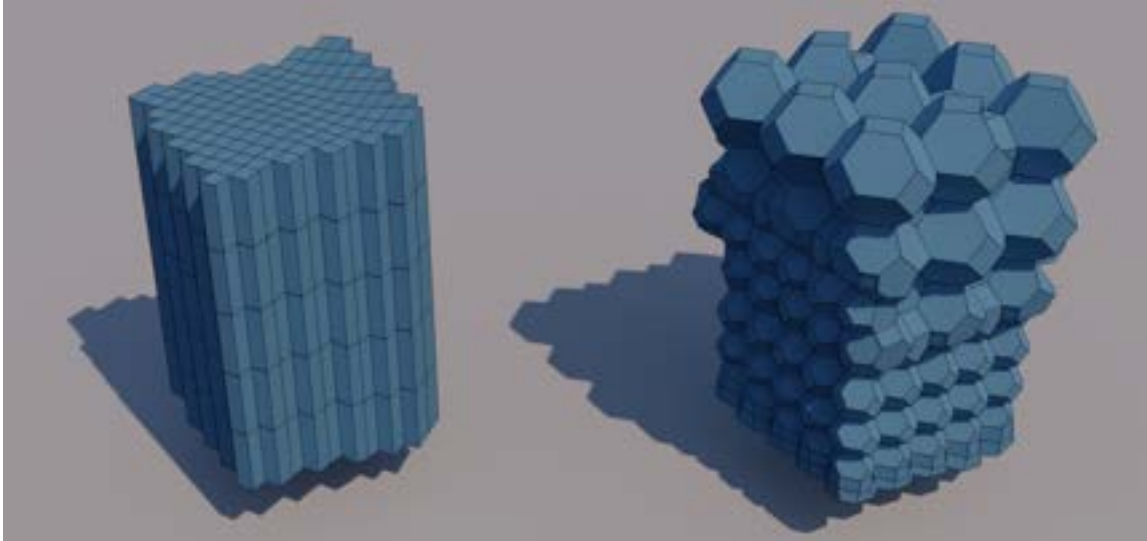
The numerical grid used in the simulation of the PSL is a three-dimensional discrete volume represented by a set of three-dimensional cells individually bounded by flat faces.

Similar to DSL surface decompositions, the three-dimensional cells in the PSL grid may consist of regular aligned boxes or more complex polygonal shapes. Note that regardless of the choice of element type, mesh generation algorithms may still produce non-planar faces and

⁵ The PBiCGStab is designed for numerical systems with an assymmetric matrix \mathbf{A} , usually produced by terms like the advection.

concave cells. Figure 35 shows two examples of three-dimensional meshes, one consisting of axis-aligned boxes and the second resulting from the **pMesh** structure mentioned earlier.

Figure 35 – Examples of PSL numerical grids. On the left, a mesh consisting of axis-aligned boxes extruded from a quadrangular surface mesh. On the right, a polyhedral mesh with varying element types and sizes.



Source: Elaborated by the author.

Boundary Conditions

The PSL model consists of Equation 3.28, Equation 3.41, and Equation 3.43. The equations contain three unknown variables: the velocity field $\mathbf{u}(\mathbf{x})$, the concentration of volume for the snow phase field $\alpha_s(\mathbf{x})$, and the hydrostatic pressure $p_{rgh}(\mathbf{x})$.

As shown by Figure 36, the boundary of the simulation domain is decomposed into six patches, one for each direction of the coordinates axis. Therefore, a boundary condition is defined for each variable over each patch. In particular, the **terrain** patch receives the boundary conditions for \mathbf{u} and α_s that represent the transition layer.

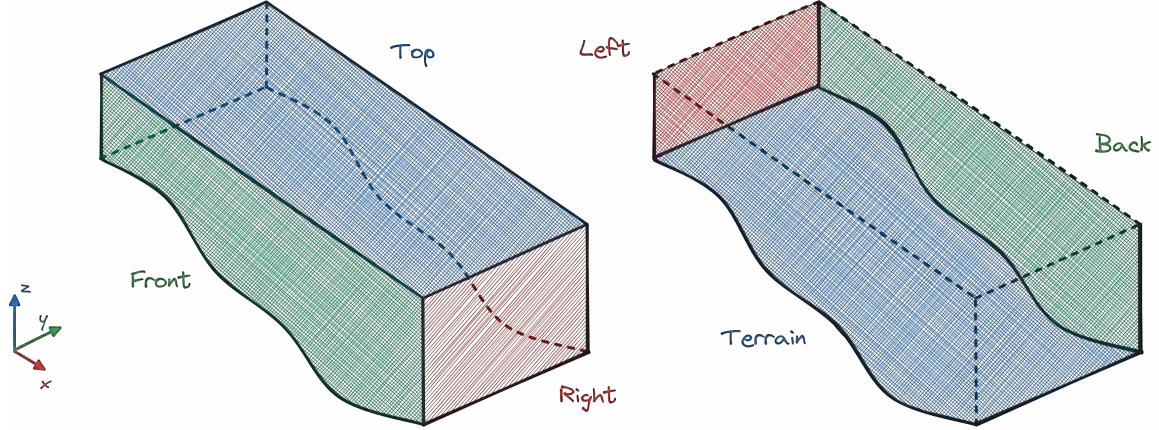
The following list presents the considered options for boundary conditions, where \star denotes any field mentioned earlier, \star_b represents a defined value for this field at the boundary, and \mathbf{n}_b is the normal of the boundary face pointing outwards the cell. Some conditions depend on the direction of the flow, dictated by $\mathbf{u} \cdot \mathbf{n}_b$, that characterizes *inflow* and *outflow* from the domain:

$$\begin{aligned} \mathbf{u} \cdot \mathbf{n}_b < 0 &\rightarrow \text{Inflow,} \\ \mathbf{u} \cdot \mathbf{n}_b > 0 &\rightarrow \text{Outflow.} \end{aligned} \tag{4.1}$$

- **Zero Gradient** — The Neumann boundary condition for zero flow.

$$\nabla_{\mathbf{n}_b} \star = 0. \tag{4.2}$$

Figure 36 – Regardless of the shape of the simulation terrain, six patches comprise the boundaries of the numerical domain. Considering the slope alignment with the Cartesian axis x , each axis associates a pair of patches respectively: **Back** and **Front** in $\pm y$ directions, **Top** and **Terrain** in $\pm z$, and **Right** and **Left** in $\pm x$.



Source: Elaborated by the author.

- **Dirichlet** — Uses a known value \star_b for the field.

$$\star = \star_b. \quad (4.3)$$

- **Free** — Allows inflow and outflow.

$$\begin{cases} \star = \star_b, & \text{Inflow,} \\ \nabla_{\mathbf{n}_b} \star = 0, & \text{Outflow.} \end{cases} \quad (4.4)$$

- **Free Velocity** — Allows velocity inflow and outflow on boundaries with Dirichlet condition for pressure.

$$\begin{cases} \mathbf{u} = -\mathbf{u} \cdot \mathbf{n}_b, & \text{Inflow,} \\ \nabla_{\mathbf{n}_b} \mathbf{u} = 0, & \text{Outflow.} \end{cases} \quad (4.5)$$

- **Slip** — Allows only tangential velocities at the boundary.

$$(\mathbf{u})_{\mathbf{n}_b} = 0. \quad (4.6)$$

- **No Slip**

$$\mathbf{u} = 0. \quad (4.7)$$

- **Total Pressure**

$$\begin{cases} p_{rgh} = p_0 - \frac{1}{2}|\mathbf{u}|^2, & \text{Inflow,} \\ p_{rgh} = p_0, & \text{Outflow,} \end{cases} \quad (4.8)$$

where p_0 is a reference pressure value.

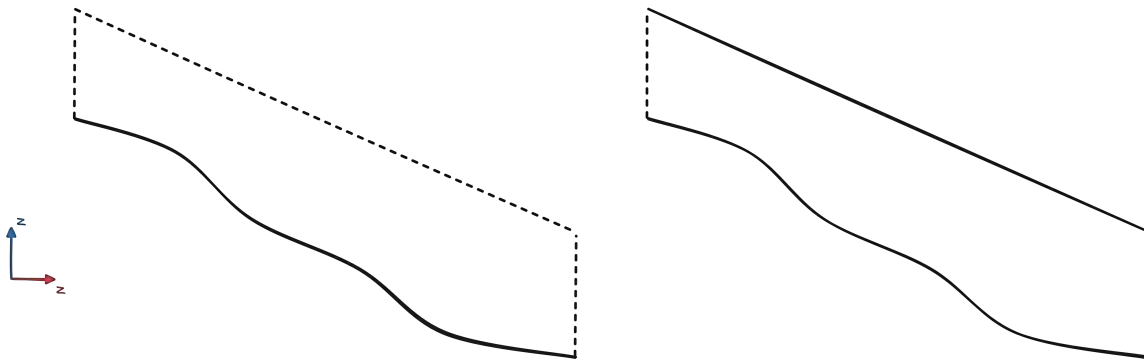
- **Fixed Flux Pressure** — Ensures no flux

$$\nabla p_{rgh} = \frac{\phi_{H/A} - \phi}{|S_f|D_p} \quad (4.9)$$

flux fixed pressure

The choices of the different types of boundary conditions listed above have an impact not only on the physical modeling of the problem but also on the stability of the numerical solution. The cubical shape of the physical domain described earlier, given by the six boundary patches, provides some combination options for boundary conditions. A natural choice is to consider all five patches, besides the *terrain* patch, as **open free** boundaries where mass can freely flow inwards and outwards — as in a large mountain. However, adding some constraints, such as wall boundaries, might increase the method's stability.

Figure 37 – Boundary patches can be modeled as closed or open boundaries. Mass will flow through open boundaries, which can be free (allowing inflow and outflow) or restricted to inflow or outflows. Although making all boundaries *free* makes sense (left), adding additional flow restrictions, such as the solid top on the right, may help the numerical method.



Source: Elaborated by the author.

Figure 37 depicts two possible configurations, which model the domain as an open box and a tunnel. Open boundaries are classified as **free**, **inlet**, and **outlet** boundaries. Inlet boundaries allow only inflow, and outlet boundaries allow only outflow. From our experiments, fixing a small velocity \mathbf{u}_ϵ at the *left* and *right* patches, like a *wind tunnel*, produced to more stable results. Table 12 details the wind tunnel approach described above, where top, front and back patches are modeled as walls. The values used in the terrain boundary condition are detailed later in subsection 4.1.3.

Accuracy

The following tables give information on the solution of the numerical method described in subsection 3.3.2. Table 13 lists the numerical schemes for interpolation used in each discretization term, and Table 14 shows the numerical solvers for each numerical system. The *vanLeer01*

Table 12 – "Wind Tunnel" PSL Boundary Conditions.

		α_s	\mathbf{u}	p_{rgh}
Front/Back	wall	0	Slip	Zero Gradient
Left	outflow	Zero Gradient	\mathbf{u}_ε	Zero Gradient
Right	inflow	0	\mathbf{u}_ε	Zero Gradient
Top	free	Free	Free (with p_b)	Total Pressure
Terrain	-	α_{inj}	\mathbf{u}_{inj}	Fixed Flux Pressure

scheme listed in Table 13 is a TVD advection scheme⁶, introduced by van Leer (1974), that uses limiter function to bound the results — in this case, to $[0, 1]$, indicated by the *01* suffix.

Table 13 – PSL Numerical Schemes.

Term	Scheme	Boundedness	Accuracy
$\nabla \cdot (\rho \Phi \bar{\mathbf{u}})$	Linear Interpolation	Unbounded	Second-Order
$\nabla \cdot (\Phi \alpha)$	vanLeer01	Bounded	Second-Order
$\partial \star / \partial t$	Implicit Euler	-	First-Order
$\nabla(\mathbf{u})$	Cell limited Gauss w/ Linear Interpolation 1.0	Unbounded	Second-Order

The numerical systems were mainly solved by the Gauss-Seidel iterative method along with the Diagonal-based Incomplete LU (DILU) preconditioner. The GAMG method, listed in Table 14, is an algebraic multi-grid method commonly used in finite volume problems for fluid simulations (GREENSHIELDS; WELLER, 2022).

Table 14 – PSL Numerical Solvers.

Term	Solver	Preconditioner
$\mathbf{A}_\alpha[\alpha_s] = \mathbf{b}_\alpha$	Gauss Seidel	-
$\mathbf{A}\mathbf{u}^* = \mathbf{b}$	Gauss Seidel	DILU
$\mathbf{A}_p[p_{rgh}] = \mathbf{b}_p$	GAMG Gauss Seidel	DILU

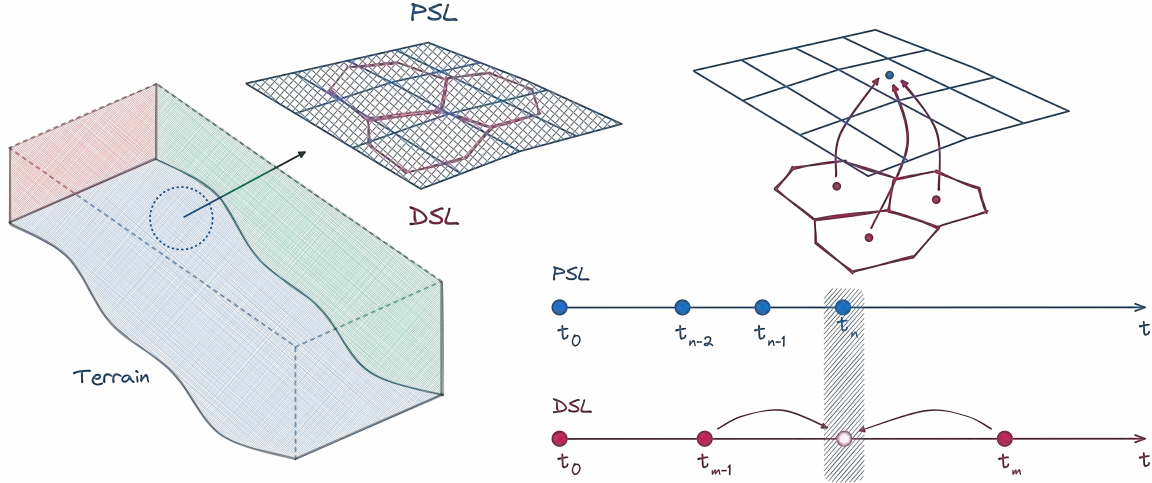
4.1.3 Transition Layer

As presented in subsection 3.3.1, the transition layer manifests as boundary conditions for the mass and velocity fields, α_s and \mathbf{u}_{psl} (the subscripts \star_{dsl} and \star_{psl} will be used in this section to facilitate the distinction of DSL and PSL values, respectively). Such conditions are defined by direct value assignment, characterizing the Dirichlet boundary condition listed for the *terrain* patch on Table 12 in the previous section.

The boundary values of α_s and \mathbf{u}_{psl} are defined for each *terrain* patch face f_b on every time step. These values are mainly based on temporal DSL fields, such as the DSL velocity field $\mathbf{u}_{dsl}(\mathbf{x}, t)$. Therefore, the *terrain* patch geometry represents the interface between both layers, since each face f_b will carry the state of the DSL at its location for a particular time t — see Figure 38.

⁶ See subsection B.1.5.

Figure 38 – The DSL and PSL simulations can share different geometry, topology, or time steps. The transition layer requires the transference of information between both layers. The example below considers a DSL simulated in a hexagonal mesh registered at times $[\dots, t_m, t_{m+1}, \dots]$. The terrain patch of the PSL grid is a quadrangular mesh and follows a different set of time steps $[\dots, t_n, t_{n+1}, \dots]$. When simulating the PSL, the DSL state is needed at time t_n , which falls between times t_{m-1} and t_m ; therefore, DSL values are interpolated temporally and spatially between cell centers.



Source: Elaborated by the author.

Note that the DSL grid and the PSL's terrain patch may not share the same geometry or topology. Moreover, since the simulation of the DSL is independent of the PSL's simulation, it may even use a different value of time steps — see Figure 38. Therefore, the interface between the original DSL fields and their counterparts in the PSL's terrain patch must map the values spatially and temporally, so

$$\star_{psl}(\mathbf{x}, t) \approx \star_{dsl}(\mathbf{x}, t), \quad (4.10)$$

for any DSL field $\star_{dsl}(\mathbf{x}, t)$ at any spatial location \mathbf{x} and time t . As shown in Figure 38, such approximation is performed by linearly interpolating values between DSL time steps and from DSL face center positions.

Front Distance

The front region of the snow avalanche comprises the eruption entrainment process and is where most of the mass and momentum exchanges happen — the closer to the front position \mathbf{x}_f , the higher the intensity of such dynamic. Therefore, α_{inj} and \mathbf{u}_{inj} injection amounts at the position \mathbf{x} depend on its distance to \mathbf{x}_f . Such dependence can be emulated by the weight function

$$w_{front}(\mathbf{x}, \mathbf{x}_f) = \exp\left(-\frac{\|\mathbf{x} - \mathbf{x}_f\|}{L_{front}}\right), \quad (4.11)$$

that decreases from 1 towards 0 as the distance $\|\mathbf{x} - \mathbf{x}_f\|$ increases. The term L_{front} roughly represents the size of the region in meters that defines the front region — i.e., the first L_{front} meters after the leading edge of the avalanche.

The distances $\|\mathbf{x} - \mathbf{x}_f\|$ are *surface distances*. The surface distance function $Sd(\mathbf{x}, \mathbf{x}_f)$ defines the shortest path between two points on a surface, restricted to the surface (like the geodesic distance). As the front position \mathbf{x}_f advances, the distance field $d(\mathbf{x})$ is calculated every time step via a *front-propagation* algorithm.

Source code 3 – Algorithm for computing front distance in the DSL.

```

1: front_cells = detectFrontCells(DSL_mesh);
2: dist(front_cells) = 0;
3: q.push(front_cells);
4: while(!q.empty()) {
5:     cell = q.front();
6:     q.pop();
7:     for(neighbor : cell.neighborsInDirection(-u(cell))) {
8:         new_dist = dist(cell) + distance(cell, neighbor);
9:         if(h(neighbor) > h_min &&
10:            dist(neighbor) > new_dist) {
11:             dist(neighbor) = new_dist;
12:             q.push(neighbor);
13:         }
14:     }
15: }
```

The algorithm, listed in [Source code 3](#), works on the DSL grid cells by (1) first detecting cells that contain the front leading edge, named *front cells*, and (2) then constructing the distance field:

1. Front Cells Detection:

Front cells are cells that intersect the front line of the DSL at a given time. The front line is defined by the DSL's height h and velocity \mathbf{u}_{dsl} . A cell C is considered to intersect the front if there is a neighbor cell N downhill ($C_z > N_z$), at the direction of $\mathbf{u}_{dsl}(C)$, that is empty ($h(N) < h_{min}$).

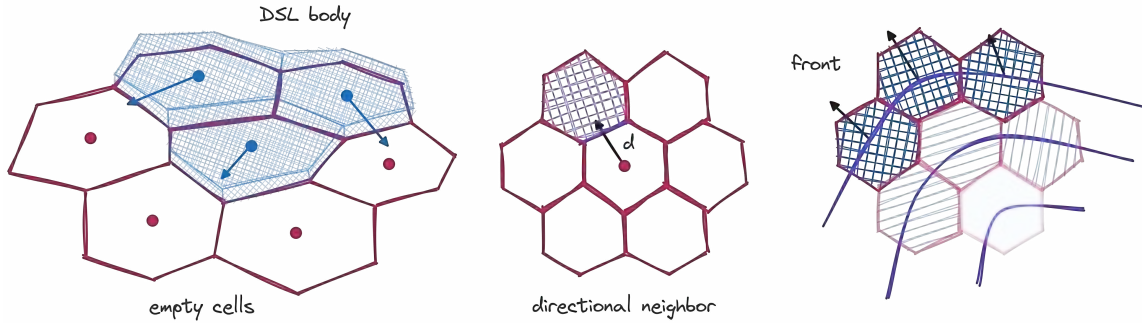
2. Distance Propagation:

The distance field computation starts by setting all front cell distances to zero and putting them into a queue (lines 2-3). While the queue is not empty, the next cell in the queue is taken, and any *affected* neighbor is pushed into the queue. A neighbor is affected if its distance value must be updated. Each cell will hold the smallest distance propagated into it.

For a given cell C , only non-empty neighbors in the upwind direction, $-\mathbf{u}_{dsl}(C)$, are considered.

In the algorithm described above, a neighbor of a cell in the direction \mathbf{d} is the neighbor cell for which the shared face intersects with the ray cast from the cell's center with direction \mathbf{d} — see Figure 39.

Figure 39 – The injection of mass and velocity depends on the distance from the avalanche's leading edge. On the left, front cells represent the leading edge, whose velocity *directional neighbors* are empty (no DSL height). A directional neighbor is a neighbor whose shared face intersects the direction ray \mathbf{d} originated from the cell's center (middle). On the right is the distance field propagated from the front cells. The propagation follows the negative direction of velocity.



Source: Elaborated by the author.

Velocity Injection

The velocity injection occurs in the normal direction of the terrain and depends directly on the front velocity, as described by Equation 3.55:

$$\mathbf{u}_{inj} = \gamma_{\mathbf{u}} \|\mathbf{u}_{front}\| (-\mathbf{n}_b).$$

Since the front region extends for at least L_{front} meters, a convenient assumption is to use the DSL velocity as the front velocity $\mathbf{u}_{front} \approx \mathbf{u}_{dsl}$ in every boundary point \mathbf{x} , so the injection velocity becomes:

$$\mathbf{u}_{inj}(\mathbf{x}) = \gamma_{\mathbf{u}} \|\mathbf{u}_{dsl}(\mathbf{x})\| (-\mathbf{n}_b(\mathbf{x})). \quad (4.12)$$

The term $\gamma_{\mathbf{u}}$ summarizes the intermittent behavior at the front region. The many factors that lead to the turbulent motion at the front include the eruption entrainment process, the air intake from the ambient air, and the violent release of trapped air underneath. Also, the entrainment of snow depends significantly on the constitutive properties of the snow cover.

The snow cover comprises multiple layers of snow of different densities, constituting a heterogeneous body of snow. As such layers interact with the avalanche, they affect the entrainment processes differently.

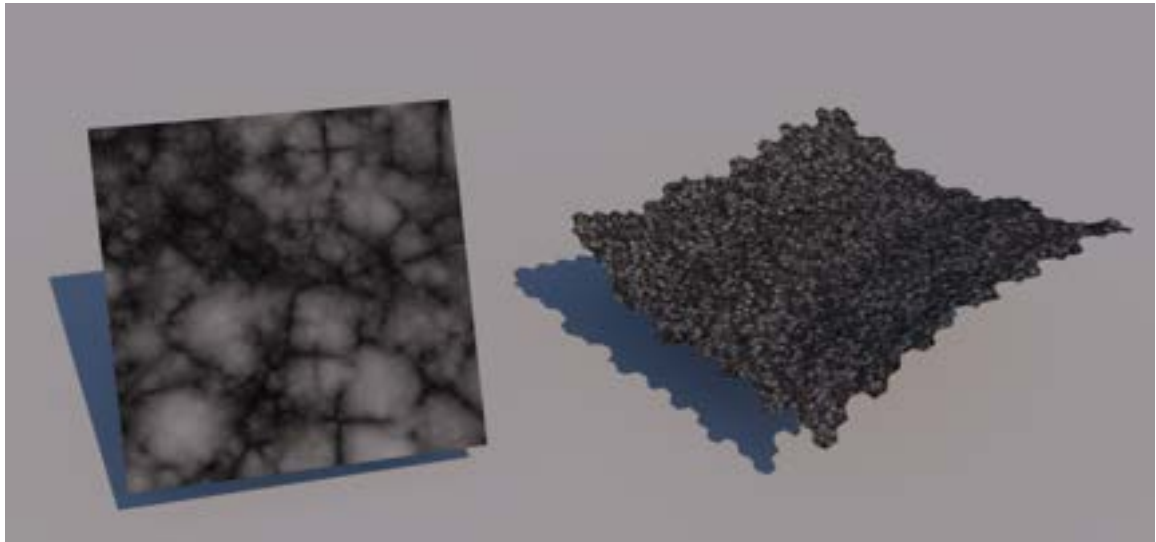
A practical solution to mimic the effects mentioned above is to use a spatial noise function $\Gamma(\mathbf{x})$ for $\gamma_{\mathbf{u}}$, so

$$\gamma_{\mathbf{u}}(\mathbf{x}) = \Gamma(\mathbf{x}), \quad (4.13)$$

which causes random perturbations into the injection velocity associated with the complexity of the snow cover body. Random surges of velocity represent chunks of weak layers being entrained

rapidly. In particular, the family of cellular noise functions, such as the Worley Noise (WORLEY, 1996), produces distinct space regions resembling natural patterns. As shown in Figure 40, once computed over the terrain surface, these regions can be seen as chunks of snow packs of variable densities.

Figure 40 – Cellular noise functions produce natural-like patterns that can compose the complex internal structure of the snow cover. Such random variations in the term U produce surges of velocity that mimic the turbulent nature of entrainment processes.



Source: Elaborated by the author.

The combination of all factors described above now integrates the term U. Considering the front weight explained earlier, the final form of the boundary condition of the velocity becomes:

$$(\mathbf{u})_b = w_{front} \mathbf{u}_{inj} + \mathbf{u}_{dsl}. \quad (4.14)$$

Mass Injection

From Equation 3.60 in subsection 3.3.1, α_{inj} is computed from the mass concentration

$$\alpha_{inj}^v = \frac{m_e}{M^v}$$

for the volume V in the boundary cell. However, the entrainment mass m_e defined in the previous chapter takes the full entrainment of the DSL, which considers injecting the same mass entrained by the DSL into the PSL. Although it does not harm the final animation, a more realistic approach is to consider that only a portion of the snow cover gets into the PSL.

Therefore, a constant $\gamma_\alpha \in [0, 1]$ can adjust the injection value to consider only a fraction of the entrained mass. The final form of the boundary condition for α_s is

$$(\alpha_s)_b = w_{front} \gamma_\alpha \alpha_{inj}^v, \quad (4.15)$$

where w_{front} is the front weight described earlier.

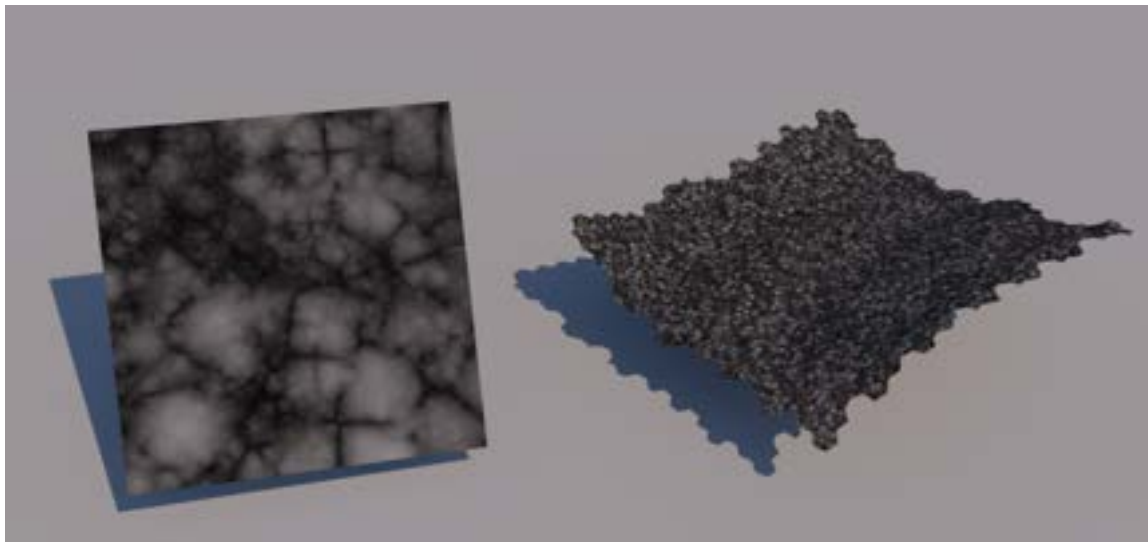
4.2 Discussions

This section explores the impact of the model's parameters on the resulting animation. Besides the value of the physical constants, such as phase densities and viscosities, entrainment options are discussed as well. Additionally, some measurements of mass and momentum conservation are presented.

Lock-Exchange

In the study of gravity flows, the lock-exchange experiment comprises releasing a fluid into another, initially separated by a vertical barrier. Due to the difference in density values between both fluids, one fluid incurs into another, forming a distinct gravity current shape — a head followed by vortices produced by Kelvin-Helmholtz instabilities — see Figure 3.

Figure 41 – Helmotz-hodge + setup birman



Source: Elaborated by the author.

In order to verify the behavior of the PSL model in such a case, the following experiments remove the DSL, meaning the terrain patch follows the boundary conditions of a simple wall.

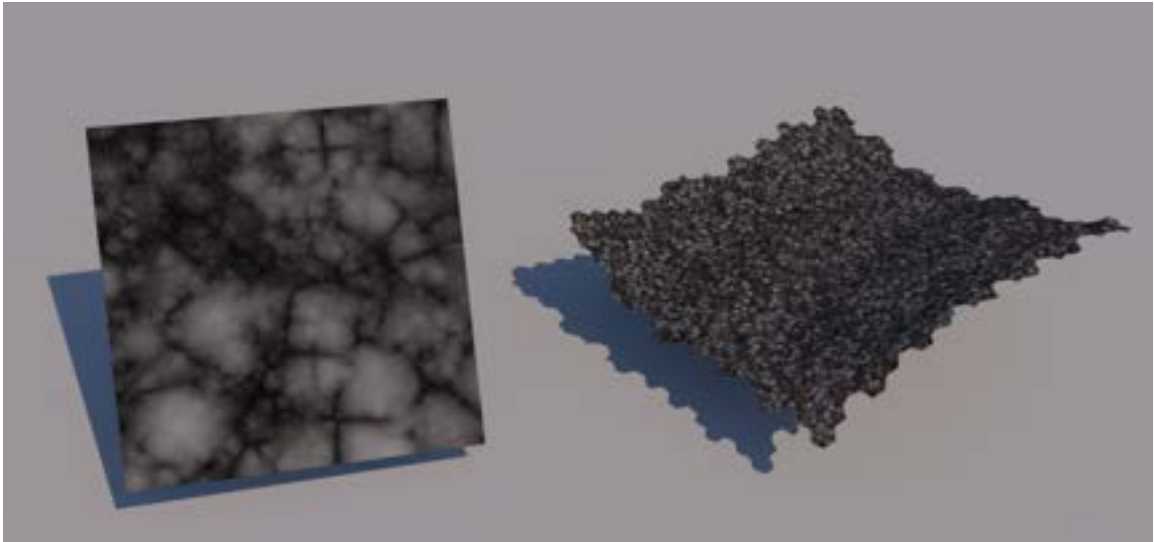
conclusions

Mass and Momentum Injections

The injection of mass and velocity into the PSL contains some parametrization that dictates the final shape of the cloud. From equations [Equation 4.11](#), [Equation 4.14](#), and [Equation 4.15](#):

- γ_α controls the percent of mass entrained by the DSL that gets into the PSL. Therefore, $\gamma_\alpha \in [0, 1]$;
- $\gamma_{\mathbf{u}}$ combines the air intake and snowpack ejection displacement translated into velocity surges. Although there is no explicit upper bound value, $\gamma_{\mathbf{u}}$ is also considered to be in

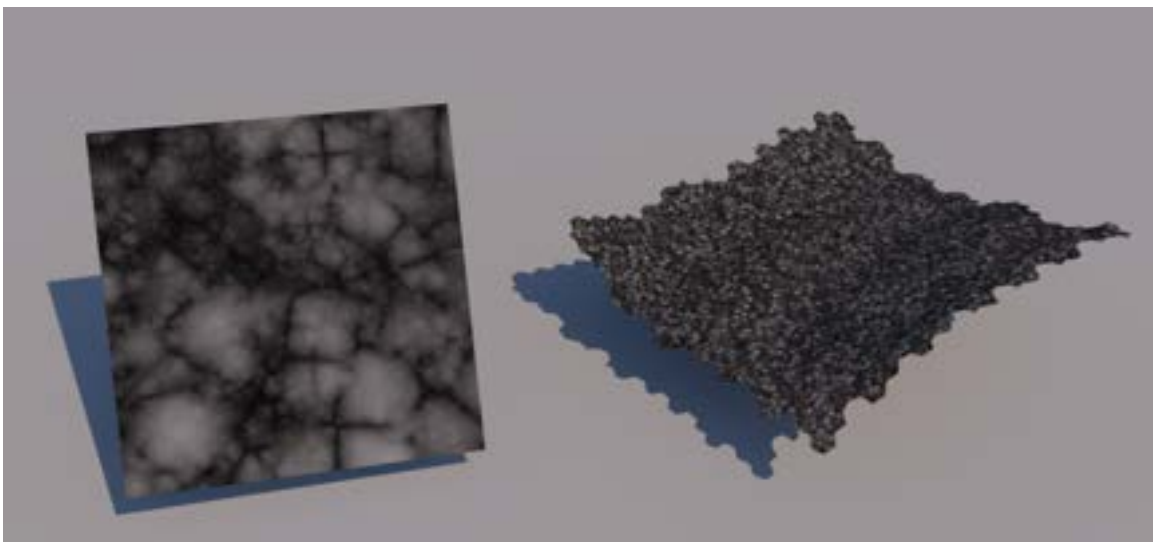
Figure 42 – Lock exchange results: different rhos



Source: Elaborated by the author.

the unity interval. Since noise functions usually produce values in such intervals, the parameters of such functions will determine the final results;

- L_{front} controls the size of the avalanche front, i.e., the region where the two parameters above have a more significant effect. L_{front} is considered to be in the range of $10 \sim 40m$.

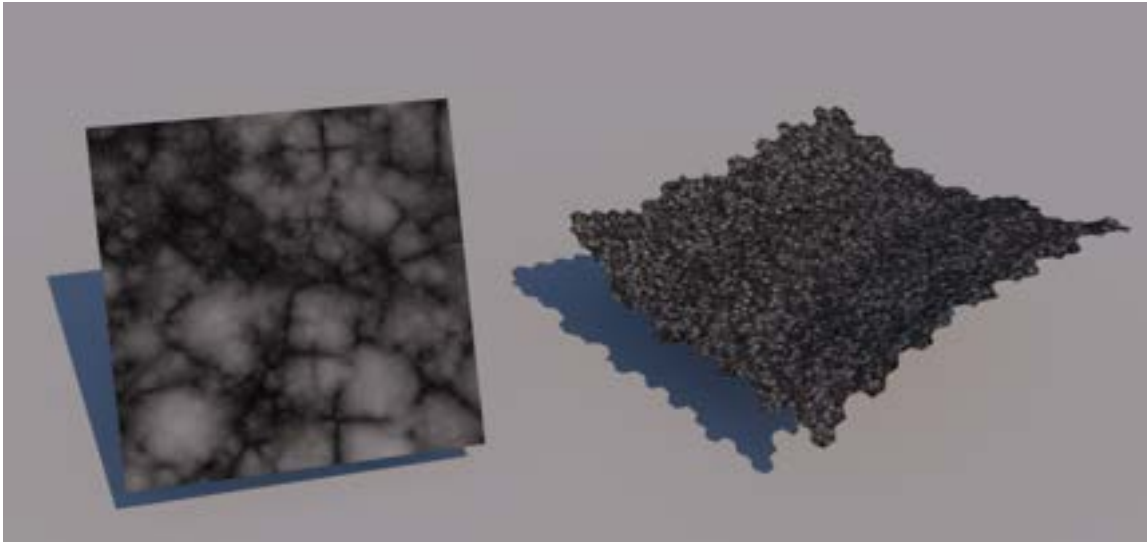
Figure 43 – γ_α 

Source: Elaborated by the author.

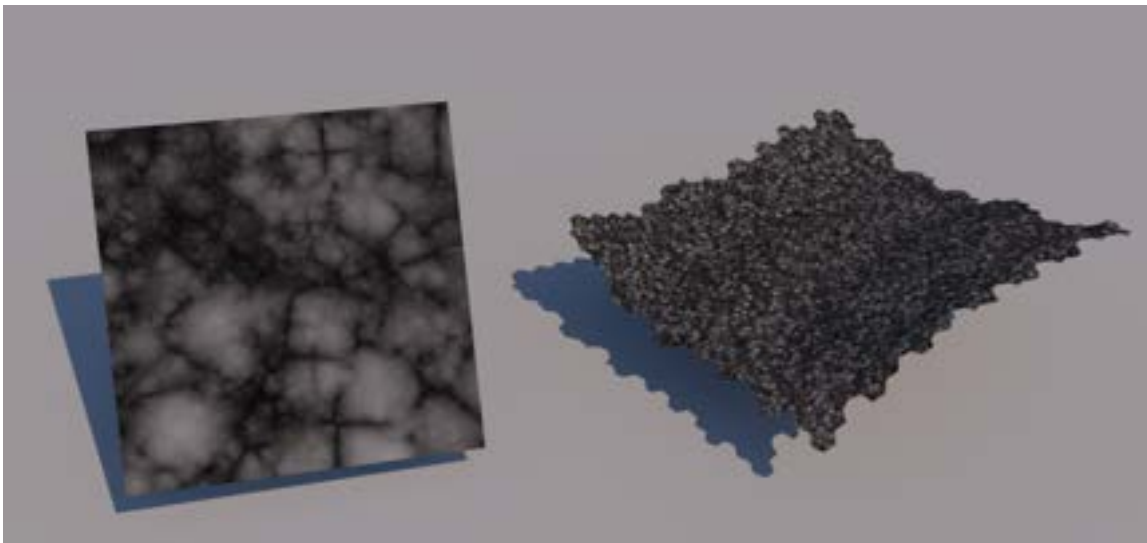
Numerical Method

CFL

convergence

Figure 44 – γ_u with without noise

Source: Elaborated by the author.

Figure 45 – L_{front} 

Source: Elaborated by the author.

4.3 Rendering

Both simulations of the DSL and PSL produce data for rendering, where each time step of the simulations provides the data for a respective frame in the final animation. Therefore, for an animation of 20 frames per second, the simulations must output data at intervals of 0.05s.

Given the inherent nature of their resulting fields, the rendering of each layer uses a different type of data:

- The resulting field of the DSL simulation is the height of the dense avalanche at each numerical cell in the terrain surface, which can be used to build a **polygonal mesh** to

represent the DSL surface.

- The PSL data is a scalar volume field representing the powder-snow concentration in every numerical cell, thus a **sparse volumetric density field** can be used to represent the powder-snow cloud.

DSL Surface

The surface render mesh of the DSL covers the set of two-dimensional cells S_{dsl} that contains enough moving mass, defined as

$$S_{dsl} = \{C_k \forall k | h_k > H_\epsilon\},$$

where h_k is the height of the avalanche in cell C_k , and H_ϵ represents the minimum height required for a cell to be considered an avalanche cell. The cells consist of the set of vertices V_{dsl} , where each vertex $v_i \in V_{dsl}$ is shared by a set of incident cells N_i .

The construction of the render mesh M_{dsl} and its vertices V_M is defined by the direct map $E : V_{dsl} \rightarrow V_M$, defined as

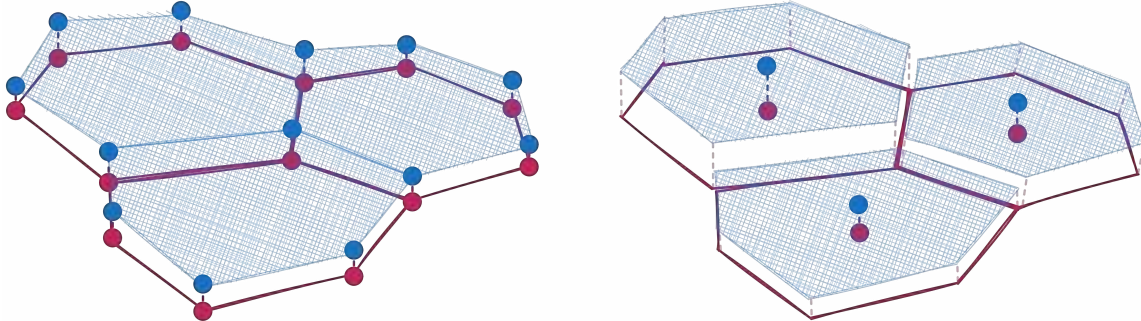
$$m_i = v_i + h_i \mathbf{n}_i, \quad (4.16)$$

where $m_i \in V_M$ is the corresponding vertex in V_M for the vertex v_i , h_i is the DSL height value at v_i , and \mathbf{n}_i is the terrain normal vector at v_i . The computation of h_i is done by averaging the cell values from the incident cells in N_i :

$$h_i = \frac{1}{|N_i|} \sum_{c \in N_i} h_c. \quad (4.17)$$

The process results in the extrusion of S_{dsl} by displacing each vertex in the normal direction of the terrain surface by an amount computed from the mean height values from the neighboring cells; see left in [Figure 46](#). Note in the same figure that it is different from extruding the cells individually, which could lead to discontinuities in the edges by producing steps between cells with different height values.

Figure 46 – The render mesh that represents the DSL surface, blue in the figure, can be constructed by extruding the elements of the simulation mesh, red in the figure. On the left, the extrusion happens on the vertices defined by the DSL height values of the incident cells. On the right, cells are extruded individually by their height values.



Source: Elaborated by the author.

PSL Cloud

As mentioned, a *volumetric density field* can represent the PSL cloud, meaning the final result will be rendered as a volume of a three-dimensional scalar field $\phi(\mathbf{x})$. Generally, the field representation considers a regular grid of cubic cells, called *voxels*, where a value of ϕ is defined for each voxel \mathbf{ijk} . This section will refer to the volumetric density field grid as the *voxel grid*.

The conversion of the simulation grid data into a voxel grid representing the PSL cloud comes from the natural translation of the volume concentration of the snow phase, $\alpha_s(\mathbf{x})$ ⁷, into density values for the voxels⁸ by a mapping function $\Gamma : \alpha_s \rightarrow \phi$ defined as

$$\Gamma(\mathbf{x}) = \gamma\alpha_s(\mathbf{x}), \quad (4.18)$$

where γ is a conversion factor that will be discussed later.

From the FVM, each simulation cell C contains a single value of α_s , localized at its center C_c , representing the mean value of the field over the cell volume C_V . Similarly, each voxel \mathbf{ijk} contains a single density value, $\phi(\mathbf{ijk})$. Therefore, the output volume is an approximation of the original field and its accuracy depends directly on the resolution of the voxel grid — see Figure 47.

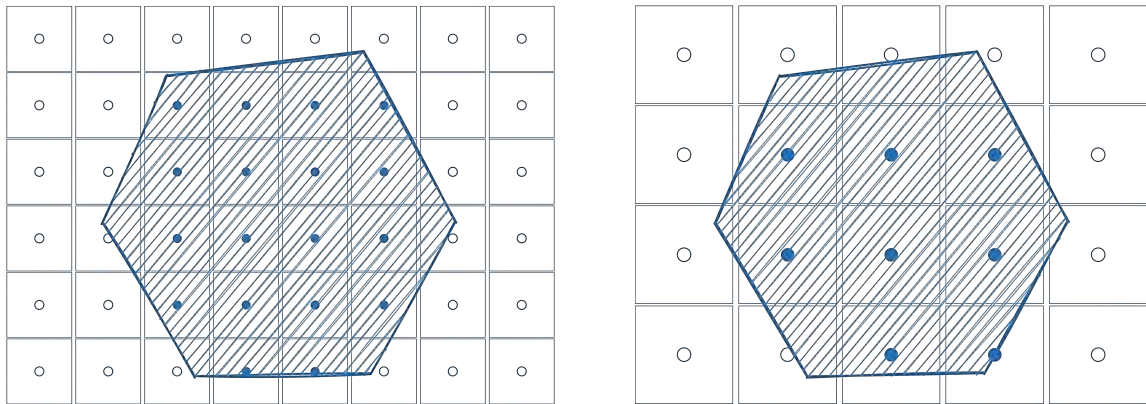
The above approximation is analogous to pixel rasterization schemes and brings inherent problems such as aliasing, as shown left in Figure 48. However, given the large size of simulation cells compared to voxel sizes, increasing the resolution of the voxel grid or applying anti-aliasing techniques to it does not necessarily solve the problem.

opendb

⁷ See section 3.3 on page 86.

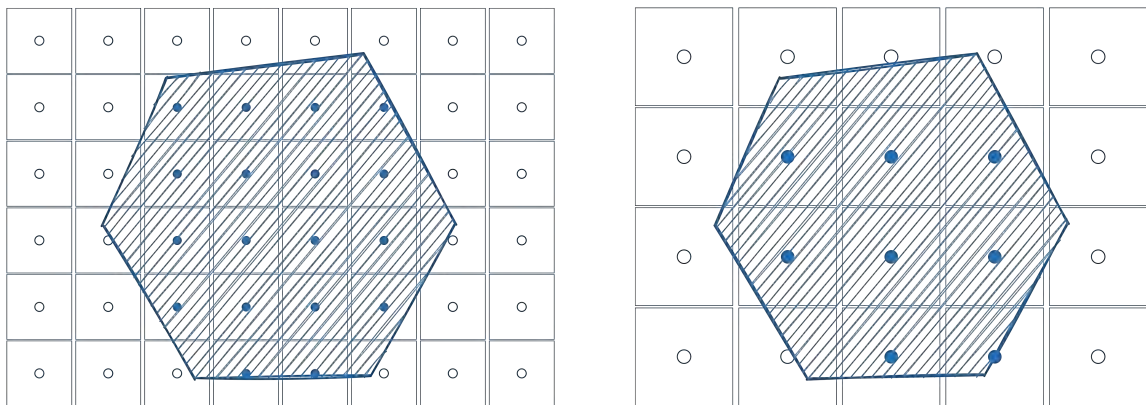
⁸ Note that the density in the volumetric density field represented by the voxel grid is not related to the physical property of density of the PSL. The term *density* in this rendering context refers to the concentration of matter that will interact with light, analogous to smoke density.

Figure 47 – Consider a hexagonal cell from the simulation grid containing a single value of α_s . The voxel grid contains samples of α_s from the underlying cell. Since the density field is defined only on the lattice points \mathbf{ijk} , the voxels' resolution has a direct impact on the final result.



Source: Elaborated by the author.

Figure 48 – XXXXXXXXX.



Source: Elaborated by the author.

The OpenVDB tree structure represents a sparse three-dimensional grid where we can store density values. The grid's resolution will influence the powder-snow cloud's final appearance.

foam2vdb

All rendered images presented in this chapter were produced with a high-end renderer called *RenderMan*® (CHRISTENSEN *et al.*, 2018), particularly with the *Non-Commercial RenderMan*®25 version⁹. *RenderMan*® is a photorealistic rendering software based on physical rendering models developed by Pixar Animation Studios. Due to the visual resemblance of the powder-snow cloud with sky clouds, the strategy presented in *RenderMan*®'s documentation¹⁰ guided the configuration of the rendering. For text completeness, Table 15 lists the main configurations used in the final results.

⁹ <<https://renderman.pixar.com/store>>

¹⁰ <<https://rmanwiki.pixar.com/display/REN25/Rendering+Clouds+with+Aggregate+Volumes>>

Figure 49 – A cloud asset rendered with the workflow considered for the powder-snow cloud.



Source: [RenderMan25 \(2023\)](#).

Table 15 – Renderer configuration.

Parameter	Value
Max Path Length	256
Multi-Scattering Approx. Bleed	0.9
Primary Anisotropy	0.8
Secondary Anisotropy	-0.2
Lobe Blend Factor	0.2

4.4 Natural Terrain Examples

This section lists some examples of powder-snow avalanches simulated in complex terrain geometries. Generally, the three-dimensional terrain geometry is constructed from two-dimensional height maps, which may originate from:

- **Procedural generation techniques:** manipulate noise functions, such as the Perlin-noise, to generate natural-like landscapes.
- **Real-world topographical data:** usually represented by Digital Elevation Models (DEMs), with files in GIS format.

The construction of the terrain geometry proceeds by projecting the map into a three-dimensional plane and extruding each vertex of the plane by the corresponding height information of the map.

Given the regular distribution of the texels in the texture, the three-dimensional mesh is initially represented by a regular grid of quadrangular cells.

extrude

The following sections utilize the mesh generation procedure detailed above and present full simulations configured with the values listed in Table 16.

Table 16 – List of parameter values utilized in the complex terrain example simulations.

Layer	Parameter	Description	Value
DSL	ρ	Snow density	
	μ	Voellmy's dry friction	
	ξ	Voellmy's dynamic friction	
	e_b	Erosion energy	
PSL	ρ_a	Air density	
	ρ_s	Powder-snow density	
	D_{ab}	Molecular diffusivity	
	ν_t	Turbulent eddy viscosity	
	Sc	Turbulent Schmidt number	

4.4.1 Wolfsgrube

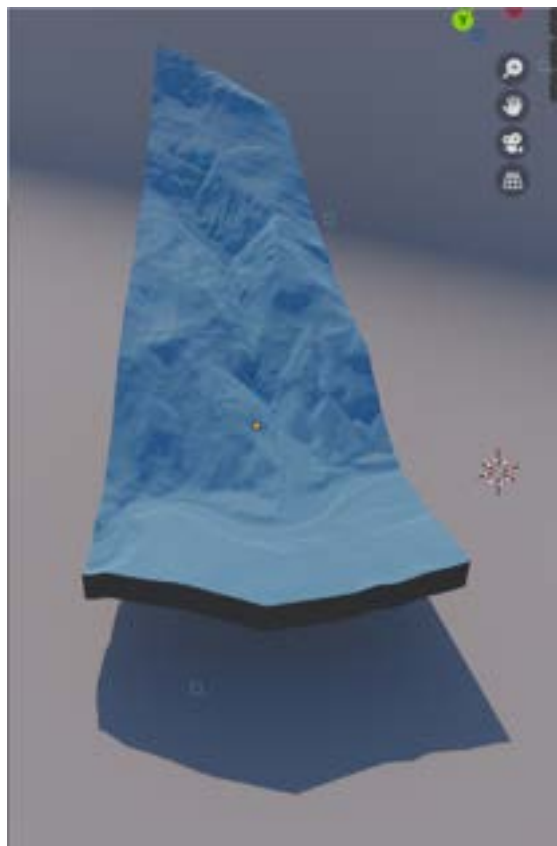
Figure 50 – Examples of graphical user interfaces of commercial software packages for snow avalanche simulation.

(a) XXXXXX.



Source: Federal Ministry Republic of Austria (2023).

(b) XXXXXXXX.



Source: Elaborated by the author.

BIBLIOGRAPHY

ABDELRAZEK, A.; KIMURA, I.; SHMIZU, Y. Numerical simulation of a small-scale snow avalanche tests using non-newtonian sph model. **Journal of Japan Society of Civil Engineers, Ser. A2 (Applied Mechanics (AM))**, v. 70, p. I_681–I_690, 01 2014. Citation on page 56.

ABRAHAM, M. T.; SATYAM, N.; PRADHAN, B.; TIAN, H. Debris flow simulation 2d (dfs 2d): Numerical modelling of debris flows and calibration of friction parameters. **Journal of Rock Mechanics and Geotechnical Engineering**, 2022. ISSN 1674-7755. Available: <<https://www.sciencedirect.com/science/article/pii/S1674775522000403>>. Citation on page 42.

AKIYAMA, J.; URA, M. Motion of 2d buoyant clouds downslope. **Journal of Hydraulic Engineering**, American Society of Civil Engineers, v. 125, n. 5, p. 474–480, 1999. Citation on page 63.

ALBABA, A.; LAMBERT, S.; FAUG, T. Dry granular avalanche impact force on a rigid wall: Analytic shock solution versus discrete element simulations. **Phys. Rev. E**, American Physical Society, v. 97, p. 052903, 5 2018. Available: <<https://link.aps.org/doi/10.1103/PhysRevE.97.052903>>. Citation on page 71.

ALDUÁN, I.; OTADUY, M. A. Sph granular flow with friction and cohesion. In: **Proceedings of the 2011 ACM SIGGRAPH/Eurographics Symposium on Computer Animation**. New York, NY, USA: Association for Computing Machinery, 2011. (SCA '11), p. 25–32. ISBN 9781450309233. Available: <<https://doi.org/10.1145/2019406.2019410>>. Citation on page 74.

ANCEY, C. **Snow Avalanches. Selected topics in geological and geomorphological fluid mechanics**. [S.l.]: Springer, Berlin, 2001. Citations on pages 48, 49, and 62.

_____. Powder snow avalanches: Approximation as non-boussinesq clouds with a richardson numberdependent entrainment function. **Journal of Geophysical Research: Earth Surface**, v. 109.0, n. F1, 2004. Available: <<https://onlinelibrary.wiley.com/doi/abs/10.1029/2003JF000052>>. Citations on pages 34 and 62.

_____. **Snow Avalanches**. Oxford University Press, 2016. Available: <<https://oxfordre.com/naturalhazardscience/view/10.1093/acrefore/9780199389407.001.0001/acrefore-9780199389407-e-17>>. Citations on pages 28, 30, 42, 57, and 63.

ANCEY, C.; GERVASONI, C.; MEUNIER, M. Computing extreme avalanches. **Cold Regions Science and Technology**, v. 39, n. 2, p. 161–180, 2004. ISSN 0165-232X. Snow And Avalanches: Papers Presented At The European Geophysical Union Conference, Nice, April 2003. Dedicated To The Avalanche Dynamics Pioneer Dr. B. Salm. Available: <<https://www.sciencedirect.com/science/article/pii/S0165232X04000436>>. Citations on pages 39 and 56.

ANCEY, C.; MEUNIER, M. Estimating bulk rheological properties of flowing snow avalanches from field data. **Journal of Geophysical Research: Earth Surface**, v. 109, n. F1, 2004. Available: <<https://agupubs.onlinelibrary.wiley.com/doi/abs/10.1029/2003JF000036>>. Citation on page 48.

ANCEY, C.; MEUNIER, M.; RICHARD, D. Inverse problem in avalanche dynamics models. **Water Resources Research**, v. 39, n. 4, 2003. Available: <<https://agupubs.onlinelibrary.wiley.com/doi/abs/10.1029/2002WR001749>>. Citation on page 56.

ANDREOTTI, B.; FORTERRE, Y.; POULIQUEN, O. **Granular media: between fluid and solid**. [S.l.]: Cambridge University Press, 2013. Citation on page 66.

ARENSEN, L. U.; COLGAN, W.; MARSHALL, H. P. Chapter 2 - physical, thermal, and mechanical properties of snow, ice, and permafrost. In: SHRODER, J. F.; HAEBERLI, W.; WHITEMAN, C. (Ed.). **Snow and Ice-Related Hazards, Risks, and Disasters**. Boston: Academic Press, 2015, (Hazards and Disasters Series). p. 35–75. ISBN 978-0-12-394849-6. Available: <<https://www.sciencedirect.com/science/article/pii/B978012394849600020>>. Citation on page 48.

ARENSEN, L. U.; SPRINGMAN, S. M.; SEGO, D. C. The rheology of frozen soils. **Applied Rheology**, v. 17, n. 1, p. 12147–1–12147–14, 2007. Available: <<https://doi.org/10.1515/arh-2007-0003>>. Citation on page 47.

ATKIN, R.; CRAINE, R. Continuum theories of mixtures: basic theory and historical development. **The Quarterly Journal of Mechanics and Applied Mathematics**, Oxford University Press, v. 29.0, n. 2, p. 209–244, 1976. Citations on pages 66 and 157.

AVAL-1D, WSL. **AVAL-1D**. 2022. [Online; accessed September 26, 2022]. Available: <<https://www.wsl.ch/en/services-et-produits/logiciels-sites-internets-et-apps/aval-1d.html>>. Citations on pages 72 and 73.

AVALANCHE.ORG. **Avalanche.org**. 2023. [Online; accessed September 09, 2023]. Available: <<https://avalanche.org/avalanche-encyclopedia/#avalanche>>. Citation on page 21.

BAGNOLD, R. A. Experiments on a gravity-free dispersion of large solid spheres in a newtonian fluid under shear. **Proceedings of the Royal Society of London. Series A. Mathematical and Physical Sciences**, The Royal Society London, v. 225, n. 1160, p. 49–63, 1954. Citations on pages 49 and 57.

_____. Auto-suspension of transported sediment; turbidity currents. **Proceedings of the Royal Society of London. Series A. Mathematical and Physical Sciences**, The Royal Society London, v. 265, n. 1322, p. 315–319, 1962. Citation on page 57.

BAINES, P. G. Mixing in flows down gentle slopes into stratified environments. **Journal of Fluid Mechanics**, Cambridge University Press, v. 443, p. 237–270, 2001. Citation on page 61.

BAKER, J. L.; BARKER, T.; GRAY, J. M. N. T. A two-dimensional depth-averaged $\mu(i)$ -rheology for dense granular avalanches. **Journal of Fluid Mechanics**, Cambridge University Press, v. 787, p. 367–395, 2016. Citation on page 56.

BAKHVALOV, N. S.; ÉGLIT, M. É. Investigation of the one-dimensional motion of a snow avalanche along a flat slope. **Fluid Dynamics**, v. 8, n. 5, p. 683–689, 9 1973. ISSN 1573-8507. Available: <<https://doi.org/10.1007/BF01023564>>. Citation on page 45.

BARALE, L. Footstep-triggered grain flows on the lee side of a desert sand dune (erg chebbi, morocco). **International Journal of Earth Sciences**, v. 104, n. 8, p. 2213–2214, Nov 2015. ISSN 1437-3262. Available: <<https://doi.org/10.1007/s00531-015-1246-3>>. Citation on page 17.

BARBOLINI, M.; BIANCARDI, A.; CAPPABIANCA, F.; NATALE, L.; PAGLIARDI, M. Laboratory study of erosion processes in snow avalanches. **Cold Regions Science and Technology**, v. 43, n. 1, p. 1–9, 2005. ISSN 0165-232X. Snow and Avalanches. Available: <<https://www.sciencedirect.com/science/article/pii/S0165232X05000807>>. Citation on page 36.

BARBOLINI, M.; GRUBER, U.; KEYLOCK, C.; NAAIM, M.; SAVI, F. Application of statistical and hydraulic-continuum dense-snow avalanche models to five real european sites. **Cold Regions Science and Technology**, v. 31, n. 2, p. 133–149, 2000. ISSN 0165-232X. Available: <<https://www.sciencedirect.com/science/article/pii/S0165232X0000082>>. Citation on page 56.

BARDOLINI, M.; ISSLER, D.; JÓHANNESSEN, T.; HÁKONARDÓTTIR, K.; LIED, K.; GAUER, P.; NAAIM, M.; FAUG, T.; NATALE, L.; CAPPABIANCA, F. *et al.* Avalanche test sites and research equipment in europe. v. 8, 2005. Citation on page 31.

BARTELT, P.; BÜHLER, Y.; BUSER, O.; GINZLER, C. Plume formation in powder snow avalanches. In: . [S.l.: s.n.], 2013. Citations on pages 24, 28, 31, and 33.

BARTELT, P.; BUSER, O.; PLATZER, K. Fluctuation-dissipation relations for granular snow avalanches. **Journal of Glaciology**, Cambridge University Press, v. 52, n. 179, p. 631–643, 2006. Citations on pages 44 and 56.

BARTELT, P.; BUSER, O.; VALERO, C. V.; BÜHLER, Y. Configurational energy and the formation of mixed flowing/powder snow and ice avalanches. **Annals of Glaciology**, Cambridge University Press, v. 57, n. 71, p. 179–188, 2016. Citations on pages 32, 67, 69, and 90.

BARTELT, P.; CHRISTEN, M.; BÜHLER, Y.; CAVIEZEL, A.; BUSER, O. Snow entrainment: Avalanche interaction with an erodible substrate. In: **Proceedings of the International Snow Science Workshop**. [S.l.: s.n.], 2018. p. 716–720. Citation on page 69.

BARTELT, P.; KERN, M.; CHRISTEN, M. A mixed flowing/powder snow avalanche model. In: **Proceeding of the International Snow Science Workshop: a merging between theory and practice (ISSW 2000)**. [S.l.: s.n.], 2000. p. 280–289. Citations on pages 67 and 69.

BARTELT, P.; MCARDELL, B. W. Granulometric investigations of snow avalanches. **Journal of Glaciology**, Cambridge University Press, v. 55, n. 193, p. 829–833, 2009. Citation on page 46.

BARTELT, P.; SALM, B.; GRUBER, U. Calculating dense-snow avalanche runout using a voellmy-fluid model with active/passive longitudinal straining. **Journal of Glaciology**, Cambridge University Press, v. 45, n. 150, p. 242–254, 1999. Citations on pages 41, 44, 46, 55, and 72.

BARTELT, P.; VALERO, C. V.; FEISTL, T.; CHRISTEN, M.; BÜHLER, Y.; BUSER, O. Modelling cohesion in snow avalanche flow. **Journal of Glaciology**, Cambridge University Press, v. 61, n. 229, p. 837–850, 2015. Citation on page 50.

BARTHOLOMEW, P.; DESKOS, G.; FRANTZ, R. A.; SCHUCH, F. N.; LAMBALLAIS, E.; LAIZET, S. Xcompact3d: An open-source framework for solving turbulence problems on a cartesian mesh. **SoftwareX**, v. 12.0, p. 100550, 2020. ISSN 2352-7110. Available: <<https://www.sciencedirect.com/science/article/pii/S2352711019303620>>. Citation on page 73.

BARTHOLOMEW, P.; LAIZET, S. A new highly scalable, high-order accurate framework for variable-density flows: Application to non-boussinesq gravity currents. **Computer Physics Communications**, v. 242.0, p. 83–94, 2019. ISSN 0010-4655. Available: <<https://www.sciencedirect.com/science/article/pii/S0010465519301006>>. Citation on page 58.

BEGHIN, P. **Etude des bouffées bidimensionnelles de densité en écoulement sur pente avec application aux avalanches de neige poudreuse**. Phd Thesis (PhD Thesis), 1979. Citation on page 62.

BEGHIN, P.; BRUGNOT, G. Contribution of theoretical and experimental results to powder-snow avalanche dynamics. **Cold Regions Science and Technology**, v. 8, n. 1, p. 67–73, 1983. ISSN 0165-232X. Available: <<https://www.sciencedirect.com/science/article/pii/0165232X83900186>>. Citation on page 62.

BEGHIN, P.; HOPFINGER, E. J.; BRITTER, R. E. Gravitational convection from instantaneous sources on inclined boundaries. **Journal of Fluid Mechanics**, Cambridge University Press, v. 107, p. 407–422, 1981. Citation on page 62.

BEGHIN, P.; OLAGNE, X. Experimental and theoretical study of the dynamics of powder snow avalanches. **Cold Regions Science and Technology**, v. 19.0, n. 3, p. 317–326, 1991. ISSN 0165-232X. Available: <<https://www.sciencedirect.com/science/article/pii/0165232X9190046J>>. Citations on pages 34 and 35.

BEGNUDELLI, L.; SANDERS, B. F. Unstructured grid finite-volume algorithm for shallow-water flow and scalar transport with wetting and drying. **Journal of Hydraulic Engineering**, v. 132.0, n. 4, p. 371–384, 2006. Available: <<https://ascelibrary.org/doi/abs/10.1061/%28ASCE%290733-9429%282006%29132%3A4%28371%29>>. Citation on page 53.

BELL, N.; YU, Y.; MUCHA, P. J. Particle-based simulation of granular materials. In: **Proceedings of the 2005 ACM SIGGRAPH/Eurographics Symposium on Computer Animation**. New York, NY, USA: Association for Computing Machinery, 2005. (SCA '05), p. 77–86. ISBN 1595931988. Available: <<https://doi.org/10.1145/1073368.1073379>>. Citation on page 74.

BENJAMIN, T. B. Gravity currents and related phenomena. **Journal of Fluid Mechanics**, Cambridge University Press, v. 31, n. 2, p. 209–248, 1968. Citations on pages 29 and 59.

BENKHALDOUN, F.; SEAD, M. A simple finite volume method for the shallow water equations. **Journal of Computational and Applied Mathematics**, v. 234.0, n. 1, p. 58–72, 2010. ISSN 0377-0427. Available: <<https://www.sciencedirect.com/science/article/pii/S0377042709008139>>. Citation on page 53.

BINGHAM, E. C. **The History of the Society of Rheology from 1924-1944**. [S.l.: s.n.], 1944. Citation on page 47.

BIRMAN, V.; MEIBURG, E. High-resolution simulations of gravity currents. **Journal of the Brazilian Society of Mechanical Sciences and Engineering**, SciELO Brasil, v. 28.0, n. 2, p. 169–173, 2006. Citation on page 58.

BORDEN, Z.; MEIBURG, E. Circulation based models for boussinesq gravity currents. **Physics of Fluids**, v. 25, n. 10, p. 101301, 2013. Available: <<https://doi.org/10.1063/1.4825035>>. Citation on page 60.

BORIS, J. P.; BOOK, D. L. Flux-corrected transport. i. shasta, a fluid transport algorithm that works. **Journal of Computational Physics**, v. 11, n. 1, p. 38–69, 1973. ISSN 0021-9991. Available: <<https://www.sciencedirect.com/science/article/pii/0021999173901472>>. Citation on page 171.

BOUCHUT, F.; MANGENEY-CASTELNAU, A.; PERTHAME, B.; VILOTTE, J.-P. A new model of saint venant and savagehutter type for gravity driven shallow water flows. **Comptes Rendus Mathématique**, v. 336.0, n. 6, p. 531–536, 2003. ISSN 1631-073X. Available: <<https://www.sciencedirect.com/science/article/pii/S1631073X03001171>>. Citation on page 53.

BOUSSINESQ, J. **Théorie Analytique de la Chaleur Mise en Harmonie Avec la Thermodynamique Et Avec la Théorie Mécanique de la Lumière: Refroidissement et échauffement par rayonnement, conductibilité des tiges, lames et masses cristallines, courants de convection, théorie mécanique de la lumière. 1903. xxxii, 625,[1] p.** [S.l.]: Gauthier-Villars, 1903. Citation on page 58.

BOVET, E.; CHIAIA, B.; PREZIOSI, L. A new model for snow avalanche dynamics based on non-newtonian fluids. **Meccanica**, v. 45, n. 6, p. 753–765, 12 2010. ISSN 1572-9648. Available: <<https://doi.org/10.1007/s11012-009-9278-z>>. Citation on page 56.

BOZHINSKIY, A.; LOSEV, K.; BARTELT, C. **The Fundamentals of Avalanche Science.** Eidgenöss. Inst. für Schnee- und Lawinenforschung, Bibliothek, 1998. (Eidgenössisches Institut für Schnee- und Lawinenforschung Weißfluhjoch: Mitteilungen des Eidgenössischen Institutes für Schnee- und Lawinenforschung). ISBN 9783905620719. Available: <<https://books.google.com.br/books?id=n0MkGQAACAAJ>>. Citations on pages 30, 45, 46, and 62.

BRIDSON, R.; HOURIHAM, J.; NORDENSTAM, M. Curl-noise for procedural fluid flow. **ACM Trans. Graph.**, Association for Computing Machinery, New York, NY, USA, v. 26.0, n. 3, p. 46es, 7 2007. ISSN 0730-0301. Available: <<https://doi.org/10.1145/1276377.1276435>>. Citation on page 74.

BRITTER, R. E.; LINDEN, P. F. The motion of the front of a gravity current travelling down an incline. **Journal of Fluid Mechanics**, Cambridge University Press, v. 99, n. 3, p. 531–543, 1980. Citation on page 61.

BROCK, R. R. Development of roll waves in open channels. California Institute of Technology, 1967. Citation on page 60.

BUSER, O.; BARTELT, P. Production and decay of random kinetic energy in granular snow avalanches. **Journal of Glaciology**, Cambridge University Press, v. 55, n. 189, p. 3–12, 2009. Citation on page 56.

BUTTINGER-KREUZHUBER, A.; HORVTH, Z.; NOELLE, S.; BLSCHL, G.; WASER, J. A fast second-order shallow water scheme on two-dimensional structured grids over abrupt topography. **Advances in Water Resources**, v. 127.0, p. 89–108, 2019. ISSN 0309-1708. Available: <<https://www.sciencedirect.com/science/article/pii/S0309170818305335>>. Citation on page 53.

CALGARO, C.; CREUSÉ, E.; GOUDON, T. Modeling and Simulation of Mixture Flows :Application to Powder-Snow Avalanches. **Computers and Fluids**, Elsevier, v. 107, p. 100–122, 2015. Available: <<https://hal.archives-ouvertes.fr/hal-00732112>>. Citation on page 67.

CAMPBELL, C. S. Rapid granular flows. **Annual Review of Fluid Mechanics**, v. 22, n. 1, p. 57–90, 1990. Available: <<https://doi.org/10.1146/annurev.fl.22.010190.000421>>. Citation on page 49.

CARROLL, C. S.; LOUGE, M. Y.; TURNBULL, B. Frontal dynamics of powder snow avalanches. **Journal of Geophysical Research: Earth Surface**, v. 118.0, n. 2, p. 913–924, 2013. Available: <<https://agupubs.onlinelibrary.wiley.com/doi/abs/10.1002/jgrf.20068>>. Citations on pages 69 and 90.

CARROLL, C. S.; TURNBULL, B.; LOUGE, M. Y. Role of fluid density in shaping eruption currents driven by frontal particle blow-out. **Physics of Fluids**, v. 24, n. 6, p. 066603, 2012. Available: <<https://doi.org/10.1063/1.4725538>>. Citation on page 69.

CHEN, C. P.; WOOD, P. E. A turbulence closure model for dilute gas-particle flows. **The Canadian Journal of Chemical Engineering**, v. 63, n. 3, p. 349–360, 1985. Available: <<https://onlinelibrary.wiley.com/doi/abs/10.1002/cjce.5450630301>>. Citation on page 66.

CHEREPANOV, G. P.; ESPARRAGOZA, I. E. A fracture-entrainment model for snow avalanches. **Journal of Glaciology**, Cambridge University Press, v. 54, n. 184, p. 182–188, 2008. Citation on page 56.

CHLDEK, M.; URIKOVI, R. Particle-based shallow water simulation for irregular and sparse simulation domains. **Computers & Graphics**, v. 53.0, p. 170 – 176, 2015. ISSN 0097-8493. Available: <<http://www.sciencedirect.com/science/article/pii/S0097849315000412>>. Citation on page 74.

CHRISTEN, M.; BARTELT, P.; GRUBER, U. Aval-1d: An avalanche dynamics program for the practice. In: **International congress interpraevent**. [S.l.: s.n.], 2002. p. 715–725. Citation on page 72.

CHRISTEN, M.; KOWALSKI, J.; BARTELT, P. Ramms: Numerical simulation of dense snow avalanches in three-dimensional terrain. **Cold Regions Science and Technology**, v. 63.0, n. 1, p. 1–14, 2010. ISSN 0165-232X. Available: <<https://www.sciencedirect.com/science/article/pii/S0165232X10000844>>. Citations on pages 43, 57, and 73.

CHRISTENSEN, P.; FONG, J.; SHADE, J.; WOOTEN, W.; SCHUBERT, B.; KENSLER, A.; FRIEDMAN, S.; KILPATRICK, C.; RAMSHAW, C.; BANNISTER, M.; RAYNER, B.; BROUILLAT, J.; LIANI, M. Renderman: An advanced path-tracing architecture for movie rendering. **ACM Trans. Graph.**, Association for Computing Machinery, New York, NY, USA, v. 37, n. 3, aug 2018. ISSN 0730-0301. Available: <<https://doi.org/10.1145/3182162>>. Citation on page 117.

Christian Kröner. **Experimental and numerical description of rapid granular flows and some baseline constraints for simulating 3-dimensional granular flow dynamics**. Phd Thesis (PhD Thesis) — Rheinische Friedrich-Wilhelms-Universität Bonn, 7 2014. Available: <<https://hdl.handle.net/20.500.11811/6138>>. Citations on pages 51 and 52.

COAZ, J. W. F. Die lawinen der schweizer alpen. p. 171, 1881. Citation on page 28.

CORDONNIER, G.; ECORMIER, P.; GALIN, E.; GAIN, J.; BENES, B.; CANI, M.-P. Interactive generation of time-evolving, snow-covered landscapes with avalanches. In: **ACM. Proceedings of the 17th ACM SIGGRAPH/Eurographics Symposium on Computer Animation**. [S.l.], 2018. Citation on page 75.

CORTEN, H. Chapter 9 - fracture mechanics of composites. In: LIEBOWITZ, H. (Ed.). **Fracture of Nonmetals and Composites**. Academic Press, 1972. p. 675–769. ISBN 978-0-12-449707-8. Available: <<https://www.sciencedirect.com/science/article/pii/B9780124497078500130>>. Citation on page 56.

CRASTER, R. V.; MATAR, O. K. Dynamics and stability of thin liquid films. **Rev. Mod. Phys.**, American Physical Society, v. 81, p. 1131–1198, 8 2009. Available: <<https://link.aps.org/doi/10.1103/RevModPhys.81.1131>>. Citation on page 54.

DAI, A.; HUANG, Y.-L. Boussinesq and non-boussinesq gravity currents propagating on unbounded uniform slopes in the deceleration phase. **Journal of Fluid Mechanics**, Cambridge University Press, v. 917, p. A23, 2021. Citation on page 34.

DAMIAN, S. M. An extended mixture model for the simultaneous treatment of short and long scale interfaces (phd thesis). **National University of the Littoral**, 2013. Citation on page 181.

DAMIÁN, S. M.; NIGRO, N. M. An extended mixture model for the simultaneous treatment of small-scale and large-scale interfaces. **International Journal for Numerical Methods in Fluids**, v. 75, n. 8, p. 547–574, 2014. Available: <<https://onlinelibrary.wiley.com/doi/abs/10.1002/fld.3906>>. Citation on page 181.

DARWISH, M.; MOUKALLED, F. **The finite volume method in computational fluid dynamics: an advanced introduction with OpenFOAM® and Matlab®**. [S.l.]: Springer, 2016. Citations on pages 159, 167, and 177.

DASGUPTA, P. Sediment gravity flow—the conceptual problems. **Earth-Science Reviews**, v. 62, n. 3, p. 265–281, 2003. ISSN 0012-8252. Available: <<https://www.sciencedirect.com/science/article/pii/S0012825202001605>>. Citation on page 18.

DECKELNICK, K.; DZIUK, G.; ELLIOTT, C. M. Computation of geometric partial differential equations and mean curvature flow. **Acta Numerica**, Cambridge University Press, v. 14, p. 139–232, 2005. Citations on pages 53 and 81.

DELLINO, P.; DIOGUARDI, F.; DORONZO, D. M.; MELE, D. The entrainment rate of non-boussinesq hazardous geophysical gas-particle flows: An experimental model with application to pyroclastic density currents. **Geophysical Research Letters**, v. 46, n. 22, p. 12851–12861, 2019. Available: <<https://agupubs.onlinelibrary.wiley.com/doi/abs/10.1029/2019GL084776>>. Citation on page 34.

DENLINGER, R. P.; IVERSON, R. M. Granular avalanches across irregular three-dimensional terrain: 1. theory and computation. **Journal of Geophysical Research: Earth Surface**, v. 109, n. F1, 2004. Available: <<https://agupubs.onlinelibrary.wiley.com/doi/abs/10.1029/2003JF000085>>. Citation on page 53.

DENT, J.; BURRELL, K.; SCHMIDT, D. S.; LOUGE, M.; ADAMS, E.; JAZBUTIS, T. Density, velocity and friction measurements in a dry-snow avalanche. **Annals of Glaciology**, Cambridge University Press, v. 26, p. 247–252, 1998. Citations on pages 31 and 36.

DENT, J.; LANG, T. Experiments on mechanics of flowing snow. **Cold Regions Science and Technology**, v. 5, n. 3, p. 253–258, 1982. ISSN 0165-232X. Available: <<https://www.sciencedirect.com/science/article/pii/0165232X82900180>>. Citation on page 46.

DONG, J.; LI, D. F. A new second-order modified hydrostatic reconstruction for the shallow water flows with a discontinuous topography. **Applied Numerical Mathematics**, v. 161.0, p. 408–424, 2021. ISSN 0168-9274. Available: <<https://www.sciencedirect.com/science/article/pii/S016892742030369X>>. Citation on page 53.

DOYLE, E. E.; HOGG, A. J.; MADER, H. M. A two-layer approach to modelling the transformation of dilute pyroclastic currents into dense pyroclastic flows. **Proceedings of the Royal Society A: Mathematical, Physical and Engineering Sciences**, The Royal Society Publishing, v. 467, n. 2129, p. 1348–1371, 2011. Citation on page 53.

DREIER, L.; BÜHLER, Y.; GINZLER, C.; BARTELT, P. Comparison of simulated powder snow avalanches with photogrammetric measurements. **Annals of Glaciology**, Cambridge University Press, v. 57, n. 71, p. 371–381, 2016. Citation on page 31.

DRUCKER, D. C.; PRAGER, W. Soil mechanics and plastic analysis or limit design. **Quarterly of Applied Mathematics**, Brown University, v. 10, n. 2, p. 157–165, 1952. ISSN 0033569X, 15524485. Available: <<http://www.jstor.org/stable/43633942>>. Citation on page 48.

DURAN, A.; LIANG, Q.; MARCHE, F. On the well-balanced numerical discretization of shallow water equations on unstructured meshes. **Journal of Computational Physics**, v. 235.0, p. 565–586, 2013. ISSN 0021-9991. Available: <<https://www.sciencedirect.com/science/article/pii/S0021999112006365>>. Citation on page 53.

DUTYKH, D.; ACARY-ROBERT, C.; BRESCH, D. Numerical simulation of powder-snow avalanche interaction with an obstacle. **Submitted to Applied Mathematical Modelling**, Cite-seer, v. 21, 2009. Citation on page 66.

_____. Mathematical modeling of powder-snow avalanche flows. **Studies in Applied Mathematics**, Wiley Online Library, v. 127, n. 1, p. 38–66, 2011. Citation on page 67.

ECKART MCELWAIN JIM, K. B. M. Turbidity currents and powder snow avalanches. In: _____. **Handbook of Environmental Fluid Dynamics**. CRC Press, 2012. chap. chapter42. Available: <<https://www.routledgehandbooks.com/doi/10.1201/b14241-46>>. Citations on pages 30, 33, and 59.

EDWARDS, A.; VIROULET, S.; JOHNSON, C.; GRAY, J. Erosion-deposition dynamics and long distance propagation of granular avalanches. **Journal of Fluid Mechanics**, Cambridge University Press, v. 915, p. A9, 2021. Citations on pages 36 and 56.

EGLIT, M. Some mathematical models of snow avalanches. **Advances in the Mechanics and the Flow of Granular Materials**, Clausthal-Zellerfeld, Trans Tech Publications Germany, v. 2, p. 577–588, 1983. Citation on page 64.

_____. Mathematical and physical modelling of powder-snow avalanches in russia. **Annals of Glaciology**, Cambridge University Press, v. 26, p. 281–284, 1998. Citations on pages 64 and 65.

_____. Mathematical modeling of dense avalanches. In: **Proceedings of the Anniversary Conference**. [S.l.: s.n.], 1998. v. 25, p. 15–18. Citation on page 45.

EGLIT, M.; DEMIDOV, K. Mathematical modeling of snow entrainment in avalanche motion. **Cold Regions Science and Technology**, v. 43, n. 1, p. 10–23, 2005. ISSN 0165-232X. Snow and Avalanches. Available: <<https://www.sciencedirect.com/science/article/pii/S0165232X05000790>>. Citations on pages 54 and 62.

EGLIT, M.; YAKUBENKO, A.; ZAYKO, J. A review of russian snow avalanche models from analytical solutions to novel 3d models. **Geosciences**, v. 10, n. 77, 2020. ISSN 2076-3263. Available: <<https://www.mdpi.com/2076-3263/10/2/77>>. Citations on pages 30, 41, 42, 46, 54, 62, and 64.

ELLISON, T. H.; TURNER, J. S. Turbulent entrainment in stratified flows. **Journal of Fluid Mechanics**, Cambridge University Press, v. 6, n. 3, p. 423-448, 1959. Citations on pages 28, 31, 60, and 61.

EPFL. **SLAB: EPFL Snow and Avalanche Simulation Laboratory**. 2022. [Online; accessed July 26, 2022]. Available: <<https://www.epfl.ch/labs/slab/>>. Citation on page 71.

ETH, Zürich. **Artikel: Über die Zerstörungskraft von Lawinen**. 2022. [Online; accessed August 02, 2022]. Available: <<https://www.e-periodica.ch/digbib/view?pid=sbz-002:1955:73::175#18911>>. Citation on page 42.

Failes, Ian. **Behind ‘Black Widow’: A helicopter, a prison, an avalanche and a digital pig**. 2021. [Online; accessed October 6, 2022]. Available: <<https://beforesandafters.com/2021/07/30/behind-black-widow-a-helicopter-a-prison-an-avalanche-and-a-digital-pig/>>. Citations on pages 74 and 75.

FAILLETTAZ, J.; LOUCHET, F.; GRASSO, J.; DAUDON, D.; DENDIEVEL, R. Scale invariance of snow avalanche triggering mechanisms. In: **Stevens JR ed Proceedings of the International Snow Science Workshop**. [S.l.: s.n.], 2002. v. 29, p. 528–531. Citation on page 34.

FARIN, M.; MANGENEY, A.; ROCHE, O. Fundamental changes of granular flow dynamics, deposition, and erosion processes at high slope angles: Insights from laboratory experiments. **Journal of Geophysical Research: Earth Surface**, v. 119, n. 3, p. 504–532, 2014. Available: <<https://agupubs.onlinelibrary.wiley.com/doi/abs/10.1002/2013JF002750>>. Citation on page 36.

FAVIER, L.; DAUDON, D.; DONZÉ, F.-V.; MAZARS, J. Predicting the drag coefficient of a granular flow using the discrete element method. **Journal of Statistical Mechanics: Theory and Experiment**, IOP Publishing, v. 2009, n. 06, p. P06012, 6 2009. Available: <<https://doi.org/10.1088/1742-5468/2009/06/p06012>>. Citation on page 71.

Federal Ministry Republic of Austria. **Association pour l’amélioration et le partage de connaissances sur les avalanches**. 2023. [Online; accessed December 5, 2023]. Available: <<https://info.bml.gv.at/en/topics/forests/forest-and-natural-hazards/what-is-an-avalanche.html>>. Citation on page 119.

FEI, J. bo; JIE, Y. xin; ZHANG, B. yin; FU, X. dong. A shallow constitutive law-based granular flow model for avalanches. **Computers and Geotechnics**, v. 68, p. 109–116, 2015. ISSN 0266-352X. Available: <<https://www.sciencedirect.com/science/article/pii/S0266352X15000786>>. Citation on page 52.

FICK, A. Ueber diffusion. **Annalen der Physik**, v. 170, n. 1, p. 59–86, 1855. Available: <<https://onlinelibrary.wiley.com/doi/abs/10.1002/andp.18551700105>>. Citation on page 157.

FISCHER, J.-T. A novel approach to evaluate and compare computational snow avalanche simulation. **Natural Hazards and Earth System Sciences**, v. 13, n. 6, p. 1655–1667, 2013. Available: <<https://nhess.copernicus.org/articles/13/1655/2013/>>. Citation on page 73.

FISCHER, J.-T.; KOFLER, A.; FELLIN, W.; GRANIG, M.; KLEEMAYR, K. Multivariate parameter optimization for computational snow avalanche simulation. **Journal of Glaciology**, Cambridge University Press, v. 61, n. 229, p. 875–888, 2015. Citations on pages 56, 57, 73, and 82.

FRANTZ, R. A.; DESKOS, G.; LAIZET, S.; SILVESTRINI, J. H. High-fidelity simulations of gravity currents using a high-order finite-difference spectral vanishing viscosity approach. **Computers & Fluids**, v. 221.0, p. 104902, 2021. ISSN 0045-7930. Available: <<https://www.sciencedirect.com/science/article/pii/S0045793021000682>>. Citation on page 73.

FUKUSHIMA, Y. Analytical study of powder snow avalanches. **Journal of the Japanese Society of Snow and Ice**, The Japanese Society of Snow and Ice, v. 48, n. 4, p. 189–197, 1986. Citation on page 63.

FUKUSHIMA, Y.; HAGIHARA, T.; SAKAMOTO, M. Dynamics of inclined suspension thermals. **Fluid Dynamics Research**, v. 26, n. 5, p. 337–354, 2000. ISSN 0169-5983. Available: <<https://www.sciencedirect.com/science/article/pii/S0169598399000313>>. Citation on page 63.

FUKUSHIMA, Y.; HAYAKAWA, N. Analysis of powder-snow avalanches using three-dimensional topographic data. **Annals of Glaciology**, Cambridge University Press, v. 18, p. 102106, 1993. Citation on page 63.

FUKUSHIMA, Y.; PARKER, G. Discontinuous turbidity currents and powder snow avalanches. In: **Unknown Host Publication Title**. [S.l.]: Am. Soc. Civ. Engrs, 1984. Citation on page 63.

_____. Numerical simulation of powder-snow avalanches. **Journal of Glaciology**, Cambridge University Press, v. 36.0, n. 123, p. 229237, 1990. Citations on pages 30 and 63.

FURDADA, G.; MARGALEF, A.; TRAPERO, L.; PONS, M.; ARENY, F.; BARÓ, M.; REYES, A.; GUINAU, M. The avalanche of les fonts d'arinsal (andorra): An example of a pure powder, dry snow avalanche. **Geosciences**, v. 10, n. 4, 2020. ISSN 2076-3263. Available: <<https://www.mdpi.com/2076-3263/10/4/126>>. Citation on page 30.

GAO, M.; PRADHANA, A.; HAN, X.; GUO, Q.; KOT, G.; SIFAKIS, E.; JIANG, C. Animating fluid sediment mixture in particle-laden flows. **ACM Trans. Graph.**, Association for Computing Machinery, New York, NY, USA, v. 37, n. 4, jul 2018. ISSN 0730-0301. Available: <<https://doi.org/10.1145/3197517.3201309>>. Citation on page 74.

GAO, M.; TAMPUBOLON, A. P.; JIANG, C.; SIFAKIS, E. An adaptive generalized interpolation material point method for simulating elastoplastic materials. **ACM Transactions on Graphics (TOG)**, ACM, v. 36.0, n. 6, p. 223, 2017. Citation on page 74.

GAUER, P. Comparison of avalanche front velocity measurements and implications for avalanche models. **Cold Regions Science and Technology**, v. 97, p. 132–150, 2014. ISSN 0165-232X. Available: <<https://www.sciencedirect.com/science/article/pii/S0165232X1300147X>>. Citation on page 30.

GAUER, P.; ISSLER, D. Possible erosion mechanisms in snow avalanches. **Annals of Glaciology**, Cambridge University Press, v. 38, p. 384392, 2004. Citations on pages 36 and 54.

GAUER, P.; ISSLER, D.; LIED, K.; KRISTENSEN, K.; SANDERSEN, F. On snow avalanche flow regimes: Inferences from observations and measurements. In: **Proceedings Whistler 2008 International Snow Science Workshop September 21-27, 2008**. [S.l.: s.n.], 2008. p. 717. Citation on page 33.

GAUME, J.; CHAMBON, G.; REIWEGER, I.; HERWIJNEN, A. van; SCHWEIZER, J. On the failure criterion of weak-snow layers using the discrete element method. In: **Proceedings ISSW**. [S.l.: s.n.], 2014. p. 681–688. Citation on page 71.

GAUME, J.; GAST, T.; TERAN, J.; HERWIJNEN, A. van; JIANG, C. Dynamic anticrack propagation in snow. **Nature Communications**, v. 9, n. 1, p. 3047, 8 2018. ISSN 2041-1723. Available: <<https://doi.org/10.1038/s41467-018-05181-w>>. Citations on pages 28, 71, and 74.

GAUME, J.; van Herwijnen, A.; GAST, T.; TERAN, J.; JIANG, C. Investigating the release and flow of snow avalanches at the slope-scale using a unified model based on the material point method. **Cold Regions Science and Technology**, v. 168, p. 102847, 2019. ISSN 0165-232X. Available: <<https://www.sciencedirect.com/science/article/pii/S0165232X19302149>>. Citations on pages 49 and 71.

GEORGE, D. L.; IVERSON, R. M. A depth-averaged debris-flow model that includes the effects of evolving dilatancy. ii. numerical predictions and experimental tests. **Proceedings of the Royal Society A: Mathematical, Physical and Engineering Sciences**, The Royal Society Publishing, v. 470, n. 2170, p. 20130820, 2014. Citation on page 53.

GISSLER, C.; HENNE, A.; BAND, S.; PEER, A.; TESCHNER, M. An implicit compressible sph solver for snow simulation. **ACM Trans. Graph.**, Association for Computing Machinery, New York, NY, USA, v. 39.0, n. 4, 7 2020. ISSN 0730-0301. Available: <<https://doi.org/10.1145/3386569.3392431>>. Citation on page 74.

GOES, F. de; WALLEZ, C.; HUANG, J.; PAVLOV, D.; DESBRUN, M. Power particles: An incompressible fluid solver based on power diagrams. **ACM Trans. Graph.**, Association for Computing Machinery, New York, NY, USA, v. 34.0, n. 4, 7 2015. ISSN 0730-0301. Available: <<https://doi.org/10.1145/2766901>>. Citation on page 74.

GONZALEZ, O.; STUART, A. M. **A first course in continuum mechanics**. [S.l.]: Cambridge University Press, 2008. Citations on pages 47, 159, and 167.

GRAY, J.; WIELAND, M.; HUTTER, K. Gravity-driven free surface flow of granular avalanches over complex basal topography. **Proceedings of the Royal Society of London. Series A: Mathematical, Physical and Engineering Sciences**, The Royal Society, v. 455.0, n. 1985, p. 1841–1874, 1999. Citation on page 52.

GRAY, J. M. N. T.; EDWARDS, A. N. A depth-averaged $\mu(i)$ -rheology for shallow granular free-surface flows. **Journal of Fluid Mechanics**, Cambridge University Press, v. 755, p. 503–534, 2014. Citations on pages 48 and 53.

GRAY, J. M. N. T.; TAI, Y.-C.; NOELLE, S. Shock waves, dead zones and particle-free regions in rapid granular free-surface flows. **Journal of Fluid Mechanics**, Cambridge University Press, v. 491, p. 161–181, 2003. Citation on page 52.

GREENSHIELDS, C. J.; WELLER, H. G. Notes on computational fluid dynamics: General principles. (**No Title**), 2022. Citations on pages 107, 171, and 184.

GREENSHIELDS, C. J.; WELLER, H. G.; GASPARINI, L.; REESE, J. M. Implementation of semi-discrete, non-staggered central schemes in a colocated, polyhedral, finite volume framework, for high-speed viscous flows. **International Journal for Numerical Methods in Fluids**, v. 63, n. 1, p. 1–21, 2010. Available: <<https://onlinelibrary.wiley.com/doi/abs/10.1002/flid.2069>>. Citation on page 94.

GREVE, R.; HUTTER, K. Motion of a granular avalanche in a convex and concave curved chute: experiments and theoretical predictions. **Philosophical Transactions of the Royal Society of London. Series A: Physical and Engineering Sciences**, v. 342, n. 1666, p. 573–600, 1993. Available: <<https://royalsocietypublishing.org/doi/abs/10.1098/rsta.1993.0033>>. Citations on pages 34 and 52.

GREVE, R.; KOCH, T.; HUTTER, K. Unconfined flow of granular avalanches along a partly curved surface. i. theory. **Proceedings of the Royal Society of London. Series A: Mathematical and Physical Sciences**, The Royal Society London, v. 445, n. 1924, p. 399–413, 1994. Citation on page 52.

GRIGORIAN, S.; EGLIT, M.; IAKIMOV, I. L. New statement and solution of the problem of the motion of snow avalanche. **Snow, Avalanches & Glaciers. Tr. Vysokogornogo Geofizich Inst**, v. 12, p. 104–113, 1967. Citation on page 45.

GRIGORIAN, S.; OSTROUMOV, A. The mathematical model for slope processes of avalanche type (in russian). scientific report 1955. **Institute for Mechanics, Moscow State University, Moscow, Russia**, 1977. Citation on page 45.

GRIGORIAN, S. S.; OSTROUMOV, A. V. On a continuum model for avalanche flow and its simplified variants. **Geosciences**, v. 10, n. 1, 2020. ISSN 2076-3263. Available: <<https://www.mdpi.com/2076-3263/10/1/35>>. Citations on pages 28, 46, 54, and 55.

GRIGORYAN, S. A new law of friction and mechanism for large-scale avalanches and landslides. In: **Soviet Physics Doklady**. [S.l.: s.n.], 1979. v. 24, p. 110. Citation on page 46.

GRÖBELBAUER, H. P.; FANNELØP, T. K.; BRITTER, R. E. The propagation of intrusion fronts of high density ratios. **Journal of Fluid Mechanics**, Cambridge University Press, v. 250, p. 669–687, 1993. Citation on page 60.

GUBLER, H. Comparison of three models of avalanche dynamics. **Annals of Glaciology**, Cambridge University Press, v. 13, p. 82–89, 1989. Citation on page 43.

_____. **Swiss avalanche-dynamics procedures for dense flow avalanches**. [S.l.]: AlpuG Davos, 2005. Citations on pages 43 and 44.

GÜÇER, D.; ÖZGÜÇ, H. B. Simulation of a flowing snow avalanche using molecular dynamics. **Turkish Journal of Electrical Engineering & Computer Sciences**, The Scientific and Technological Research Council of Turkey, v. 22.0, n. 6, p. 1596–1610, 2014. Citation on page 75.

GURJAR, S. **Numerical Simulation of a Powder Snow Avalanche**. Phd Thesis (PhD Thesis) — ETH Zurich, 2023. Citation on page 67.

HAERI, A.; SKONIECZNY, K. Three-dimensional granular flow continuum modeling via material point method with hyperelastic nonlocal granular fluidity. **Computer Methods in Applied Mechanics and Engineering**, v. 394, p. 114904, 2022. ISSN 0045-7825. Available: <<https://www.sciencedirect.com/science/article/pii/S0045782522001876>>. Citation on page 71.

HAFF, P. K. Grain flow as a fluid-mechanical phenomenon. **Journal of Fluid Mechanics**, Cambridge University Press, v. 134, p. 401–430, 1983. Citations on pages 44 and 49.

HARBITZ, C. **A survey of computational models for snow avalanche motion**. [S.l.]: NGI report, Oslo, 1998. Citation on page 30.

HARBITZ, C. B.; ISSLER, D.; KEYLOCK, C. J. Conclusions from a recent survey of avalanche computational models. In: . [S.l.: s.n.], 1998. Citations on pages 30 and 37.

HEIMGARTNER, M. On the flow of avalanching snow. **Journal of Glaciology**, Cambridge University Press, v. 19, n. 81, p. 357–363, 1977. Citation on page 43.

HERGARTEN, S.; ROBL, J. Modelling rapid mass movements using the shallow water equations in cartesian coordinates. **Natural Hazards and Earth System Sciences**, v. 15.0, p. 671–685, 2015. Citation on page 53.

HERMANN, F.; HUTTER, K. Laboratory experiments on the dynamics of powder-snow avalanches in the run-out zone. **Journal of Glaciology**, Cambridge University Press, v. 37, n. 126, p. 281295, 1991. Citations on pages 34 and 35.

HILL, S. **1/9 Debris Flow**. 2019. [Online; accessed September 09, 2023]. Available: <<https://sbbucketbrigade.org/timeline/1-9-debris-flow/>>. Citation on page 17.

HOLZMANN, T. Mathematics, numerics, derivations and openfoam®. **Loeben, Germany: Holzmann CFD**, 2016. Citation on page 177.

HOPFINGER, E. J. Snow avalanche motion and related phenomena. **Annual Review of Fluid Mechanics**, v. 15, n. 1, p. 47–76, 1983. Available: <<https://doi.org/10.1146/annurev.fl.15.010183.000403>>. Citations on pages 30, 54, 58, and 60.

HOPFINGER, E. J.; TOCHON-DANGUY, J.-C. A model study of powder-snow avalanches. **Journal of Glaciology**, Cambridge University Press, v. 19.0, n. 81, p. 343356, 1977. Citation on page 61.

HOU, J.; LIANG, Q.; SIMONS, F.; HINKELMANN, R. A 2d well-balanced shallow flow model for unstructured grids with novel slope source term treatment. **Advances in Water Resources**, v. 52.0, p. 107–131, 2013. ISSN 0309-1708. Available: <<https://www.sciencedirect.com/science/article/pii/S0309170812002230>>. Citation on page 53.

_____. A stable 2d unstructured shallow flow model for simulations of wetting and drying over rough terrains. **Computers & Fluids**, v. 82.0, p. 132–147, 2013. ISSN 0045-7930. Available: <<https://www.sciencedirect.com/science/article/pii/S0045793013001552>>. Citation on page 53.

HUANG, Z.; AODE, H. A laboratory study of rheological properties of mudflows in hangzhou bay, china. **International Journal of Sediment Research**, v. 24, n. 4, p. 410–424, 2009. ISSN 1001-6279. Available: <<https://www.sciencedirect.com/science/article/pii/S1001627910600145>>. Citation on page 47.

HUBBARD, M. Multidimensional slope limiters for muscl-type finite volume schemes on unstructured grids. **Journal of Computational Physics**, v. 155.0, n. 1, p. 54–74, 1999. ISSN 0021-9991. Available: <<https://www.sciencedirect.com/science/article/pii/S0021999199963295>>. Citation on page 53.

HUI, W.; LI, P.; LI, Z. A unified coordinate system for solving the two-dimensional euler equations. **Journal of Computational Physics**, v. 153, n. 2, p. 596–637, 1999. ISSN 0021-9991. Available: <<https://www.sciencedirect.com/science/article/pii/S0021999199962952>>. Citation on page 53.

- HUNGR, O. A model for the runout analysis of rapid flow slides, debris flows, and avalanches. **Canadian Geotechnical Journal**, v. 32, n. 4, p. 610–623, 1995. Available: <<https://doi.org/10.1139/t95-063>>. Citations on pages 41 and 52.
- HUPPERT, H. E. Gravity currents: a personal perspective. **Journal of Fluid Mechanics**, Cambridge University Press, v. 554, p. 299–322, 2006. Citations on pages 57 and 60.
- HUSSIN, H. Y.; LUNA, B. Q.; WESTEN, C. J. van; CHRISTEN, M.; MALET, J.-P.; ASCH, T. W. J. van. Parameterization of a numerical 2-d debris flow model with entrainment: a case study of the faucon catchment, southern french alps. **Natural Hazards and Earth System Sciences**, v. 12, n. 10, p. 3075–3090, 2012. Available: <<https://nhess.copernicus.org/articles/12/3075/2012/>>. Citation on page 42.
- HUTTER, K. Avalanche dynamics. In: _____. **Hydrology of Disasters**. Dordrecht: Springer Netherlands, 1996. p. 317–394. ISBN 978-94-015-8680-1. Available: <https://doi.org/10.1007/978-94-015-8680-1_11>. Citation on page 47.
- HUTTER, K.; KOCH, T. Motion of a granular avalanche in an exponentially curved chute: experiments and theoretical predictions. **Philosophical Transactions of the Royal Society of London. Series A: Physical and Engineering Sciences**, The Royal Society London, v. 334, n. 1633, p. 93–138, 1991. Citations on pages 50 and 52.
- HUTTER, K.; RAJAGOPAL, K. R. On flows of granular materials. **Continuum Mechanics and Thermodynamics**, v. 6, n. 2, p. 81–139, 6 1994. ISSN 1432-0959. Available: <<https://doi.org/10.1007/BF01140894>>. Citation on page 49.
- HUTTER, K.; SAVAGE, S. B.; NOHGUCHI, Y. Numerical, analytical, and laboratory experimental studies of granular avalanche flows. **Annals of Glaciology**, Cambridge University Press, v. 13, p. 109–116, 1989. Citation on page 50.
- HUTTER, K.; WANG, Y.; PUDASAINI, S. P. The savage–hutter avalanche model: how far can it be pushed? **Philosophical Transactions of the Royal Society A: Mathematical, Physical and Engineering Sciences**, The Royal Society London, v. 363, n. 1832, p. 1507–1528, 2005. Citations on pages 51 and 52.
- HWANG, H.; HUTTER, K. A new kinetic model for rapid granular flow. **Continuum Mechanics and Thermodynamics**, Springer, v. 7, n. 3, p. 357–384, 1995. Citation on page 52.
- imageworks. **Mulan**. 2020. [Online; accessed October 6, 2022]. Available: <<https://www.imageworks.com/our-craft/vfx/movies/mulan>>. Citations on pages 74 and 75.
- ISSA, R. Solution of the implicitly discretised fluid flow equations by operator-splitting. **Journal of Computational Physics**, v. 62, n. 1, p. 40–65, 1986. ISSN 0021-9991. Available: <<https://www.sciencedirect.com/science/article/pii/0021999186900999>>. Citation on page 182.
- ISSLER, D. Modelling of snow entrainment and deposition in powder-snow avalanches. **Annals of Glaciology**, Cambridge University Press, v. 26, p. 253258, 1998. Citations on pages 69, 70, and 72.
- _____. Experimental information on the dynamics of dry-snow avalanches. In: _____. **Dynamic Response of Granular and Porous Materials under Large and Catastrophic Deformations**. Berlin, Heidelberg: Springer Berlin Heidelberg, 2003. p. 109–160. ISBN 978-3-540-36565-5. Available: <https://doi.org/10.1007/978-3-540-36565-5_4>. Citation on page 33.

_____. Dynamically consistent entrainment laws for depth-averaged avalanche models. **Journal of Fluid Mechanics**, Cambridge University Press, v. 759, p. 701738, 2014. Citations on pages 23, 36, and 54.

_____. The 2017 rigopiano avalanchodynamics inferred from field observations. **Geosciences**, v. 10, n. 466, 2020. ISSN 2076-3263. Available: <<https://www.mdpi.com/2076-3263/10/11/466>>. Citation on page 30.

ISSLER, D.; ERRERA, A.; PRIANO, S.; GUBLER, H.; TEUFEN, B.; KRUMMENACHER, B. Inferences on flow mechanisms from snow avalanche deposits. **Annals of Glaciology**, Cambridge University Press, v. 49, p. 187–192, 2008. Citation on page 36.

ISSLER, D.; GAUER, P.; BARBOLINI, M.; BALEAN, R. Continuum models of particle entrainment and deposition in snow drift and avalanche dynamics. In: **Models of Continuum Mechanics in Analysis and Engineering. Proc. of a conference held at the Technische Universität Darmstadt, Sept.** [S.l.: s.n.], 2000. v. 30, p. 58–80. Citations on pages 66 and 72.

ISSLER, D.; GAUER, P.; SCHAER, M.; KELLER, S. Inferences on mixed snow avalanches from field observations. **Geosciences**, v. 10, n. 1, 2020. ISSN 2076-3263. Available: <<https://www.mdpi.com/2076-3263/10/1/2>>. Citations on pages 30 and 36.

ISSLER, D.; JENKINS, J. T.; MCELWAIN, J. N. Comments on avalanche flow models based on the concept of random kinetic energy. **Journal of Glaciology**, Cambridge University Press, v. 64, n. 243, p. 148–164, 2018. Citation on page 57.

ISSLER, D.; JÓHANNESSON, T. Dynamically consistent entrainment and deposition rates in depth-averaged gravity mass flow models. **Norwegian Geotechnical Institute, Oslo, Technial hlte U**, v. 111, p. 1200–1, 2011. Citation on page 36.

ISSLER, D.; PÉREZ, M. P. Interplay of entrainment and rheology in snow avalanches: a numerical study. **Annals of Glaciology**, Cambridge University Press, v. 52, n. 58, p. 143–147, 2011. Citation on page 54.

IVANOVA, K.; CAVIEZEL, A.; BHLER, Y.; BARTELT, P. Numerical modeling of turbulent geophysical flows using a hyperbolic shear shallow water model: Application to powder snow avalanches. **Computers & Fluids**, p. 105211, 2021. ISSN 0045-7930. Available: <<https://www.sciencedirect.com/science/article/pii/S004579302100325X>>. Citations on pages 30, 69, and 91.

IVERSON, R. M. The physics of debris flows. **Reviews of geophysics**, Wiley Online Library, v. 35.0, n. 3, p. 245–296, 1997. Citation on page 53.

IVERSON, R. M.; DENLINGER, R. P. Flow of variably fluidized granular masses across three-dimensional terrain: 1. coulomb mixture theory. **Journal of Geophysical Research: Solid Earth**, v. 106, n. B1, p. 537–552, 2001. Available: <<https://agupubs.onlinelibrary.wiley.com/doi/abs/10.1029/2000JB900329>>. Citations on pages 48 and 53.

IVERSON, R. M.; GEORGE, D. L. A depth-averaged debris-flow model that includes the effects of evolving dilatancy. i. physical basis. **Proceedings of the Royal Society A: Mathematical, Physical and Engineering Sciences**, The Royal Society Publishing, v. 470, n. 2170, p. 20130819, 2014. Citation on page 53.

IVERSON, R. M.; OUYANG, C. Entrainment of bed material by earth-surface mass flows: Review and reformulation of depth-integrated theory. **Reviews of Geophysics**, v. 53, n. 1, p. 27–58, 2015. Available: <<https://agupubs.onlinelibrary.wiley.com/doi/abs/10.1002/2013RG000447>>. Citation on page 55.

JAMIESON, B.; MARGRETH, S.; JONES, A. Application and limitations of dynamic models for snow avalanche hazard mapping. In: **Proceedings Whistler 2008 International Snow Science Workshop September 21-27, 2008**. [S.l.: s.n.], 2008. p. 730. Citations on pages 44 and 72.

JASAK, H.; JEMCOV, A.; TUKOVIĆ Željko. Openfoam: A c++ library for complex physics simulations. In: . [s.n.], 2007. Available: <<https://api.semanticscholar.org/CorpusID:35226827>>. Citation on page 177.

JIANG, C.; GAST, T.; TERAN, J. Anisotropic elastoplasticity for cloth, knit and hair frictional contact. **ACM Transactions on Graphics (TOG)**, ACM, v. 36.0, n. 4, p. 152, 2017. Citation on page 74.

JIANG, C.; SCHROEDER, C.; SELLE, A.; TERAN, J.; STOMAKHIN, A. The affine particle-in-cell method. **ACM Transactions on Graphics (TOG)**, ACM, v. 34.0, n. 4, p. 51, 2015. Citation on page 74.

JONTHAN, Å.; DANIEL, C. **Slab and Powder-Snow avalanche animation on the GPU**. 2021. Citation on page 74.

JUEZ, C.; MURILLO, J.; GARCÍA-NAVARRO, P. 2d simulation of granular flow over irregular steep slopes using global and local coordinates. **Journal of Computational Physics**, v. 255, p. 166–204, 2013. ISSN 0021-9991. Available: <<https://www.sciencedirect.com/science/article/pii/S0021999113005275>>. Citation on page 53.

KABORE, B. W.; PETERS, B.; MICHAEL, M.; NICOT, F. A discrete element framework for modeling the mechanical behaviour of snow—part i: Mechanical behaviour and numerical model. **Granular Matter**, v. 23, n. 2, p. 42, 4 2021. ISSN 1434-7636. Available: <<https://doi.org/10.1007/s10035-020-01083-1>>. Citation on page 71.

KAPLER, A. Avalanche! snowy fx for xxx. In: ACM. **ACM SIGGRAPH 2003 Sketches & Applications**. [S.l.], 2003. p. 1–1. Citations on pages 74 and 75.

KARMAN, T. V. The engineer grapples with nonlinear problems. **Bulletin of the American Mathematical Society**, American Mathematical Society, v. 46, n. 8, p. 615–683, 1940. Citations on pages 29 and 59.

KAY, M. **Practical Hydraulics and Water Resources Engineering (3rd ed.)**. [S.l.]: CRC Press., 2017. ISBN 9781315380674. Citation on page 41.

KAZHIKHOV, A. V.; SMAGULOV, S. The correctness of boundary-value problems in a diffusion model of an inhomogeneous liquid. In: **Soviet Physics Doklady**. [S.l.: s.n.], 1977. v. 22, p. 249. Citation on page 67.

KELLER, S. Measurements of powder snow avalanches-laboratory. **Surveys in Geophysics**, Springer, v. 16, n. 5, p. 661–670, 1995. Citation on page 34.

KERN, M.; BARTELT, P.; SOVILLA, B.; BUSER, O. Measured shear rates in large dry and wet snow avalanches. **Journal of Glaciology**, Cambridge University Press, v. 55, n. 190, p. 327–338, 2009. Citation on page 36.

KERN, M.; TIEFENBACHER, F.; MCELWAIN, J. The rheology of snow in large chute flows. **Cold Regions Science and Technology**, v. 39, n. 2, p. 181–192, 2004. ISSN 0165-232X. Snow And Avalanches: Papers Presented At The European Geophysical Union Conference, Nice, April 2003. Dedicated To The Avalanche Dynamics Pioneer Dr. B. Salm. Available: <<https://www.sciencedirect.com/science/article/pii/S0165232X04000230>>. Citation on page 66.

KIM, T.; THÜREY, N.; JAMES, D.; GROSS, M. Wavelet turbulence for fluid simulation. **ACM Trans. Graph.**, Association for Computing Machinery, New York, NY, USA, v. 27.0, n. 3, p. 16, 9 2008. ISSN 0730-0301. Available: <<https://doi.org/10.1145/1360612.1360649>>. Citation on page 74.

KIM, T.-Y.; FLORES, L. Snow avalanche effects for mummy 3. In: **ACM SIGGRAPH**. [S.l.: s.n.], 2008. p. 11–15. Citations on pages 74 and 75.

KOCH, T.; GREVE, R.; HUTTER, K. Unconfined flow of granular avalanches along a partly curved surface. ii. experiments and numerical computations. **Proceedings of the Royal Society of London. Series A: Mathematical and Physical Sciences**, The Royal Society London, v. 445, n. 1924, p. 415–435, 1994. Citations on pages 52 and 80.

KONOPLIV, N. A.; SMITH, S. G. L.; MCELWAIN, J. N.; MEIBURG, E. Modelling gravity currents without an energy closure. **Journal of Fluid Mechanics**, Cambridge University Press, v. 789, p. 806–829, 2016. Citation on page 60.

KULIKOVSKII, A.; SVESHNIKOVA, E. A model for simulation of a powder snow avalanche. **Mater. Glyatsiologicheskikh Issled.(Data Glaciol. Stud.)**, v. 53, p. 108–112, 1977. Citation on page 61.

KÖHLER, A.; MCELWAIN, J. N.; SOVILLA, B. Geodar data and the flow regimes of snow avalanches. **Journal of Geophysical Research: Earth Surface**, v. 123, n. 6, p. 1272–1294, 2018. Available: <<https://agupubs.onlinelibrary.wiley.com/doi/abs/10.1002/2017JF004375>>. Citation on page 33.

LABUZ JOSEPH F.AND ZANG, A. Mohr–coulomb failure criterion. **Rock Mechanics and Rock Engineering**, v. 45, n. 6, p. 975–979, Nov 2012. ISSN 1434-453X. Available: <<https://doi.org/10.1007/s00603-012-0281-7>>. Citation on page 48.

LACHAPPELLE, E. R. Snow avalanches: A review of current research and applications. **Journal of Glaciology**, Cambridge University Press, v. 19, n. 81, p. 313324, 1977. Citations on pages 28 and 42.

LAGOTALA, H. Étude de l'avalanche des pèlerins (chamonix) 10-11 avril 1924. **Le Globe. Revue genevoise de géographie**, Persée-Portail des revues scientifiques en SHS, v. 66, n. 1, p. 37–85, 1927. Citation on page 40.

LAISET, S.; LAMBALLAIS, E. **Xcompact3d in turbulence we trust**. 2022. [Online; accessed September 26, 2022]. Available: <<https://www.incompact3d.com/>>. Citation on page 74.

LAUNDER, B.; SPALDING, D. The numerical computation of turbulent flows. **Computer Methods in Applied Mechanics and Engineering**, v. 3, n. 2, p. 269–289, 1974. ISSN 0045-7825. Available: <<https://www.sciencedirect.com/science/article/pii/0045782574900292>>. Citation on page 66.

Lê, L.; PITMAN, E. B. A model for granular flows over an erodible surface. **SIAM Journal on Applied Mathematics**, v. 70, n. 5, p. 1407–1427, 2010. Available: <<https://doi.org/10.1137/060677501>>. Citation on page 53.

LEMONS, D. S. An introduction to stochastic processes in physics. **American Journal of Physics**, v. 71, n. 2, p. 191–191, 2003. Available: <<https://doi.org/10.1119/1.1526134>>. Citation on page 57.

LEPERA, R. Modeling and simulation of rapid granular flows. application to powder snow avalanches. 2020. Citation on page 66.

LEVEQUE, R. J. **Finite Volume Methods for Hyperbolic Problems**. [S.l.]: Cambridge University Press, 2002. (Cambridge Texts in Applied Mathematics). Citation on page 53.

LI, R.; ZHANG, X. **A Finite Volume Scheme for Savage-Hutter Equations on Unstructured Grids**. 2019. Citation on page 53.

LI, X.; SOVILLA, B.; JIANG, C.; GAUME, J. The mechanical origin of snow avalanche dynamics and flow regime transitions. **The Cryosphere**, v. 14, n. 10, p. 3381–3398, 2020. Available: <<https://tc.copernicus.org/articles/14/3381/2020/>>. Citation on page 71.

_____. Three-dimensional and real-scale modeling of flow regimes in dense snow avalanches. **Landslides**, Springer, v. 18, n. 10, p. 3393–3406, 2021. Citations on pages 28 and 71.

LI, X.; SOVILLA, B.; LIGNEAU, C.; JIANG, C.; GAUME, J. Different erosion and entrainment mechanisms in snow avalanches. **Mechanics Research Communications**, v. 124, p. 103914, 2022. ISSN 0093-6413. Available: <<https://www.sciencedirect.com/science/article/pii/S0093641322000647>>. Citations on pages 55, 56, and 71.

LIANG, Q.; MARCHE, F. Numerical resolution of well-balanced shallow water equations with complex source terms. **Advances in Water Resources**, v. 32.0, n. 6, p. 873–884, 2009. ISSN 0309-1708. Available: <<https://www.sciencedirect.com/science/article/pii/S0309170809000396>>. Citation on page 53.

LIED, K.; BAKKEHØI, K. Empirical calculations of snow–avalanche run–out distance based on topographic parameters. **Journal of Glaciology**, Cambridge University Press, v. 26, n. 94, p. 165–177, 1980. Citation on page 38.

LIED, K.; WEILER, C.; BAKKEHOI, S.; HOPF, J. Calculation methods for avalanche run-out distance for the austrian alps. In: **Les apports de la recherche scientifique à la sécurité neige glace et avalanche**. [S.l.: s.n.], 1995. Citation on page 44.

LIGNEAU, C.; SOVILLA, B.; GAUME, J. Numerical investigation of the effect of cohesion and ground friction on snow avalanches flow regimes. **PloS one**, Public Library of Science San Francisco, CA USA, v. 17, n. 2, p. e0264033, 2022. Citations on pages 44 and 48.

LINDEN, P. F.; SIMPSON, J. E. Gravity-driven flows in a turbulent fluid. **Journal of Fluid Mechanics**, Cambridge University Press, v. 172, p. 481–497, 1986. Citation on page 34.

LIU, W.; HE, S.-m.; ONYANG, C.-j. Dynamic process simulation with a savage-hutter type model for the intrusion of landslide into river. **Journal of Mountain Science**, v. 13, n. 7, p. 1265–1274, 7 2016. ISSN 1993-0321. Available: <<https://doi.org/10.1007/s11629-015-3439-4>>. Citation on page 53.

LIU, X.; CHEN, Y.; ZHANG, H.; ZOU, Y.; WANG, Z.; PENG, Q. Physically based modeling and rendering of avalanches. **The Visual Computer**, v. 37, n. 9, p. 2619–2629, Sep 2021. ISSN 1432-2315. Available: <<https://doi.org/10.1007/s00371-021-02215-1>>. Citation on page 75.

LIU, Y.; ZHOU, J.; SONG, L.; ZOU, Q.; LIAO, L.; WANG, Y. Numerical modelling of free-surface shallow flows over irregular topography with complex geometry. **Applied Mathematical Modelling**, v. 37.0, n. 23, p. 9482–9498, 2013. ISSN 0307-904X. Available: <<https://www.sciencedirect.com/science/article/pii/S0307904X13003077>>. Citation on page 53.

LOUCHET, F. **Snow Avalanches: Beliefs, Facts, and Science**. [S.l.]: Oxford University Press, USA, 2021. Citation on page 30.

LOUGE, M. Y.; CARROLL, C. S.; TURNBULL, B. Role of pore pressure gradients in sustaining frontal particle entrainment in eruption currents: The case of powder snow avalanches. **Journal of Geophysical Research: Earth Surface**, v. 116, n. F4, 2011. Available: <<https://agupubs.onlinelibrary.wiley.com/doi/abs/10.1029/2011JF002065>>. Citation on page 69.

LOWE, D. R. Subaqueous liquefied and fluidized sediment flows and their deposits. **Sedimentology**, v. 23, n. 3, p. 285–308, 1976. Available: <<https://onlinelibrary.wiley.com/doi/abs/10.1111/j.1365-3091.1976.tb00051.x>>. Citation on page 16.

_____. Sediment Gravity Flows: Their Classification and Some Problems of Application to Natural Flows and Deposits. In: **Geology of Continental Slopes**. SEPM Society for Sedimentary Geology, 1979. ISBN 9781565761575. Available: <<https://doi.org/10.2110/pec.79.27.0075>>. Citation on page 17.

LUCA, I.; HUTTER, K.; TAI, Y. C.; KUO, C. Y. A hierarchy of avalanche models on arbitrary topography. **Acta Mechanica**, v. 205, n. 1, p. 121–149, 6 2009. ISSN 1619-6937. Available: <<https://doi.org/10.1007/s00707-009-0165-4>>. Citation on page 53.

MAHAJAN, P.; BROWN, R. L. A microstructure-based constitutive law for snow. **Annals of Glaciology**, Cambridge University Press, v. 18, p. 287–294, 1993. Citation on page 49.

MAJOR, J. J.; PIERSON, T. C. Debris flow rheology: Experimental analysis of fine-grained slurries. **Water resources research**, Wiley Online Library, v. 28, n. 3, p. 841–857, 1992. Citation on page 47.

MANGENEY-CASTELNAU, A.; VILOTTE, J.-P.; BRISTEAU, M. O.; PERTHAME, B.; BOUCHUT, F.; SIMEONI, C.; YERNENI, S. Numerical modeling of avalanches based on saint venant equations using a kinetic scheme. **Journal of Geophysical Research: Solid Earth**, v. 108, n. B11, 2003. Available: <<https://agupubs.onlinelibrary.wiley.com/doi/abs/10.1029/2002JB002024>>. Citation on page 53.

MCCLUNG, D.; LIED, K. Statistical and geometrical definition of snow avalanche runout. **Cold Regions Science and Technology**, v. 13, n. 2, p. 107–119, 1987. ISSN 0165-232X. Available: <<https://www.sciencedirect.com/science/article/pii/0165232X87900498>>. Citation on page 38.

MCCLUNG, D.; MEARS, A.; SCHAEERER, P. Extreme avalanche run-out: Data from four mountain ranges. **Annals of Glaciology**, Cambridge University Press, v. 13, p. 180–184, 1989. Citation on page 38.

MCCLUNG, D. M. Extreme avalanche runout in space and time. **Canadian Geotechnical Journal**, v. 37, n. 1, p. 161–170, 2000. Available: <<https://doi.org/10.1139/t99-081>>. Citation on page 38.

MCCLUNG, D. M.; MEARS, A. I. Dry-flowing avalanche run-up and run-out. **Journal of Glaciology**, Cambridge University Press, v. 41, n. 138, p. 359–372, 1995. Citation on page 44.

MCELWAINE, J.; NISHIMURA, K. Ping-pong ball avalanche experiments. **Annals of Glaciology**, Cambridge University Press, v. 32, p. 241–250, 2001. Citation on page 35.

MCGILL, Z. **The Nine Avalanche Problems Explained**. 2023. [Online; accessed September 09, 2023]. Available: <<https://www.bakermountainguides.com/avalanche-problems/>>. Citation on page 21.

MEIBURG, E.; RADHAKRISHNAN, S.; NASR-AZADANI, M. Modeling Gravity and Turbidity Currents: Computational Approaches and Challenges. **Applied Mechanics Reviews**, v. 67, n. 4, 7 2015. ISSN 0003-6900. 040802. Available: <<https://doi.org/10.1115/1.4031040>>. Citations on pages 57 and 58.

MELLOR, M. **Avalanches**. [S.l.]: Cold Regions Research and Engineering Laboratory (US), 1968. Citation on page 30.

_____. **A review of basic snow mechanics**. [S.l.]: US Army Cold Regions Research and Engineering Laboratory Hanover, NH, 1974. Citation on page 49.

_____. Chapter 23 - dynamics of snow avalanches. In: VOIGHT, B. (Ed.). **Rockslides and Avalanches**, 1. Elsevier, 1978, (Developments in Geotechnical Engineering, v. 14). p. 753–792. Available: <<https://www.sciencedirect.com/science/article/pii/B9780444415073500313>>. Citation on page 30.

MEUNIER, M.; ANCEY, C. Towards a conceptual approach to predetermining long-return-period avalanche run-out distances. **Journal of Glaciology**, Cambridge University Press, v. 50, n. 169, p. 268–278, 2004. Citations on pages 39 and 56.

MIDDLETON, G. V.; HAMPTON, M. A. Part i. sediment gravity flows: mechanics of flow and deposition. Pacific section SEPM, 1973. Citation on page 16.

MISHRA, A.; MAHAJAN, P. A constitutive law for snow taking into account the compressibility. **Annals of Glaciology**, Cambridge University Press, v. 38, p. 145–149, 2004. Citation on page 49.

MORTON, B. R.; TAYLOR, G. I.; TURNER, J. S. Turbulent gravitational convection from maintained and instantaneous sources. **Proceedings of the Royal Society of London. Series A. Mathematical and Physical Sciences**, v. 234, n. 1196, p. 1–23, 1956. Available: <<https://royalsocietypublishing.org/doi/abs/10.1098/rspa.1956.0011>>. Citations on pages 60 and 61.

MOSHER, D.; CAMPBELL, D.; GARDNER, J.; PIPER, D.; CHAYTOR, J.; REBESCO, M. The role of deep-water sedimentary processes in shaping a continental margin: The northwest atlantic. **Marine Geology**, v. 393, p. 245–259, 2017. ISSN 0025-3227. Advancements in Understanding

Deep-Sea Clastic Sedimentation Processes. Available: <<https://www.sciencedirect.com/science/article/pii/S0025322717304073>>. Citation on page 59.

MOUGIN, P. Les avalanches en savoie, vol. iv. **Ministère de l'Agriculture, Direction Générale des Eaux et Forêts, Service des Grandes Forces Hydrauliques, Paris**, 1922. Citations on pages 28 and 40.

MULAK, D.; GAUME, J. Numerical investigation of the mixed-mode failure of snow. **Computational Particle Mechanics**, v. 6, n. 3, p. 439–447, 7 2019. ISSN 2196-4386. Available: <<https://doi.org/10.1007/s40571-019-00224-5>>. Citation on page 71.

NAAIM, M. Modélisation numérique des avalanches aérosols. **La Houille Blanche**, EDP Sciences, n. 5-6, p. 56–62, 1995. Citation on page 66.

NAAIM, M.; DURAND, Y.; ECKERT, N.; CHAMBON, G. Dense avalanche friction coefficients: influence of physical properties of snow. **Journal of Glaciology**, Cambridge University Press, v. 59, n. 216, p. 771–782, 2013. Citations on pages 48 and 56.

NAAIM, M.; GURER, I. Two-phase numerical model of powder avalanche theory and application. **Natural Hazards**, Springer, v. 17.0, n. 2, p. 129–145, 1998. Citation on page 66.

NAAIM, M.; MARTINEZ, H. Experimental and theoretical determination of concentration profiles and influence of particle characteristics in blowing snow. **Surveys in Geophysics**, v. 16, n. 5, p. 695–710, Nov 1995. ISSN 1573-0956. Available: <<https://doi.org/10.1007/BF00665749>>. Citation on page 36.

NAAIM, M.; NAAIM-BOUVET, F.; FAUG, T.; BOUCHET, A. Dense snow avalanche modeling: flow, erosion, deposition and obstacle effects. **Cold Regions Science and Technology**, v. 39, n. 2, p. 193–204, 2004. ISSN 0165-232X. Snow And Avalanches: Papers Presented At The European Geophysical Union Conference, Nice, April 2003. Dedicated To The Avalanche Dynamics Pioneer Dr. B. Salm. Available: <<https://www.sciencedirect.com/science/article/pii/S0165232X04000643>>. Citation on page 55.

NARAIN, R.; SEWALL, J.; CARLSON, M.; LIN, M. C. Fast animation of turbulence using energy transport and procedural synthesis. In: **ACM SIGGRAPH Asia 2008 Papers**. Association for Computing Machinery, 2008. (SIGGRAPH Asia '08). ISBN 9781450318310. Available: <<https://doi.org/10.1145/1457515.1409119>>. Citation on page 74.

NAZAROV, A. N. Mathematical modeling of a snow-powder avalanche in the framework of the equations of two-layer shallow water. **Fluid Dynamics**, v. 26, n. 1, p. 70–75, Jan 1991. ISSN 1573-8507. Available: <<https://doi.org/10.1007/BF01050115>>. Citation on page 64.

NI, Y.; CAO, Z.; LIU, Q. Mathematical modeling of shallow-water flows on steep slopes. **Journal of Hydrology and Hydromechanics**, Sciendo, v. 67.0, n. 3, p. 252–259, 2019. Citation on page 53.

NICOT, F. Constitutive modelling of snow as a cohesive-granular material. **Granular Matter**, v. 6, n. 1, p. 47–60, 6 2004. ISSN 1434-7636. Available: <<https://doi.org/10.1007/s10035-004-0159-9>>. Citations on pages 48 and 49.

NISHIMURA, K.; BARPI, F.; ISSLER, D. Perspectives on snow avalanche dynamics research. **Geosciences**, v. 11, n. 2, 2021. ISSN 2076-3263. Available: <<https://www.mdpi.com/2076-3263/11/2/57>>. Citation on page 30.

NISHIMURA, K.; MAENO, N.; SANDERSEN, F.; KRISTENSEN, K.; NOREM, H.; LIED, K. Observations of the dynamic structure of snow avalanches. **Annals of Glaciology**, Cambridge University Press, v. 18, p. 313–316, 1993. Citation on page 36.

NOREM, H.; IRGENS, F.; SCHIELDROP, B. Simulation of snow-avalanche flow in run-out zones. **Annals of Glaciology**, Cambridge University Press, v. 13, p. 218–225, 1989. Citation on page 44.

OLLER, P.; JANERAS, M.; de Buen, H.; ARNÓ, G.; CHRISTEN, M.; GARCÍA, C.; MARTÍNEZ, P. Using aval-1d to simulate avalanches in the eastern pyrenees. **Cold Regions Science and Technology**, v. 64, n. 2, p. 190–198, 2010. ISSN 0165-232X. International Snow Science Workshop 2009 Davos. Available: <<https://www.sciencedirect.com/science/article/pii/S0165232X10001576>>. Citation on page 72.

OUILLO, R.; MEIBURG, E.; SUTHERLAND, B. R. Turbidity currents propagating down a slope into a stratified saline ambient fluid. **Environmental Fluid Mechanics**, Springer, v. 19, n. 5, p. 1143–1166, 2019. Citation on page 58.

PAIVA, A.; PETRONETTO, F.; LEWINER, T.; TAVARES, G. Particle-based viscoplastic fluid/solid simulation. **Computer-Aided Design**, Elsevier, v. 41.0, n. 4, p. 306–314, 2009. Citation on page 74.

PANTIN, H. Interaction between velocity and effective density in turbidity flow: Phase-plane analysis, with criteria for autosuspension. **Marine Geology**, v. 31, n. 1, p. 59–99, 1979. ISSN 0025-3227. Available: <<https://www.sciencedirect.com/science/article/pii/0025322779900574>>. Citation on page 57.

PARKER, G. Conditions for the ignition of catastrophically erosive turbidity currents. **Marine Geology**, v. 46, n. 3, p. 307–327, 1982. ISSN 0025-3227. Available: <<https://www.sciencedirect.com/science/article/pii/002532278290086X>>. Citation on page 57.

PARKER, G.; FUKUSHIMA, Y.; PANTIN, H. M. Self-accelerating turbidity currents. **Journal of Fluid Mechanics**, Cambridge University Press, v. 171.0, p. 145181, 1986. Citations on pages 30, 61, 63, and 67.

PARSONS, J. D.; FRIEDRICHS, C. T.; TRAYKOVSKI, P. A.; MOHRIG, D.; IMRAN, J.; SYVITSKI, J. P. M.; PARKER, G.; PUIG, P.; BUTTLES, J. L.; GARCÍA, M. H. The mechanics of marine sediment gravity flows. In: _____. **Continental Margin Sedimentation**. John Wiley & Sons, Ltd, 2007. p. 275–337. ISBN 9781444304398. Available: <<https://onlinelibrary.wiley.com/doi/abs/10.1002/9781444304398.ch6>>. Citation on page 57.

PATANKAR, S. V.; SPALDING, D. B. A calculation procedure for heat, mass and momentum transfer in three-dimensional parabolic flows. In: **Numerical prediction of flow, heat transfer, turbulence and combustion**. [S.l.]: Elsevier, 1983. p. 54–73. Citation on page 182.

PATRA, A.; BAUER, A.; NICHITA, C.; PITMAN, E.; SHERIDAN, M.; BURSIK, M.; RUPP, B.; WEBBER, A.; STINTON, A.; NAMIKAWA, L.; RENSCHLER, C. Parallel adaptive numerical simulation of dry avalanches over natural terrain. **Journal of Volcanology and Geothermal Research**, v. 139, n. 1, p. 1–21, 2005. ISSN 0377-0273. Modeling and Simulation of Geophysical Mass Flows. Available: <<https://www.sciencedirect.com/science/article/pii/S0377027304002288>>. Citation on page 74.

PATRA, A.; BEVILACQUA, A.; AKHAVAN-SAFAEI, A.; PITMAN, E. B.; BURSİK, M.; HYMAN, D. Comparative analysis of the structures and outcomes of geophysical flow models and modeling assumptions using uncertainty quantification. **Frontiers in Earth Science**, Frontiers, v. 8, p. 275, 2020. ISSN 2296-6463. Citation on page 74.

PERLA, R.; CHENG, T. T.; MCCLUNG, D. A twoparameter model of snowavalanche motion. **Journal of Glaciology**, Cambridge University Press, v. 26, n. 94, p. 197207, 1980. Citation on page 44.

PERLA, R.; LIED, K.; KRISTENSEN, K. Particle simulation of snow avalanche motion. **Cold Regions Science and Technology**, v. 9, n. 3, p. 191–202, 1984. ISSN 0165-232X. Available: <<https://www.sciencedirect.com/science/article/pii/0165232X84900661>>. Citation on page 44.

PETROFF, M. **A picture of Morning Glory Clouds, from Gulf of Carpentaria, Australia**. 2009. [Online; accessed September 09, 2023]. Available: <https://commons.wikimedia.org/wiki/File:Morning_glory_clouds.jpg>. Citation on page 19.

PIERSON, T. C.; COSTA, J. E. A rheologic classification of subaerial sediment-water flows. **Debris flows/avalanches: process, recognition, and mitigation. Reviews in Engineering Geology**, v. 7.0, p. 1–12, 1987. Citation on page 18.

PIRULLI, M.; SORBINO, G. Assessing potential debris flow runout: a comparison of two simulation models. **Natural Hazards and Earth System Sciences**, v. 8, n. 4, p. 961–971, 2008. Available: <<https://nhess.copernicus.org/articles/8/961/2008/>>. Citation on page 42.

PITMAN, E. B.; NICHITA, C. C.; PATRA, A.; BAUER, A.; SHERIDAN, M.; BURSİK, M. Computing granular avalanches and landslides. **Physics of Fluids**, v. 15, n. 12, p. 3638–3646, 2003. Available: <<https://doi.org/10.1063/1.1614253>>. Citations on pages 53, 55, and 74.

PLAPP, J. E.; MITCHELL, J. P. A hydrodynamic theory of turbidity currents. **Journal of Geophysical Research (1896-1977)**, v. 65, n. 3, p. 983–992, 1960. Available: <<https://agupubs.onlinelibrary.wiley.com/doi/abs/10.1029/JZ065i003p00983>>. Citations on pages 30 and 57.

POPOVA, E.; POPOV, V. L. The research works of coulomb and amontons and generalized laws of friction. **Friction**, v. 3, n. 2, p. 183–190, 6 2015. ISSN 2223-7704. Available: <<https://doi.org/10.1007/s40544-015-0074-6>>. Citation on page 41.

PROSPERETTI, A.; TRYGGVASON, G. **Computational Methods for Multiphase Flow**. [S.l.]: Cambridge University Press, 2007. Citation on page 64.

PUDASAINI, S. P.; HUTTER, K. Rapid shear flows of dry granular masses down curved and twisted channels. **Journal of Fluid Mechanics**, Cambridge University Press, v. 495, p. 193–208, 2003. Citation on page 52.

_____. **Avalanche dynamics: dynamics of rapid flows of dense granular avalanches**. [S.l.]: Springer Science & Business Media, 2007. Citations on pages 19, 20, 30, 44, 47, and 71.

RAM, D.; GAST, T.; JIANG, C.; SCHROEDER, C.; STOMAKHIN, A.; TERAN, J.; KAVEHPOUR, P. A material point method for viscoelastic fluids, foams and sponges. In: **ACM. Proceedings of the 14th ACM SIGGRAPH/Eurographics Symposium on Computer Animation**. [S.l.], 2015. p. 157–163. Citation on page 74.

RAMMS, WSL. **RAMMS - Rapid Mass Movement Simulation**. 2022. [Online; accessed September 26, 2022]. Available: <<https://ramms.slf.ch/en/modules/avalanche.html>>. Citation on page 73.

RANKINE, W. J. M. Ii. on the stability of loose earth. **Philosophical transactions of the Royal Society of London**, The Royal Society London, n. 147, p. 9–27, 1857. Citation on page 43.

RASTELLO, M.; HOPFINGER, E. J. Sediment-entraining suspension clouds: a model of powder-snow avalanches. **Journal of Fluid Mechanics**, Cambridge University Press, v. 509.0, p. 181206, 2004. Citation on page 63.

RAUTER, M.; KOFLER, A.; HUBER, A.; FELLIN, W. fasavagehutterfoam 1.0: depth-integrated simulation of dense snow avalanches on natural terrain with openfoam. **Geoscientific Model Development**, v. 11.0, n. 7, p. 2923–2939, 2018. Available: <<https://gmd.copernicus.org/articles/11/2923/2018/>>. Citations on pages 28, 53, 54, and 82.

RAUTER, M.; KÖHLER, A. Constraints on entrainment and deposition models in avalanche simulations from high-resolution radar data. **Geosciences**, v. 10, n. 1, 2020. ISSN 2076-3263. Available: <<https://www.mdpi.com/2076-3263/10/1/9>>. Citation on page 57.

RAUTER, M.; TUKOVI, . A finite area scheme for shallow granular flows on three-dimensional surfaces. **Computers & Fluids**, v. 166.0, p. 184–199, 2018. ISSN 0045-7930. Available: <<https://www.sciencedirect.com/science/article/pii/S0045793018300732>>. Citations on pages 54, 57, and 81.

REIWEGER, I.; GAUME, J.; SCHWEIZER, J. A new mixed-mode failure criterion for weak snowpack layers. **Geophysical Research Letters**, v. 42, n. 5, p. 1427–1432, 2015. Available: <<https://agupubs.onlinelibrary.wiley.com/doi/abs/10.1002/2014GL062780>>. Citation on page 48.

RenderMan25. **Association pour l'amélioration et le partage de connaissances sur les avalanches**. 2023. [Online; accessed December 5, 2023]. Available: <<https://rmanwiki.pixar.com/display/REN25/Rendering+Clouds+with+Aggregate+Volumes>>. Citation on page 118.

ROCHE, O.; ATTALI, M.; MANGENEY, A.; LUCAS, A. On the run-out distance of geophysical gravitational flows: Insight from fluidized granular collapse experiments. **Earth and Planetary Science Letters**, v. 311, n. 3, p. 375–385, 2011. ISSN 0012-821X. Available: <<https://www.sciencedirect.com/science/article/pii/S0012821X11005371>>. Citation on page 34.

RODRIGUEZ-PAZ, M.; BONET, J. A corrected smooth particle hydrodynamics formulation of the shallow-water equations. **Computers & Structures**, v. 83.0, n. 17, p. 1396 – 1410, 2005. ISSN 0045-7949. Advances in Meshfree Methods. Available: <<http://www.sciencedirect.com/science/article/pii/S0045794905000714>>. Citation on page 53.

ROMANOVA, D. I. 3d avalanche flow modeling using openfoam. **Proceedings of the Institute for System Programming of the RAS**, Institute for System Programming of the Russian Academy of Sciences, v. 29.0, n. 1, p. 85–100, 2017. Citation on page 66.

ROTTMAN, J. W.; LINDEN, P. F. Gravity currents. In: _____. **Environmental Stratified Flows**. Boston, MA: Springer US, 2002. p. 89–117. ISBN 978-0-306-48024-9. Available: <https://doi.org/10.1007/0-306-48024-7_4>. Citation on page 59.

SALM, B. Contribution to avalanche dynamics. **IASH-AIHS Pub.**, v. 69, p. 199–214, 1966. Citation on page 43.

_____. **On nonuniform, steady flow of avalanching snow**. [S.l.]: Ceuterick, 1967. Citation on page 43.

_____. Grundlagen des lawinenverbaus. **Bündnerwald**, v. 9, p. 67–81, 1972. Citation on page 43.

_____. Mechanical properties of snow. **Reviews of Geophysics**, v. 20, n. 1, p. 1–19, 1982. Available: <<https://agupubs.onlinelibrary.wiley.com/doi/abs/10.1029/RG020i001p00001>>. Citation on page 49.

_____. Flow, flow transition and runout distances of flowing avalanches. **Annals of Glaciology**, Cambridge University Press, v. 18, p. 221–226, 1993. Citation on page 43.

_____. A short and personal history of snow avalanche dynamics. **Cold Regions Science and Technology**, v. 39, n. 2, p. 83–92, 2004. ISSN 0165-232X. Snow And Avalanches: Papers Presented At The European Geophysical Union Conference, Nice, April 2003. Dedicated To The Avalanche Dynamics Pioneer Dr. B. Salm. Available: <<https://www.sciencedirect.com/science/article/pii/S0165232X04000588>>. Citations on pages 28 and 43.

SALM, B.; BURKARD, A.; GUBLER, H. **Berechnung von Fließlawinen: eine Anleitung für Praktiker mit Beispielen**. [S.l.]: Eidgenössisches Institut für Schnee-und Lawinenforschung, Weissfluhjoch/Davos, 1990. Citation on page 43.

SALM, B.; GUBLER, H. Measurement and analysis of the motion of dense flow avalanches. **Annals of Glaciology**, Cambridge University Press, v. 6, p. 26–34, 1985. Citations on pages 43, 44, and 45.

SAMPL, P.; GRANIG, M. Avalanche simulation with samos-at. **ISSW 09 - International Snow Science Workshop, Proceedings**, p. 519–523, 1 2009. Citations on pages 68, 73, and 77.

SAMPL, P.; ZWINGER, T. Avalanche simulation with samos. **Annals of Glaciology**, Cambridge University Press, v. 38.0, p. 393398, 2004. Citations on pages 68 and 72.

SANZ-RAMOS, M.; BLADÉ, E.; OLLER, P.; ANDRADE, C. A.; FURDADA, G. Role of friction terms in two-dimensional modelling of dense snow avalanches. **Natural Hazards and Earth System Sciences Discussions**, Copernicus GmbH, p. 1–31, 2020. Citation on page 48.

SARTORIS, G.; BARTELT, P. Upwinded finite difference schemes for dense snow avalanche modeling. **International Journal for Numerical Methods in Fluids**, v. 32, n. 7, p. 799–821, 2000. Available: <<https://onlinelibrary.wiley.com/doi/abs/10.1002/%28SICI%291097-0363%2820000415%2932%3A7%3C799%3A%3AAID-FLD989%3E3.0.CO%3B2-2>>. Citation on page 55.

SAVAGE, S. B. The mechanics of rapid granular flows. In: HUTCHINSON, J. W.; WU, T. Y. (Ed.). Elsevier, 1984, (Advances in Applied Mechanics, v. 24). p. 289–366. Available: <<https://www.sciencedirect.com/science/article/pii/S0065215608700474>>. Citation on page 49.

SAVAGE, S. B.; HUTTER, K. The motion of a finite mass of granular material down a rough incline. **Journal of Fluid Mechanics**, Cambridge University Press, v. 199.0, p. 177215, 1989. Citations on pages 28 and 50.

_____. The dynamics of avalanches of granular materials from initiation to runout. part i: Analysis. **Acta Mechanica**, Springer, v. 86.0, n. 1, p. 201–223, 1991. Citations on pages 50, 52, and 80.

SAVAGE, S. B.; SAYED, M. Stresses developed by dry cohesionless granular materials sheared in an annular shear cell. **Journal of Fluid Mechanics**, Cambridge University Press, v. 142, p. 391–430, 1984. Citation on page 36.

SCHEIWILLER, T. **Dynamics of powder-snow avalanches**. Phd Thesis (PhD Thesis) — ETH Zurich, 1986. Citation on page 65.

SCHRAML, K.; THOMSCHITZ, B.; MCADELL, B. W.; GRAF, C.; KAITNA, R. Modeling debris-flow runout patterns on two alpine fans with different dynamic simulation models. **Natural Hazards and Earth System Sciences**, v. 15, n. 7, p. 1483–1492, 2015. Available: <<https://nhess.copernicus.org/articles/15/1483/2015/>>. Citation on page 42.

SCHWEIZER, J.; BARTELT, P.; van Herwijnen, A. Chapter 12 - snow avalanches. In: HAE-BERLI, W.; WHITEMAN, C. (Ed.). **Snow and Ice-Related Hazards, Risks, and Disasters (Second Edition)**. Second edition. Elsevier, 2021, (Hazards and Disasters Series). p. 377–416. ISBN 978-0-12-817129-5. Available: <<https://www.sciencedirect.com/science/article/pii/B9780128171295000019>>. Citation on page 38.

SELIGMAN, G.; SELIGMAN, G. A.; DOUGLAS, C. **Snow structure and ski fields: being an account of snow and ice forms met with in nature, and a study on avalanches and snowcraft**. [S.l.]: Macmillan and Company, limited, 1936. Citation on page 28.

SHIN, J. O.; DALZIEL, S. B.; LINDEN, P. F. Gravity currents produced by lock exchange. **Journal of Fluid Mechanics**, Cambridge University Press, v. 521, p. 1–34, 2004. Citation on page 35.

SIMAKOV, N. A.; JONES-IVEY, R. L.; AKHAVAN-SAFAEI, A.; AGHAKHANI, H.; JONES, M. D.; PATRA, A. K. Modernizing titan2d, a parallel amr geophysical flow code to support multiple rheologies and extendability. In: SPRINGER. **International Conference on High Performance Computing**. [S.l.], 2019. p. 101–112. Citation on page 74.

SIMPSON, J. E. **Gravity currents: In the environment and the laboratory**. [S.l.]: Cambridge university press, 1999. Citations on pages 19 and 57.

SINGH, A. K.; SRIVASTAVA, P.; KUMAR, N.; MAHAJAN, P. A fabric tensor based small strain constitutive law for the elastoplastic behavior of snow. **Mechanics of Materials**, v. 165, p. 104182, 2022. ISSN 0167-6636. Available: <<https://www.sciencedirect.com/science/article/pii/S0167663621003938>>. Citation on page 49.

SINICKAS, A. **Field-based statistical modelling of snow avalanche runout**. PRISM, 2013. Available: <<https://prism.ucalgary.ca/handle/11023/953>>. Citation on page 38.

SLF. **WSL Institute of Snow and Avalanche Research SLF**. 2022. [Online; accessed July 26, 2022]. Available: <<https://www.slf.ch/en/index.html>>. Citations on pages 20, 43, and 72.

SOLENTHALER, B.; BUCHER, P.; CHENTANEZ, N.; MLLER, M.; GROSS, M. SPH Based Shallow Water Simulation. In: BENDER, J.; ERLEBEN, K.; GALIN, E. (Ed.). **Workshop in Virtual Reality Interactions and Physical Simulation "VRIPHYS" (2011)**. [S.l.]: The Eurographics Association, 2011. ISBN 978-3-905673-87-6. Citation on page 74.

Song, L.; Zhou, J.; Zou, Q.; Guo, J.; Liu, Y. Two-dimensional dam-break flood simulation on unstructured meshes. In: **2010 International Conference on Parallel and Distributed Computing, Applications and Technologies**. [S.l.: s.n.], 2010. p. 465–469. Citation on page 53.

SOVILLA, B. **Field experiments and numerical modelling of mass entrainment and deposition processes in snow avalanches**. Phd Thesis (PhD Thesis) — ETH Zurich, 2004. Citations on pages 31, 46, and 55.

Sovilla, B.; Bartelt, P. Observations and modelling of snow avalanche entrainment. **Natural Hazards and Earth System Sciences**, v. 2, p. 169–179, Jan. 2002. Citations on pages 36 and 43.

SOVILLA, B.; BURLANDO, P.; BARTELT, P. Field experiments and numerical modeling of mass entrainment in snow avalanches. **Journal of Geophysical Research: Earth Surface**, v. 111, n. F3, 2006. Available: <<https://agupubs.onlinelibrary.wiley.com/doi/abs/10.1029/2005JF000391>>. Citations on pages 23, 30, 31, and 55.

SOVILLA, B.; MARGRETH, S.; BARTELT, P. On snow entrainment in avalanche dynamics calculations. **Cold Regions Science and Technology**, v. 47.0, n. 1, p. 69–79, 2007. ISSN 0165-232X. A Selection of papers presented at the International Snow Science Workshop, Jackson Hole, Wyoming, September 19-24, 2004. Available: <<https://www.sciencedirect.com/science/article/pii/S0165232X06001261>>. Citation on page 55.

SOVILLA, B.; MCELWAIN, J. N.; KHLER, A. The intermittency regions of powder snow avalanches. **Journal of Geophysical Research: Earth Surface**, v. 123, n. 10, p. 2525–2545, 2018. Available: <<https://agupubs.onlinelibrary.wiley.com/doi/abs/10.1029/2018JF004678>>. Citations on pages 24 and 33.

SOVILLA, B.; MCELWAIN, J. N.; LOUGE, M. Y. The structure of powder snow avalanches. **Comptes Rendus Physique**, v. 16.0, n. 1, p. 97–104, 2015. ISSN 1631-0705. Granular physics / Physique des milieux granulaires. Available: <<https://www.sciencedirect.com/science/article/pii/S1631070514001844>>. Citation on page 33.

SOVILLA, B.; MCELWAIN, J. N.; SCHAER, M.; VALLET, J. Variation of deposition depth with slope angle in snow avalanches: Measurements from valle de la sionne. **Journal of Geophysical Research: Earth Surface**, v. 115, n. F2, 2010. Available: <<https://agupubs.onlinelibrary.wiley.com/doi/abs/10.1029/2009JF001390>>. Citation on page 31.

SOVILLA, B.; SCHAER, M.; RAMMER, L. Measurements and analysis of full-scale avalanche impact pressure at the vallée de la sionne test site. **Cold Regions Science and Technology**, v. 51, n. 2, p. 122–137, 2008. ISSN 0165-232X. International Snow Science Workshop (ISSW) 2006. Available: <<https://www.sciencedirect.com/science/article/pii/S0165232X07001188>>. Citations on pages 31 and 32.

St. Lawrence, W.; LANG, T. A constitutive relation for the deformation of snow. **Cold Regions Science and Technology**, v. 4, n. 1, p. 3–14, 1981. ISSN 0165-232X. Available: <<https://www.sciencedirect.com/science/article/pii/0165232X81900264>>. Citation on page 49.

STACEY, M. W.; BOWEN, A. J. The vertical structure of density and turbidity currents: Theory and observations. **Journal of Geophysical Research: Oceans**, v. 93, n. C4, p. 3528–3542, 1988. Available: <<https://agupubs.onlinelibrary.wiley.com/doi/abs/10.1029/JC093iC04p03528>>. Citation on page 61.

STEINKOGLER, W.; GAUME, J.; LÖWE, H.; SOVILLA, B.; LEHNING, M. Granulation of snow: From tumbler experiments to discrete element simulations. **Journal of Geophysical Research: Earth Surface**, v. 120, n. 6, p. 1107–1126, 2015. Available: <<https://agupubs.onlinelibrary.wiley.com/doi/abs/10.1002/2014JF003294>>. Citation on page 35.

STEINKOGLER, W.; SOVILLA, B.; LEHNING, M. Influence of snow cover properties on avalanche dynamics. **Cold Regions Science and Technology**, v. 97, p. 121–131, 2014. ISSN 0165-232X. Available: <<https://www.sciencedirect.com/science/article/pii/S0165232X13001535>>. Citation on page 36.

STEWART, J. **Incredible Photos of Massive Dust Storm Taken From Fleeting News Helicopter**. 2018. [Online; accessed September 09, 2023]. Available: <<https://mymodernmet.com/arizona-dust-storm-news-helicopter/>>. Citation on page 19.

STOMAKHIN, A.; SCHROEDER, C.; CHAI, L.; TERAN, J.; SELLE, A. A material point method for snow simulation. **ACM Transactions on Graphics (TOG)**, ACM, v. 32.0, n. 4, p. 102, 2013. Citation on page 74.

STOMAKHIN, A.; SCHROEDER, C.; JIANG, C.; CHAI, L.; TERAN, J.; SELLE, A. Augmented mpm for phase-change and varied materials. **ACM Transactions on Graphics (TOG)**, ACM, v. 33.0, n. 4, p. 138, 2014. Citation on page 74.

SULSKY, D.; ZHOU, S.-J.; SCHREYER, H. L. Application of a particle-in-cell method to solid mechanics. **Computer physics communications**, Elsevier, v. 87.0, n. 1-2, p. 236–252, 1995. Citation on page 71.

TAI, Y.-C.; HUTTER, K.; GRAY, J. Dense granular avalanches: Mathematical description and experimental validation. In: _____. **Geomorphological Fluid Mechanics**. Berlin, Heidelberg: Springer Berlin Heidelberg, 2001. p. 339–366. ISBN 978-3-540-45670-4. Available: <https://doi.org/10.1007/3-540-45670-8_14>. Citations on pages 48 and 49.

TAI, Y. C.; KUO, C. Y. A new model of granular flows over general topography with erosion and deposition. **Acta Mechanica**, v. 199, n. 1, p. 71–96, Aug 2008. ISSN 1619-6937. Available: <<https://doi.org/10.1007/s00707-007-0560-7>>. Citation on page 53.

TAKAHASHI, T. **Debris flow: mechanics, prediction and countermeasures**. [S.l.]: CRC press, 2014. Citation on page 18.

TAKAHASHI, T.; TSUJIMOTO, H. Granular flow model of avalanche and its application. **Proceedings of Hydraulic Engineering**, Japan Society of Civil Engineers, v. 42, p. 907–912, 1998. Citation on page 52.

TALLING, P. J.; BAKER, M. L.; POPE, E. L.; RUFFELL, S. C.; JACINTO, R. S.; HEIJNEN, M. S.; HAGE, S.; SIMMONS, S. M.; HASENHÜNDL, M.; HEEREMA, C. J.; MCGHEE, C.; APPRIOUAL, R.; FERRANT, A.; CARTIGNY, M. J. B.; PARSONS, D. R.; CLARE, M. A.; TSHIMANGA, R. M.; TRIGG, M. A.; CULA, C. A.; FARIA, R.; GAILLOT, A.; BOLA, G.; WALLANCE, D.; GRIFFITHS, A.; NUNNY, R.; URLAUB, M.; PEIRCE, C.; BURNETT, R.; NEASHAM, J.; HILTON, R. J. Longest sediment flows yet measured show how major rivers connect efficiently to deep sea. **Nature Communications**, v. 13, n. 1, p. 4193, Jul 2022. ISSN 2041-1723. Available: <<https://doi.org/10.1038/s41467-022-31689-3>>. Citation on page 17.

TAMPUBOLON, A. P.; GAST, T.; KLÁR, G.; FU, C.; TERAN, J.; JIANG, C.; MUSETH, K. Multi-species simulation of porous sand and water mixtures. **ACM Transactions on Graphics (TOG)**, ACM, v. 36.0, n. 4, p. 105, 2017. Citation on page 74.

THIBERT, E.; BELLOT, H.; RAVANAT, X.; OUSSET, F.; PULFER, G.; NAAIM, M.; HAGEN-MULLER, P.; NAAIM-BOUVET, F.; FAUG, T.; NISHIMURA, K.; ITO, Y.; BAROUDI, D.; PROKOP, A.; SCHÖN, P.; SORUCO, A.; VINCENT, C.; LIMAM, A.; HÉNO, R. The full-scale avalanche test-site at lautaret pass (french alps). **Cold Regions Science and Technology**, v. 115, p. 30–41, 2015. ISSN 0165-232X. Available: <<https://www.sciencedirect.com/science/article/pii/S0165232X15000622>>. Citation on page 30.

TIEFENBACHER, F.; KERN, M. Experimental devices to determine snow avalanche basal friction and velocity profiles. **Cold Regions Science and Technology**, v. 38, n. 1, p. 17–30, 2004. ISSN 0165-232X. Available: <<https://www.sciencedirect.com/science/article/pii/S0165232X03000600>>. Citation on page 36.

TILLGREN, S. **Generating 3D Avalanche Slabs with Voronoi Tessellation in Real-Time on the CPU**. 2020. 38 p. Citation on page 75.

TOCHON-DANGUY, J.; HOPFINGER, E. Simulation of the dynamics of powder avalanches. In: **Snow Mechanics Symposium**. [S.l.: s.n.], 1975. Citation on page 61.

TROTTET, B.; SIMENHOIS, R.; BOBILLIER, G.; BERGFELD, B.; HERWIJNEN, A. van; JIANG, C.; GAUME, J. Transition from sub-rayleigh anticrack to supershear crack propagation in snow avalanches. **Nature Physics**, 7 2022. ISSN 1745-2481. Available: <<https://doi.org/10.1038/s41567-022-01662-4>>. Citation on page 71.

Trésorier, Marc. **Association pour l'amélioration et le partage de connaissances sur les avalanches**. 2021. [Online; accessed June 29, 2022]. Available: <<http://www.data-avalanche.org/>>. Citation on page 30.

TSUDA, Y.; YUE, Y.; DOBASHI, Y.; NISHITA, T. Visual simulation of mixed-motion avalanches with interactions between snow layers. **The Visual Computer**, Springer, v. 26.0, n. 6-8, p. 883–891, 2010. Citation on page 75.

TSUNEMATSU, K.; MAENO, F.; NISHIMURA, K. Application of an inertia dependent flow friction model to snow avalanches: Exploration of the model using a ping-pong ball experiment. **Geosciences**, v. 10, n. 11, 2020. ISSN 2076-3263. Available: <<https://www.mdpi.com/2076-3263/10/11/436>>. Citation on page 35.

TUKOVI, .; JASAK, H. A moving mesh finite volume interface tracking method for surface tension dominated interfacial fluid flow. **Computers & Fluids**, v. 55.0, p. 70–84, 2012. ISSN 0045-7930. Available: <<https://www.sciencedirect.com/science/article/pii/S0045793011003380>>. Citation on page 53.

TUKOVIĆ, Ž. **Metoda kontrolnih volumena na domenama promjenjivog oblika**. Phd Thesis (PhD Thesis) — Sveučilište u Zagrebu, Fakultet strojarstva i brodogradnje, 2005. Citation on page 174.

TURNBULL, B.; BARTELT, P. Mass and momentum balance model of a mixed flowing/powder snow avalanche. **Surveys in geophysics**, Springer, v. 24, n. 5, p. 465–477, 2003. Citation on page 63.

TURNBULL, B.; MCELWAIN, J. A comparison of powder-snow avalanches at vallée de la sionne, switzerland, with plume theories. **Journal of Glaciology**, Cambridge University Press, v. 53, n. 180, p. 30–40, 2007. Citations on pages 31 and 35.

TURNBULL, B.; MCELWAIN, J. N. Experiments on the non-boussinesq flow of self-igniting suspension currents on a steep open slope. **Journal of Geophysical Research: Earth Surface**, v. 113, n. F1, 2008. Available: <<https://agupubs.onlinelibrary.wiley.com/doi/abs/10.1029/2007JF000753>>. Citation on page 34.

TURNBULL, B.; MCELWAIN, J. N.; ANCEY, C. Kulikovskiy–sveshnikova–beghin model of powder snow avalanches: Development and application. **Journal of Geophysical Research: Earth Surface**, v. 112, n. F1, 2007. Available: <<https://agupubs.onlinelibrary.wiley.com/doi/abs/10.1029/2006JF000489>>. Citation on page 63.

TURNER, J. S. **Buoyancy Effects in Fluids**. [S.l.]: Cambridge University Press, 1973. (Cambridge Monographs on Mechanics). Citations on pages 60 and 61.

UNGARISH, M. **An introduction to gravity currents and intrusions**. [S.l.]: CRC press, 2009. Citation on page 57.

VACONDIO, R.; ROGERS, B. D.; STANSBY, P. K. Accurate particle splitting for smoothed particle hydrodynamics in shallow water with shock capturing. **International Journal for Numerical Methods in Fluids**, v. 69.0, n. 8, p. 1377–1410, 2012. Available: <<https://onlinelibrary.wiley.com/doi/abs/10.1002/fld.2646>>. Citation on page 53.

VALERO, C. V.; JONES, K. W.; BÜHLER, Y.; BARTELT, P. Release temperature, snow-cover entrainment and the thermal flow regime of snow avalanches. **Journal of Glaciology**, Cambridge University Press, v. 61, n. 225, p. 173–184, 2015. Citation on page 57.

VALERO, C. V.; WEVER, N.; CHRISTEN, M.; BARTELT, P. Modeling the influence of snow cover temperature and water content on wet-snow avalanche runout. **Natural Hazards and Earth System Sciences**, v. 18, n. 3, p. 869–887, 2018. Available: <<https://nhess.copernicus.org/articles/18/869/2018/>>. Citation on page 50.

VALLET, J.; TURNBULL, B.; JOLY, S.; DUFOUR, F. Observations on powder snow avalanches using videogrammetry. **Cold Regions Science and Technology**, v. 39, n. 2, p. 153–159, 2004. ISSN 0165-232X. Snow And Avalanches: Papers Presented At The European Geophysical Union Conference, Nice, April 2003. Dedicated To The Avalanche Dynamics Pioneer Dr. B. Salm. Available: <<https://www.sciencedirect.com/science/article/pii/S0165232X04000461>>. Citation on page 31.

van Leer, B. Towards the ultimate conservative difference scheme. ii. monotonicity and conservation combined in a second-order scheme. **Journal of Computational Physics**, v. 14, n. 4, p. 361–370, 1974. ISSN 0021-9991. Available: <<https://www.sciencedirect.com/science/article/pii/0021999174900199>>. Citation on page 107.

VARNES, D. J. Slope movement types and processes. **Special report**, v. 176.0, p. 11–33, 1978. Citation on page 18.

VÉDRINE, L.; LI, X.; GAUME, J. Detrainment and braking of snow avalanches interacting with forests. **Natural Hazards and Earth System Sciences**, v. 22, n. 3, p. 1015–1028, 2022. Available: <<https://nhess.copernicus.org/articles/22/1015/2022/>>. Citation on page 71.

VENANT, B. D. S. Theorie du mouvement non-permanent des eaux avec application aux crues des rivières et à l'introduction des marées dans leur lit. **Académie de Sci. Comptes Rendus**, v. 73, n. 99, p. 148–154, 1871. Citations on pages 28 and 42.

VIDIC, L. **Half-mile avalanche shaves snow from Bald Mountain**. 2022. [Online; accessed September 09, 2023]. Available: <<https://www.summitdaily.com/news/half-mile-avalanche-shaves-snow-from-bald-mountain/>>. Citation on page 21.

VIROULET, S.; BAKER, J. L.; EDWARDS, A. N.; JOHNSON, C. G.; GJALTEMA, C.; CLAVEL, P.; GRAY, J. M. N. T. Multiple solutions for granular flow over a smooth two-dimensional bump. **Journal of Fluid Mechanics**, Cambridge University Press, v. 815, p. 77–116, 2017. Citation on page 53.

VOELLMY, A. Über die zerstörungskraft von lawinen. **Schweizerische Bauzeitung, Jahrg.**, v. 73, p. 159–162, 1955. Citations on pages 28 and 41.

VORST, H. A. van der. Bi-cgstab: A fast and smoothly converging variant of bi-cg for the solution of nonsymmetric linear systems. **SIAM Journal on Scientific and Statistical Computing**, v. 13, n. 2, p. 631–644, 1992. Available: <<https://doi.org/10.1137/0913035>>. Citation on page 103.

VRIEND, N. M.; MCELWAIN, J. N.; SOVILLA, B.; KEYLOCK, C. J.; ASH, M.; BRENNAN, P. V. High-resolution radar measurements of snow avalanches. **Geophysical Research Letters**, v. 40, n. 4, p. 727–731, 2013. Available: <<https://agupubs.onlinelibrary.wiley.com/doi/abs/10.1002/grl.50134>>. Citation on page 31.

WANG, C.; ZHANG, Q.; KONG, F.; GAO, Y. Fast animation of debris flow with mixed adaptive grid refinement. **Computer Animation and Virtual Worlds**, v. 26.0, n. 1, p. 3–14, 2015. Available: <<https://onlinelibrary.wiley.com/doi/abs/10.1002/cav.1542>>. Citation on page 74.

WANG, X.; LIU, S.; BAN, X.; XU, Y.; ZHOU, J.; KOSINKA, J. Robust turbulence simulation for particle-based fluids using the Rankine vortex model. **The Visual Computer**, Springer, v. 36.0, n. 10, p. 2285–2298, 2020. Citation on page 74.

WANGER, R. E-periodica: die plattform für digitalisierte schweizer zeitschriften. In: _____. **Bibliotheken der Schweiz: Innovation durch Kooperation; Festschrift für Susanna Bliggenstorfer anlässlich ihres Rücktrittes als Direktorin der Zentralbibliothek Zürich**. Berlin: De Gruyter, 2018. p. 401 – 413. ISBN 978-3-11-055182-2. Citation on page 42.

WELLS, M. G.; DORRELL, R. M. Turbulence processes within turbidity currents. **Annual Review of Fluid Mechanics**, v. 53, n. 1, p. 59–83, 2021. Available: <<https://doi.org/10.1146/annurev-fluid-010719-060309>>. Citation on page 57.

WIELAND, M.; GRAY, J. M. N. T.; HUTTER, K. Channelized free-surface flow of cohesionless granular avalanches in a chute with shallow lateral curvature. **Journal of Fluid Mechanics**, Cambridge University Press, v. 392, p. 73–100, 1999. Citation on page 52.

WOLPER, J.; CHEN, Y.; LI, M.; FANG, Y.; QU, Z.; LU, J.; CHENG, M.; JIANG, C. Anisompm: Animating anisotropic damage mechanics. **ACM Trans. Graph.**, Association for Computing Machinery, New York, NY, USA, v. 39, n. 4, aug 2020. ISSN 0730-0301. Available: <<https://doi.org/10.1145/3386569.3392428>>. Citation on page 74.

WORLEY, S. A cellular texture basis function. In: **Proceedings of the 23rd annual conference on Computer graphics and interactive techniques**. [S.l.: s.n.], 1996. p. 291–294. Citation on page 111.

XIA, X.; LIANG, Q. A gpu-accelerated smoothed particle hydrodynamics (sph) model for the shallow water equations. **Environmental Modelling & Software**, v. 75, p. 28–43, 2016. ISSN 1364-8152. Available: <<https://www.sciencedirect.com/science/article/pii/S1364815215300608>>. Citation on page 74.

_____. A new depth-averaged model for flow-like landslides over complex terrains with curvatures and steep slopes. **Engineering Geology**, v. 234.0, p. 174 – 191, 2018. ISSN 0013-7952. Available: <<http://www.sciencedirect.com/science/article/pii/S0013795217306324>>. Citation on page 53.

YNDESTAD, L. K. H. **Particle-based Powder-snow Avalanche Simulation Using GPU**. Master's Thesis (Master's Thesis) — Institutt for datateknikk og informasjonsvitenskap, 2011. Citation on page 74.

YU, M.-h. Advances in strength theories for materials under complex stress state in the 20th century. **Appl. Mech. Rev.**, v. 55, n. 3, p. 169–218, 2002. Citation on page 47.

YUAN, L.; LIU, W.; ZHAI, J.; WU, S. F.; PATRA, A. K.; PITMAN, E. B. Refinement on non-hydrostatic shallow granular flow model in a global cartesian coordinate system. **Computational Geosciences**, v. 22, n. 1, p. 87–106, 2 2018. ISSN 1573-1499. Available: <<https://doi.org/10.1007/s10596-017-9672-x>>. Citation on page 53.

YUE, Y.; SMITH, B.; BATTY, C.; ZHENG, C.; GRINSPUN, E. Continuum foam: A material point method for shear-dependent flows. **ACM Transactions on Graphics (TOG)**, ACM, v. 34.0, n. 5, p. 160, 2015. Citation on page 74.

ZAHIBO, N.; PELINOVSKY, E.; TALIPOVA, T.; NIKOLKINA, I. Savage-hutter model for avalanche dynamics in inclined channels: Analytical solutions. **Journal of Geophysical Research: Solid Earth**, v. 115, n. B3, 2010. Available: <<https://agupubs.onlinelibrary.wiley.com/doi/abs/10.1029/2009JB006515>>. Citation on page 53.

ZHAI, J.; YUAN, L.; LIU, W.; ZHANG, X. Solving the savage–hutter equations for granular avalanche flows with a second-order godunov type method on gpu. **International Journal for Numerical Methods in Fluids**, v. 77, n. 7, p. 381–399, 2015. Available: <<https://onlinelibrary.wiley.com/doi/abs/10.1002/fld.3988>>. Citation on page 53.

ZHANG, S.; KONG, F.; LI, C.; WANG, C.; QIN, H. Hybrid modeling of multiphysical processes for particle-based volcano animation. **Computer Animation and Virtual Worlds**, v. 28, n. 3-4, p. e1758, 2017. E1758 cav.1758. Available: <<https://onlinelibrary.wiley.com/doi/abs/10.1002/cav.1758>>. Citation on page 74.

ZHAO, J.; CHEN, Y.; ZHANG, H.; XIA, H.; WANG, Z.; PENG, Q. Physically based modeling and animation of landslides with mpm. **The Visual Computer**, v. 35, n. 9, p. 1223–1235, 9 2019. ISSN 1432-2315. Available: <<https://doi.org/10.1007/s00371-019-01709-3>>. Citations on pages 71 and 74.

ZHAO, J.; ZHEN, I.; LIANG, D.; HINKELMANN, R. Improved multislope muscl reconstruction on unstructured grids for shallow water equations. **International Journal for Numerical Methods in Fluids**, v. 87.0, n. 8, p. 401–436, 2018. Available: <<https://onlinelibrary.wiley.com/doi/abs/10.1002/fld.4499>>. Citation on page 53.

ZHOU, G. G.; DU, J.; SONG, D.; CHOI, C. E.; HU, H.; JIANG, C. Numerical study of granular debris flow run-up against slit dams by discrete element method. **Landslides**, Springer, v. 17, n. 3, p. 585–595, 2020. Citation on page 71.

ZHU, B.; LU, W.; CONG, M.; KIM, B.; FEDKIW, R. A new grid structure for domain extension. **ACM Transactions on Graphics (TOG)**, ACM, v. 32.0, n. 4, p. 63, 2013. Citation on page 74.

ZHU, K.; HE, X.; LI, S.; WANG, H.; WANG, G. Shallow sand equations: Real-time height field simulation of dry granular flows. **IEEE Computer Architecture Letters**, IEEE Computer Society, n. 01, p. 1–1, 2019. Citation on page 74.

ZWINGER, T.; KLUWICK, A.; SAMPL, P. Numerical simulation of dry-snow avalanche flow over natural terrain. In: _____. **Dynamic Response of Granular and Porous Materials under Large and Catastrophic Deformations**. Berlin, Heidelberg: Springer Berlin Heidelberg, 2003. p. 161–194. ISBN 978-3-540-36565-5. Available: <https://doi.org/10.1007/978-3-540-36565-5_5>. Citations on pages 65, 68, and 72.

ÉTIENNE, J.; SARAMITO, P.; HOPFINGER, E. J. Numerical simulations of dense clouds on steep slopes: application to powder-snow avalanches. **Annals of Glaciology**, Cambridge University Press, v. 38, p. 379–383, 2004. Citations on pages 67 and 68.

Appendix

BACKGROUND CONCEPTS

A.1 Eulerian and Lagrangian Descriptions

A.2 Continuum Mixture Theory

The Continuum Mixture Theory (CMT) (ATKIN; CRAINE, 1976), which has long roots in the work of Fick (1855), deals with substances in nature whose materials consist of more than one constituent. The CMT characterizes the mixture as a superposition of multiple single continua representing the different constituents whose particles can occupy each domain location simultaneously.

Let the subscript $(\cdot)_\gamma$ indicate a field of constituent \mathcal{C}_γ , then for a set of n constituents and the position function ϕ_t^γ for \mathcal{C}_γ , the motion of the mixture is described by n equations

$$\mathbf{x} = \phi_t^\gamma(\mathbf{X}_\gamma, t), \quad 1 \leq \gamma \leq n, \quad (\text{A.1})$$

The equation comes from a Continuum Mechanics perspective, which considers a body under deformation over time. The reference state, with material point locations represented in Lagrangian coordinates \mathbf{X} , and the deformed state, with locations represented in Eulerian coordinates \mathbf{x} , are mapped by the deformation function ϕ_t^γ — see appendix section A.1 on page 157 for a brief introduction on coordinate references. For each location \mathbf{X} , ϕ gives the spatial location \mathbf{x} that characterizes the deformed state of the body for constituent \mathcal{C}_γ after a given time t . Consequently, the velocity field \mathbf{v}_γ of constituent \mathcal{C}_γ is

$$\mathbf{u}_\gamma = \frac{\partial \phi_t^\gamma}{\partial t}. \quad (\text{A.2})$$

The material derivatives for constituent \mathcal{C}_γ , $\frac{D^\gamma}{D_t}$, for an arbitrary scalar function $s(\mathbf{x}, t)$ and an arbitrary vector function $\mathbf{w}(\mathbf{x}, t)$ are

$$\frac{D^\gamma s}{D_t} = \frac{\partial s}{\partial t} + \mathbf{u}_\gamma \cdot \nabla s \quad (\text{A.3})$$

and

$$\frac{D^{\gamma}\mathbf{w}}{D_t} = \frac{\partial\mathbf{w}}{\partial t} + (\nabla\mathbf{w})\mathbf{u}_{\gamma}. \quad (\text{A.4})$$

The motion of the mixture can be computed by defining a mean velocity \mathbf{u} of the mixture following the requirement that the total mass flow is the sum of the individual flows so that

$$\rho\mathbf{u} = \sum_{\gamma} \rho_{\gamma}\mathbf{u}_{\gamma}, \quad (\text{A.5})$$

where ρ_{γ} represents the average density of \mathcal{C}_{γ} over a small volume of the mixture and the mass density of the mixture, ρ , is given by

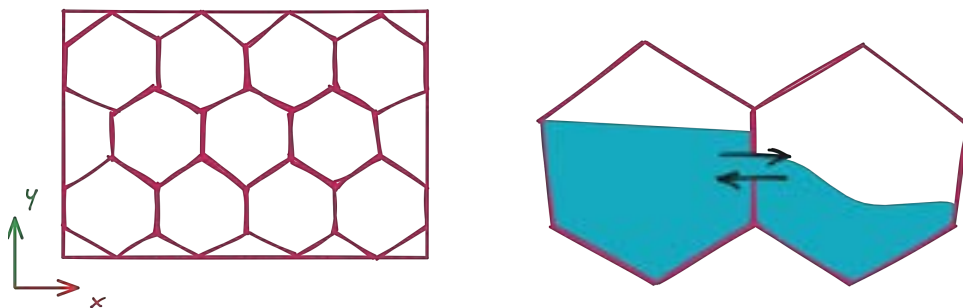
$$\rho = \sum_{\gamma} \rho_{\gamma}. \quad (\text{A.6})$$

NUMERICAL METHODS

B.1 Finite Volume Method

Finite Volume Methods (FVMs) are derived directly from the integral form of conservation laws. The FVM subdivides the physical domain into cells, named *finite volumes*, and keeps track of the fluxes of physical quantities between cells — see Figure 51. Applying the Gauss theorem connects the surface fluxes to volume quantities, allowing the discretization of the governing equations over the finite volumes. This chapter is heavily based on (GONZALEZ; STUART, 2008) and (DARWISH; MOUKALLED, 2016), refer to these books for a complete discussion on the FVM.

Figure 51 – The FVM decomposes the physical domain into finite volumes (left). The figure on the right illustrates mass fluxes between cells as the water flow between two tanks. From a conservation perspective, the mass in a finite volume will change only due to fluxes at the boundaries.



Source: Elaborated by the author.

Consider the one-dimensional case for an arbitrary quantity specified by the unknown function $q(x,t)$ at a given location x and time t . If this quantity represents the density of a substance, the sum

$$\int_{x_a}^{x_b} q(x,t) dx \quad (\text{B.1})$$

gives the total mass of the substance in the section between x_a and x_b at a particular time t . As the flow evolve, the mass of the substance in $[x_a, x_b]$ might change over time due to the flux of matter at the endpoints x_a and x_b . If we know the flow velocity function $u(x, t)$, then the flux of mass $f(x, t)$ can be defined as

$$f(x, t) = u(x, t)q(x, t). \quad (\text{B.2})$$

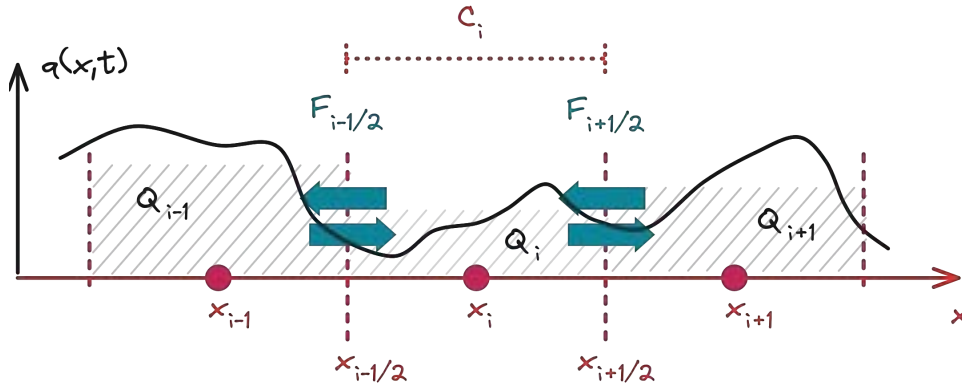
The following *integral form* gives the change of mass over time:

$$\frac{d}{dt} \int_{x_a}^{x_b} q(x, t) dx = -f(x, t) \Big|_{x_a}^{x_b}. \quad (\text{B.3})$$

In particular, if q and f are smooth, the equation above can be written in the *differential form*

$$\begin{aligned} \frac{d}{dt} \int_{x_a}^{x_b} q(x, t) dx &= - \int_{x_a}^{x_b} \frac{\partial}{\partial x} f(x, t) dx \\ \therefore \int_{x_a}^{x_b} \left[\frac{\partial}{\partial t} q(x, t) + \frac{\partial}{\partial x} f(x, t) \right] dx &= 0 \\ \therefore \frac{\partial}{\partial t} q(x, t) + \frac{\partial}{\partial x} f(x, t) &= 0. \end{aligned} \quad (\text{B.4})$$

Figure 52 – The continuous field $q(x, t)$ represents the distribution of a physical quantity over the physical domain at a given time t . The FVM decomposes the domain into cells C_i centered at positions x_i . Cell faces at $x_{i\pm\frac{1}{2}}$ represent the boundaries through which q flows. The average value Q_i approximates q inside C_i , and $F_{i\pm\frac{1}{2}}$ approximate the flux at faces in $x_{i\pm\frac{1}{2}}$.



Source: Elaborated by the author.

The 1D domain decomposition in Figure 52 defines cells centered at x_i locations with faces at $x_{i\pm\frac{1}{2}}$ locations. The value Q_i is the approximation of q in the cell centered at x_i and is the average value of q over the interval $C_i = (x_{i-\frac{1}{2}}, x_{i+\frac{1}{2}})$:

$$Q_i \approx \frac{1}{\Delta x_i} \int_{C_i} q(x, t) dx, \quad (\text{B.5})$$

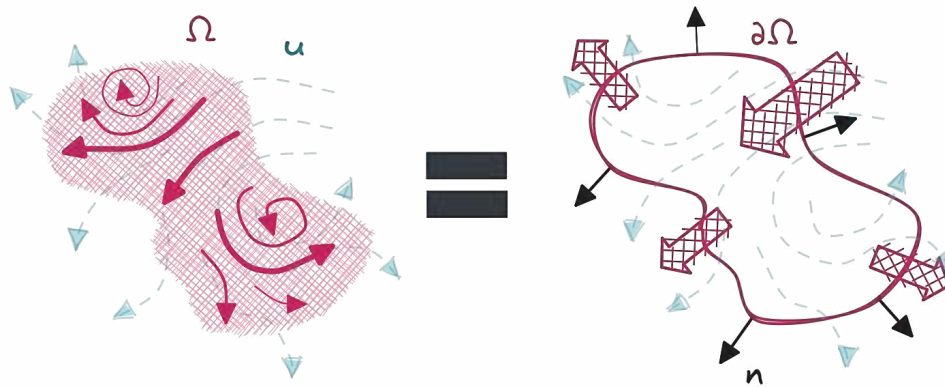
where $\Delta x_i = |C_i|$. Similarly, the functions

$$\begin{aligned} F_{i-\frac{1}{2}}(Q_{i-1}, Q_i) &\approx \frac{1}{\Delta t} \int_{t_n}^{t_{n+1}} f(x_{i-\frac{1}{2}}, t) dt \\ F_{i+\frac{1}{2}}(Q_i, Q_{i+1}) &\approx \frac{1}{\Delta t} \int_{t_n}^{t_{n+1}} f(x_{i+\frac{1}{2}}, t) dt \end{aligned} \quad (\text{B.6})$$

approximate the fluxes of q at the face locations $x_{i\pm\frac{1}{2}}$. Notice that F depends only on the neighboring values Q_i and $Q_{i\pm 1}$ over the time interval $\Delta t = t_{n+1} - t_n$. By time integrating Equation B.3 over the time interval Δt , the approximations above, Q_i and $F_{i\pm\frac{1}{2}}$, can be used directly to approximate Equation B.3 entirely¹. This procedure illustrates the essence of the FVM: approximate differential equations by using just volume quantities and boundary fluxes.

B.1.1 The Divergence Theorem

Figure 53 – The visual illustration of the Divergence Theorem: The total divergence of a vector field \mathbf{u} inside a volume Ω equals the total net flux of \mathbf{u} passing through the boundary surface $\partial\Omega$ with the unit vector field \mathbf{n} pointing outwards $\partial\Omega$.



Source: Elaborated by the author.

The central tool of the FVM is the Gauss theorem, also known as the *Divergence Theorem*. For a given bounded region Ω with boundary $\partial\Omega$, the theorem connects the total volume divergence of a vector field $\mathbf{u}(\mathbf{x}, t)$ inside Ω with the net flux of \mathbf{u} through $\partial\Omega$ – see Figure 53. Let $\mathbf{n}(\mathbf{x})$ be the field of unit vectors normal to $\partial\Omega$; the divergence theorem reads:

$$\int_{\Omega} (\nabla \cdot \mathbf{u}) d\Omega = \oint_{\partial\Omega} (\mathbf{u} \cdot \mathbf{n}) d\partial\Omega. \quad (\text{B.7})$$

In the discrete setting, the boundary surface $\partial\Omega$ is approximated by a set of polygonal faces $S \approx \partial\Omega$. The following sum approximates the integral in the right-hand side of Equation B.7:

$$\oint_{\partial\Omega} (\mathbf{u} \cdot \mathbf{n}) d\partial\Omega \approx \sum_{f_i \in S} \int_{f_i} (\mathbf{u} \cdot \mathbf{n}) dS \quad (\text{B.8})$$

where f_i , with index $i \in [1, |S|]$, represents each face in S . The Gauss quadrature can approximate the solution of the face integral inside the sum in Equation B.8. Using the trapezoidal rule in any face f_i , only one integration point located at f_i 's center f_{ci} results in second-order accuracy.

¹ Let the superscript $(\cdot)^n$ denote the time step index, then it is possible to obtain the following explicit form for Equation B.3: $Q_i^{n+1} = Q_i^n + \frac{\Delta t}{\Delta x} (F_{i-\frac{1}{2}}^n - F_{i+\frac{1}{2}}^n)$.

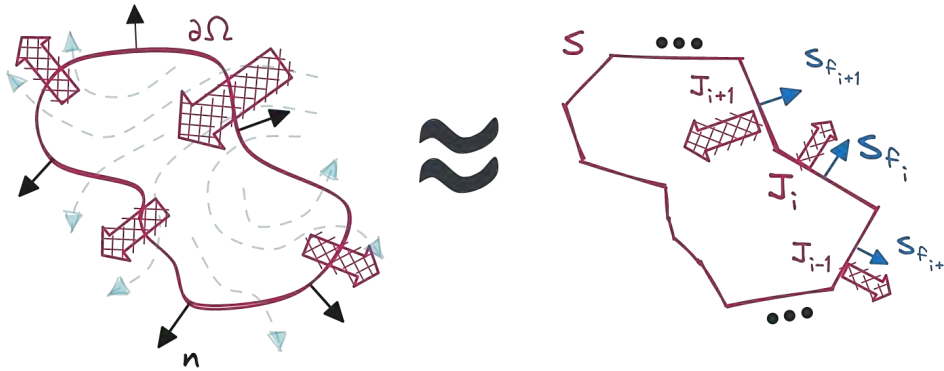
Thus, for the face area vector \mathbf{S}_{f_i} that points outwards the finite volume at face f_i , the integral is approximated by

$$\int_{f_i} (\mathbf{u} \cdot \mathbf{n}) dS \approx (\mathbf{u})_{f_{ci}} \cdot \mathbf{S}_{f_i} = \mathbf{J}_i \cdot \mathbf{S}_{f_i}, \quad (\text{B.9})$$

where the subscript $(\star)_{\mathbf{p}}$ indicates the value of the quantity realized in the point \mathbf{p} . The symbol \mathbf{J}_i will be used for now on to represent the quantity transported on the flux evaluated at f_{ci} . The final definition of $\mathbf{J}_i \cdot \mathbf{S}_{f_i}$, discussed later in [subsection B.1.6](#), will produce the linear system of equations that will provide the numerical solution for the PDEs. As represented in [Figure 54](#), applying [Equation B.9](#) in [Equation B.8](#) gives the approximated solution of the total flux passing through the surface S :

$$\oint_{\partial\Omega} (\mathbf{u} \cdot \mathbf{n}) d\partial\Omega \approx \sum_{f_i \in S} \mathbf{J}_i \cdot \mathbf{S}_{f_i}. \quad (\text{B.10})$$

Figure 54 – The total surface flux passing through the boundary surface $\partial\Omega$ can be approximated by the sum of the individual face fluxes $\mathbf{J}_i \cdot \mathbf{S}_{f_i}$ in the discrete surface S .



Source: Elaborated by the author.

The single-point Gauss quadrature could also be applied to approximate the volume integral in [Equation B.7](#). For the mid-point c , and Ω volume V , the volume integral is approximated by

$$\int_{\Omega} (\nabla \cdot \mathbf{u}) d\Omega \approx (\nabla \cdot \mathbf{u})_c V, \quad (\text{B.11})$$

which combined to [Equation B.10](#), gives the approximation for $\nabla \cdot \mathbf{u}$ over Ω :

$$(\nabla \cdot \mathbf{u})_c \approx \frac{1}{V} \sum_{f_i \in S} \mathbf{J}_i \cdot \mathbf{S}_{f_i}. \quad (\text{B.12})$$

The Gauss theorem is not restricted to vector fields such as \mathbf{u} and the internal product (\cdot) . The general form of the theorem is

$$\int_{\Omega} (\nabla * \Psi) d\Omega = \oint_{\partial\Omega} (\Psi * \mathbf{n}) d\partial\Omega, \quad (\text{B.13})$$

where Ψ is a generic tensor field that accepts any particular product operation $*$. This generalization enables the discretization of most differential terms in the Partial-Differential Equations (PDEs) commonly solved by FVMs. The following section details the discretization process of such equations, including the terms that do not accept the divergence theorem.

B.1.2 Spatial Discretization

This section lists the types of terms that appear in common physical models solved by FVMs, such as the velocity divergent term $\nabla \cdot \mathbf{u}$ in the previous section. In this section, $\rho(\mathbf{x}, t)$, $p(\mathbf{x}, t)$, $q(\mathbf{x}, t)$, and $\phi(\mathbf{x}, t)$ are scalar fields, $\mathbf{f}_b(\mathbf{x}, t)$ and $\mathbf{u}(\mathbf{x}, t) = (u_x, u_y, u_z)$ are vector fields, and Γ , μ , and ν are constants. Some equations decouple \mathbf{n} from \mathbf{S}_f by recalling

$$\mathbf{S}_f = (S_{fx}, S_{fy}, S_{fz}) = \mathbf{n} \|\mathbf{S}_f\| = \mathbf{n} S_f$$

- **Divergent term $\nabla \cdot \mathbf{u}$:**

$$\int_{\Omega} \nabla \cdot \mathbf{u} d\Omega = \oint_{\partial\Omega} (\mathbf{u} \cdot \mathbf{n}) d\partial\Omega \approx \sum_{f_i \in S} (\mathbf{u})_{f_{ci}} \cdot \mathbf{S}_{f_i}. \quad (\text{B.14})$$

- **Convective term $\nabla \cdot (\rho \mathbf{u} \phi)$:**

$$\int_{\Omega} \nabla \cdot (\rho \mathbf{u} \phi) d\Omega = \oint_{\partial\Omega} ((\rho \mathbf{u} \phi) \cdot \mathbf{n}) d\partial\Omega \approx \sum_{f_i \in S} (\rho \mathbf{u} \phi)_{f_{ci}} \cdot \mathbf{S}_{f_i}. \quad (\text{B.15})$$

- **Convective term $\nabla \cdot (\rho \mathbf{u} \otimes \mathbf{u})$:**

$$\int_{\Omega} \nabla \cdot (\rho \mathbf{u} \otimes \mathbf{u}) d\Omega = \oint_{\partial\Omega} ((\rho \mathbf{u} \otimes \mathbf{u}) \cdot \mathbf{n}) d\partial\Omega \approx \sum_{f_i \in S} (\rho \mathbf{u} \otimes \mathbf{u})_{f_{ci}} \cdot \mathbf{S}_{f_i}. \quad (\text{B.16})$$

$$(\rho \mathbf{u} \otimes \mathbf{u})_{f_c} \cdot \mathbf{S}_f =$$

$$\rho \begin{pmatrix} u_x u_x & u_x u_y & u_x u_z \\ u_y u_x & u_y u_y & u_y u_z \\ u_z u_x & u_z u_y & u_z u_z \end{pmatrix}_{f_c} \cdot \mathbf{S}_f = \rho \begin{pmatrix} u_x u_x S_{fx} + u_x u_y S_{fy} + u_x u_z S_{fz} \\ u_y u_x S_{fx} + u_y u_y S_{fy} + u_y u_z S_{fz} \\ u_z u_x S_{fx} + u_z u_y S_{fy} + u_z u_z S_{fz} \end{pmatrix}_{f_c}. \quad (\text{B.17})$$

- **Diffusion term $\nabla \cdot (\Gamma \nabla \phi)$:**

$$\int_{\Omega} \nabla \cdot (\Gamma \nabla \phi) d\Omega = \oint_{\partial\Omega} (\Gamma \nabla_{\mathbf{n}} \phi) d\partial\Omega \approx \sum_{f_i \in S} (\Gamma \nabla_{\mathbf{n}} \phi)_{f_{ci}} S_{f_i}, \quad (\text{B.18})$$

where $S_{f_i} = \|\mathbf{S}_{f_i}\|$. The computation of the gradient of ϕ is discussed in [subsection B.1.4](#).

- **Diffusion term $\nabla \cdot (\nu \nabla \otimes \mathbf{u})$:**

$$\int_{\Omega} \nabla \cdot (\nu \nabla \otimes \mathbf{u}) d\Omega = \oint_{\partial\Omega} ((\nu \nabla \otimes \mathbf{u}) \cdot \mathbf{n}) d\partial\Omega \approx \sum_{f_i \in S} (\nu \nabla \otimes \mathbf{u})_{f_{ci}} \cdot \mathbf{S}_{f_i}. \quad (\text{B.19})$$

$$(\nu \nabla \otimes \mathbf{u})_{f_c} \cdot \mathbf{S}_f =$$

$$\nu \begin{pmatrix} \frac{\partial u_x}{\partial x} & \frac{\partial u_y}{\partial x} & \frac{\partial u_z}{\partial x} \\ \frac{\partial u_x}{\partial y} & \frac{\partial u_y}{\partial y} & \frac{\partial u_z}{\partial y} \\ \frac{\partial u_x}{\partial z} & \frac{\partial u_y}{\partial z} & \frac{\partial u_z}{\partial z} \end{pmatrix}_{f_c} \cdot \mathbf{S}_f = \nu \begin{pmatrix} \frac{\partial u_x}{\partial x} S_{fx} + \frac{\partial u_y}{\partial x} S_{fy} + \frac{\partial u_z}{\partial x} S_{fz} \\ \frac{\partial u_x}{\partial y} S_{fx} + \frac{\partial u_y}{\partial y} S_{fy} + \frac{\partial u_z}{\partial y} S_{fz} \\ \frac{\partial u_x}{\partial z} S_{fx} + \frac{\partial u_y}{\partial z} S_{fy} + \frac{\partial u_z}{\partial z} S_{fz} \end{pmatrix}_{f_c}. \quad (\text{B.20})$$

- **Tensor term** $\nabla \cdot (\boldsymbol{\mu}(\nabla \otimes \mathbf{u})^T)$:

$$\int_{\Omega} \nabla \cdot (\boldsymbol{\mu}(\nabla \otimes \mathbf{u})^T) d\Omega = \oint_{\partial\Omega} ((\boldsymbol{\mu}(\nabla \otimes \mathbf{u})^T) \cdot \mathbf{n}) d\partial\Omega \approx \sum_{f_i \in \mathcal{S}} (\boldsymbol{\mu}(\nabla \otimes \mathbf{u})^T)_{f_{ci}} \cdot \mathbf{S}_{f_i}. \quad (\text{B.21})$$

$$\begin{aligned} (\boldsymbol{\mu}(\nabla \otimes \mathbf{u})^T)_{f_c} \cdot \mathbf{S}_{\mathbf{f}} = \\ \boldsymbol{\mu} \begin{pmatrix} \frac{\partial u_x}{\partial x} & \frac{\partial u_x}{\partial y} & \frac{\partial u_x}{\partial z} \\ \frac{\partial u_y}{\partial x} & \frac{\partial u_y}{\partial y} & \frac{\partial u_y}{\partial z} \\ \frac{\partial u_z}{\partial x} & \frac{\partial u_z}{\partial y} & \frac{\partial u_z}{\partial z} \end{pmatrix}_{f_c} \cdot \mathbf{S}_{\mathbf{f}} = \boldsymbol{\mu} \begin{pmatrix} \frac{\partial u_x}{\partial x} S_{fx} + \frac{\partial u_x}{\partial y} S_{fy} + \frac{\partial u_x}{\partial z} S_{fz} \\ \frac{\partial u_y}{\partial x} S_{fx} + \frac{\partial u_y}{\partial y} S_{fy} + \frac{\partial u_y}{\partial z} S_{fz} \\ \frac{\partial u_z}{\partial x} S_{fx} + \frac{\partial u_z}{\partial y} S_{fy} + \frac{\partial u_z}{\partial z} S_{fz} \end{pmatrix}_{f_c}. \end{aligned} \quad (\text{B.22})$$

- **Scalar gradient term** $\nabla \phi$:

In this particular case, the Green-Gauss theorem² is used instead:

$$\int_{\Omega} \nabla \phi d\Omega = \oint_{\partial\Omega} (\phi \mathbf{n}) d\partial\Omega \approx \sum_{f_i \in \mathcal{S}} (\phi)_{f_{ci}} \mathbf{S}_{f_i}. \quad (\text{B.23})$$

Note that the discretizations above require evaluating values in face locations, such as the fields \mathbf{u} and ϕ , and even a differential operator, as the gradient $\nabla \phi$ in Equation B.18. The computation of such values depends directly on how the fields are stored in the numerical mesh. Moreover, the mesh's geometry also affects the accuracy of the computations, as detailed in subsection B.1.4 on page 167.

The divergence theorem does not work for all terms found in equations. *Transient* and *source* terms, marked in the equations bellow, are examples of terms that do not need the transformation of their volume integrals into surface integrals. Their discretization comes directly from the approximation of volume integral:

$$\underbrace{\frac{\partial(\rho\phi)}{\partial t}}_{\text{transient}} + \nabla \cdot (\rho \mathbf{u} \phi) = \nabla \cdot (\Gamma \nabla \phi) + \underbrace{q}_{\text{source}}, \quad (\text{B.24})$$

$$\underbrace{\frac{\partial \mathbf{u}}{\partial t}}_{\text{transient}} + \nabla \cdot (\mathbf{u} \otimes \mathbf{u}) - \nabla \cdot (\nu \nabla \otimes \mathbf{u}) = -\nabla p + \underbrace{\mathbf{f}_b}_{\text{source}}. \quad (\text{B.25})$$

The following approximations consider the single-point volume integration with integration point located at the cell center C_c and cell volume C_V :

- **Source terms** q and \mathbf{f}_b :

$$\int_{\Omega} q d\Omega \approx (q)_{C_c} C_V \quad \text{and} \quad \int_{\Omega} \mathbf{f}_b d\Omega \approx (\mathbf{f}_b)_{C_c} C_V. \quad (\text{B.26})$$

² The Green-Gauss theorem states that the surface integral of a scalar function ϕ is equal to the volume integral of the gradient of ϕ , $\nabla \phi$.

- **Transient terms** $\frac{\partial(\rho\phi)}{\partial t}$ and $\frac{\partial\mathbf{u}}{\partial t}$:

Assuming that Ω does not change its volume in time, i.e. C_V is constant, then the transient term discretization can also be approximated by the Gauss quadrature for the volume integral:

$$\int_{\Omega} \frac{\partial(\rho\phi)}{\partial t} d\Omega \approx \frac{\partial(\rho\phi)_{C_c}}{\partial t} C_V \quad \text{and} \quad \frac{\partial(\mathbf{u})}{\partial t} d\Omega \approx \frac{\partial(\mathbf{u})_{C_c}}{\partial t} C_V. \quad (\text{B.27})$$

To illustrate the process of the FVM, consider Equation B.24. The first step is to set the proper integration for each term:

$$\int_{\Omega} \frac{\partial(\rho\phi)}{\partial t} d\Omega + \oint_{\partial\Omega} ((\rho\mathbf{u}\phi) \cdot \mathbf{n}) d\partial\Omega = \oint_{\partial\Omega} ((\Gamma\nabla\phi) \cdot \mathbf{n}) d\partial\Omega + \int_{\Omega} q d\Omega, \quad (\text{B.28})$$

and then perform the approximations

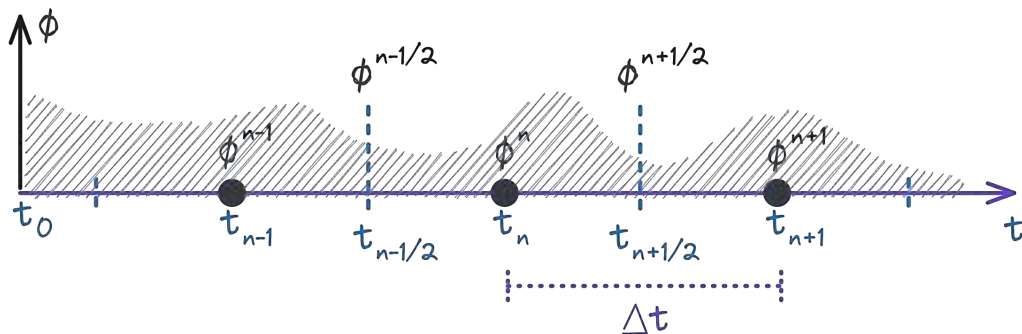
$$\boxed{\frac{\partial(\rho\phi)_{C_c}}{\partial t} C_V} + \sum_{f_i \in S} (\rho\mathbf{u}\phi)_{f_i} \cdot \mathbf{S}_{f_i} = \sum_{f_i \in S} (\Gamma\nabla\phi)_{f_i} \cdot \mathbf{S}_{f_i} + (q)_{C_c} C_V. \quad (\text{B.29})$$

The next step is to discretize the temporal derivative, marked in the equation above. The following section discusses the approximation of the transient term.

B.1.3 Time Integration

The process of temporal discretization follows the same approach taken until now, which consists of the integration over the time variable t . Like the one-dimensional spatial discretization presented earlier, temporal cells T_n of size Δt split the timeline, so the time index $n \in [0, +\infty)$ represents the *temporal cell* center $t_n = t_0 + n\Delta t$ — see Figure 55. Similarly, the *temporal face* location happens on indices $n \pm \frac{1}{2}$. The transient solution solves the equations in order $[t_0, \dots, t_{n-1}, t_n, t_{n+1}, \dots]$.

Figure 55 – The discretization in time splits the temporal line into temporal cells of size Δt . Similar to spatial flux computations, temporal face locations are also of interest in temporal discretization. The temporal dependency makes the computation of ϕ values follow the order $[\dots, n-1, n, n+1, \dots]$.



Source: Elaborated by the author.

In particular, the integration for the temporal cell T_n , i.e. for the time interval $[t_{n-\frac{1}{2}}, t_{n+\frac{1}{2}}]$, of Equation B.29 results in

$$\int_{t_n-\frac{\Delta t}{2}}^{t_n+\frac{\Delta t}{2}} \frac{\partial(\rho\phi)_{C_c}}{\partial t} C_V dt + \int_{t_n-\frac{\Delta t}{2}}^{t_n+\frac{\Delta t}{2}} \left[\sum_{f_i \in S} (\rho\mathbf{u}\phi)_{f_i} \cdot \mathbf{S}_{f_i} \right] dt = \int_{t_n-\frac{\Delta t}{2}}^{t_n+\frac{\Delta t}{2}} \left[\sum_{f_i \in S} (\Gamma\nabla\phi)_{f_i} \cdot \mathbf{S}_{f_i} \right] dt + \int_{t_n-\frac{\Delta t}{2}}^{t_n+\frac{\Delta t}{2}} [(q)_{C_c} C_V] dt \quad (\text{B.30})$$

For simplicity, let $L(\phi)$ represent the sum of all spatially discretized terms except the transient term and rewrite the equation above as

$$\int_{t_n-\frac{\Delta t}{2}}^{t_n+\frac{\Delta t}{2}} \frac{\partial(\rho\phi)_{C_c}}{\partial t} C_V dt + \int_{t_n-\frac{\Delta t}{2}}^{t_n+\frac{\Delta t}{2}} L dt = 0. \quad (\text{B.31})$$

One possible approach is to solve the second term with the mid point rule:

$$\int_{t_n-\frac{\Delta t}{2}}^{t_n+\frac{\Delta t}{2}} L dt \approx (L)^n \Delta t, \quad (\text{B.32})$$

where the superscript $(\cdot)^n$ indicates the temporal location of the variables in L . In the FVM, the first term is approximated by the face fluxes in the same manner as in the previous sections:

$$\int_{t_n-\frac{\Delta t}{2}}^{t_n+\frac{\Delta t}{2}} \frac{\partial(\rho\phi)_{C_c}}{\partial t} C_V dt \approx C_V \left((\rho\phi)_{C_c}^{n+\frac{1}{2}} - (\rho\phi)_{C_c}^{n-\frac{1}{2}} \right). \quad (\text{B.33})$$

Putting all together, Equation B.31 becomes

$$\frac{C_V}{\Delta t} \left((\rho\phi)_{C_c}^{n+\frac{1}{2}} - (\rho\phi)_{C_c}^{n-\frac{1}{2}} \right) + (L)^n = 0. \quad (\text{B.34})$$

Note that the equation above contains samples from times $[t_{n-\frac{1}{2}}, t_n, t_{n+\frac{1}{2}}]$. The form of how these elements are computed will depend on the choice of interpolation for the temporal fluxes located at $t_{n-\frac{1}{2}}$ and $t_{n+\frac{1}{2}}$. Figure 56 illustrates the two common approaches listed here:

- **Implicit Euler Scheme:**

The first-order implicit Euler scheme, or *first-order upwind*, considers the value of the element at t_k to be the same as the value at $t_{k+\frac{1}{2}}$. In other words, unknown values receive the same values of locations halfway backward. Therefore, the flux terms in Equation B.34 receive the same values of the respective cell centers:

$$\frac{C_V}{\Delta t} \left((\rho\phi)_{C_c}^n - (\rho\phi)_{C_c}^{n-1} \right) + (L)^n = 0. \quad (\text{B.35})$$

Note that only the data from time t_{n-1} is available at this point. The time of the new values, t_n , is the same as the time of the spatial term $(L)^n$. It means that $(L)^n$ is not available yet, and the whole system of equations for both terms needs to be solved together.

• **Explicit Euler Scheme:**

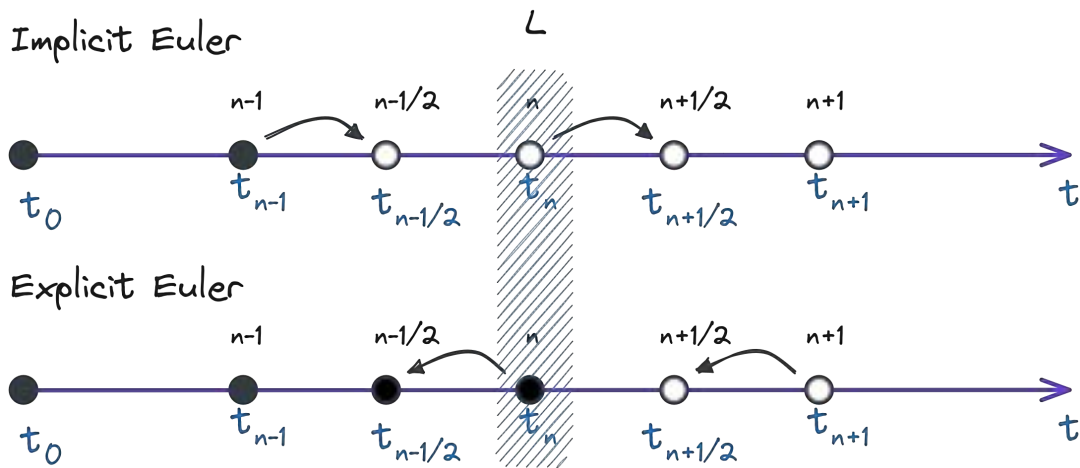
The first-order explicit Euler scheme considers the value of the element at t_k to be the same as the value at $t_{k-\frac{1}{2}}$. Therefore, face fluxes receive the same values of cell centers halfway forward:

$$\frac{C_V}{\Delta t} \left((\rho\phi)_{C_c}^{n+1} - (\rho\phi)_{C_c}^n \right) + (L)^n = 0. \tag{B.36}$$

The spatial discretization lies in a previous time t_n regarding the new time t_{n+1} . All data is available for time t_n , meaning that the new step can be computed directly as:

$$(\rho\phi)_{C_c}^{n+1} = (\rho\phi)_{C_c}^n - \frac{\Delta t}{C_V} (L)^n. \tag{B.37}$$

Figure 56 – This figure visually represents implicit and explicit Euler schemes at step N in time t_n . Filled circles in the timeline represent data available for the computation. The dashed column represents the location in time of the spatial discretization L . In the case of the implicit Euler scheme, ϕ^n is unknown, then $(L)^n$ must be computed along with the new transient term.



Source: Elaborated by the author.

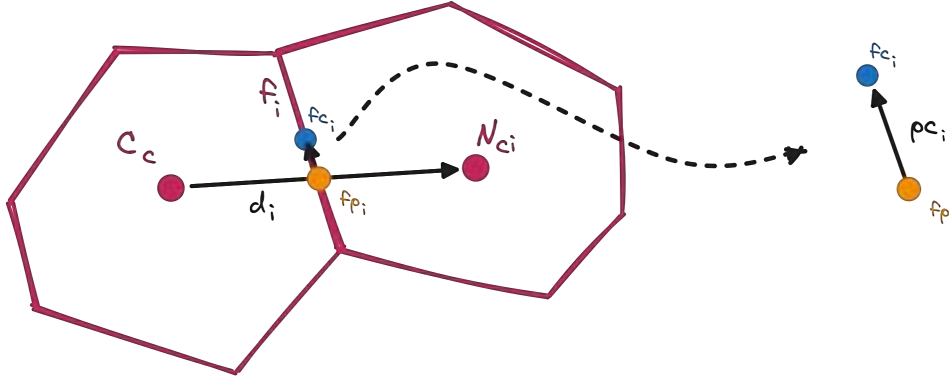
The literature offers a variety of temporal discretization methods, including higher-order Euler schemes, the Crank-Nicholson method, which uses a central difference scheme, and methods that consider non-uniform time steps. Refer to [Gonzalez and Stuart \(2008\)](#) and [Darwish and Moukalled \(2016\)](#) for further information.

B.1.4 Face Computations

As mentioned earlier, the computation of the fluxes $\mathbf{J}_i \cdot \mathbf{S}_{f_i}$ requires the evaluation of values at the face centers f_{ci} . Some numerical settings conveniently store fields in face centers, the case of staggered grids with velocity components. However, values resulting from volume integrals are located at cell centers. In such cases, the interpolation of cell values must be interpolated to face locations.

[Figure 57](#) depicts two pairs of cells, C and N_i , with respective centers C_c and N_{ci} , and volumes C_V and N_{Vi} , shared by a single face f_i with center f_{ci} . Let $\mathbf{d}_i = N_{ci} - C_c$ connect both

Figure 57 – The flux of a face f_i requires field values at the face center f_{ci} . Usually the field values are found in the cell centers, C_c and N_{ci} , and must be interpolated to the face locations. The usual approach is to interpolate along the line \mathbf{d}_i that connects both cell centers at the intersection point f_{pi} . In skewed grids, f_{pi} deviates away from f_{ci} by $\bar{\mathbf{p}}\mathbf{c}_i$, requiring further calculations for f_{ci} .



Source: Elaborated by the author.

cell centers and intersect the face f_i at point f_{pi} , where f_{pi} is not necessarily the same as f_{ci} ³, as shown in the figure. Suppose the cell values for the scalar field $\phi(\mathbf{x})$ for both cells are

$$\phi_C = (\phi)_{C_c} C_V \quad \text{and} \quad \phi_{N_i} = (\phi)_{N_{ci}} N_{Vi}. \quad (\text{B.38})$$

The common approach is to assume that ϕ varies linearly along \mathbf{d}_i , meaning that the estimate at f_{pi} is the linear interpolation of ϕ_C and ϕ_N :

$$\phi_{f_{pi}} = \lambda_C \phi_C + \lambda_N \phi_N. \quad (\text{B.39})$$

where λ_C and λ_N are interpolation coefficients. However, the second order accuracy of the flux discretization requires a value located at the face center f_{ci} . Therefore, a *skewness correction* must be performed in order to compute $\phi_{f_{ci}}$:

$$\phi_{f_{ci}} = \phi_{f_{pi}} + (\nabla_{\mathbf{d}_i} \phi)_{f_{pi}} \cdot \bar{\mathbf{p}}\mathbf{c}_i, \quad (\text{B.40})$$

where $\bar{\mathbf{p}}\mathbf{c}_i = f_{ci} - f_{pi}$ and the gradient $(\nabla_{\mathbf{d}_i} \phi)_{f_{pi}}$ can be computed as

$$\left(\frac{\partial \phi}{\partial \mathbf{d}_i} \right)_{f_{pi}} = \frac{\phi_N - \phi_C}{\|\mathbf{d}_i\|}. \quad (\text{B.41})$$

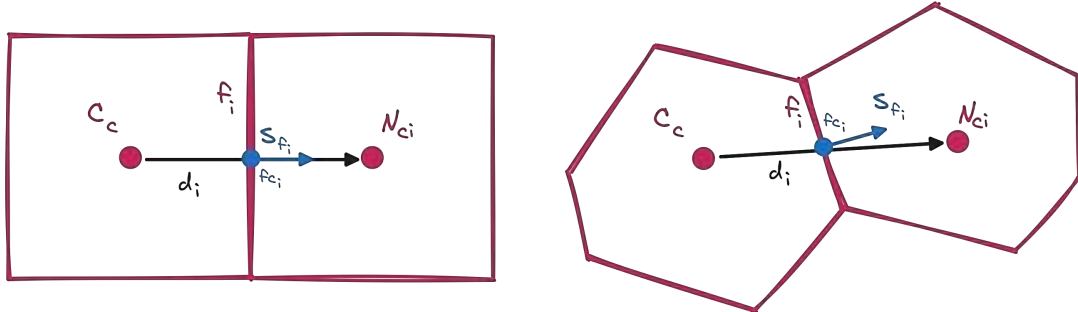
Some flux equations will contain differential operators, such as the gradient operator $\nabla \phi$ in the diffusion term described in Equation B.18 on page 163. Let $\Gamma = 1$ in the equation and the face normal vector \mathbf{n}_i be decoupled from $\mathbf{S}_{f_i} = \mathbf{n}_i |\mathbf{S}_{f_i}| = \mathbf{n}_i S_{f_i}$, then:

$$\mathbf{J}_i \cdot \mathbf{S}_{f_i} = (\nabla \phi)_{f_{ci}} \cdot \mathbf{S}_{f_i} = (\nabla \phi \cdot \mathbf{n}_i)_{f_{ci}} S_{f_i} = (\nabla_{\mathbf{n}_i} \phi)_{f_{ci}} S_{f_i}. \quad (\text{B.42})$$

³ In *skewed* grids, \mathbf{d}_i may not intersect the face at its mid-points.

⁴ The operator $\nabla_{\mathbf{n}}$ is referred to as the *surface normal gradient*.

Figure 58 – Depending on the orthogonality of the grid, the connecting vector \mathbf{d}_i deviates from \mathbf{S}_{f_i} . Both directions are equal on the left, and the vectors are colinear. In such a case, the direction of \mathbf{d}_i fully represents the flux direction. The same cannot be said about the setting on the right, where the flux will contain a non-orthogonal component.



Source: Elaborated by the author.

In the track of the effects skewed grids produce on interpolation methods for face values, the non-orthogonality of grids will also directly impact flux computations. Figure 58 presents two cases that show the alignment of the vector \mathbf{d}_i with \mathbf{S}_{f_i} . In the simpler case, where \mathbf{d}_i aligns with \mathbf{n}_i , yielding

$$(\nabla_{\mathbf{n}_i} \phi)_{f_{ci}} = \left(\frac{\partial \phi}{\partial \mathbf{n}_i} \right)_{f_{ci}} = \left(\frac{\partial \phi}{\partial \mathbf{d}_i} \right)_{f_{ci}} = \frac{\phi_{N_{ci}} - \phi_C}{\|\mathbf{d}_i\|}, \quad (\text{B.43})$$

The equation above works because since the flux flows parallel to \mathbf{d}_i , and the fact that \mathbf{d}_i is perpendicular to f_i implies that $\mathbf{J}_i \cdot \mathbf{S}_{f_i}$ describes the whole flux quantity. Therefore, the gradient along \mathbf{d}_i is valid and sufficient.

For non-orthogonal cases, when there is an angle $\theta > 0$ between \mathbf{n}_i and \mathbf{d}_i , the accuracy of Equation B.42 can be maintained by decomposing the discretization into two parts:

$$(\nabla_{\mathbf{n}_i} \phi)_{f_{ci}} = \underbrace{(\phi_{N_{ci}} - \phi_C)}_{\text{orthogonal part}} \underbrace{\not\propto_{corr_i}}_{\text{correction}} + \underbrace{(\nabla \phi)_{f_{ci}} \cdot (\mathbf{n}_i - \not\propto_{corr_i} \mathbf{d}_i)}_{\text{correction}}. \quad (\text{B.44})$$

where the *correction* half is computed from **known** values of ϕ . There are various strategies to define $\not\propto_{corr_i}$. The following three examples (a) enforce $\mathbf{d}_i \perp (\mathbf{n}_i - \mathbf{d}_i)$, (b) pretend the \mathbf{d}_i direction is orthogonal to the face f_i , and (c) make $(\mathbf{n}_i - \mathbf{d}_i) \perp \mathbf{S}_{f_i}$:

a) *minimum correction*

$$\not\propto_{corr_i} = \frac{\cos \theta}{\|\mathbf{d}_i\|}. \quad (\text{B.45})$$

b) *orthogonal correction*

$$\not\propto_{corr_i} = \frac{1}{\|\mathbf{d}_i\|}. \quad (\text{B.46})$$

c) *over-relaxed*

$$\not\propto_{corr_i} = \frac{1}{\|\mathbf{d}_i\| \cos \theta}. \quad (\text{B.47})$$

The next step is assembling a numerical system of equations from the resulting discretizations described so far. However, before proceeding to this final step in [subsection B.1.6](#), the following section discusses further the discretization of convection terms.

B.1.5 Advection Schemes

The convective terms listed in [subsection B.1.2](#), [Equation B.15](#), and [Equation B.16](#) model the transport of physical quantities by a velocity field. A more generic form is

$$\nabla \cdot (\mathbf{u} * \Psi)^5, \quad (\text{B.48})$$

where Ψ can be a tensor of any rank field with its appropriate product $*$. The transport phenomenon described above is referred to as *advection*⁶, and its physical meaning provides an alternative computation of the discretized term.

Consider the following example of a mass flux carrying a scalar property given by $\phi(\mathbf{x})$:

$$\begin{aligned} \int_{\Omega} \nabla \cdot (\rho \mathbf{u} \phi) d\Omega &= \oint_{\partial\Omega} ((\rho \mathbf{u} \phi) \cdot \mathbf{n}) d\partial\Omega \approx \sum_{f_i \in \mathcal{S}} (\rho \mathbf{u} \phi)_{f_i} \cdot \mathbf{S}_{f_i} \\ &\approx \sum_{f_i \in \mathcal{S}} (\rho \mathbf{u})_{f_i} \cdot \mathbf{S}_{f_i} \phi_{f_i} \\ &\approx \sum_{f_i \in \mathcal{S}} \Phi_{f_i} \phi_{f_i}, \end{aligned} \quad (\text{B.49})$$

where $\Phi_{f_i} = (\rho \mathbf{u})_{f_i} \cdot \mathbf{S}_{f_i}$ is the mass flux at f_i , which can be computed via interpolation. Applying the same interpolation strategy for the computation of ϕ_{f_i} , although as accurate as Φ_{f_i} , may lead to an unstable numerical method. The solution should come from the physical interpretation of the transport phenomenon that carries ϕ along with the flux.

The idea is that the quantity ϕ_{f_i} at the face must come only from one side of the face, the side against the flow direction, called the *upwind*. Conversely, the side along the flow direction is called the *downwind*. In other words, the value of ϕ_{f_i} comes from the *upwind cell* and is given by an *upwind scheme*.

In the simple setting of the upwind scheme, the value of ϕ_{f_i} is given by

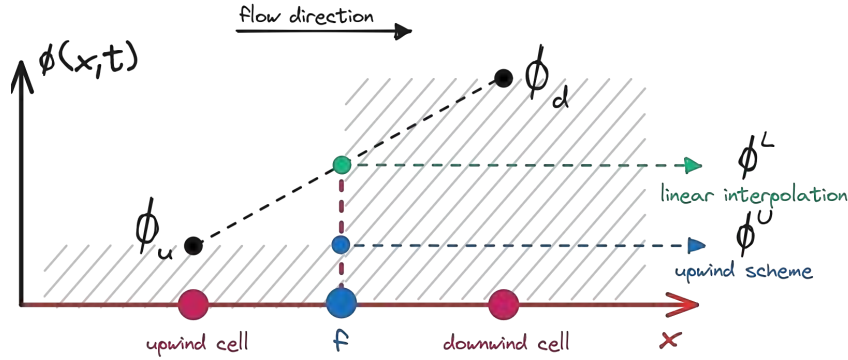
$$\phi_{f_i} = \begin{cases} \phi_u, & \Phi_{f_i} \geq 0, \\ \phi_d, & \Phi_{f_i} < 0, \end{cases} \quad (\text{B.50})$$

where ϕ_u is the upwind cell value of ϕ , and ϕ_d is the downwind cell value. [Figure 59](#) depicts both the interpolation and the upwind schemes; note how the linear interpolation scheme is numerically more accurate, but physically the upwind scheme makes more sense.

⁵ Sometimes the form includes density as well, $\nabla(\rho \mathbf{u} * \Psi)$, implying a mass flux.

⁶ In literature, advection and convection are used almost interchangeably, with the common difference that in convection, the transport is also caused by diffusion.

Figure 59 – A one-dimensional example comparing the results produced by linear interpolation and a simple upwind scheme, ϕ^L and ϕ^U . The former uses both upwind and downwind cell values, ϕ_u and ϕ_d , but is not physically accurate. The latter uses just ϕ_u , since it is carried by the flow in the right direction.



Source: Adapted from Greenshields and Weller (2022).

Despite its physical argument, however, the upwind scheme suffers from high diffusivity due to its low numerical accuracy. Therefore, diverse alternative upwind schemes try to diminish these issues, such as combining both methods:

$$\phi_{f_{ci}} = (1 - \beta)\phi^U + \beta\phi^L, \tag{B.51}$$

where ϕ^L is the value provided by the interpolation method, and ϕ^U is given by the upwind scheme, Equation B.50. The interpolation factor β can be optimized for each face in the numerical grid and various schemes define formulations for β , such as the so-called Total Variation Diminishing (TVD) schemes. Refer to Greenshields and Weller (2022) for a introduction about TVD schemes and others.

The linear interpolation scheme does not guarantee bounded solutions for $\nabla \cdot \mathbf{u}\phi$, resulting in ϕ values outside the interval $[\min(\phi_u, \phi_d), \max(\phi_u, \phi_d)]$. Boundedness is particularly important when dealing with bounded properties, such as the concentration of volume $\alpha \in [0, 1]$. The TVD schemes mentioned above try to diminish the unboundedness problem, but another class of schemes takes a different approach.

The Flux-Corrected Transport (FCT) methods, introduced by Boris and Book (1973), use low and high-order⁷ methods to compute flux values, Φ^L and Φ^H , respectively, to produce a bounded flux. The final flux is given by

$$\Phi = \Phi^L + \lambda(\Phi^H - \Phi^L), \tag{B.52}$$

where $\lambda \in [0, 1]$ is the weighting factor. The trick relies on the computation of λ , which takes into account all fluxes in a particular cell, instead of a single face. The desired result is that no new minima or maxima values of ϕ appear from one time step to the next.

⁷ The reasoning comes the fact that low-order methods are bounded, but less accurate, while high-order methods are accurate but unbounded.

With all discretizations in place, it is now possible to construct a numerical system of equations that will provide the solution for the equations. The following section combines all the steps described so far and completes this introduction to FMVs.

B.1.6 Numerical System

The last piece in the puzzle relies on finalizing the computation of the face fluxes. Consider a more general flux function $F(f) = F_f = \mathbf{J}_f \cdot \mathbf{S}_f$ for an arbitrary quantity $q(\mathbf{x}, t)$. Different ways exist to compute F_f ; however, the computation schemes generally rely on the values from the two neighboring cells. Like the one-dimensional flux functions $F_{i\pm 1}$ on page 160, the idea is that the flux of any face will depend only on the values "Q_i" of the two connected cells. In particular, the flux $F(f)$ between two cells C and N connected by the face f is defined as

$$F(f) = \mathbf{J}_f \cdot \mathbf{S}_f = \alpha_C Q_C + \alpha_N Q_N + \beta, \quad (\text{B.53})$$

where α_C and α_N are the linear coefficients for the averaged⁸ values of q , named Q_C and Q_N , for cells C and N , respectively. The last term, β , is the non-linear term of the combination. The decomposition of $F(f)$ described above is called *flux linearization* and is the building block for the final system of discretized equations:

$$\mathbf{A}\mathbf{x} = \mathbf{b}, \quad (\text{B.54})$$

where \mathbf{A} is a matrix of coefficients provided by the discretization, \mathbf{x} is the vector of unknown values for a particular variable, and \mathbf{b} is a vector of the correspondent source and non-orthogonal values. This numerical system will provide an approximate solution for the original equations. Take as an example the diffusion equation for a scalar field ϕ with its source q :

$$-\nabla \cdot (\nabla \phi) = q. \quad (\text{B.55})$$

From Equation B.18 and Equation B.26, the discretized form for the cell C with center C_c and volume C_V is

$$-\sum_{f_i \in S} (\nabla_{\mathbf{n}_i} \phi)_{f_{ci}} S_{f_i} = (q)_{C_c} C_V. \quad (\text{B.56})$$

Using the flux solution for $(\nabla_{\mathbf{n}_i} \phi)_{f_{ci}} S_{f_i}$ given by Equation B.44 for non-orthogonal grids, the left hand side of the equation above expands as

$$\begin{aligned} -\sum_{f_i \in S} (\nabla_{\mathbf{n}_i} \phi)_{f_{ci}} S_{f_i} &= -\sum_{f_i \in S} (\phi_{N_i} - \phi_C) \cancel{\mathcal{L}}_{corr_i} S_{f_i} - \sum_{f_i \in S} (\nabla \phi)_{f_{ci}} \cdot (\mathbf{n}_i - \cancel{\mathcal{L}}_{corr_i} \mathbf{d}_i) S_{f_i} \\ &= \sum_{f_i \in S} \phi_C \cancel{\mathcal{L}}_{corr_i} S_{f_i} - \sum_{f_i \in S} \phi_{N_i} \cancel{\mathcal{L}}_{corr_i} S_{f_i} - \sum_{f_i \in S} \underbrace{(\nabla \phi)_{f_{ci}} \cdot (\mathbf{n}_i - \cancel{\mathcal{L}}_{corr_i} \mathbf{d}_i) S_{f_i}}_{\text{here we use known values of } \phi} \\ &= \left(\sum_{f_i \in S} \alpha_{C_i} \right) \phi_C + \sum_{f_i \in S} \alpha_{N_i} \phi_{N_i} + \sum_{f_i \in S} \beta_i, \end{aligned} \quad (\text{B.57})$$

⁸ Similar to the one-dimensional example for density along a segment given by Equation B.5 on page 160, but for volumes.

where $(\nabla\phi)_{f_{ci}}$ is computed using Equation B.68 and

$$\begin{aligned}\alpha_{N_i} &= -\mathcal{L}_{corr_i} S_{f_i}, \\ \alpha_{C_i} &= -\alpha_{N_i}, \\ \beta_i &= (\nabla\phi)_{f_{ci}} \cdot (\mathbf{n}_i - \mathcal{L}_{corr_i} \mathbf{d}_i) S_{f_i}.\end{aligned}\tag{B.58}$$

Equation B.56 now becomes

$$\left(\sum_{f_i \in S} \alpha_{C_i}\right) \phi_C + \sum_{f_i \in S} \alpha_{N_i} \phi_{N_i} + \sum_{f_i \in S} \beta_i = (q)_{C_c} C_V,\tag{B.59}$$

which can be rewritten in the convenient form

$$a_C \phi_C + \sum_{f_i \in S} a_{N_i} \phi_{N_i} = b_C,\tag{B.60}$$

where

$$a_C = \sum_{f_i \in S} \alpha_{C_i}, \quad a_{N_i} = \alpha_{N_i}, \quad b_C = (q)_{C_c} C_V - \sum_{f_i \in S} \beta_i.\tag{B.61}$$

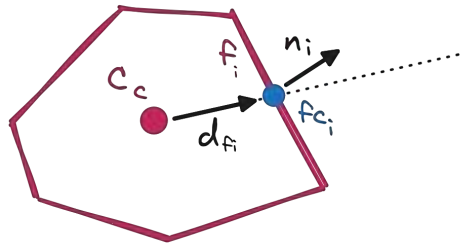
Note that the simplified form given by Equation B.60 resembles the system $\mathbf{Ax} = \mathbf{b}$ mentioned earlier. In particular, the system of numerical equations for the diffusion equation above is given by

$$\mathbf{A}[\phi] = \mathbf{b},\tag{B.62}$$

where \mathbf{A} is composed of diagonal values a_{C_j} and off-diagonal values $a_{N_{ji}}$, $[\phi]$ is the vector of all cell values ϕ_{C_j} , and \mathbf{b} is the vector of all source terms b_{C_j} , with $j \in [1, \text{number of cells}]$.

B.1.7 Boundary Conditions

Figure 60 – Boundary faces of the numerical domain connect to a single cell. Therefore, boundary conditions specify field values at the face center f_{ci} . Note that the non-orthogonality may also appear in boundary faces since the connecting vector \mathbf{d}_{fi} may not align to the face normal \mathbf{n}_i .



Source: Elaborated by the author.

The flux in faces that belong to the boundaries of the numerical domain requires special treatment. Mesh boundary faces have only one cell connected, requiring a direct substitution of values in Equation B.53. The value at the boundary must be specified at the face integration point f_c and use the direction vector $\mathbf{d}_{fi} = f_{ci} - C_c$, connecting the cell center to the face center, unlike the previous vector \mathbf{d}_i that connected two cell centers – see Figure 60. Such specifications are called *boundary conditions*, and the two most common are:

- **Dirichlet Boundary Condition:**

The Dirichlet boundary condition directly specifies the value of the field at the the face center f_c . In the case the diffusion equation discussed in the previous section, the fluxes in left hand side of Equation B.56 would have a specified value for $\phi(f_{ci}) = \phi_{fci}$:

$$\begin{aligned} -(\nabla_{\mathbf{n}_i}\phi)_{f_{ci}}S_{f_i} &= -(\phi_{f_{ci}} - \phi_C) \mathcal{L}_{corr_{f_i}} S_{f_i} - (\nabla\phi)_{f_{ci}} \cdot (\mathbf{n}_i - \mathcal{L}_{corr_{f_i}} \mathbf{d}_{f_i}) S_{f_i} \\ &= \phi_C \mathcal{L}_{corr_{f_i}} S_{f_i} - \phi_{N_i} \mathcal{L}_{corr_{f_i}} S_{f_i} - (\nabla\phi)_{f_{ci}} \cdot (\mathbf{n}_i - \mathcal{L}_{corr_{f_i}} \mathbf{d}_{f_i}) S_{f_i} \quad (\text{B.63}) \\ &= \alpha_{C_i} \phi_C + \beta_i \end{aligned}$$

Note that since $\phi_{f_{ci}}$ is given, the term respective to α_N is merged to β .

- **Neumann Boundary Condition:**

The Neumann boundary condition directly specifies the value $F_f = \mathbf{J}_f \cdot \mathbf{n}_f$ of the flux along the normal \mathbf{n}_f of f :

$$\begin{aligned} \mathbf{J}_f \cdot \mathbf{S}_f &= \mathbf{J}_f \cdot \mathbf{n}_f S_f \\ &= F_f S_f \quad (\text{B.64}) \\ &= \beta \end{aligned}$$

The Neumann Boundary condition is the same for non-orthogonal grids, the flux value becomes a source term β in the final system of equations.

B.2 Finite Area Method

The Finite Area Method (FAM), introduced by [Tuković \(2005\)](#), is a specialization of the FVM, described in the previous chapter, for solving PDEs on curved surfaces. Mainly, the FAM splits the surface domain into discrete cells, called finite areas, defined by flat polygonal areas bounded by straight edges — left side in [Figure 61](#). Therefore, the area integral of a given cell C representing a surface area Γ can be approximated by the midpoint rule as

$$\int_{\Gamma} \phi d\Gamma \approx \phi_C C_A, \quad (\text{B.65})$$

where C_A is the area of C and ϕ_C is the cell value of ϕ in C . The cell value comes from the midpoint approximation of the area integral, $(\phi)_{C_c}$, where C_c is the center point of C . In the following, the subscript $(\star)_p$ indicates the value of a field at the location p , $(\star)_A$ denotes the area of a cell, and $(\star)_c$ denotes the center point.

Like FVMs, the discretization in the FAM also uses the divergence theorem⁹ and analogously defines the fluxes in the edges. Each cell C may share its edge e_i with the neighbor cell N_i ,

⁹ See [subsection B.1.1](#).

with index $i \in [0, \text{number of edges of } C]$. The flux through the edge e_i is computed in the center point of the edge, e_{ci} , and uses the edge length vector¹⁰

$$\mathbf{L}_{e_i} = \mathbf{m}_{e_i} |\mathbf{L}_{e_i}| = \mathbf{m}_{e_i} L_{e_i}, \tag{B.66}$$

where \mathbf{m}_{e_i} is one of the bi-normal vectors associated with the edge e_i , along with \mathbf{n}_{e_i} , and has the same direction of $e_{ci} - C_c$ — see right side of Figure 61.

Figure 61 – The FAM applies the strategy of FVMs on curved surface domains by discretizing the integrals over finite areas. These cells are polygonal areas bounded by edges. The flux between two neighbor cells, C and N_i , passes through their shared edge, e_i . Each cell has a surface normal vector \mathbf{n}_C , and each edge has two bi-normal vectors, \mathbf{n}_i and \mathbf{m}_i , which define the edge length vector \mathbf{L}_{e_i} .



Source: Elaborated by the author.

The discretization under the FAM scheme is analogous to the FVM, and uses Equation B.66 to compute the fluxes. Here are some examples:

- **Divergent term $\nabla \cdot \mathbf{u}$:**

$$\int_{\Gamma} \nabla \cdot \mathbf{u} d\Gamma = \oint_{\partial\Gamma} (\mathbf{u} \cdot \mathbf{m}) d\partial\Gamma \approx \sum_{e_i \in E} (\mathbf{u})_{e_{ci}} \cdot \mathbf{L}_{e_i}, \tag{B.67}$$

where \mathbf{m} is the normal field pointing outward Γ , E is the set of edges that approximate $\partial\Gamma$, and $\mathbf{u}(\mathbf{x})$ is a vector field.

- **Scalar gradient term $\nabla \phi$:**

$$\int_{\Gamma} \nabla \phi d\Gamma = \oint_{\partial\Gamma} (\phi \mathbf{m}) d\partial\Gamma \approx \sum_{e_i \in E} (\phi)_{e_{ci}} \mathbf{L}_{e_i}, \tag{B.68}$$

where $\phi(\mathbf{x})$ is a scalar field.

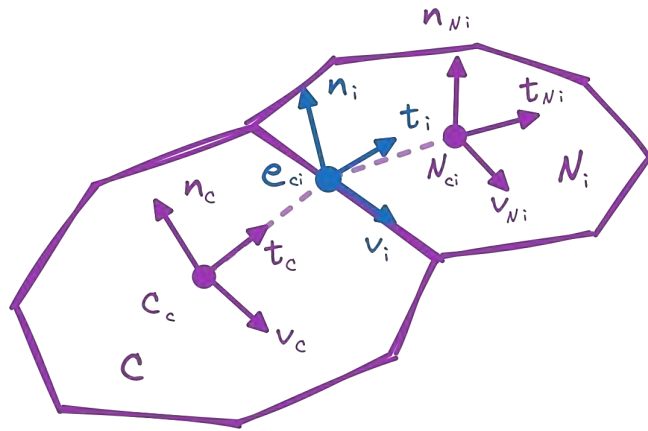
Note that the discretizations above require the value of fields at edge centers. For scalar fields, the value can be computed via linear interpolation or upwind schemes, as described in

¹⁰ The length vector \mathbf{L}_e is analogous to the face area vector \mathbf{S}_f used in FVMs.

subsection B.1.4. However, the direct interpolation of vector quantities does not guarantee a resulting vector tangential to the domain surface.

In order to produce edge vectors that are tangential to the domain surface, the cell vector quantities are interpolated in their local cell coordinates. A different local coordinate system for each cell is defined based on the target edge. Figure 62 shows the local coordinate systems used in the interpolation between two cells, C and N_i . The local coordinates of the cell C is composed by the surface normal vector \mathbf{n}_C , and two tangential vectors, $\mathbf{t}_C = \frac{e_{ci} - C_c}{\|e_{ci} - C_c\|}$ and $\mathbf{v}_C = \mathbf{t}_C \times \mathbf{n}_C$.

Figure 62 – Interpolations of cell vector quantities to the center of edges use local coordinates defined in each point to guarantee surface-tangential resulting vectors.



Source: Elaborated by the author.

Let \mathbf{T}_\star be the transformation into the local coordinates system of C , N_i , or e_i . Then the interpolation of the vector field \mathbf{u} into the edge center e_{ci} is given by

$$(\mathbf{u})_{e_{ci}} = \mathbf{T}_{e_i}^{-1}(w_i \mathbf{T}_C \mathbf{u}_C + (1 - w_i) \mathbf{T}_{N_i} \mathbf{u}_{N_i}), \quad (\text{B.69})$$

where w_i is the interpolation factor.

OPENFOAM

OpenFOAM¹ is an open-source software that serves as a C++ toolbox for developing numerical solutions for various CFD problems. The OpenFOAM Foundation maintains and distributes the source code under the GNU General Public License Version 3. Due to its open access, flexibility, and robustness, OpenFOAM established a large community of users and developers in academia, research institutions, and industry. Its success is because OpenFOAM provides convenient usage of its wide variety of solvers for users, and its architecture benefits developers who need to modify existing solvers or create new ones.

Primarily, OpenFOAM uses the Finite Volume Method to discretize and solve a given set of PDEs — see [section B.1](#). Once a finite volume mesh representing the solution domain contains the fields of the variables for a given set of equations, OpenFOAM’s discretization functions offer a direct way to express the equations in code. Take, for example, the equation:

$$\frac{\partial T}{\partial t} + \nabla \cdot (T\mathbf{u}) = 0, \quad (\text{C.1})$$

for a scalar field T transported by a velocity field \mathbf{u} . In OpenFOAM the equation is transcribed to [Source code 4](#). See [section C.2](#) for a list of discretization functions.

Source code 4 – OpenFOAM’s version of [Equation C.1](#) for C++.

```
1: solve (
2:     fvm::ddt(T) + fvm::div(u, T)
3: );
```

This chapter introduces the concepts and pieces of OpenFOAM relevant to the project. Refer to [Jasak, Jemcov and Tuković \(2007\)](#) for a general introduction on the code design, [Holzmann \(2016\)](#) for mathematical derivations on OpenFoam, and [Darwish and Moukalled \(2016\)](#) for a comprehensive material on Finite Volume method applications in OpenFOAM.

¹ The name OpenFOAM stands for *Open-source Field Operation And Manipulation*.

C.1 Field Representations

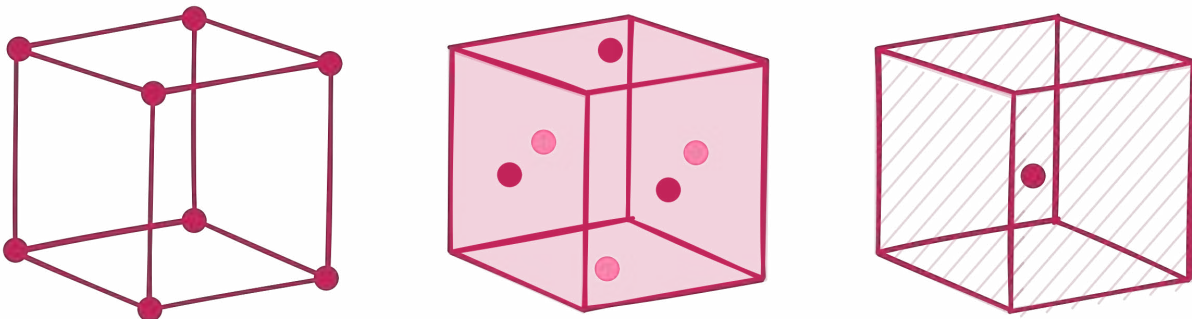
OpenFOAM can represent dimensional and dimensionless scalar, vector, and tensor variable fields. Many field operations have convenient C++ operators, such as the dot-product for two vector fields listed in [Source code 5](#).

Source code 5 – OpenFOAM provides operators for common operations. For example, the `&` operator performs the scalar product between two vector fields a and b .

```
1:     scalarField c = a & b;
```

OpenFOAM defines *Geometric Fields* as the spatial distribution of the physical quantities over the physical domain for which the solution is calculated. A geometrical mesh decomposes the domain into disjoint cells called volumes. Field values are then stored in specific locations inside each volume to possibilitate the numerical discretizations of the equations. Such locations describe the quantities of a particular field over the physical domain. The discretization defines the proper location of each field in the mesh, and fields can be assigned to vertex positions, face centers, or cell centers as shown in [Figure 63](#).

Figure 63 – Common mesh locations for field spatial locations in the physical domain, from left to right, vertices, face centers, and cell centers.



Source: Elaborated by the author.

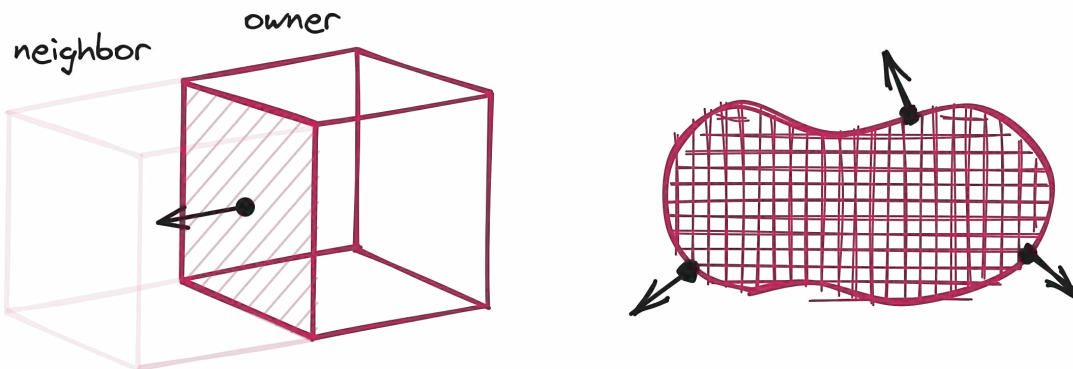
In particular, OpenFOAM utilizes a data structure for the numerical mesh called *polyMesh*. The *polyMesh* structure can handle polyhedral cells bounded by arbitrary polygonal faces. This configuration allows unstructured meshes with different types of elements containing a variable amount of faces, however, with specific requirements:

- Cells must be convex;
- Every edge in the cell must be used by exactly two faces of the same cell;
- Cells must not overlap one another.

The central element in the *polyMesh* is the face, which provides the mesh's topology. Each face connects at most two cells and obligatorily belongs to one of the connecting cells,

called the *owner*. Thus, each face is associated with an owner and may or may not connect to a second cell called the *neighbor* — boundary faces do not have their neighbor cell. The orientation of a face determines which cell is its owner cell, producing consistent indexing throughout the mesh. In particular, the face's normal always points outwards the owner cell — see Figure 64.

Figure 64 – The polyMesh structure associates a owner cell and a neighbor cell for each face based on the face's orientation. The normal of a face always points outwards the owner cell, see the left figure. Consequently, the normals at the boundaries also point outwards the numerical domain, on the right.



Source: Elaborated by the author.

OpenFOAM makes a distinction between *internal faces* and *boundary faces*. Boundary faces are faces that are connected to only a single cell, the owner cell. However, boundary faces additionally carry extra information that the solver uses to define the boundary conditions for the numerical system. Defining fields stored only by boundary or internal faces is also possible.

C.2 Discretizations

This section lists some of the discretization functions provided by OpenFOAM for the terms encountered in equations. As described in subsection B.1.6 on page 172, the discretizations compose the final system of numerical equations:

$$\mathbf{Ax} = \mathbf{b}, \quad (\text{C.2})$$

where \mathbf{x} is the set of unknowns, \mathbf{A} is the matrix of discretized coefficients, referred to as *implicit terms*, and \mathbf{b} contains the source terms, also referred to as *explicit terms*. Therefore, known values marked by the superscript $(\star)^o$, including values from previous time steps i , $(\star)^{n-i}$, are handled as explicit terms.

OpenFOAM provides two modules with discretization functions for implicit and explicit terms, called *fvm* and *fvc*, respectively. Values are naturally computed and stored in cell centers, marked in the equations by the subscripts $(\star)_{C_c}$ and $(\star)_{N_{ci}}$. Values computed at face centers are marked with the subscript $(\star)_{f_{ci}}$. In the following, the discretizations consider a cell C with volume C_V and center C_c .

- `fmv::ddt(★)`

– First-Order Implicit Euler

$$\left(\frac{\partial \star}{\partial t}\right)_{C_c} \approx \frac{C_V}{\Delta t} ((\star)^n - (\star)^{n-1})_{C_c}. \quad (\text{C.3})$$

– Second-Order Implicit Euler

$$\left(\frac{\partial \star}{\partial t}\right)_{C_c} \approx \frac{C_V}{2\Delta t} \left(3(\star)^n - 4(\star)^{n-1} + (\star)^{n-2}\right)_{C_c}. \quad (\text{C.4})$$

- `fmv::div(Φo, ★)`

$$\nabla \cdot (\Phi^o \otimes \star)_{C_c} \approx \sum_{f_i \in S} (\Phi^o \otimes \star)_{f_{ci}}, \quad \text{where } \Phi_{f_{ci}}^o = (\rho \mathbf{u})_{f_{ci}}^o. \quad (\text{C.5})$$

– Interpolation

$$\sum_{f_i \in S} (w_i \Phi^o)_{f_{ci}} \otimes (\star)_{C_c} + \sum_{f_i \in S} ((1 - w_i) \Phi^o)_{f_{ci}} \otimes (\star)_{N_{ci}}, \quad (\text{C.6})$$

where w_i is the interpolation weight based on the cell center to face centers distances, $\mathbf{d}_C = f_{ci} - C_c$ and $\mathbf{d}_{N_i} = N_{ci} - f_{ci}$:

$$w_i = \frac{\mathbf{n} \cdot \mathbf{d}_{N_i}}{\mathbf{n} \cdot (\mathbf{d}_C + \mathbf{d}_{N_i})}. \quad (\text{C.7})$$

– Upwind

$$(\star)_{f_{ci}} = \begin{cases} (\star)_{C_c}, & \Phi_{f_{ci}}^o \geq 0, \\ (\star)_{N_{ci}}, & \Phi_{f_{ci}}^o < 0. \end{cases} \quad (\text{C.8})$$

- `fvm::laplacian(★)2`

$$\begin{aligned} (\Delta \star)_{C_c} &\approx \sum_{f_i \in S} (\nabla_{\mathbf{n}_i} \otimes \star)_{f_{ci}} S_{f_i} \\ &\approx a_C (\star)_{C_c} + \sum_{f_i \in S} a_{N_i} (\star)_{N_i} + b_C. \end{aligned} \quad (\text{C.9})$$

- `fvc::flux(★)`

$$(\star)_{f_c} \cdot \mathbf{S}_f. \quad (\text{C.10})$$

- `fvc::interpolate(★)`

$$(\star)_{f_c} = \lambda_C \star_C + \lambda_N \star_N. \quad (\text{C.11})$$

- `fvc::grad(★)`

$$(\nabla \otimes \star)_{C_c} \approx \frac{1}{C_V} \sum_{f_i \in S} (\star)_{f_{ci}} \otimes \mathbf{S}_{f_i}. \quad (\text{C.12})$$

² See [subsection B.1.6](#).

- `fv::div(★)`

$$(\nabla \cdot \star)_{C_c} \approx \frac{1}{C_V} \sum_{f_i \in S} (\star)_{f_{ci}} \cdot \mathbf{S}_{f_i}. \quad (\text{C.13})$$

- `MULES::explicitSolve`

OpenFOAM provides a Flux Corrected Transport (FCT)³ method implementation called Multidimensional Universal Limiter for Explicit Solution (MULES) (DAMIÁN; NIGRO, 2014). The FCT method guarantees boundedness in the solution of the convection equation by computing the flux Φ as Equation B.52

$$\Phi = \Phi^L + \lambda(\Phi^H - \Phi^L),$$

where Φ^L and Φ^H are fluxes computed from low-order and high-order methods, respectively, and λ is computed iteratively. MULES solves explicitly the transport equation

$$\frac{\partial \phi}{\partial t} + \nabla \cdot \Phi = 0 \quad (\text{C.14})$$

for a scalar field ϕ through the discretization

$$\phi^{n+1} = \phi^n - \frac{\Delta t}{C_V} \sum_{f_i} (\Phi)_{f_{ci}}^n. \quad (\text{C.15})$$

The procedure for computing the values of λ uses local and global extrema for ϕ^n , as detailed by section 2.6.3 in Damian (2013).

An equivalent set of functions for the FAM is provided by OpenFOAM with the correspondent function namespaces `fam` and `fac`.

C.3 Numerical Algorithm

Physical models such as the Navier-Stokes Equations for incompressible flows

$$\nabla \cdot \mathbf{u} = 0, \quad (\text{C.16})$$

$$\frac{\partial \mathbf{u}}{\partial t} + \nabla \cdot (\mathbf{u} \otimes \mathbf{u}) = -\frac{1}{\rho} \nabla p - \nabla \cdot \boldsymbol{\tau} + \mathbf{g}, \quad (\text{C.17})$$

$$\boldsymbol{\tau} = 2\mu \mathbf{D} - \frac{2}{3}\mu(\nabla \cdot \mathbf{u}) \quad \text{and} \quad \mathbf{D} = \frac{1}{2}(\nabla \otimes \mathbf{u} + (\nabla \otimes \mathbf{u})^T) \quad (\text{C.18})$$

belong to the family of *coupling problems*. That is because Equation C.17 equation couples velocity and pressure, which poses an initial challenge to the solution of the problem⁴. The solution is only possible because Equation C.16 adds extra conditions for the velocity. Moreover, the non-linear nature of the equation requires iterative methods for this solution. The example of algorithm below splits the equations, so each iteration i performs the following steps:

³ See subsection B.1.5.

⁴ There are three momentum equations, one for each velocity component, but four unknown variables, the three velocity components, and the pressure.

1. Use the previously computed (or estimated) values \mathbf{u}^{i-1} and p^{i-1} , and solve for \mathbf{u}^* :

$$\begin{aligned} \frac{\partial \mathbf{u}^*}{\partial t} + \nabla \cdot (\mathbf{u}^{i-1} \otimes \mathbf{u}^*) &= -\frac{1}{\rho} \nabla p^{i-1} - \nabla \cdot \boldsymbol{\tau}^* + \mathbf{g}, \\ \boldsymbol{\tau}^* &= \nu \nabla \otimes \mathbf{u}^* + \nu (\nabla \otimes \mathbf{u}^*)^T - \frac{2}{3} \nu (\nabla \cdot \mathbf{u}^*) \mathbf{I}, \\ \mathbf{A} \mathbf{u}^* &= \mathbf{b} \end{aligned} \quad (\text{C.19})$$

where $\nu = \mu/\rho$. Note that the non-linearity of the advection term is solved by the use of \mathbf{u}^{i-1} , allowing the use of advection schemes (see [subsection B.1.5](#)). This step is generally referred to as *momentum prediction*.

2. Use the intermediary velocity field \mathbf{u}^* solve the pressure equation⁵ for p^i :

$$\begin{aligned} \frac{1}{\rho} \nabla^2 p^i + \nabla \cdot (\nabla (\mathbf{u}^* \otimes \mathbf{u}^*)) &= 0, \\ \mathbf{A}[p^i] &= \mathbf{b}. \end{aligned} \quad (\text{C.20})$$

3. Use \mathbf{u}^* and p^i to *correct* the values of \mathbf{u} for the next step. As explained later, this process includes a *flux correction* and a *momentum correction*. The result is \mathbf{u}^i , which becomes the \mathbf{u}^{i-1} in the next iteration, and the same happens to p^i .

The *prediction-correction* algorithm above follows the idea of the well known Semi-Implicit Method for Pressure-Linked Equations (SIMPLE) ([PATANKAR; SPALDING, 1983](#)) algorithm. However, the SIMPLE algorithm is primarily designed to only solve steady-state problems, which is not the case of the equations listed above. Transient solutions can be achieved through the variations of the SIMPLE algorithm called Pressure Implicit with Splitting of Operators (PISO) ([ISSA, 1986](#)), and the widely used combination of both, the PIMPLE algorithm. OpenFOAM provides the implementation for all the three algorithms.

⁵ The equation above comes from applying the divergence operator on the momentum equation, [Equation C.17](#), and using the continuity equation, [Equation C.16](#), (assuming ν constant):

$$\begin{aligned} \frac{\partial \nabla \cdot \mathbf{u}}{\partial t} + \nabla \cdot (\nabla \cdot (\mathbf{u} \otimes \mathbf{u})) &= -\frac{1}{\rho} \nabla \cdot (\nabla p) - \nabla \cdot \underbrace{(\nabla \cdot \boldsymbol{\tau})}_{\text{expand}} + \nabla \cdot \mathbf{g} \\ \nabla \cdot (\nabla \cdot (\mathbf{u} \otimes \mathbf{u})) &= -\frac{1}{\rho} \nabla \cdot (\nabla p) - \nabla \cdot \left(\nabla \cdot (\nu \nabla \otimes \mathbf{u}) + \underbrace{\nabla \cdot (\nu (\nabla \otimes \mathbf{u})^T)}_{\equiv} - \frac{2}{3} \nabla \cdot (\nu (\nabla \cdot \mathbf{u}) \mathbf{I}) \right) \\ \nabla \cdot (\nabla \cdot (\mathbf{u} \otimes \mathbf{u})) &= -\frac{1}{\rho} \nabla \cdot (\nabla p) - \underbrace{\nabla \cdot (\nabla \cdot (\nu \nabla \otimes \mathbf{u}))}_{\equiv} - \nabla \cdot \left(\nu \nabla (\nabla \cdot \mathbf{u}) + \underbrace{(\nabla \nu) \cdot (\nabla \otimes \mathbf{u})}_{\equiv} \right) \\ \frac{1}{\rho} \nabla^2 p + \nabla \cdot (\nabla \cdot (\mathbf{u} \otimes \mathbf{u})) &= \nabla^2 (\nabla \cdot \mathbf{u}) \end{aligned}$$

The PISO algorithm repeats the steps 2 and 3 in order to improve the accuracy of the output values of velocity and pressure within each time step, which increases the accuracy of the transient term in step 1. In turn, The PIMPLE algorithm essentially adds another loop, including step 1 and the PISO loop, within each time step. The main advantage of the PIMPLE algorithm is that it can handle larger Courant numbers⁶ $Co \gg 1$, leading to larger simulation time steps.

In order to describe the PIMPLE algorithm, let us put the pressure term $-\nabla p$ aside from the momentum equation system $\mathbf{A}\mathbf{u} = \mathbf{b}$ and separate the diagonal from the matrix \mathbf{A} , so $\mathbf{A} = \mathbf{A}_{diag} + \mathbf{A}_{off}$, where \mathbf{A}_{diag} is the matrix containing the only the diagonal entries of \mathbf{A} and \mathbf{A}_{off} contains the off-diagonal entries. Let $\mathbf{B}(\mathbf{u})$ be a function of \mathbf{u} representing all off-diagonal elements and source terms,

$$\mathbf{B}(\mathbf{u}) = -\mathbf{A}_{off}\mathbf{u} + \mathbf{b}, \quad (\text{C.21})$$

so the original system, with the pressure term, is reconstructed as

$$\mathbf{A}_{diag}\mathbf{u} = \mathbf{B}(\mathbf{u}) - \nabla p. \quad (\text{C.22})$$

Since \mathbf{A}_{diag} is a diagonal matrix, it will be used as a scalar field A_{diag} in the following equations. The **momentum correction** is expressed as

$$\mathbf{u} \leftarrow \frac{\mathbf{B}(\mathbf{u}^o)}{A_{diag}} - \frac{\nabla p^o}{A_{diag}}, \quad (\text{C.23})$$

where \mathbf{u}^o and p^o represent previous (or intermediary) values, which are essentially explicit terms in the system above. The same procedure can be applied to the **flux correction** of Φ_f :

$$\Phi_f \leftarrow \mathbf{S}_f \cdot \left(\frac{\mathbf{B}(\mathbf{u})}{A_{diag}} \right)_f - \left(\frac{|\mathbf{S}_f|}{A_{diag}} \right)_f \nabla_{\mathbf{n}} p_f. \quad (\text{C.24})$$

The **pressure equation**, Equation C.20, becomes

$$\nabla \cdot \frac{1}{A_{diag}} \nabla p = \nabla \cdot \left(\frac{\mathbf{B}(\mathbf{u})}{A_{diag}} \right), \quad (\text{C.25})$$

and will use the previous equations. As characterized in the first step of the algorithm described earlier, the **momentum prediction**⁷ computes an intermediary velocity field \mathbf{u}^* from previous/initial states of \mathbf{u}^o and p^o .

As mentioned, the PIMPLE algorithm loops over the *prediction-correction* scheme within each time step, where the correction half contains the PISO loop. The outer loop, called the PIMPLE loop, increases the system's overall accuracy and allows for $Co > 1$. For non-orthogonal meshes, an extra loop adds the non-orthogonal contribution $V_{corr}(\nabla p) = (\nabla p)_{f_c} \cdot \mathbf{V}_f$

⁶ The Courant number $Co = \frac{u\Delta t}{\Delta x}$ measures how fast information travels through the numerical grid. A $Co > 1$ means that a fluid particle will move a distance greater than one cell length. The Co has direct relation to the convergence of the numerical algorithm.

⁷ This text omits some details about the momentum prediction step. In reality, the system is partially solved first, through *under-relaxation*, using the momentum equation without the pressure term. Then, it is solved again with the pressure term included.

to the discretization of the pressure equation — see [subsection B.1.4](#) on [page 167](#). Essentially, the computed pressure p is fed back as p^o to the same equation as an explicit term for the non-orthogonal term:

$$\nabla \cdot \frac{1}{A_{diag}} \nabla p = \nabla \cdot \left(\frac{\mathbf{B}(\mathbf{u})}{A_{diag}} \right) + V_{corr}(\nabla p^o). \quad (\text{C.26})$$

[Figure 65](#) illustrates the description above and [Source code 6](#) shows an example of the controls OpenFOAM provides for the PIMPLE algorithm. In OpenFOAM, the number `nCorrectors` correspond to the number of PISO loops, `nOuterCorrectors` to PIMPLE loops, and for the non-orthogonal correction loops described above, `nNonOrthogonalCorrectors`.

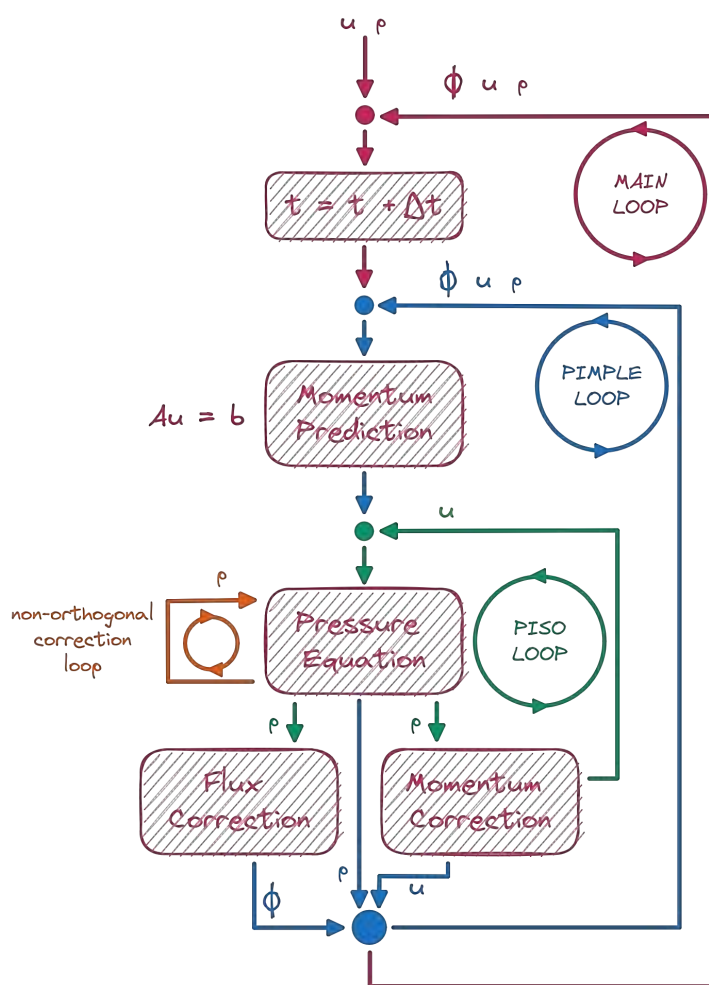
Source code 6 – Example of configuration of the PIMPLE algorithm in OpenFOAM.

```

1:     PIMPLE
2:     {
3:         momentumPredictor    yes;
4:         nOuterCorrectors      1;
5:         nCorrectors            2;
6:         nNonOrthogonalCorrectors 2;
7:     }
```

This section only briefly describes the type of numerical algorithm provided by OpenFOAM. Therefore, many details not mentioned deserve attention, such as solvers of linear systems of equations, accuracy, under-relaxation, and convergence. Refer to [Greenshields and Weller \(2022\)](#) for a comprehensive introduction on all topics.

Figure 65 – The PIMPLE algorithm alternates between prediction and correction phases by nested loops. The loops are executed within each main iteration, guaranteeing the method’s accuracy and convergence for larger time steps.



Source: Elaborated by the author.

TODO LIST

TODO	72
TODO	72
TODO	72
TODO	75
flux fixed pressure	106
conclusions	112
CFL	113
convergence	113
openvdb	116
foam2vdb	117
extrude	118

